The Ionospheric Current System and its Temporal Evolution during Rapid Solar Wind Dynamic Pressure Increases

Michael Madelaire

Thesis for the Degree of Philosophiae Doctor (PhD)
University of Bergen, Norway
2024

UNIVERSITY OF BERGEN

The Ionospheric Current System and its Temporal Evolution during Rapid Solar Wind Dynamic Pressure Increases

Michael Madelaire

Thesis for the Degree of Philosophiae Doctor (PhD)
at the University of Bergen

Date of defence: 04.04.2024

Year: 2024

Title: The Ionospheric Current System and its Temporal Evolution during Rapid Solar Wind Dynamic Pressure Increases

Name: Michael Madelaire

Print: Skipnes Kommunikasjon / University of Bergen

Abstract

Research is a quest for knowledge of the unknown. In this thesis, we try to further our collective understanding of the complex interactions within the dynamic magnetosphere-ionosphere system. One might be tempted to suggest that this work is driven by the potential to address societal challenges, such as the effects of ground-induced currents on electrical infrastructure. However, that would not be entirely truthful. The true motivation behind this research is pure curiosity. After four years of diving head-first into every rabbit hole that presented itself, I have gained an appreciation of how little I know.

We investigate the temporal development of the ionospheric current system during rapid increases in solar wind dynamic pressure using ground-based magnetic field measurements. In Paper I, we utilize machine learning to develop an algorithm capable of detecting abrupt increases in the solar wind dynamic pressure. By applying the algorithm to over two decades of in-situ solar wind data, we compile a list of events and determine their arrival at Earth. Paper II conducts a statistical analysis of the high-latitude geomagnetic response to the events identified in Paper I, revealing distinct patterns and asymmetries that shed light on the underlying physical processes. In Paper III, we tackle the challenge of spatial resolution in empirical models of the ionospheric current system, a crucial aspect of interpreting data from the upcoming EZIE cubesat mission. The methodology we develop enhances our ability to design and evaluate the performance of empirical models. Paper IV introduces a novel technique for estimating the often-neglected ionospheric induction electric field, highlighting its significance in the dynamic behavior of the ionosphere. Collectively, this body of work advances our understanding and modeling capabilities of the temporal evolution of the ionospheric current system.

Abstrakt

Forskning er en jakt på kunnskap om det ukjente. I denne avhandlingen prøver vi å utvide vår kollektive forståelse av de komplekse samspillene innenfor det dynamiske magnetosfære-ionosfæresystemet. Man kunne fristes til å antyde at dette arbeidet er drevet av potensialet for å adressere samfunnsutfordringer, som for eksempel effekten av induserte strømmer på elektrisk infrastruktur. Det ville imidlertid ikke være helt ærlig. Den sanne motivasjonen bak denne forskningen er ren nysgjerrighet. Etter fire år med å dykke hode først inn i hvert eneste mysterium jeg har støtt på, har jeg fått en anerkjennelse av hvor lite jeg faktisk vet.

Vi undersøker den tidsmessige utviklingen av ionosfærestrømsystemet under raske økninger i solvindens dynamiske trykk ved hjelp av målinger av det magnetfeltet på bakken. I Artikkel I bruker vi maskinlæring for å utvikle en algoritme som kan oppdage raske økninger i solvindens dynamiske trykk. Ved å bruke algoritmen på mer enn to tiår med in situ solvinddata, lager vi en liste over begivenheter og bestemmer deres ankomst til Jorden. I Artikkel II utfører vi en statistisk analyse av den høye breddegrads geomagnetiske respons på hendelsene identifisert i Artikkel I, og avslører distinkte mønstre og asymmetrier som kaster lys over de underliggende fysiske prosessene. I Artikkel III tar vi for oss utfordringen med romlig oppløsning i empiriske modeller av ionosfærens strømsystem, et kritisk aspekt ved tolkning av data fra den kommende EZIE-cubesatmisjonen. Metodikken vi utvikler forbedrer vår evne til å designe og evaluere ytelsen til empiriske modeller. I Artikkel IV introduserer vi en ny teknikk for å estimere det ofte oversette induksjonselektriske feltet i ionosfæren, noe som fremhever dets betydning i ionosfærens dynamiske atferd. Samlet sett tar dette arbeidet vår forståelse og modelleringskapasitet av ionosfærens strømsystems tidsutvikling fremover.

Acknowledgements

This thesis would not have been possible without the guidance from my supervisors Kalle Laundal, Jone Reistad, and Spencer Hatch. Thank you for steering me in the right direction while allowing me the creative freedom to explore my interests. Your inclusion of me in various projects has been invaluable, offering a glimpse into international collaborations and what I can expect from an academic career.

To my fellow PhD students, thank you for transforming our otherwise dull corridor into a fun workplace, whether through paper airplane competitions or *throwing cows*.

My decision to move to Bergen was heavily influenced by my family's encouragement. Mom, Dad, Martin, and Morten, I know I'm bad at calling, but just knowing that you're always there for me means a lot. I'd say I'll call more, but let's be realistic.

And Salina, this hasn't been easy for us. Your patience and support means everything to me. Thank you for just being you.

Michael Madelaire
Bergen, December 2023

List of publications

This thesis and the four papers included are submitted for the degree of philosophiae doctor (Ph.D.) in physics at the Department of Physics and Technology, University of Bergen.

Paper I M. Madelaire, K.M. Laundal, J.P. Reistad, S.M. Hatch, A. Ohma, S. Haaland, *Geomagnetic Response to Rapid Increases in Solar Wind Dynamic Pressure: Event Detection and Large Scale Response*, Frontiers in Astronomy and Space Science, Vol. 9, Article 904620, https://doi.org/10.3389/fspas.2022.904620, 2022

Paper II M. Madelaire, K.M. Laundal, J.P. Reistad, S.M. Hatch, A. Ohma, *Transient high latitude geomagnetic response to rapid increases in solar wind dynamic pressure*, Frontiers in Astronomy and Space Science, Vol. 9, Article 953954, https://doi.org/10.3389/fspas.2022.953954, 2022

Paper III M. Madelaire, K.M. Laundal, J. Gjerloev, S.M. Hatch, J.P. Reistad, H. Vanhamäki, C. Waters, A. Ohma, V. Merkin, R. Mesquita, *Spatial Resolution in Inverse Problems: The EZIE satellite mission*, Journal of Geophysical Research: Space Physics, Vol. 128, Article 5, https://doi.org/10.1029/2023JA031394, 2023

Paper IV M. Madelaire, K.M. Laundal, S.M. Hatch, H. Vanhamäki, J.P. Reistad, A. Ohma, V. Merkin, D. Lin *Estimating the Induction Electric Field in the Ionosphere Using Ground Magnetometer Data*, In review

During my PhD studies, I have also contributed to the following publications.

1. K.M. Laundal, J.H. Yee, V.G. Merkin, J.W Gjerloev, H. Vanhamäki, J.P. Reistad, M. Madelaire, K. Sorathia, P.J Espy, *Electrojet Estimates From Mesospheric Magnetic Field Measurements*, Journal of Geophysical Research: Space Physics, https://doi.org/10.1029/2020JA028644, 2021

2. K.M. Laundal, J.P. Reistad, S.M. Hatch, M. Madelaire, S.J. Walker, A.Ø. Hovland, A. Ohma, V.G. Merkin, K.A. Sorathia, *Local Mapping of Polar Ionospheric Electrodynamics*, Journal of Geophysical Research: Space Physics, https://doi.org/10.1029/2022JA030356, 2022

3. A.Ø. Hovland, K.M. Laundal, J.P. Reistad, S.M. Hatch, S.J. Walker, M. Madelaire, A. Ohma, *The Lompe code: A Python toolbox for ionospheric data analysis*, Frontiers in Astronomy and Space Science, https://doi.org/10.3389/fspas.2022.1025823, 2022

4. K.M. Laundal, M. Madelaire, A. Ohma, J.P. Reistad, S.M. Hatch, *The relationhip between interhemispheric asymmetries in polar ionospheric convection and the magnetic field line footpoint displacement field*, Frontiers in Astronomy and Space Science, https://doi.org/10.3389/fspas.2022.957223, 2022

5. A. Ohma, M. Madelaire, K.M. Laundal, J.P. Reistad, S.M. Hatch, S. Gasparini, S.J. Walker, *Background Removal from Auroral Images: Data driven dayglow modeling*, Earth and Planetary Physics, https://doi.org/10.26464/epp2023051, 2023

6. R. Elhawary, K.M. Laundal, J.P. Reistad, M. Madelaire, A. Ohma, *Substorm impact on dayside ionospheric currents*, Geophysical Research Letters, https://doi.org/10.1029/2023GL104800, 2023

7. A. Ohma, K.M. Laundal, M. Madelaire, S.M. Hatch, S. Gasparini, J.P. Reistad, S.J. Walker, M. Decotte, *Excitation and decay of the auroral oval*, in review, https://doi.org/10.22541/essoar.169447428.84472457/v1, 2023

List of Abbreviations

ACE	Advanced Composition Explorer
AMIE	Assimilative Mapping of Ionospheric Electrodynamics
CF	Curl-free
DF	Divergence-free
DSCOVR	Deep Space Climate Observatory
EZIE	Electrojet Zeeman Imaging Explorer
FAC	Field-Aligned Current
FTW	For The Win
GIC	Ground-Induced Current
IMF	Interplanetary Magnetic Field
Lompe	Local Mapping of Polar Ionospheric Electrodynamics
L1	The first Lagrange point located $\sim 1.5 \times 10^6$ km from Earth towards the Sun
MHD	Magnetohydrodynamic
MI	Main Impulse
PI	Preliminary Impulse
PSF	Point-Spread Function
REMIX	RE-developed Magnetosphere-Ionosphere Coupler/Solver
SC	Sudden Commencement
SECS	Spherical Elementary Current System
SH	Spherical Harmonic

SNR	Signal-to-Noise Ratio
SOHO	Solar and Heliospheric Observatory
SVD	Singular Value Decomposition
WTF	What The Fuck
Wind	Wind Satellite

Contents

Chapter 1

Introduction

The ionosphere, a region of Earth's upper atmosphere energized by solar radiation and characterized by its ionized state, is a crucible for complex electrodynamical processes. It is a domain that couples with the magnetosphere and where the Earth's magnetic field interacts with charged particles, with profound implications for communication systems, navigation, and our electrical infrastructure. This thesis is dedicated to dissecting the electrodynamics of the ionosphere, focusing on the geomagnetic response to dynamic events imposed by the solar wind and the intrinsic electric fields that are fundamental to understanding ionospheric behavior.

In the body of this work, we explore both theoretical concepts and practical techniques to better understand the behavior of electric currents within the ionosphere. We introduce innovative techniques for probing the electric fields and currents to reveal the intricate behaviors that govern this region of our atmosphere.

Paper I lays the groundwork by employing machine learning to detect significant events impacting the ionospheric dynamics. This approach not only highlights the influence of solar wind pressure changes but also serves as a precursor to understanding the subsequent geomagnetic perturbations.

Moving beyond detection, Paper II provides an in-depth analysis of the geomagnetic response to these dynamic events. Through careful modeling of ground-based magnetic field measurements, we retrieve the patterns of geomagnetic perturbations at high latitudes, adding clarity to the current understanding of ionospheric electrodynamics.

In Paper III, we address a critical challenge in modeling ionospheric processes—the spatial resolution of inverse problems, particularly in light of the data from the upcoming EZIE cubesat mission. Our contributions aim to improve our interpretations of

ionospheric observations, ensuring that we can distinguish between model artifacts and genuine physical phenomena.

Finally, Paper IV confronts a traditionally neglected aspect of ionospheric electric fields: the induction electric field. We introduce a technique to quantify this component from ground magnetometer data, improving the accuracy of ionospheric models during dynamic events and highlighting the importance of considering the full suite of electric fields in our analyses.

This thesis begins with a brief introduction to the geomagnetic field's interaction with the solar wind. It then moves on to set the foundational understanding of ionospheric electrodynamics, followed by a synopsis of the methods and tools that have been utilized in the research presented in the subsequent papers. The concluding chapter offers a concise overview of the papers.

Paper I :

Geomagnetic Response to Rapid Increases in Solar Wind Dynamic Pressure: Event Detection and Large Scale Response

Paper II :

Transient High Latitude Geomagnetic Response to Rapid Increases in Solar Wind Dynamic Pressure

Paper III :

Spatial Resolution in Inverse Problems: The EZIE Satellite Mission

Paper IV :

Estimating the Ionospheric Induction Electric Field using Ground Magnetometer Measurements

Chapter 2

Solar wind

The space between the Sun, the Earth, and our neighboring planets is not completely empty. It is permeated by the *solar wind*—a plasma that originates from the Sun. This solar wind interacts with Earth's magnetic field, creating a sharp boundary known as the magnetopause. The magnetopause defines a cavity in space dominated by Earth's magnetic field, while beyond it, the Sun's magnetic influence prevails. The magnetopause's shape and the volume it encloses are determined by the balance of forces between Earth's magnetic field and the solar wind.

In this chapter, we give a brief introduction to the solar wind: origin, characteristics, large-scale structures, and how it is measured. This chapter aims to equip the reader with a conceptual understanding of the solar wind before proceeding to the implications of its interaction with Earth's magnetic field.

2.1 The Sun's magnetic field

The following section is a brief introduction to the Sun's magnetic field. The reader is referred to books such as Gombosi [1998]; Lang [2009]; Moldwin [2008] for a more in-depth review of the Sun's magnetic field, including its topology, temporal evolution, and the formation of open magnetic field lines, as well as phenomena like coronal holes, sunspots, etc.

The Sun's magnetic field undergoes an approximately 11-year *solar cycle*. At the start of the cycle, the Sun's magnetic field resembles a dipole. However, the Sun's rotation and the electromagnetic dynamics in its outer plasma layer cause the magnetic field lines to gradually tangle. This outer layer is *frozen-in* (see Baumjohann and Treumann

[2012]), allowing plasma to move along magnetic field lines but not across them. The Sun's rotation varies with latitude, with the equatorial region completing a rotation more quickly than the higher latitudes. This differential rotation twists the Sun's magnetic field, increasing the complexity of the magnetic topology. The solar cycle comprises two phases: the solar minimum, with a predominantly dipolar magnetic field, and the solar maximum, marked by a more intricate magnetic field.

During solar minimum, magnetic field lines near the heliographic equator are usually closed, with both ends anchored to the Sun. Towards the poles, field lines are more likely to be open, that is, with only one footpoint on the Sun. See Section 3.2.1 for a brief explanation of how magnetic field lines transition between being open and closed. Open field lines can lead to the formation of coronal holes, which appear as dark spots on the Sun, especially near the poles but sometimes closer to the equator. The radial configuration of field lines in a coronal hole restricts plasma convection, resulting in cooler temperatures and a darker appearance. The open lines also allow plasma to escape, reducing plasma density within these holes.

Coronal holes may persist into the solar maximum, but this phase is predominantly characterized by sunspots, which are dark patches on the Sun but much smaller than coronal holes and occur where the magnetic field lines are closed. Sunspots form when the magnetic field becomes tightly coiled, creating magnetic flux ropes (collections of magnetic field lines) that emerge from and re-enter the Sun's surface. The convective motion of plasma is reduced at these locations, giving sunspots their dark appearance. Additionally, plasma follows the magnetic field lines into the flux rope, leading to a higher density in sunspots as opposed to the lower density in coronal holes. The frequency of sunspots correlates with the solar cycle, serving as an indicator of its phase. Figure 2.1 illustrates the 11-year periodicity of observed sunspots.

2.2 Solar wind characteristics

The solar wind flows radially away from the Sun, but not uniformly. Near the Sun's equatorial plane, where the planets of our solar system tend to orbit, the solar wind is generally slower compared to higher heliographic latitudes [McComas et al., 2000]. Figure 2.2 shows the variation in solar wind speed with heliographic latitude observed by the Ulysses spacecraft as it orbited the Sun during a solar minimum. At Earth, it ranges from about 250 to 800 km/s, with speeds above and below approximately 450 km/s considered fast and slow, respectively [Schwenn, 1990, 2006; Temmer, 2021; Yermolaev et al., 2009]. It is common to classify the ambient solar wind as either slow

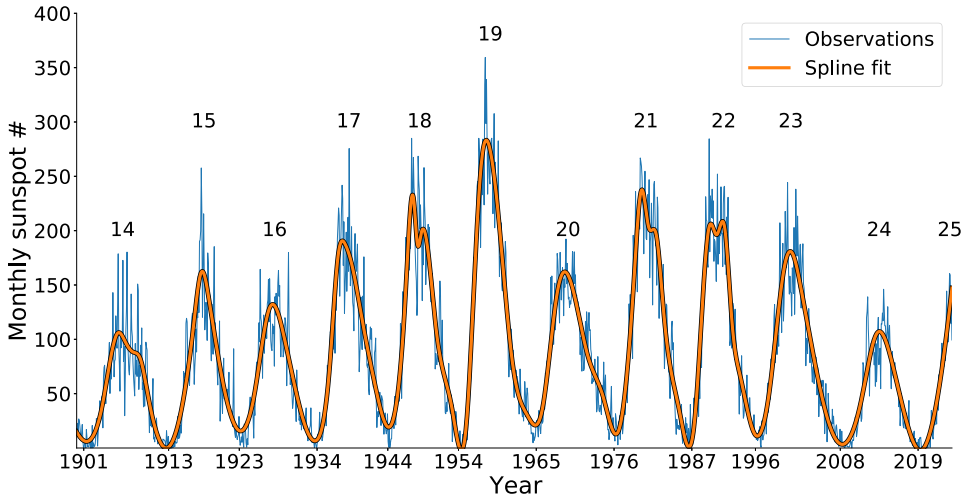

Figure 2.1: Number of observed sunspots as a function of time. The black line illustrates the number of sunspots observed each month. The red line is a spline fit for visualization purposes. The numbers above each peak indicate the solar cycle number. Data courtesy of WDC-SILSO, Royal Observatory of Belgium, Brussels and available at https://www.sidc.be/SILSO/datafiles.

or fast. Slow solar wind originates from areas of the Sun with closed magnetic field lines, whereas fast solar wind is associated with coronal holes [Schwenn, 2006; Temmer, 2021]. The reader is referred to Camporeale et al. [2017] for a discussion on the solar wind classes and an alternative classification based on machine learning.

The Sun consists mainly of hydrogen. Consequently, the solar wind plasma is primarily composed of electrons and hydrogen nuclei (protons). The density decreases with distance from the Sun. Near Earth, the number density is 10.8 ± 7.1 cm^{-3} for slow solar wind and 6.6 ± 5.1 cm^{-3} for fast solar wind [Temmer, 2021; Yermolaev et al., 2009]. However, the solar wind can also contain helium nuclei (alpha particles), which have four times the mass of hydrogen nuclei. The ratio between helium and hydrogen nuclei is $4.7 \pm 6.6\%$ for slow solar wind and $6.6 \pm 8.0\%$ for fast solar wind [Yermolaev and Stupin, 1997]. Therefore, it is crucial to consider the composition, as it can significantly affect the solar wind's dynamic pressure,

$$p_{dyn} = \sum n_i m_i v_i^2. \tag{2.1}$$

Here, n_i, m_i, and v_i are the number density, mass, and bulk speed of the ith ion species, respectively.

Although the solar wind flows radially outward from the Sun, the Sun itself rotates with

a period of approximately 27 days, known as a Carrington rotation. This rotation causes the solar wind to take on a spiral shape, known as the Parker spiral [Parker, 1958]. The angle of the arms in the Parker spiral increases with distance to the Sun. They typically have an angle of 45 degrees relative to the Sun-Earth line at 1 AU. Moreover, since the solar wind is a collisionless plasma, it can be considered *frozen-in* (see Baumjohann and Treumann [2012]), carrying the Sun's magnetic field into interplanetary space, thus termed the Interplanetary Magnetic Field (IMF). The solar wind plasma *carries* the IMF given the solar winds high plasma-beta, meaning that its thermal pressure is greater than the magnetic pressure [Baumjohann and Treumann, 2012]. The IMF flux density decreases with distance from the Sun, following a power-law relationship. The magnitude of the IMF, at Earth, is 5.9 ± 2.9 nT for slow solar wind and 6.4 ± 3.5 nT for fast solar wind [Temmer, 2021; Yermolaev et al., 2009].

During solar minimum, the solar wind near the heliographic equator is mainly confined to closed magnetic field lines, resulting in the magnetic field lines being stretched to form two planes, approximately parallel to the equatorial plane, of anti-parallel magnetic field lines. This configuration, following Ampère's law, constitutes the Heliospheric Current Sheet (HCS). Nearer to the solar maximum, when the magnetic field is more complex, the magnetic equator deviates from the heliographic equator defined by the Sun's rotational axis, taking on a wavy shape. A conceptual illustration of the HCS around solar maximum is provided in Figure 2.3. As depicted by the orbital rings, the planets cross the HCS as the Sun rotates.

2.3 Large-scale solar wind structures

Slow and fast solar wind streams can intersect along the Sun-Earth line due to the Sun's rotation. Sometimes fast solar wind overtakes slower wind, leading to compression and the formation of a Stream Interaction Region (SIR). The transition through an SIR may occur gradually or abruptly. An abrupt transition detected across multiple solar wind parameters suggests the presence of a magnetohydrodynamic shock, known as an interplanetary shock [Oliveira, 2015]. However, abrupt transitions may also occur in a single parameter, like number density, resulting in a sudden change in solar wind dynamic pressure. When an SIR persists for more than one Carrington rotation, it is referred to as a Corotating Interaction Region (CIR).

SIRs are not the only sources of interplanetary shocks. Magnetic field configurations associated with sunspots can trigger magnetic reconnection (see Section 3.2.1) at the sun. This can lead to a Coronal Mass Ejection (CME), which is the release of magnetic flux

Figure 2.2: Illustration of solar wind speed variability with heliographic latitude during solar minimum. Credit: McComas et al. [1998].

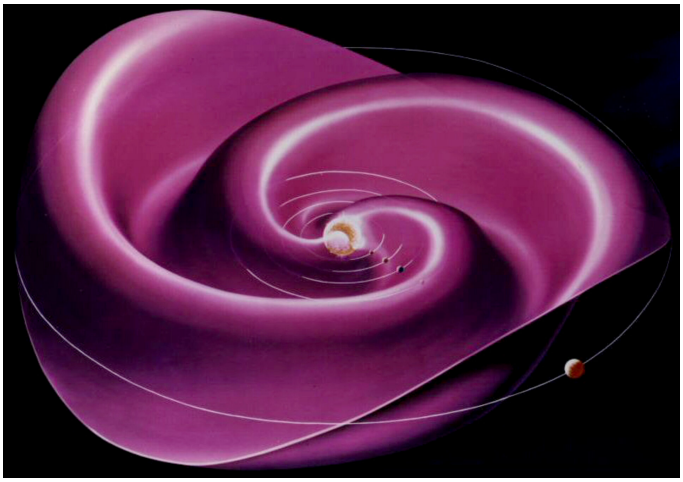

Figure 2.3: Conceptual illustration of the HCS. Credit: Werner Heil, NASA artists, developed by Prof. John Wilcox.

and plasma from the Sun. The CME structure typically comprises three segments: the leading shock wave, the ejected plasma, and the magnetic flux. Once a CME propagates through interplanetary space, it is termed an Interplanetary CME (ICME). The expanding ejected magnetic flux causes the ICME to cover a vast area. Near Earth, the shock wave usually travels at speeds of 410 ± 90 km/s and carries a density of 7.8 ± 5.3 cm^{-3} [Yermolaev et al., 2009], although ICMEs with velocities exceeding 1000 km/s have been observed near Earth. Additionally, the region of compressed solar wind immediately following the shock wave exhibits, on average, a number density that is twice as high. The frequency of ICMEs is linked to sunspots and thus increases during the solar maximum.

Not all abrupt increases in solar wind dynamic pressure are accompanied by interplanetary shocks. Often, these increases are associated with a rise in solar wind number density without a simultaneous increase in velocity [Dalin et al., 2002; Khabarova and Zastenker, 2011; Madelaire et al., 2022b]. The origins of such dynamic pressure increases are not fully understood, but as argued by Dalin et al. [2002], they are unlikely to originate from the Sun as they would dissipate before reaching Earth. Khabarova et al. [2021] demonstrated that these increases are not related to SIRs and CIRs but are correlated with crossings of the HCS. They suggest that bends and kinks in the HCS could be the cause of these pressure increases.

2.4 Measuring the solar wind

Monitoring the solar wind is highly important, as space weather events can significantly impact our infrastructure [Baker et al., 2004; Boteler, 1994; Schrijver et al., 2015]. Intense space weather conditions pose risks to humans in space and can damage electronic systems on satellites. Variations in Earth's magnetic field can induce currents in the subsurface, potentially harming our electrical grid.

Observing sunspots is possible from Earth's surface, but remote monitoring of the solar wind is not. There are five ideal locations for continuous in-situ solar wind measurements, known as Lagrange points, where the gravitational forces of the Sun and Earth are balanced. Among these, only the first Lagrange point (L1) lies between the Sun and Earth. This strategic position is why spacecrafts such as ACE [Stone et al., 1998], Wind [Wilson III et al., 2021], DSCOVR [Burt and Smith, 2012], and SOHO [Domingo et al., 1995] orbit L1. ACE, Wind, and DSCOVR provide in-situ solar wind data, while SOHO also observes the Sun, detecting activity like flares (potential precursors to CMEs) and CMEs themselves, which pose hazards to humans and electronic equipment in space.

The average distance between the Sun and Earth, one astronomical unit (AU), is about 1.5×10^8 km. In heliophysics, solar radii are commonly used as a unit of measure, whereas in space weather research, AU is preferred. Near Earth, measurements are often in Earth radii (approximately 6371 km). L1 is located roughly 1.5×10^6 km from Earth toward the Sun, or about 0.01 AU or 235 Earth radii. At an average solar wind speed of 450 km/s, solar wind observed at L1 takes about an hour to reach Earth. However, the distances between Earth and the spacecrafts that orbit L1 vary by tens of Earth radii. This variation, combined with the fact that solar wind structures are not always aligned perpendicularly to the Sun-Earth line, introduces significant challenges in predicting the exact arrival time of solar wind phenomena at Earth [Mailyan et al., 2008; Ridley, 2000; Weimer et al., 2003]. In Paper I, we determined the arrival time in two steps. First, the solar wind is propagated to 10 Earth radii along the Sun-Earth line using the observed solar wind speed, assuming no drag and that the solar wind discontinuity is perpendicular to the Sun-Earth line. Second, the initial arrival time estimate is updated based on a correlation analysis between the solar wind dynamic pressure (Equation 2.1) and the geomagnetic signature of magnetospheric compression as indicated by SYM-H (see Section 3.5.2).

Chapter 3

The geomagnetic field

The geomagnetic field, extending from Earth's interior into space, interacts dynamically with the solar wind. Its configuration is determined by contributions from both internal and external sources. Internal sources encompass the core and lithospheric magnetic fields, while external sources relate to electric currents in the magnetosphere and ionosphere.

At Earth's surface, the magnetic field is primarily attributed to the core, characterized predominantly by a dipolar configuration. This dipole is tilted approximately 10° from Earth's rotational axis and permeates vast stretches of space, shaping conditions for the existence of external fields. However, a core magnetic field is not a prerequisite for external sources, as demonstrated by the presence of magnetospheres on other planets, such as Venus [Bertucci et al., 2011].

This chapter outlines the various sources contributing to the geomagnetic field, emphasizing the role of the ionosphere. Section 3.1 discusses the characteristics and contributions of the core and lithospheric magnetic fields. Section 3.2 examines how the geomagnetic field interacts with the solar wind, leading to the formation of magnetospheric currents. Section 3.3 focuses on the ionosphere, presenting the process of electric current generation and its effects on the observed magnetic field at Earth's surface. Section 3.4 introduces the sudden commencement, a dynamic geomagnetic event. Section 3.5 outlines the techniques utilized for measuring the magnetic field below the ionosphere and the subsequent derivation of relevant geomagnetic indices.

3.1 Core and lithospheric magnetic field

The core and lithospheric magnetic fields, integral components of Earth's geomagnetic field, exhibit distinct properties and mechanisms of generation. This section provides a brief introduction to their origins and characteristics. The reader is referred to [e.g. Lowrie, 2007; Olsen and Stolle, 2012; Schubert, 2015] for more information on the core and lithospheric magnetic fields.

Originating from the geodynamo process within Earth's outer core, the core magnetic field is a consequence of convective movements and the corotation of liquid metal. This dynamic process is akin to that producing the Sun's magnetic field. Similar to the Sun's cyclical nature, the Earth's magnetic field undergoes reversals, where the magnetic poles switch hemispheres. However, on Earth, these events are not periodic and occur over long timescales, spanning hundreds of thousands of years.

One manifestation of these magnetic reversal events is observable at the mid-Atlantic ridge. As tectonic plates diverge in this region, they facilitate the escape of magma rich in ferromagnetic minerals from the mantle. Upon contact with ocean water, the lava cools, and the ferromagnetic minerals are locked in place as the temperature falls below the Curie point, thereby preserving a record of the ambient geomagnetic orientation.

Magnetic anomalies, like those at the mid-Atlantic ridge, can form in various ways. The magnetized materials within the Earth's crust constitute the lithospheric magnetic field. While its global influence is minimal compared to the core field, the lithospheric magnetic field is of substantial local importance. For instance, ground magnetometers are aligned with the core magnetic field during their installation. This is important for the subtraction of the baseline before retrieving magnetic perturbations. However, magnetic anomalies, such as the crustal magnetic field or man-made disturbances, can interfere with the magnetometer's orientation during its installation, resulting in systematic measurement errors.

At Earth's surface, the strength of the core magnetic field ranges approximately between 35,000 and 60,000 nT from the equator to the poles, respectively. In contrast, the lithospheric magnetic field measures a relatively minor few hundred nT. These differences highlight the dominant role of the core magnetic field in shaping Earth's geomagnetic environment.

3.2 The magnetosphere

The interaction between the solar wind and Earth's geomagnetic field gives rise to complex dynamics that shape the near-Earth space environment. This section serves as a brief introduction to the magnetosphere and its coupling to the solar wind (see Chapter 2).

As the solar wind approaches Earth, it encounters the geomagnetic field, resulting in the deflection of the plasma flow and the formation of a shock known as the bow shock. Beyond this initial boundary lies the magnetosheath, filled with shocked solar wind plasma. In this region, charged particles are subject to the Lorentz force ($\boldsymbol{v} \times \boldsymbol{B}$), where $\boldsymbol{v}$ represents the solar wind velocity and $\boldsymbol{B}$ the geomagnetic field. The force's direction depends on the particles' charge, causing differential motion between electrons and ions and leading to the creation of the Chapman-Ferraro current [Chapman and Ferraro, 1930], also known as the magnetopause current.

The magnetopause current, along with its associated magnetic field, establishes a distinct boundary—the magnetopause. This boundary defines a cavity (illustrated in Figure 3.1) within interplanetary space, dominated by the geomagnetic field, beyond which the IMF prevails. This cavity has a droplet-like shape, extending about 10 Earth radii toward the Sun, and several hundred Earth radii away from it, discussed further in Section 3.2.1.

Within this cavity reside Earth, the ionosphere (see Section 3.3), and the magnetosphere. The magnetosphere occupies the bulk of this space, while the ionosphere serves as a conductive inner layer. Several currents flow within the magnetosphere, as outlined in Figure 3.1. The ring current, one of the most prominent in terms of magnetic perturbation on Earth's surface, is briefly discussed in Section 3.2.2.

3.2.1 Dungey cycle

Solar wind particles generally cannot penetrate the magnetopause. However, under certain conditions, magnetic reconnection allows for the coupling between the interplanetary magnetic field (IMF) and the geomagnetic field, enabling the transfer of solar wind plasma into previously segregated regions. Magnetic reconnection involves the merging of two magnetic fields and is a process where ideal magnetohydrodynamics breaks down, allowing for the free flow of ions and electrons. The physics of magnetic reconnection is not yet fully understood [Hesse and Cassak, 2020]. For ease of understanding, we often visualize convection and magnetic reconnection using magnetic field lines, although they are not real.

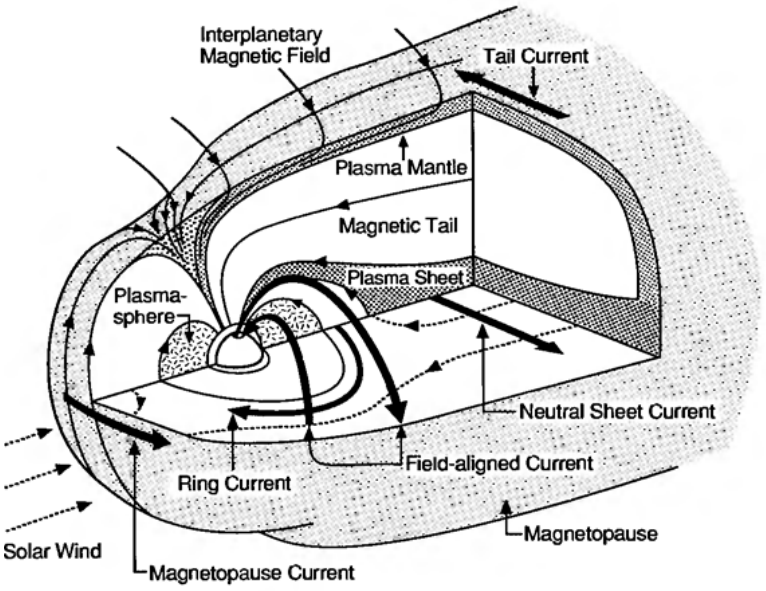

Figure 3.1: Sketch of the magnetospheric currents generated due to interaction between the solar wind and the geomagnetic field. Credit: Russel [1995]

Magnetic reconnection occurs when interacting magnetic field lines, which are anti-parallel, are forced together by external forces. As frozen-in plasma from two distinct magnetic domains converges, the magnetic field takes on an X-configuration (see Figure 3.2). Under sufficient pressure, the ions and electrons become demagnetized, meaning they no longer strictly adhere to the magnetic field lines. Consequently, this leads to a restructuring of the magnetic topology, effectively splicing the field lines together. Following a magnetic field line emerging from Earth's southern magnetic pole, we find that the Earth's magnetic field points northward at the sub-solar point. Thus, optimal conditions for reconnection at the sub-solar point occur when the IMF is southward.

The Dungey cycle [Dungey, 1961] describes the solar wind-magnetosphere interaction through reconnection, as shown in Figure 3.3. The cycle begins with reconnection at the sub-solar point (step 1), transforming involved magnetic field lines from *closed* to *open*. Each resulting line has a footpoint on Earth in opposing hemispheres, with the other end coupled to the solar wind. Due to the solar wind's *frozen-in* nature, the opened field lines are dragged from the dayside to the nightside (steps 2-5). This process, combined with the pressure balance between the solar wind and the geomagnetic field, transforms Earth's dipolar-like magnetic field into a teardrop shape. The magnetopause is situated about 10 Earth radii from the Earth towards the Sun, and it stretches up to 250 Earth radii away from the Sun. Eventually, the open magnetic field lines reconnect

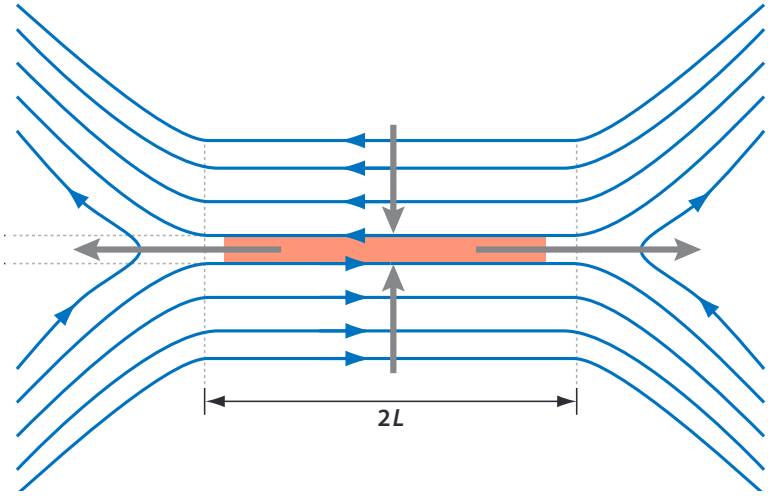

Figure 3.2: Sketch of magnetic reconnection. Credit: Zweibel and Yamada [2009]

on the nightside (steps 6-7), becoming *closed* again, each with two footpoints on Earth. The newly closed field line is stretched and experiences significant magnetic tension, propelling it toward Earth (steps 6-8) and around the planet towards the dayside, where it may undergo reconnection again (steps 8-9). The drift along the flanks is asymmetrical due to Earth's rotation, resulting in a skewed distribution favoring the dawn side [Decotte et al., 2023].

During periods of northward IMF, reconnection at the sub-solar point ceases, and the IMF drapes over the magnetosphere. This creates potential reconnection sites at the magnetic cusps—funnel-like structures over the magnetic poles—where lobe reconnection between Earth's magnetic field and the IMF can occur.

3.2.2 Ring current

A particle's velocity can be broken down into components parallel and perpendicular to the magnetic field, forming its velocity vector. The pitch angle is defined as the angle between the velocity vector and the magnetic field. A charged particle's gyrofrequency is influenced by the magnetic field strength, which varies along the field line—being weakest at the equator and strongest at the poles. As a result, the pitch angle changes as the charged particle moves along the magnetic field, in accordance with the conservation of magnetic moment. There exists a point along the magnetic field line where all parallel energy is converted into perpendicular energy—the mirror point—beyond which the particle cannot move. Any perturbation of the particle or the magnetic field can cause

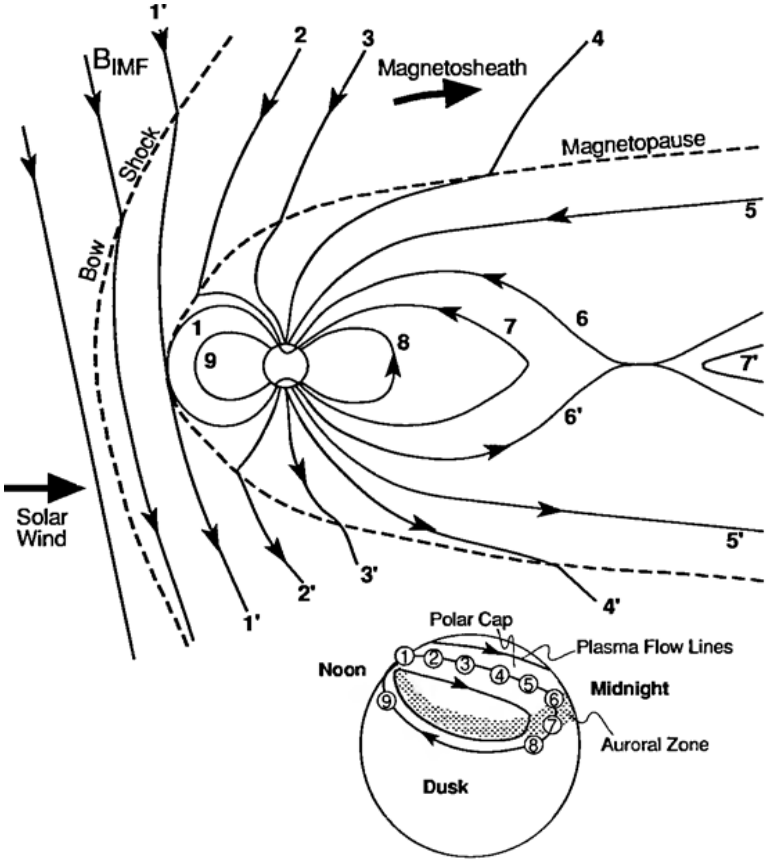

Figure 3.3: Sketch of the Dungey cycle. The illustration at the top shows the convection of magnetic field lines in the magnetosphere, while the bottom illustration is of the northern polar hemisphere. Credit: Hughes [1995]

it to gain momentum back along the direction it came—it is reflected. The reflected particle moves back towards the equator and then to the mirror point in the opposite hemisphere, a motion known as *bouncing*. The specific location of the mirror point is determined by the particle's equatorial pitch angle. Charged particles with mirror points within the atmosphere are likely to collide with atmospheric particles and be *lost* due to recombination.

During their bouncing motion, charged particles are also subject to gradient and curvature drifts, which cause a bulk motion around Earth—the direction of which is determined by the particle's charge. Hence, electrons and ions drift in opposite directions—eastward and westward, respectively. The combined motion of these charged particles constitutes the ring current, typically situated between approximately 2–9 Earth radii from the Earth (e.g., Shen et al. [2014]). To a first approximation, the magnetopause current and the ring current create opposing dipole magnetic fields, equivalent to a uniform magnetic field in $\hat{\boldsymbol{z}}$ on Earth.

3.3 The ionosphere

In the magnetosphere, the gyro frequencies of both ions (Ω_i) and electrons (Ω_e) significantly exceed their respective collision frequencies (ν_i and ν_e), allowing the plasma to be considered *frozen-in* to the magnetic field. However, this assumption starts to fail as we transition into the ionosphere, which extends from approximately 70 to 1,000 km in altitude [e.g. Baumjohann and Treumann, 2012; Olsen and Stolle, 2012]. The deviation mainly arises from the increased density of neutral particles at lower altitudes, leading to a change in the ratios of Ω_i to ν_i and Ω_e to ν_e, as illustrated in Figure 3.4.

The ionosphere acts as the inner conductive boundary of the magnetosphere and consists primarily of plasma produced by the ionization of the neutral atmosphere due to solar irradiation [Baumjohann and Treumann, 2012]. This ionization process is more pronounced on the dayside, resulting in a plasma density gradient between the Earth's day and nightside.

Within the ionosphere, different layers exhibit varying degrees of *frozen-in* plasma. In the D-region (below 90 km), plasma is not *frozen-in* because collision frequencies surpass gyro frequencies. Due to its high recombination rate and consequently short-lived plasma, the D-region is often overlooked.

Above the D-region is the E-region, with its ionization peak at 110 km, where ion collision frequencies are relatively high, and electron collision frequencies are low compared to

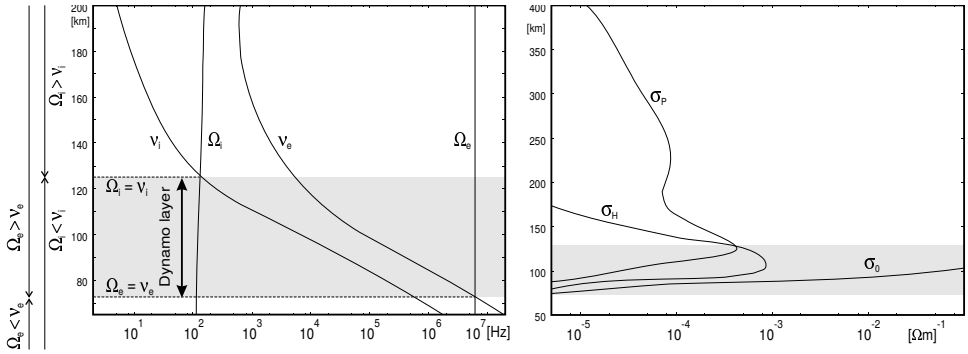

Figure 3.4: Height profile of collision frequency (ν_e and ν_i), gyrofrequency (Ω_e and Ω_i), and the conductivity (σ_H, σ_P, and $\sigma_{||}$) based of the International Reference Ionosphere. Credit: C. Finlay and N. Olsen.

their gyro frequencies. Thus, electrons are considered *frozen-in*, while ions are not, leading to relative motion between the two. The F-region, the uppermost layer with peak ionization at 300 km, is subdivided into F1 and F2 layers, differing in collision frequencies. In the F2-region, both ions and electrons are considered *frozen-in*, while in the F1-region, ions gradually transition to a less *frozen-in* state before reaching the E-region. The E and F1 regions, known as the ionospheric dynamo region, allow neutral winds to create relative motion between ions and electrons through collisions with ions.

The subsequent sections will explore how magnetospheric currents close through the ionosphere, provide a mathematical description of the ionospheric current system, and discuss the observed magnetic field perturbations below the ionosphere.

3.3.1 Ionospheric convection

The Dungey cycle, described in Section 3.2.1, offers a framework for comprehending the coupling between the solar wind and the magnetosphere. As magnetic field lines convect within the magnetosphere, this motion influences the ionosphere. Figure 3.3 depicts the ionospheric convection pattern that accompanies the opening and closing of magnetic field lines, as per the Dungey cycle. During dayside reconnection, newly opened field lines move anti-sunward across the polar cap, while sunward return flow at lower latitudes corresponds with newly closed field lines from nightside reconnection. This dynamic generates a two-cell convection pattern.

Within the conductive ionosphere, the convection of magnetic field lines induces a system of electric currents flowing parallel and perpendicular to the convection direction, as well as along the magnetic field lines. Figure 3.5 conceptualizes the ionospheric current

system during a convection pattern akin to the Dungey cycle. Since only the electrons are frozen-in, the relative motion between ions and electrons constitutes an electric current in the direction of convection (indicated by orange arrows). Furthermore, the bending of magnetic field lines during convection creates a curl in the magnetic field, which, by Ampère's law, results in an electric current perpendicular to the bend (indicated by green arrows). In a uniformly conductive ionosphere, the current parallel and perpendicular to the convection is known as a Hall and Pedersen current, respectively. A more thorough discussion on ionospheric currents, including decompositions such as Hall/Pedersen and divergence-free/curl-free, is found in Sections 3.3.2-3.3.3. The Pedersen current also serves as a closure current for field-aligned currents (FACs) generated in regions of shear flow, such as the boundary between anti-sunward and sunward convection.

The two-celled convection gives rise to two sets of FACs, termed region 1 and region 2. Region 1 FACs are found at the boundary of anti-sunward and sunward flow (indicated by the most poleward FACs in Figure 3.5). Region 2 FACs are located between the return flow and the relatively stationary magnetic field lines at lower latitudes (indicated by the equatorward most FACs). On the flanks, between regions 1 and 2, the magnitude of the current tends to be strong (illustrated by the larger orange arrows) and results in significant magnetic field perturbation on the ground. Therefore, this part of the ionospheric electric current is commonly referred to as auroral electrojets.

The orientation of the IMF plays a crucial role in determining the ionospheric convection pattern, see e.g. Cowley and Lockwood [1992]. During purely southward IMF, reconnection occurs at the subsolar point. However, when the IMF has both a southward and east/west component, the reconnection site is displaced east/west. Consequently, one convection cell becomes circular, while the other takes on a crescent shape. The polarity of the IMF's east/west component determines whether the dawn or dusk cell becomes circular or crescent-shaped. On the other hand, during northward IMF, the two-cell convection pattern associated with southward IMF tends to vanish. The ionospheric convection pattern resulting from lobe reconnection also comprises a two-cell system. However, the convection in this case is directed sunward between the cells. These cells are spatially limited and located where the cusp region maps into the ionosphere. The FAC associated with this convection pattern is commonly referred to as region-0 or NBZ currents. Similar to the case of southward IMF, a non-zero east/west component affects this two-cell system. The cells undergo changes in spatial extent and magnitude to the extent that only one cell is present.

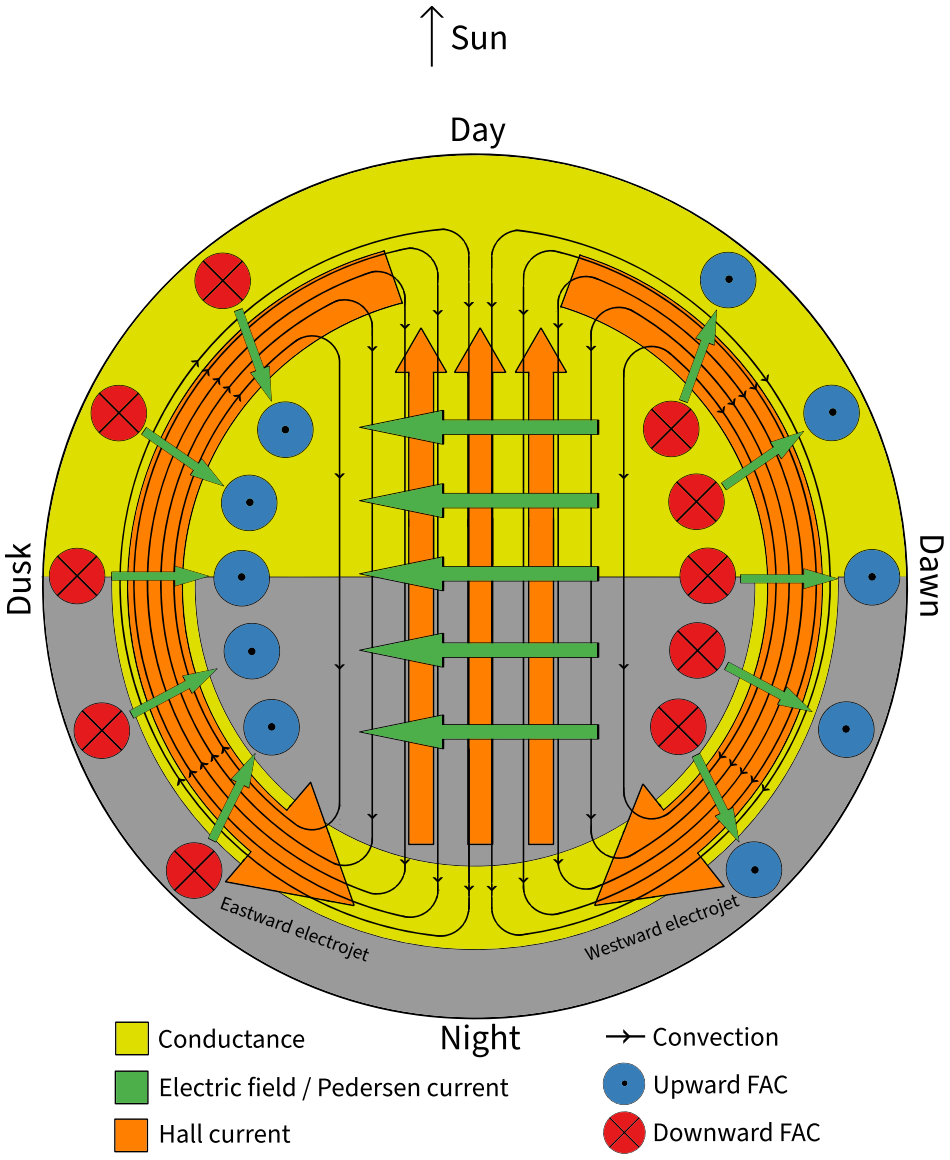

Figure 3.5: Conceptual illustration of the high-latitude steady state current system during southward IMF. Convection of magnetic field lines is illustrated by black lines. The Hall current associated with convection is illustrated by orange arrows. The ionospheric (potential) electric field and Pedersen current are illustrated by green arrows. The inward and outward FACs are indicated by the red and blue circles, respectively. The dayside is colored yellow to indicate conductance generated from solar irradiation, while the grey color on the nightside indicates the lack of conductance. The yellow band following the convection lines indicates conductance on the nightside from the convection of plasma and precipitation associated with FACs.

3.3.2 Ionospheric Ohm's law

Ionospheric electric currents arise from the convection of magnetic field lines, as detailed in Section 3.2.1, and are described by the ionospheric Ohm's law [e.g. Baumjohann and Treumann, 2012; Brekke, 2015; Kelley, 2009]:

$$\boldsymbol{j} = \sigma_P \boldsymbol{E}_\perp + \sigma_H \left(\hat{\boldsymbol{b}} \times \boldsymbol{E}_\perp \right) + \sigma_{||} E_{||} \hat{\boldsymbol{b}}, \tag{3.1}$$

where $\boldsymbol{j}$ denotes current density, $\boldsymbol{E}$ the electric field in the neutral frame of reference, $\hat{\boldsymbol{b}}$ the unit vector of the magnetic field $\boldsymbol{B}$, and σ_P, σ_H, $\sigma_{||}$ the Pedersen, Hall, and parallel conductivities, respectively. The subscript $\perp$ and $||$ signify components perpendicular and parallel to $\hat{\boldsymbol{b}}$, different from spherical coordinate directions. If the magnetic field lines are radial, these components align with horizontal and radial directions (see Section 3.3.3).

Due to the high electron mobility, the electric field is generally thought to map along the magnetic field [Hesse et al., 1997]. Thus, Equation 3.1 can be height integrated as

$$\boldsymbol{J}_\perp = \Sigma_P \boldsymbol{E}_\perp + \Sigma_H \left(\hat{\boldsymbol{b}} \times \boldsymbol{E}_\perp \right), \tag{3.2}$$

expressing the horizontal current on a spherical shell, provided the magnetic field lines are radial. The shell is commonly placed around 110 km corresponding to the peak in Hall and Pedersen conductivity, see Figure 3.4. Σ_P and Σ_H denote the height-integrated Pedersen and Hall conductivities, respectively.

Equations 3.1 and 3.2 can be derived from the ion and electron momentum equations under specific assumptions [e.g. Brekke, 2015]. These assumptions include:

- *Quasi steady-state*: The steady-state assumption implies a lack of time dependence ($\partial/\partial t = 0$). In deriving the ionospheric Ohm's law, time-dependent terms in the ion and electron momentum equations are omitted. We refer to this approximation as a quasi steady-state because it allows the system to evolve, albeit at a sufficiently slow rate of change. As a result, $\boldsymbol{E}_\perp$ encompasses both potential and inductive components. Nevertheless, for practical applications, such as in ionospheric solvers for MHD simulations and empirical models (see Section 4.4), inductive effects are commonly disregarded effectively assuming a true steady-state.
- *Charge neutrality*: It is assumed that the electron and ion densities are equal ($n_e = n_i$), maintaining charge neutrality. An additional simplification assumes a uniform ion species, characterized by a single representative mass and charge. In the context of the quasi steady-state, the displacement current ($\frac{\partial}{\partial t}\boldsymbol{E}$) is neglected,

implying that the current is divergence-free ($\boldsymbol{\nabla} \cdot \boldsymbol{J} = 0$) and that charge neutrality is preserved over time.

- *Known neutral velocity*: The electric field ($\boldsymbol{E}_\perp$) in Equation 3.2, is expressed as $\boldsymbol{E}_\perp = \boldsymbol{E}'_\perp + \boldsymbol{u} \times \boldsymbol{B}$, where $\boldsymbol{u}$ represents the neutral wind velocity and $\boldsymbol{E}_\perp$ is the electric field observed in the neutral wind's frame of reference. The interaction of the neutral wind with ions is central to the ionospheric dynamo; however, $\boldsymbol{u}$ is often unknown. As a result, we typically work under the assumption that $\boldsymbol{u}$ is zero.

- *Thermal equilibrium and isotropic pressure*: Assuming thermal equilibrium in the ionosphere allows us to use the ideal gas law to represent pressure, circumventing the need for energy conservation equations. Moreover, in a collisionless plasma, the pressure tensor can often be assumed to be diagonal. However, in the ionosphere, collisions lead to isotropic pressure, allowing the pressure to be represented by a scalar.

The divergence of Equation 3.2 in the perpendicular plane leads to field-aligned currents (FACs) expressed as:

$$\begin{aligned} \boldsymbol{J}_{||} &= \boldsymbol{\nabla}_\perp \cdot (\boldsymbol{\Sigma} \cdot \boldsymbol{E}_\perp) \\ &= \Sigma_P \left(\boldsymbol{\nabla}_\perp \cdot \boldsymbol{E}_\perp\right) + \boldsymbol{E}_\perp \cdot \boldsymbol{\nabla}_\perp \Sigma_P + \Sigma_H \left[\boldsymbol{\nabla}_\perp \cdot \left(\widehat{\boldsymbol{b}} \times \boldsymbol{E}_\perp\right)\right] + \left(\widehat{\boldsymbol{b}} \times \boldsymbol{E}_\perp\right) \cdot \boldsymbol{\nabla}_\perp \Sigma_H. \end{aligned} \tag{3.3}$$

Each term in Equation 3.3 corresponds to a situation where FACs can be found. The first term, $\Sigma_P \left(\boldsymbol{\nabla}_\perp \cdot \boldsymbol{E}_\perp\right)$, indicates the presence of FACs, closed by a Pedersen current when the electric field converges or diverges. These FACs are typically associated with regions 0, 1, and 2. The second term, $\boldsymbol{E}_\perp \cdot \boldsymbol{\nabla}_\perp \Sigma_P$, arises when there is a gradient in the Pedersen conductance along the direction of the electric field. The third term, $\Sigma_H \left[\boldsymbol{\nabla}_\perp \cdot \left(\widehat{\boldsymbol{b}} \times \boldsymbol{E}_\perp\right)\right]$, can be neglected. By expanding the term using a vector identity[1], we find that it relies on $\boldsymbol{\nabla} \times \widehat{\boldsymbol{b}}$ and $\boldsymbol{\nabla} \times \boldsymbol{E}_\perp$. Here, $\boldsymbol{\nabla} \times \boldsymbol{E}_\perp$ is often ignored because it is small (see Paper IV) and otherwise zero under the assumption of steady state, and $\boldsymbol{\nabla} \times \widehat{\boldsymbol{b}}$ is zero if the magnetic field is assumed radial. The fourth term, $\left(\widehat{\boldsymbol{b}} \times \boldsymbol{E}_\perp\right) \cdot \boldsymbol{\nabla}_\perp \Sigma_H$, emerges when there is a gradient in the Hall conductance perpendicular to the ionospheric electric field. This can occur at the edges of the aurora as well as across the day/night terminator, where differences in production/loss (e.g., solar radiance/recombination) result in a conductance gradient.

In summary, studying the complex interactions between the magnetosphere and ionosphere is crucial for understanding the behavior of the ionospheric current system and

[1] $\boldsymbol{\nabla} \cdot \left(\widehat{\boldsymbol{b}} \times \boldsymbol{E}_\perp\right) = \left(\boldsymbol{\nabla} \times \widehat{\boldsymbol{b}}\right) \cdot \boldsymbol{E}_\perp - \widehat{\boldsymbol{b}} \cdot (\boldsymbol{\nabla} \times \boldsymbol{E}_\perp)$

the underlying physical processes in space physics research. In Sections 3.3.3-3.3.4, we discuss the decomposition and interpretation of the ionospheric current system, the magnetic field produced below the ionosphere, and the ionospheric current system when going beyond steady state.

3.3.3 Magnetic field perturbation below the ionosphere

The study of ionospheric electrodynamics has historically relied on ground-based measurements of magnetic perturbations, enabling the determination of equivalent horizontal ionospheric electrical currents [Amm et al., 2010; Friis-Christensen et al., 1988]. Advanced empirical modeling techniques (see Chapter 4) are now frequently employed to create regional and global estimates of the ionospheric current system. While these models are valuable, it is essential to consider the underlying assumptions made about the physical system to avoid misinterpretation.

Deriving information about the ionospheric current system using ground-based magnetic field measurements can involve simply applying Ampere's law: a 90° clockwise rotation of the observed magnetic perturbation, assuming it is caused solely by an overhead ionospheric electrical current. However, the ground magnetic perturbation can not fully describe the ionospheric current system unless more information is provided. Fukushima's theorem is frequently invoked [Fukushima, 1969, 1976] for this reason. The theorem, building on the work by Kern [1966]; Tamao [1964], states that magnetic perturbation associated with the Pedersen current is canceled by those of the FACs below the ionosphere, given two assumptions: first, the magnetic field is purely radial; second, conductance is uniform.

Examining Equation 3.3 and assuming uniform conductance, we find that only the first term on the right-hand side remains, indicating that the FACs close through the ionosphere via Pedersen currents. Similarly, taking the curl of Equation 3.2 under similar conditions reveals that only the Hall current contributes to the curl. Recall that Equation 3.2 already assumes radial field lines. Therefore, if Fukushima's theorem holds, then the equivalent current derived from ground magnetometers can be regarded as a Hall current. The equivalent current thus reflects ionospheric convection and directly ties magnetic perturbations observed below the ionosphere to solar wind-magnetosphere coupling.

Fukushima's theorem is often applied to equate the equivalent current with the Hall current [e.g. Fujita et al., 2003a,b; Tanaka et al., 2020]. This approximation generally holds on a global scale Amm [1997], and the assumption of radial field lines is reasonable at

auroral latitudes [Untiedt and Baumjohann, 1993]. However, ionospheric conductance is rarely uniform [Kosch et al., 2000; Lummerzheim et al., 1991], and gradients in conductance significantly affect the ionospheric current system [Ellis and Southwood, 1983; Laundal et al., 2016; Lynch et al., 2022].

A more general way of decomposing the ionospheric current system is to apply Helmholtz's theorem. Thereby, the current system can be decomposed into its divergence-free (DF) and curl-free (CF) components [Sabaka et al., 2010; Vasyliunas, 1970]:

$$\boldsymbol{J}_{\perp} = \boldsymbol{J}_{\mathtt{DF}} + \boldsymbol{J}_{\mathtt{CF}}. \tag{3.4}$$

Assuming radial magnetic field lines, the magnetic perturbation from FACs and $\boldsymbol{J}_{\mathtt{CF}}$ cancel out below the ionosphere Amm [1997]; Untiedt and Baumjohann [1993]. Hence, ground-based magnetic perturbations is solely produced by $\boldsymbol{J}_{\mathtt{DF}}$. This statement can be made without requiring any assumption regarding conductance. Both Hall and Pedersen currents are present in $\boldsymbol{J}_{\mathtt{DF}}$ and $\boldsymbol{J}_{\mathtt{CF}}$ when the conductance is not uniform. Incorrectly attributing the source of observed magnetic perturbations can lead to erroneous conclusions, particularly regarding ionospheric convection. It is for this reason we use the term *transient current vortex* instead of *transient convection cell* in Paper II.

To illustrate the differences in the Hall/Pedersen and DF/CF components, we will decompose the ionospheric current resulting from a synthetic example of a two-cell convection system associated with a southward IMF, corresponding to Figure 3.3. We chose this scenario, instead of a more dynamic one, to test if $\boldsymbol{J}_{\mathtt{DF}}$ can be approximated as $\boldsymbol{J}_{H}$. The purpose is simply to illustrate the different decompositions and to demonstrate that even in this scenario, the Pedersen current does contribute to the magnetic perturbation below the ionosphere.

Figures 3.6-3.7 present various decompositions of the ionospheric current and the resulting magnetic field perturbation, derived from a Lompe model [Laundal et al., 2022] using the potential electric field, FACs, and conductance data from the global MHD simulation described in Shi et al. [2022], which also contributed to synthetic data for Paper IV. We chose the Lompe model as it provides an empirical modeling framework for ionospheric electrodynamics based on SECS (see Section 4.1.2), allowing measurements of different quantities to be linked via ionospheric Ohm's law (Equation 3.2) to create a self-consistent model of the ionospheric potential electric field. Empirical modeling techniques are further discussed in Chapter 4.

Figure 3.6a illustrates the ionospheric potential electric field for a two-cell convection pattern during southward IMF. Figures 3.6b-c depict the Hall and Pedersen conductances, respectively. The resulting horizontal ionospheric electric current is displayed

in Figure 3.6d. The Hall/Pedersen and DF/CF decompositions of the total horizontal current are shown in Figures 3.6e-f and Figures 3.6g and 3.6j, respectively. The Hall current is very similar to the DF current, both indicating convection related to the two-cell pattern. Likewise, the Pedersen current resembles the CF current, both showing convergence/divergence patterns linked to regions 1 and 2 FACs. Notable differences exist between the two decompositions, however. Figures 3.6h-i and 3.6k-l separate the DF and CF currents into their Hall and Pedersen components. The Hall and Pedersen components predominate in the DF and CF currents, respectively. However, a DF Pedersen current vortex is observed, associated with conductance gradients due to the latitudinal variation in solar irradiation. At the center of this DF Pedersen vortex, a CF Hall current diverges, indicating a FAC closed by Hall currents.

Although Figures 3.6-3.7 are not associated with a dynamic event, there are still large-scale DF Pedersen and CF Hall currents with magnitudes roughly a third of their counterparts. The magnetic perturbation associated with the total DF current, the DF Hall current, and the DF Pedersen current (Figures 3.6g-i) is displayed in Figure 3.7. As expected, the DF Hall component predominantly shapes the ground magnetic signature. However, the radial component of the ground magnetic perturbation reaches approximately 75 nT below the DF Pedersen current vortex, as seen in Figure 3.7i. This indicates that, while on a large scale and under non-dynamic conditions, the ground magnetic perturbation may be assumed to originate from an overhead Hall current. However, this example also shows that during a non-dynamic scenario, a large-scale Pedersen current can produce measurable magnetic perturbation on the ground.

Other sources also contribute to ground-based magnetic perturbations besides ionospheric currents. Excluding secular variations relevant to core magnetic field modeling, three key sources stand out. First, magnetospheric currents (see Section 3.2) generate, to first order, an external magnetic dipole field that predominantly maps into the radial component at high latitudes. Yet, asymmetries arise: the magnetopause current has more impact on the dayside than the nightside, the tail current does the opposite, and the ring current introduces its own asymmetry [Haaland and Gjerloev, 2013; Lühr et al., 2017; Newell and Gjerloev, 2012]. Second, the validity of purely radial magnetic field lines diminishes with decreasing latitude. Amm [1995]; Tamao [1986]; Untiedt and Baumjohann [1993] show that the effect of tilted FACs is small at high latitudes. However, improvements in empirical modeling techniques, the amount of data, and the quality of data might, in the future, necessitate the consideration of tilted FACs.

The third significant factor is ground-induced currents (GICs), which arise from time-varying magnetic fields. These currents, induced within the Earth's crust, lithosphere, and mantle, pose a considerable risk to electrical infrastructures [Boteler, 1994; Pirjola,

2002; Pulkkinen et al., 2017]. The depth at which GICs form is frequency-dependent, with lower frequencies affecting greater depths [Weidelt, 1973]. Additionally, the strength and location of GICs are influenced by the subsurface's 3D conductivity profile. Areas with conductance gradients, such as coastlines [McKay and Whaler, 2006; Nakamura et al., 2018; Parkinson and Jones, 1979] or Fennoscandia [Dimmock et al., 2019], can experience localized, high-magnitude GICs.

In summary, when employing Fukushima's theorem, one must consider that the ionospheric source current is not exclusively a Hall current. Discrepancies between statistical equivalent current maps [Friis-Christensen and Wilhjelm, 1975] and ionospheric convection maps [Haaland et al., 2007; Heppner and Maynard, 1987; Pettigrew et al., 2010; Weimer, 2005] support this. Moreover, magnetospheric currents, GICs, and FACs add complexity, increasing the difference between the equivalent ionospheric current and $\boldsymbol{J}_{\mathrm{DF}}$ and complicating its interpretation. The challenges associated with empirical modeling of the ionospheric current system based on ground-based magnetic field measurements are addressed in Chapter 4.

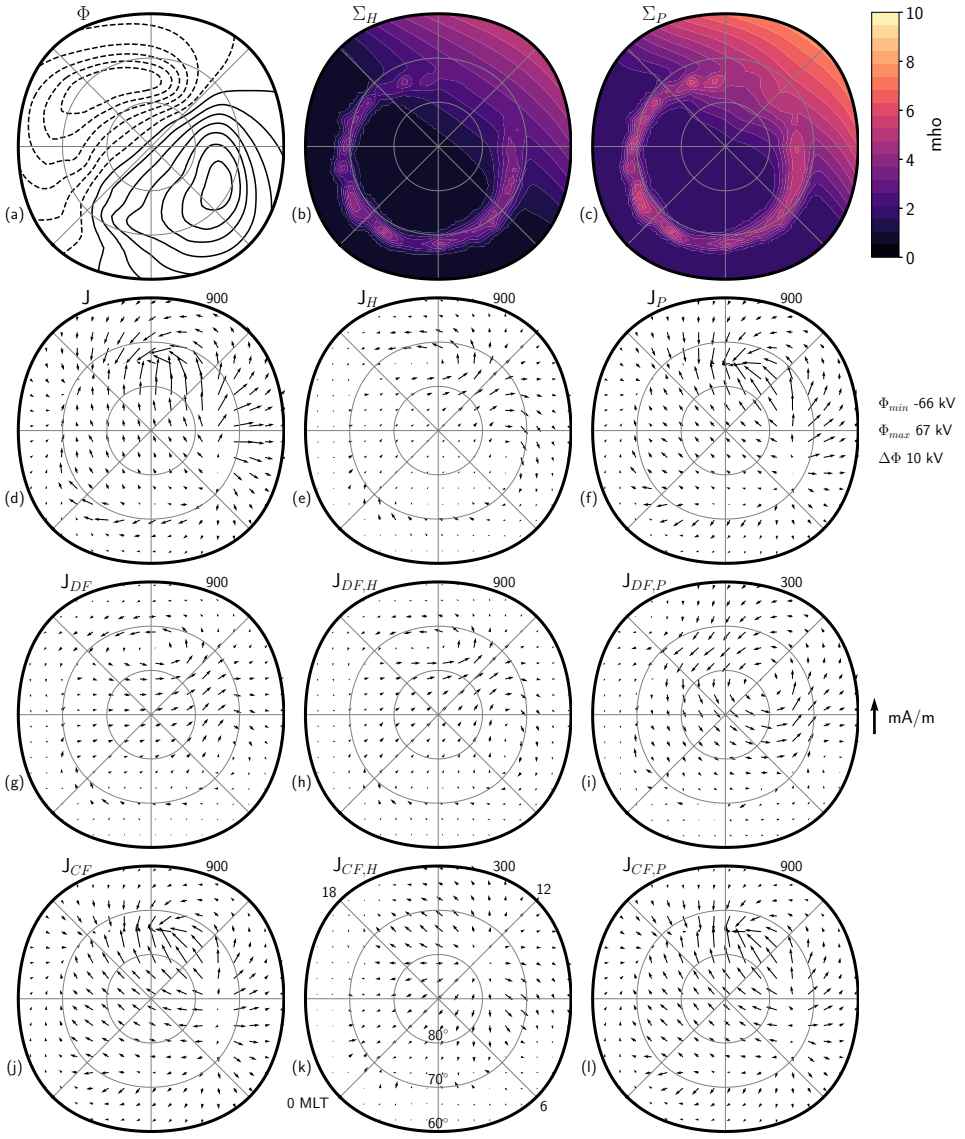

Figure 3.6: Decomposition of the ionospheric current based on a Lompe model of the output from an MHD simulation. Figures 3.6a-c show the electric potential, Hall conductance, and Pedersen conductance. Figure 3.6d shows the horizontal ionospheric current. Figures 3.6e-l show various decompositions of Figure 3.6. The subscripts H, P, DF, and CF refer to Hall, Pedersen, DF, and CF components, respectively. That means, $J_{DF,H}$ is the Hall part of the DF horizontal ionospheric current. The maximum, minimum, and step size of the contour in Figure 3.6a are given on the right-hand side. The magnitude of the currents in Figures 3.6d-l is indicated by the number listed above each image, which represents the magnitude of the arrow on the right-hand side.

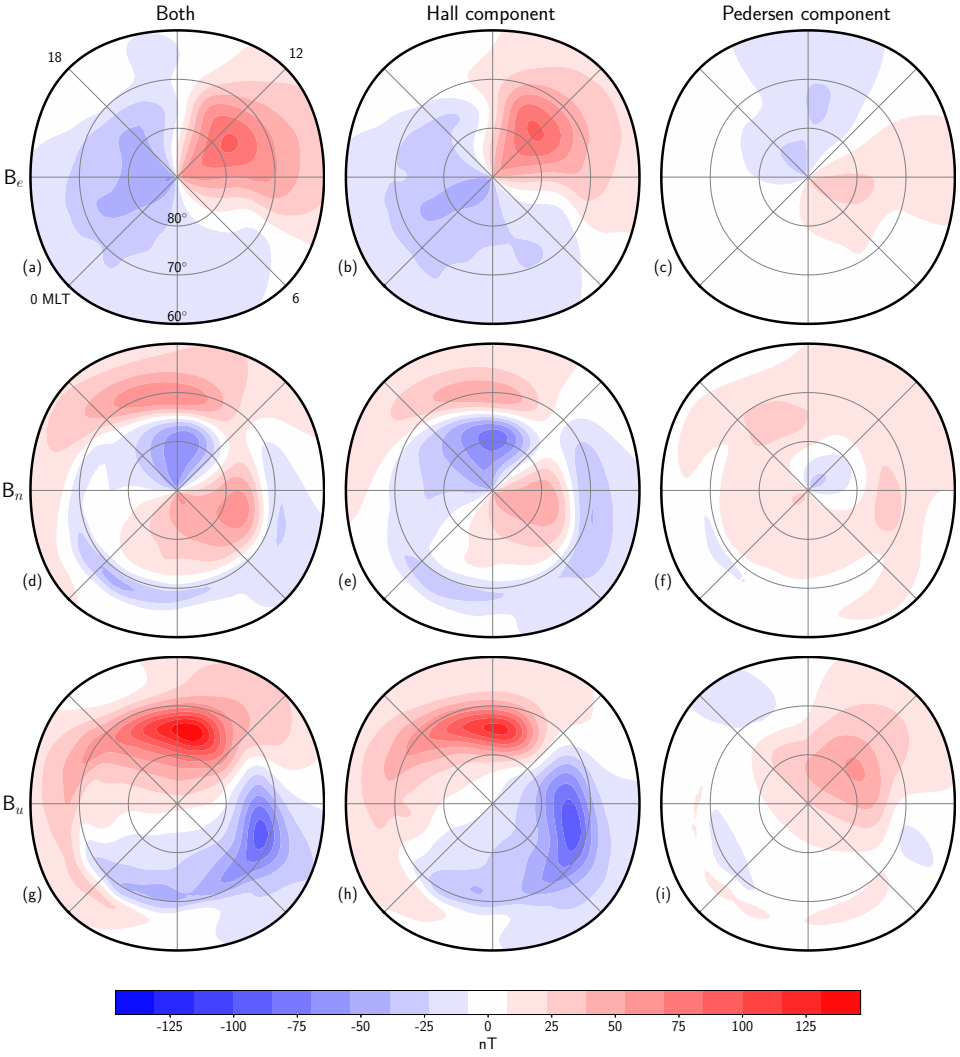

Figure 3.7: Decomposition of ground magnetic perturbation, resulting from the ionospheric electric currents illustrated in Figures 3.6d-f.

3.3.4 Beyond steady state

Steady state is a near-universal assumption in ionospheric electrodynamics, see Sections 3.3.1-3.3.3. This assumption presumes that temporal changes are negligible ($\partial/\partial t = 0$), leading to the simplification of the ionospheric electric field to a potential field ($\nabla \times \boldsymbol{E} = 0$), and thereby, disregarding any induction electric field ($\boldsymbol{E}_{ind}$) that arises in time-varying scenarios. However, the ionospheric current system is intrinsically dynamic. Takeda [2008] showed that changes on time scales shorter than 5 minutes can lead to non-negligible induction effects.

The induction electric field is a fundamental aspect of ionospheric electrodynamics described by Faraday's law of electromagnetic induction ($\nabla \times \boldsymbol{E} = -\frac{\partial}{\partial t}\boldsymbol{B}$) [Faraday, 1832]. Dynamic events, such as sudden commencements (see Section 3.4) or substorm expansion phases, feature magnetic field changes on the order of seconds to minutes. Ignoring the induction electric field neglects the mutual interaction between electrostatic and inductive processes, leading to an incomplete picture. In the following section, we discuss the process of ionospheric induction and attempt to provide a more complete picture of how the ionospheric current system evolves temporally.

Central to the time-dependent ionospheric current system is the generation of $\boldsymbol{E}_{ind}$ and the associated time-varying magnetic field. Unfortunately, Faraday's law of induction does not describe the causality in such a system. Here, we give a conceptual explanation of cause and effect, which we believe follows a chronological order, using a hypothetical dynamic event: A considerable amount of magnetic flux opens on the dayside. These newly opened magnetic field lines, propelled anti-sunward by the solar wind, instigate corresponding ionospheric convection and a flow channel formation. For simplification, consider a slab geometry where the ionosphere is infinitely thin and uniformly conductive. Under this scenario, DF and CF currents are reduced to their Hall and Pedersen currents, respectively (see Section 3.3.3). This simplification is useful as it distinguishes between electron-driven Hall currents and ion-driven Pedersen currents, which possess distinct physical behaviors.

Figures 3.8a and 3.8c illustrate the steady-state systems before and after the magnetic field lines are bent. Figure 3.8a shows the unperturbed system with vertical magnetic field lines in red and no electric current. Figure 3.8c shows the perturbed system, also in steady state, where bent magnetic field lines are blue. The magnetospheric driver causes a bend in the x-direction, but y-direction bending also occurs, which is important for the system's evolution and will be discussed shortly. The blue-shaded lines represent the projection of magnetic field lines onto the ionospheric plane, solely for visualization. In reality, the transition from blue to red field lines is gradual, suggesting that the

deformation of the magnetic field lines extends beyond the initial flow channel. The CF current system, depicted by solid orange and green lines, includes vertical FACs (green for electron-driven currents) and horizontal CF Pedersen currents (orange for ion-driven currents). The DF Hall current appears as a sheet current in green.

In the unperturbed system (Figure 3.8a), magnetic flux is uniformly distributed. In the perturbed system (Figure 3.8c), magnetic flux and plasma density are higher and lower near the upward and downward FACs, respectively. Since the CF current is not carried entirely by ions or electrons, a pile-up of plasma will occur. The convergence and divergence of plasma related to the CF current can be considered additions to the production and loss terms. Nevertheless, in steady state, the pile-up remains constant in time. The question is, what processes evolve the unperturbed steady state system into the perturbed steady state system?

A change within the magnetosphere-ionosphere (MI) system is communicated through shear Alfvén waves. When these waves encounter the conductive ionosphere, they undergo reflection and mode conversion [e.g. Yoshikawa and Itonaga, 2000], akin to the behavior of electromagnetic waves at the boundary of media with different refractive indices. Energy conservation dictates that if an incident shear Alfvén wave is not fully transformed into a compression wave, a portion must be reflected. The ionosphere's ability to resist change, imposed by the magnetosphere through shear Alfvén waves, depends on the ionospheric conductivity Yoshikawa and Itonaga [2000]. The ratio of reflection to mode conversion is proportional to the conductivity. Dreher [1997] demonstrated in a 2.5D MHD simulation that the ionospheric current system requires several cycles of shear Alfvén waves before a steady state is reached, a process that can take several minutes given the finite speed of Alfvén waves [Song and Vasyliūnas, 2014; Tu et al., 2014]. Furthermore, an interhemispheric asymmetry in ionospheric conductivity, related to dipole tilt, could result in an asymmetry in the reconfiguration between hemispheres.

Conceptually, a shear Alfvén wave can be visualized as a bend traveling between the magnetosphere to the ionosphere along a magnetic field line. Figure 3.8b1 illustrates the bend in the field lines, due to a change in the magnetosphere, before the information has reached the ionosphere. In reality, there should be FACs and closure currents in Figure 3.8b1. However, for simplicity, we assume infinite Alfvén speed, meaning that the information is transmitted instantaneously between the ionosphere and magnetosphere. Figure 3.8b2 illustrates the instance where the wave/bend reaches the ionosphere. A CF horizontal current is generated perpendicular to the bend, in accordance with Ampere's law, and FACs are generated in regions of shear flow. The initial CF current system is carried entirely by electrons, indicated by the green color, due to their high mobility. The electron-carried horizontal CF current compresses and expands the magnetic flux

in the y-direction, perpendicular to the initial bend, as illustrated in Figure 3.8b3. The compression and expansion result in a curl in the magnetic field that, again, according to Ampere's law, constitutes a current. This current is the DF current system illustrated by the green sheet current in the ionospheric plane. As the DF current system is set up, the ions experience a Lorentz force ($\boldsymbol{j} \times \boldsymbol{B}$) in the y-direction and thus contribute to the CF current system, indicated by the dashed orange and green line in Figure 3.8b4. Over time, the compression and expansion of magnetic flux facilitate a stronger DF current system, leading to the ions experiencing a stronger Lorentz force and completely taking over the horizontal part of the CF current system. The system eventually converges on a new steady state (Figure 3.8c).

The illustration provided in Figure 3.8, while offering a conceptual framework, is an oversimplification of the intricate processes at play. The omission of wave reflection and the iterative nature of the incident and reflected waves represent significant simplifications, thus rendering the actual temporal evolution of the ionospheric current system more complex. Additionally, while $\boldsymbol{E}_{ind}$ is not explicitly depicted, it plays a critical role in shaping ionospheric electrodynamics. The rotational electric field encompasses both the horizontal CF Hall current and a horizontal DF Pedersen current. Both the horizontal DF Hall and Pedersen currents contribute to the observable magnetic perturbations beneath the ionosphere, albeit in opposing directions. Insights into the dynamics of the ionospheric current system are derived through $\boldsymbol{E}_{ind}$, interpreted from consecutive magnetic field measurements. Acknowledging the limitations of our models and the complexity of inductive effects is essential for advancing our understanding of the ionosphere's evolution under the influence of external drivers. The following chapter (4) introduces some of the widely used empirical modeling techniques (see Sections 4.1.1-4.1.2) and discusses a novel method for estimating the ionospheric induction electric field based on ground magnetic field perturbations (see Section 4.4), as related to Paper IV.

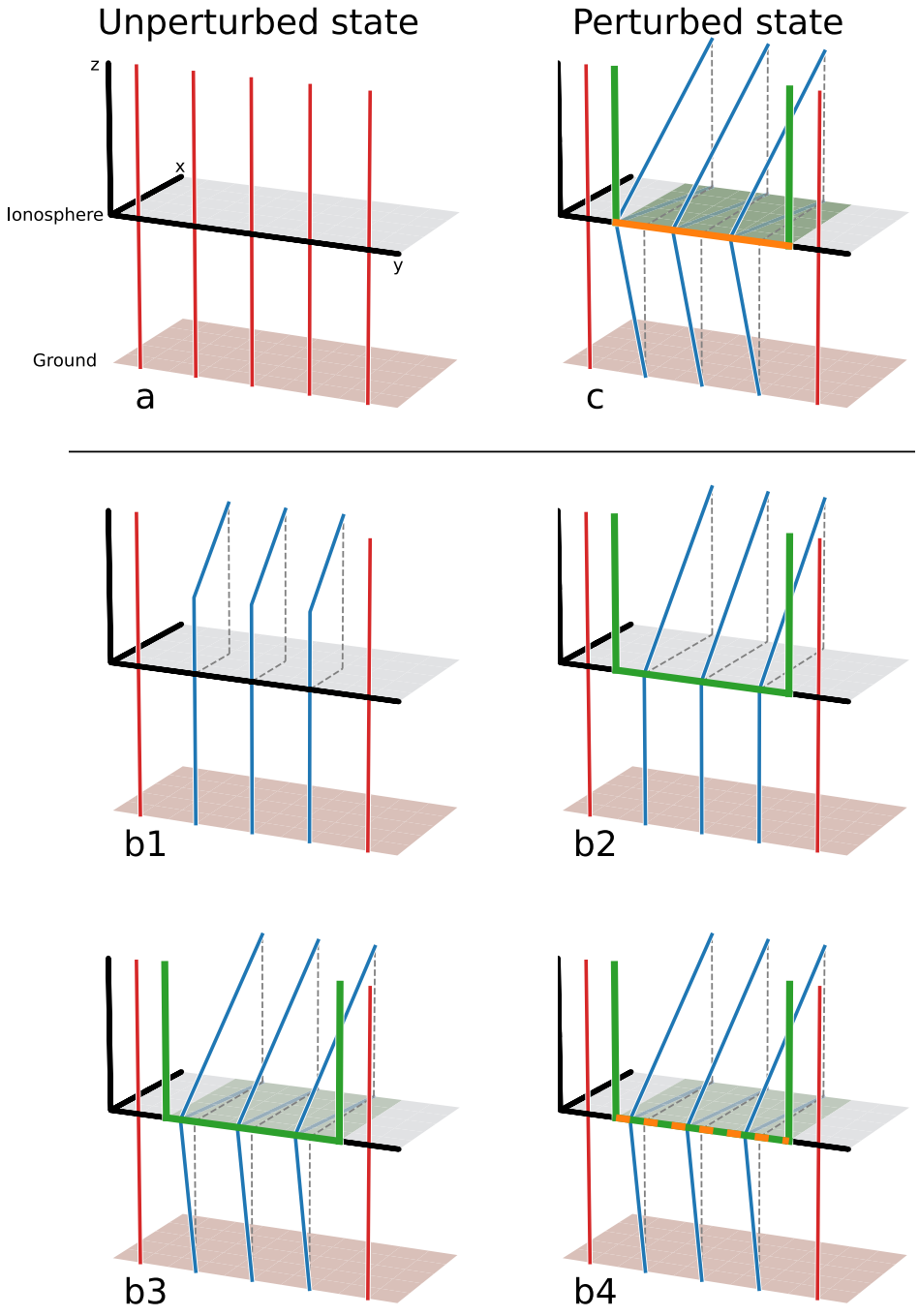

Figure 3.8: Conceptual illustration outlining the intermediary steps (Figures 3.8b1-b4) that transition between the initial (Figure 3.8a) and final steady-state (Figure 3.8c) ionospheric current systems. Magnetic field lines are represented in red (vertical) and blue (bent). The electric currents, differentiated by carriers, are color-coded with green indicating electron flow and orange representing ion flow.

3.4 Sudden commencement

Research can be approached in various ways. In the case of ionospheric electrodynamics, you can carry out case studies or perform statistical analyses of multiple events. The focus can be global or regional. The ionospheric current system can be studied in steady-state or during dynamic times. No matter the choice, it will hopefully shed light on some characteristics of the system and improve our general understanding.

In this section, we introduce the concept of a sudden commencement (SC) which occurs in response to a rapid increase in solar wind dynamic pressure. The SC is a valuable tool for examining the temporal evolution of the ionospheric current system as it results in a significant perturbations of the MI system. Abrupt pressure increases are often associated with space weather events like CMEs and CIRs but can also occur without the presence of an interplanetary shock; see Section 2.3.

Following Araki [1994], the geomagnetic response (D_{SC}) can be decomposed as

$$D_{SC} = D_L + D_P. \tag{3.5}$$

Here, D_L refers to a large-scale step-like change in the geomagnetic field strength. The perturbations is caused by compression of the magnetosphere which generates, to first order, a uniform magnetic field in $\hat{\boldsymbol{z}}$. At low- and mid-latitudes this is mainly observed as an increase of the horizontal magnetic field component. At high-latitude. the external field maps into the radial component and, therefore, decreases the overall field strength. D_P is confined to high-latitude and results from transient ionospheric convection cells. D_P is itself decomposed into the preliminary impulse (PI) and the main impulse (MI),

$$D_P = D_{PI} + D_{MI}, \tag{3.6}$$

that are associated with two different sets of transient convection cells. We will return to their origin shortly.

The first, indirect, studies of SCs date back to the 19th century in connection with geomagnetic storms. Although the idea of a simultaneous onset of magnetic variation was proposed in the 19th century, it was not until the 20th century that continuous and simultaneous measurements of an SC were made around the world. The reader is referred to Curto et al. [2007] for an in-depth historical overview of the SC. We follow their suggestion to use the term SC, although *storm sudden commencement* and *sudden impulse* can also be found in the literature.

Friis-Christensen et al. [1988] challenged the prevailing theory of the high-latitude mag-

netic signature's magnetospheric origin: it was theorized that the magnetic signature was a result of flux transfer events. By comparing in-situ solar wind data and observations of ground magnetic perturbations, they concluded that SCs are related to abrupt increases in solar wind dynamic pressure. Building on the work by Friis-Christensen et al. [1988], several theories on the magnetospheric origin of the sudden commencement have been put forth [e.g., Araki, 1994; Glassmeier and Heppner, 1992; Glassmeier et al., 1989; Kivelson and Southwood, 1991; Sibeck, 1990].

Figures 3.9-3.10 illustrate the general concept presented by Sibeck [1990]. Figure 3.9 summarizes the double-stepped response of the magnetopause to a pressure pulse in the solar wind. When the solar wind structure encounters the geomagnetic field, a compression wave is launched in the magnetosphere. The wave propagates through the magnetosphere, past the Earth, and into the tail, at Alfvénic speed (generally faster than the solar wind). In Figure 3.9, the compression wave is illustrated by the outward motion of the magnetopause prior to the solar wind discontinuity. The inward motion illustrates magnetospheric compression resulting from the new force balance between the upwind solar wind and the geomagnetic field. In summary, the abrupt pressure increase results in an outward and inward motion of the magnetopause.

The magnetopause motion excites convection of magnetic field lines, forming two convection cells of opposite orientation. Figure 3.10 illustrates the FACs, associated with the convection, mapping into the ionosphere, which subsequently result in the high-latitude geomagnetic signature observed by ground-based magnetometers. The magnetospheric convection cells propagate with the compression wave and the solar wind along the flanks of the magnetosphere, resulting in transient ionospheric convection cells. Figure 3.10 only shows the convection cells that form on the duskside. A similar set of cells form on the dawnside; however, they are of opposite orientation. Therefore, the FACs associated with the compression wave go into and out of the ionosphere at dusk and dawn, respectively. The opposite is true for the FACs associated with the inward motion of the magnetopause.

Figure 3.11 shows the temporal evolution of the high-latitude ionospheric current system in response to an abrupt solar wind pressure increase from a global MHD simulation by Keller et al. [2002]. Figure 3.11a displays the FACs associated with a two-celled convection system prior to the pressure increase. Figure 3.11b shows the arrival of the twin convection cells associated with the compression wave, referred to as the PI. Figure 3.11c demonstrates the arrival of the second set of convection cells, known as the MI, associated with the inward motion of the magnetosphere. As the MI grows in magnitude and spatial extent, the PI slowly decays. In Figure 3.11d, the PI has completely disappeared, and only the MI remains.

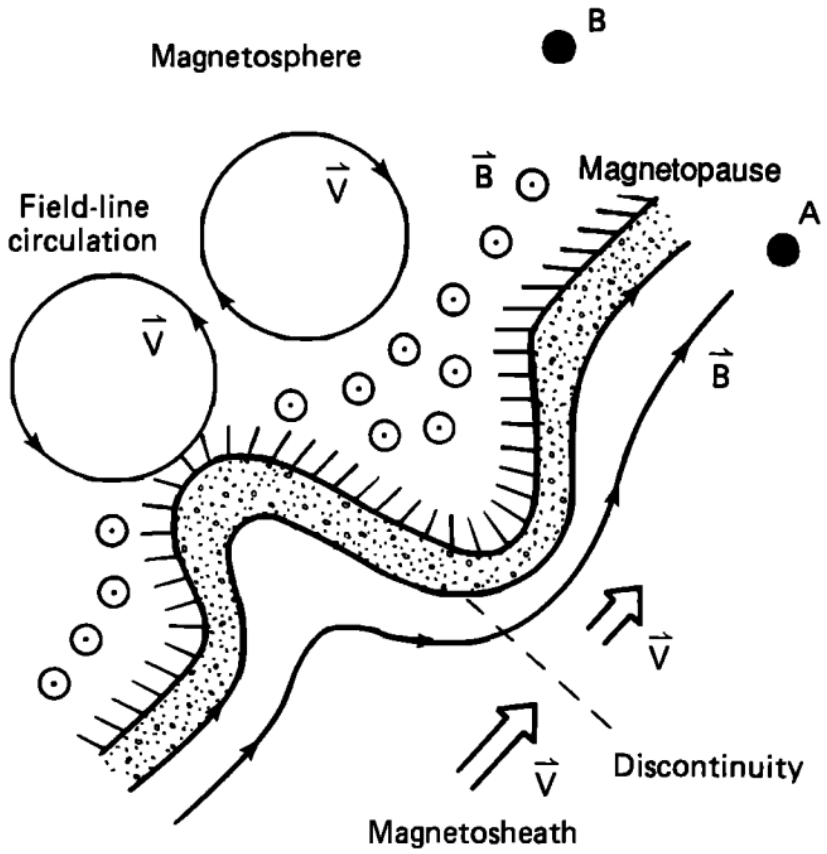

Figure 3.9: Conceptual illustration of how an abrupt solar wind pressure increase induces convection of magnetic field lines in the magnetosphere. The outward motion of the magnetopause is a result of a compression wave launched in the magnetospheric cavity. The subsequent inward motion is caused by the increased solar wind dynamic pressure. Credit: Sibeck [1990].

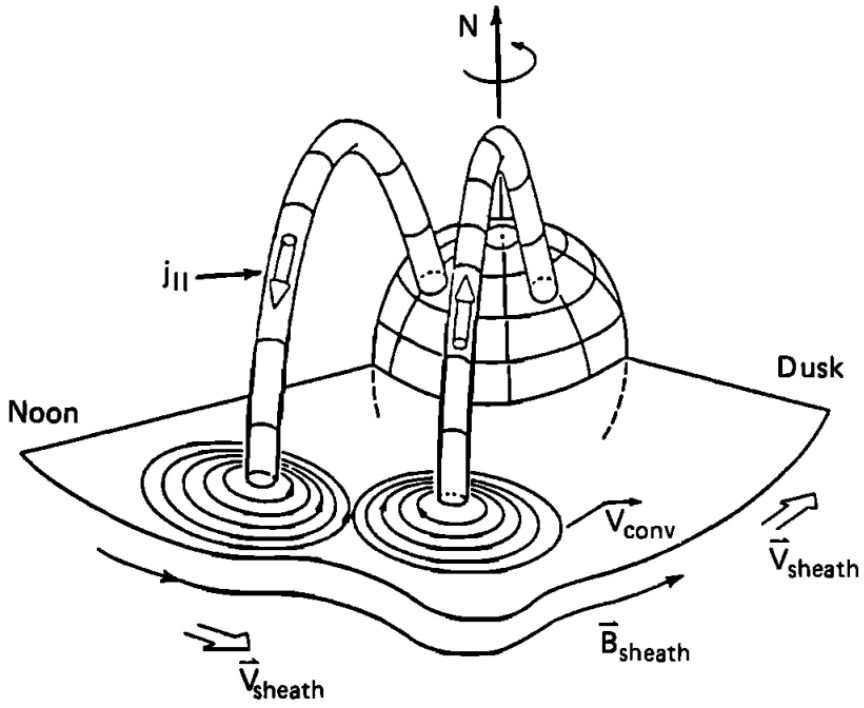

Figure 3.10: Conceptual illustration of how the induced convection in Figure 3.9 results in FACs that close through the ionosphere. Credit: Sibeck [1990].

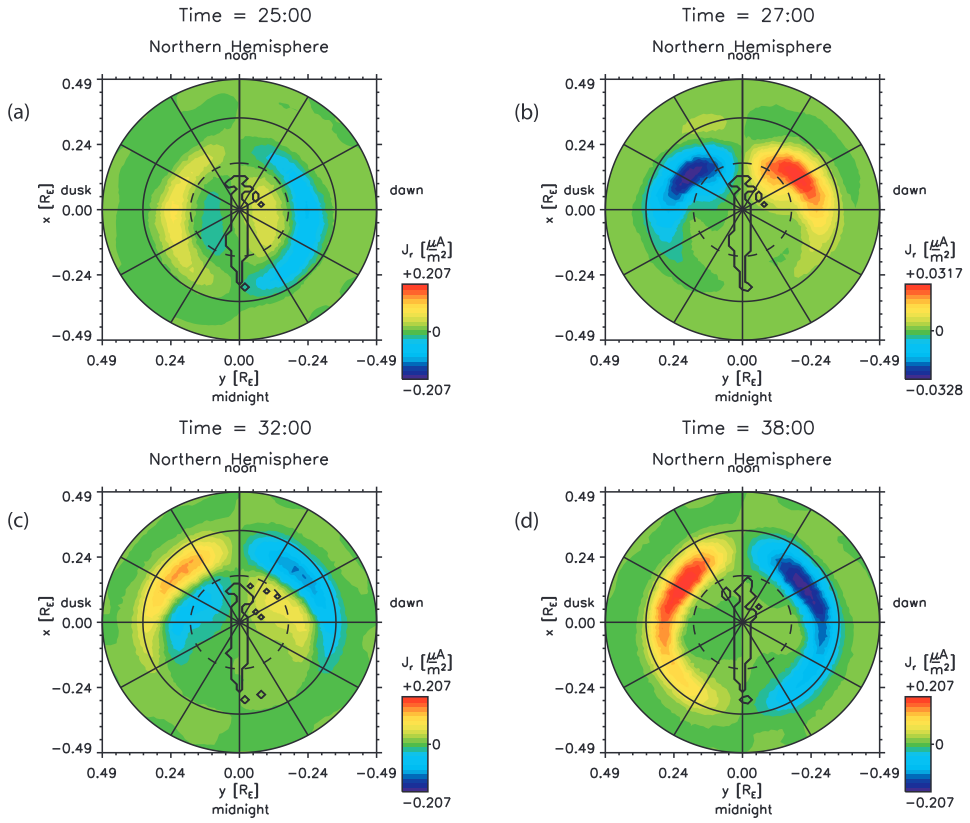

Figure 3.11: Visualization of the ionospheric current system's temporal evolution due to an abrupt solar wind pressure increase. The illustrations are based on an MHD simulation carried out by Keller et al. [2002] and show the FACs. Credit: Keller et al. [2002].

3.5 Observing the magnetic field

This section provides an overview of the various methods used to measure the geomagnetic field, focusing on the instrumentation and key geomagnetic indices used in the analysis in this thesis.

3.5.1 Instrumentation

Historically, ground magnetometers have played a crucial role in the study of the geomagnetic field, particularly in ionospheric electrodynamics [Amm et al., 2010]. Observations of ground magnetic perturbations have enabled the determination of equivalent horizontal ionospheric electrical currents [Friis-Christensen et al., 1988]. This, in turn, gives insight into the solar wind-magnetosphere-ionosphere coupling.

Ground-based observatories are strategically positioned worldwide, continuously monitoring the temporal variations of the magnetic field. Although individual ground magnetometers are typically operated by various organizations, the data are often publicly accessible from platforms like INTERMAGNET (`https://intermagnet.org/`) and SuperMAG (`https://supermag.jhuapl.edu/`). Using SuperMAG as an example, data from 214 observatories is available for the 1st Jan 2022. These platforms ensure comparability between data from different instruments by applying standard post-processing techniques [e.g. Gjerloev, 2012].

An example of such an observatory is located at Brorfelde, near Roskilde, Denmark. This observatory uses a three-axis fluxgate instrument to measure variations in the vector geomagnetic field, conducting weekly calibrations with various specialized equipment. This approach emphasizes the precision and reliability of these traditional measurement techniques. Though the commonly used fluxgate magnetometer has a measurement uncertainty of approximately 1 nT, post-processing, to retrieve the perturbation magnetic field, can introduce additional uncertainties [e.g. Gjerloev, 2012; Waters et al., 2015].

The realm of geomagnetic field measurements has expanded significantly due to advancements in space technology. Satellite missions, such as Swarm and CHAMP, equipped with onboard magnetometers, offer comprehensive geomagnetic data from vantage points inaccessible to ground-based facilities. Furthermore, as discussed in Section 3.3.3, ground magnetometers can only see the magnetic perturbation from the DF ionospheric current, while space-based magnetometers also see that of the CF current system. These advancements have not only enriched our understanding of conditions in the upper ionosphere and magnetosphere but have also enhanced studies of the internal magnetic field [e.g.

Finlay et al., 2020].

The upcoming NASA-funded EZIE (Electrojet Zeeman Imaging Explorer) mission seeks to further this progress. EZIE plans to use remote sensing to observe the oxygen thermal emission from the mesosphere. Based on the Zeeman split of the spectrum, and its polarization, the ambient magnetic field can be derived [Yee et al., 2017, 2021]. This unique measurement of the geomagnetic field, at approximately 85 km altitude, allows for high-resolution reconstruction of the ionospheric current system [Laundal et al., 2021; Madelaire et al., 2023] and marks an innovative step in geomagnetic research.

3.5.2 Geomagnetic indices

The intensity of the geomagnetic storms correlates significantly with the ring current's strength (see Section 3.2.2). Given that the magnetic field generated by the ring current is perceived as almost uniform on Earth's surface, it is rational to quantify the ring current's strength through ground-based magnetometer observations [Dessler and Parker, 1959; Olbert et al., 1968; Sckopke, 1966]. The Dst index [Sugiura, 1964; Sugiura and Kamel, 1991] serves this purpose, formulated based on data from four magnetometer stations, highlighted in blue in Figure 3.12. Although traditionally provided hourly, an alternative 1-minute resolution version, SYM-H [Iyemori et al., 2010], is available. However, the ring current's asymmetry, as noted by Haaland and Gjerloev [2013], poses challenges in interpretations.

An extension of this is the SMR index [Newell and Gjerloev, 2012], which, unlike SYM-H, is provided in four local time versions. The differentiation between SYM-H and SMR is not merely in local time versions but also the network of contributing stations. SYM-H draws from 11 stations, shown as magenta dots in Figure 3.12. However, only six are utilized simultaneously, while the additional stations ensure redundancy. Conversely, SMR incorporates all available stations, from SuperMAG, within the -50° and 50° latitude range, indicated by green lines in Figure 3.12, facilitating the local time subdivisions. However, the indices' formulation could be more meticulous. The latitude-specific selection of Dst-contributing stations ensures minimal interference from both equatorial and auroral electrojets, a consideration partially extended to SYM-H. In contrast, SMR's inclusivity of equatorial and subauroral stations subjects it to contamination during dynamic geomagnetic events, affecting the interpretation in relation to the ring current (Paper I and II).

Furthermore, the PCN index [Willer, 2021], based on the Thule magnetometer station, was used. This index gauges the solar wind's energy input into the magnetosphere,

estimating the anti-sunward plasma convection in the northern polar cap. Distinct from ring current indices, the PC index incorporates not just magnetic field measurements but also the merging electric field at the magnetopause, necessitating in-situ solar wind observations.

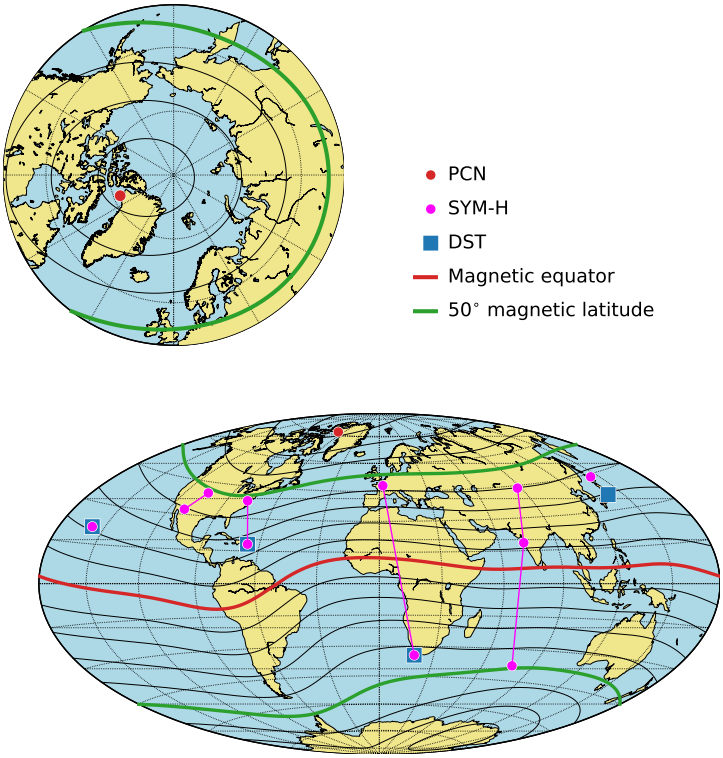

Figure 3.12: Illustration of the ground magnetometers used in the derivation of various geomagnetic indices. The four stations used to derive Dst are marked with blue squares. The 11 stations used to derive SYM-H are marked with magenta dots. Only six of the 11 stations are used at any given time as indicated by the magenta lines. The Thule station used to derive the PCN index is marked with a red dot. The SMR index is derived from all stations available on SuperMAG between -50° and 50° latitude as indicated by the green lines. This means the many tens of stations can be used in the derivation of the SMR index.

Chapter 4

Empirical modeling of the external magnetic field

Magnetic perturbations below the ionosphere offer insights into the ionospheric current system. Section 3.3.3 explains that in the absence of magnetospheric currents, GICs, and oblique FACs, the divergence-free ionospheric current ($\boldsymbol{J}_{\mathrm{DF}}$) is the only source of these perturbations. One straightforward approach to analyzing $\boldsymbol{J}_{\mathrm{DF}}$ through Ampere's law is the application of a 90° clockwise rotation to the magnetic perturbation to align with an overhead current [e.g. Friis-Christensen and Wilhjelm, 1975; Stauning and Troshichev, 2008].

More sophisticated techniques have been developed, each suited to either global or regional analysis. The pioneering effort in empirical modeling of the Earth's internal magnetic field came from Carl Friedrich Gauss. In 1838, Gauss introduced the first mathematical model of the Earth's magnetic field using spherical harmonics [Gauss, 1877]. This methodology remains prevalent in geomagnetism research, particularly in core and lithospheric field modeling [e.g. Alken et al., 2021; Finlay et al., 2020].

Empirical modeling is a crucial tool in the study of ionospheric electrodynamics, allowing for the examination of complex systems without a complete understanding of the underlying mechanisms. As such, it can reveal interdependencies with exogenous parameters that are not evident through theoretical analysis alone. The research presented in this thesis makes extensive use of empirical modeling, and this chapter provides an introduction to the empirical modeling of the ionospheric current system based on magnetic field perturbations from external sources.

Section 4.1 presents the spherical harmonic and spherical elementary current system techniques. The section also provides a basic introduction to inverse theory, highlighting

some challenges encountered during its application. Section 4.2 discuss the inherent limitations in resolution when constructing an empirical model, illustrated by specific examples. Finally, Section 4.3 explores other sources of magnetic perturbation and discusses strategies to mitigate their impact.

4.1 Modeling techniques and inverse theory

The spherical harmonic technique, as detailed in Section 4.1.1, is well-suited for global model construction. However, a global approach is ill-suited for high-latitude electrodynamics as it is regionally confined. Moreover, capturing the spatial structures within the high-latitude ionospheric current systems necessitates spatially dense, regional observations. Consequently, regional modeling techniques are invaluable. The spherical elementary current technique, described in Section 4.1.2, is particularly effective for creating regional models. Regardless of the technique employed, model formulation inevitably involves solving a linear inverse problem. Section 4.1.3 provides a brief introduction to inverse theory and the critical role of regularization.

4.1.1 The spherical harmonic technique

The spherical harmonic (SH) technique takes advantage of the properties of the magnetic potential in the non-conductive region between the ionosphere and the ground, the atmosphere. In this region, both $\boldsymbol{\nabla} \cdot \boldsymbol{B} = 0$ and $\boldsymbol{\nabla} \times \boldsymbol{B} = 0$, which simplifies the magnetic potential to a scalar potential, V. Consequently, V satisfies the Laplace equation and can be expressed through an SH expansion [Chapman and Bartels, 1940],

$$V(r,\lambda,\phi) = a \sum_{n=1}^{\infty} \sum_{m=0}^{n} \Bigg([g_n^m \cos(m\phi) + h_n^m \sin(m\phi)] \left(\frac{a}{r}\right)^{n+1} + [q_n^m \cos(m\phi) + s_n^m \sin(m\phi)] \left(\frac{r}{a}\right)^{n} \Bigg) P_n^m(\cos(\lambda)). \tag{4.1}$$

Here, g_n^m, h_n^m, q_n^m, and s_n^m are SH coefficients, with n representing the SH degree, and m the SH order. The coordinates (r, λ, ϕ) signify the radius, co-latitude, and longitude, respectively, at the point where V is evaluated. The term a is a reference radius for the SH coefficients, and $P_n^m(\cos(\lambda))$ denotes the Schmidt quasi-normalized Legendre polynomial.

The SH representation naturally facilitates the separation of internal and external sources relative to a. The coefficients g_n^m and h_n^m describe the internal source, while q_n^m and s_n^m

refer to the external source. The assumption of a scalar potential is valid only within the non-conductive region, necessitating that both r and a be larger than the Earth's radius and smaller than the ionosphere's radius. Moreover, the SH expansion, theoretically an infinite series, is in practice implemented as a finite series implying a truncation of n. The wavelength of the SH surface waves decreases with increasing n, representing progressively smaller spatial structures. A natural truncation degree, therefore, does not permit finer spatial resolution than the available observations can resolve.

The magnetic field associated with V can be derived as the potential's negative spatial derivative. Here we show the magnetic field for an external source:

$$\begin{aligned} B_r &= -\sum_{n=1}^{\infty}\sum_{m=0}^{n} n\left[q_n^m \cos(m\phi) + s_n^m \sin(m\phi)\right]\left(\frac{r}{a}\right)^{n-1} P_n^m(\cos(\lambda)) \\ B_\lambda &= -\sum_{n=1}^{\infty}\sum_{m=0}^{n} \left[q_n^m \cos(m\phi) + s_n^m \sin(m\phi)\right]\left(\frac{r}{a}\right)^{n-1} \frac{\partial}{\partial\theta} P_n^m(\cos(\lambda)) \\ B_\phi &= \frac{1}{\sin(\theta)}\sum_{n=1}^{\infty}\sum_{m=0}^{n} m\left[q_n^m \sin(m\phi) - s_n^m \cos(m\phi)\right]\left(\frac{r}{a}\right)^{n-1} P_n^m(\cos(\lambda)). \end{aligned} \tag{4.2}$$

This magnetic field, attributable to the external source, corresponds to an equivalent horizontal ionospheric current. Similar to the magnetic field, the equivalent horizontal ionospheric current can be fully described by a scalar potential [Laundal et al., 2016],

$$\Psi = \frac{a}{\mu_0}\sum_{n=1}^{\infty}\sum_{m=0}^{n} \frac{2n+1}{n+1}\left(\frac{a+h}{a}\right)^{n}\left[q_n^m \cos(m\phi) + s_n^m \sin(m\phi)\right] P_n^m(\cos(\lambda)). \tag{4.3}$$

Here, μ_0 is the vacuum permeability and h is the altitude of the equivalent horizontal ionospheric current relative to a. The equivalent current can be computed as

$$\boldsymbol{J}_{eq,\perp} = \hat{\boldsymbol{r}} \times \nabla\Psi. \tag{4.4}$$

It is further possible to derive equivalent FACs as Paper II describes. However, interpreting them as FACs requires Fukushima's theorem to hold, see Section 3.3.3, while also knowing the ratio between Hall and Pedersen conductance.

The SH technique is particularly advantageous for global modeling due to its globally defined basis functions [e.g. Alken et al., 2021; Finlay et al., 2020]. However, robust global solutions require global and uniformly distributed data coverage. It is possible to model only one hemisphere by using only $n - m$ odd terms, thus enforcing hemispheric symmetry [e.g. Elhawary et al., 2023; Laundal et al., 2016; Madelaire et al., 2022a]. To overcome the limitations of the technique in local modeling Haines [1985] introduced spherical cap harmonics, facilitating regional analyses. The reader is referred to Torta

[2020] and references therein for more information on spherical cap harmonics.

4.1.2 The spherical elementary current system technique

In recent times, the SECS technique has gained prominence [e.g. Laundal et al., 2021, 2022; Madelaire et al., 2023; Vanhamäki and Juusola, 2020; Walker et al., 2023; Weygand et al., 2011, 2021]. Proposed by Amm [1997] and building on foundational work by Fukushima [1976]; Tamao [1986], this technique exploits the Helmholtz decomposition of ionospheric currents on a spherical shell. In accordance with Helmholtz's theorem, a vector field can be decomposed into a divergence-free (DF) and a curl-free (CF) vector field. The DF and CF vector fields can be described by a system of DF and CF elementary currents, respectively. It is this system of elementary currents that gives the technique its name. A conceptual illustration of the two types of elementary currents is provided in Figure 4.1. The CF elementary current has a Dirac δ-function divergence, and the DF elementary current has a δ-function curl at its pole, with uniform and oppositely directed sources elsewhere.

Magnetic perturbation below the ionosphere from the CF ionospheric current cancel out those from radial FACs. Therefore, the observed magnetic perturbation is produced solely by the DF current and can be represented by a DF SECS. The electric current, on a spherical shell of radius R_I, produced by a SECS composed of K DF elementary currents is

$$\boldsymbol{J}_\perp = \sum_{i=1}^{K} \frac{S_i^{\mathtt{DF}}}{4\pi R_I} \cot\left(\frac{\pi/2 - \theta_i'}{2}\right) \boldsymbol{T}_i \hat{\boldsymbol{\phi}}_i'. \tag{4.5}$$

Here, $S_i^{\mathtt{DF}}$ is the amplitude of the ith DF elementary current pole, θ_i' and $\hat{\boldsymbol{\phi}}_i'$ are the latitude and eastward unit vector, respectively, in the coordinate system where the ith DF elementary current pole is the north pole, and $\boldsymbol{T}_i$ is a transformation matrix between the coordinate system of the ith elementary current and the coordinate system in which the SECS is defined. The transformation matrix can be derived from Equations 2.16-2.20 in Section 2.5 of [Vanhamäki and Juusola, 2020].

The magnetic field produced by a single DF elementary current is

$$\begin{aligned} B_r^{\mathtt{DF}} &= \frac{\mu_0 S^{\mathtt{DF}}}{4\pi r} \begin{cases} \frac{1}{\sqrt{1+s^2-2s\sin(\theta')}} - 1, & r < R \\ \frac{1}{\sqrt{1+s^2-2s\sin(\theta')}} - s, & r > R \end{cases} \\ B_{\theta'}^{\mathtt{DF}} &= \frac{-\mu_0 S^{\mathtt{DF}}}{4\pi r \cos(\theta')} \begin{cases} \frac{s-\sin(\theta')}{\sqrt{1+s^2-2s\sin(\theta')}} - \sin(\theta'), & r < R \\ \frac{1-s\sin(\theta')}{\sqrt{1+s^2-2s\sin(\theta')}} - 1, & r > R, \end{cases} \end{aligned} \tag{4.6}$$

where $s = \min(r, R)/\max(r, R)$. This configuration implies that the magnetic field perturbation below the spherical shell of radius R, as a result of a DF SECS, is

$$\begin{aligned} B_r &= \frac{\mu_0 S^{\mathrm{DF}}}{4\pi r} \sum_{i=1}^{K} \frac{1}{\sqrt{1+s^2-2s\sin(\theta_i')}} - 1 \\ \boldsymbol{B}_\perp &= \frac{-\mu_0 S^{\mathrm{DF}}}{4\pi r \cos(\theta')} \sum_{i=1}^{K} \left[\frac{s-\sin(\theta')}{\sqrt{1+s^2-2s\sin(\theta')}} - \sin(\theta') \right] \boldsymbol{T}_i \hat{\boldsymbol{\theta}}_i'. \end{aligned} \tag{4.7}$$

The SECS technique is extremely flexible as the shape and dimensions of the grid on which it is defined can be customized for a given situation. An SECS composed of 100 elementary currents can be placed in various configurations, e.g., 10×10 or 4×25. Furthermore, by varying the grid spacing, the spatial extent of the SECS can be altered. Therefore, the SECS technique offers adaptability and detailed regional analyses, with the flexibility to handle varying data coverage. The reader is referred to Vanhamäki and Juusola [2020] and references therein for a detailed introduction to the SECS technique.

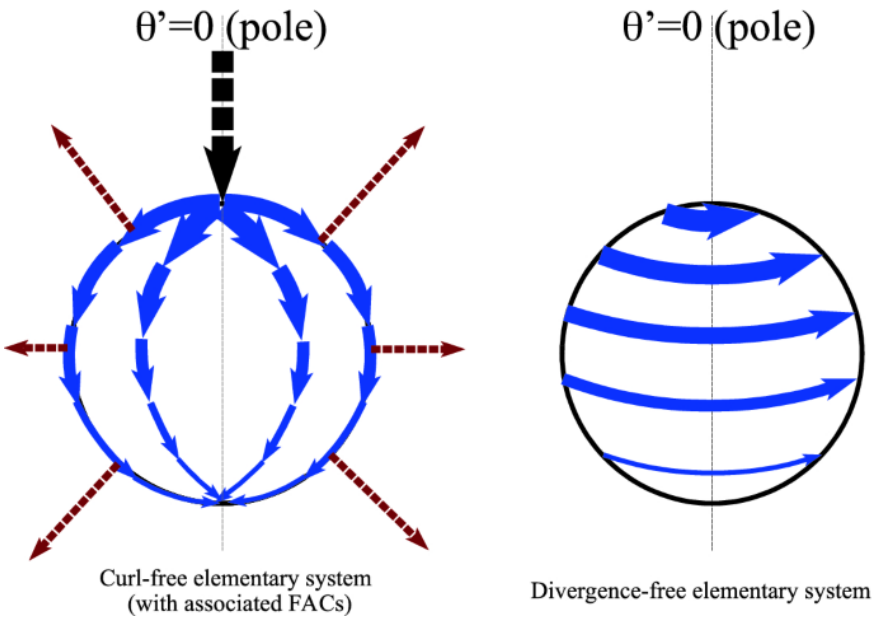

Figure 4.1: Conceptual illustration of the CF (left) and DF (right) elementary currents. Credit: Vanhamäki and Juusola [2020].

4.1.3 Basic inverse theory

The modeling techniques presented in Sections 4.1.1 and 4.1.2 provide a linear relationship between ground magnetic field perturbation and an equivalent ionospheric current. Given multiple measurements of the magnetic field, a system of linear equations can be made. However, the retrieval of the coefficients q_n^m, s_n^m, and S^{DF} requires solving an inverse problem. The following section is a basic introduction to inverse theory. The reader is referred to [e.g. Aster et al., 2013; Tarantola, 2005] for a detailed introduction to inverse theory. Both the SH and SECS representation of the magnetic field, Equations 4.2 and 4.7, can be cast into a matrix equation as

$$\boldsymbol{d} = \boldsymbol{G}\boldsymbol{m}. \tag{4.8}$$

Here, $\boldsymbol{d}$ is a column vector of magnetic field measurements, $\boldsymbol{m}$ is a column vector containing the amplitude of the SECS poles or SH coefficients, and $\boldsymbol{G}$ is a matrix containing the linear relation between the $\boldsymbol{d}$ and $\boldsymbol{m}$.

The forward problem, Equation 4.8, is a system of linear equations. We wish to estimate $\boldsymbol{m}$, the state of the system, based on $\boldsymbol{d}$, observations of the system. This is inherently a probabilistic endeavour; observations are in their nature probability distributions that frequently are summarized by only their mode. Consider the joint probability distribution $p(\boldsymbol{m}, \boldsymbol{d})$ for parameters $\boldsymbol{m}$ and $\boldsymbol{d}$

$$p(\boldsymbol{m}, \boldsymbol{d}) = p(\boldsymbol{m}|\boldsymbol{d})\, p(\boldsymbol{d}) = p(\boldsymbol{d}|\boldsymbol{m})\, p(\boldsymbol{m}). \tag{4.9}$$

In our case, Equation 4.8, it is $\boldsymbol{m}$ that we are interested in and, therefore, the probability distribution $p(\boldsymbol{m}|\boldsymbol{d})$. By isolating $p(\boldsymbol{m}|\boldsymbol{d})$ in Equation 4.9,

$$p(\boldsymbol{m}|\boldsymbol{d}) = \frac{p(\boldsymbol{d}|\boldsymbol{m})\, p(\boldsymbol{m})}{p(\boldsymbol{d})}, \tag{4.10}$$

Bayes theorem, and the general solution to the inverse problem, is retrieved. Here, $p(\boldsymbol{m}|\boldsymbol{d})$, $p(\boldsymbol{d}|\boldsymbol{m})$, $p(\boldsymbol{m})$, and $p(\boldsymbol{d})$ are the posterior model distribution, the likelihood, the prior model distribution, and the evidence, respectively. The posterior model distribution defines the probability of the model given a set of observations. The likelihood is the probability of the observations given a model. If the observations are of a known probability distribution the likelihood is easily calculated from the misfit between model prediction and observations. The prior model distribution is the information regarding the model prior to the introduction of data. The evidence is the probability of the observations and is frequently neglected as it simply acts as a normalization factor and is irrelevant for parameter estimation. However, the evidence is not negligible when

comparing the probability of models determined from different datasets.

In general, there is no guarantee that the shape of the probability distributions is known or if the inverse problem is linear. In fact, $p(\boldsymbol{m}|\boldsymbol{d})$ might be multi-modal and contain multiple solutions of equally high probability. The result is the lack of an analytical solution. However, there are numerous algorithms for estimating $p(\boldsymbol{m}|\boldsymbol{d})$ through an iterative sampling approach. The reader is referred to [e.g. Brooks et al., 2011; Gelman et al., 2004] for a detailed introduction of algorithms for sampling $p(\boldsymbol{m}|\boldsymbol{d})$. In the rest of this section, we will focus on the least squares method for solving linear inverse problems. The least squares method provides an analytical solution given an assumption of Gaussian probability distributions.

Solving a linear inverse problem can be simplified significantly by assuming Gaussian probability distributions. The least squares solution is an analytical solution to the inverse problem that provides the maximum likelihood solution when minimizing the squared norm of the data misfit. Formally, this involves minimizing the objective function

$$\Phi(\boldsymbol{m}) = (\boldsymbol{d} - \boldsymbol{G}\boldsymbol{m})^T \boldsymbol{C}_d^{-1} (\boldsymbol{d} - \boldsymbol{G}\boldsymbol{m}) + (\boldsymbol{m} - \boldsymbol{m}_{pri})^T \boldsymbol{C}_m^{-1} (\boldsymbol{m} - \boldsymbol{m}_{pri}), \tag{4.11}$$

where $\boldsymbol{C}_d$ is the data covariance matrix, and $\boldsymbol{m}_{pri}$ and $\boldsymbol{C}_m$ are the mode and covariance matrix of the prior model distribution. By differentiating Equation 4.11 with respect to $\boldsymbol{m}$ and setting it equal to zero, the least squares solution can be written as

$$\widetilde{\boldsymbol{m}} = \left(\boldsymbol{G}^T \boldsymbol{C}_d^{-1} \boldsymbol{G} + \boldsymbol{C}_m^{-1}\right)^{-1} \left(\boldsymbol{G}^T \boldsymbol{C}_d^{-1} \boldsymbol{d} + \boldsymbol{C}_m^{-1} \boldsymbol{m}_{pri}\right), \tag{4.12}$$

where $\widetilde{\boldsymbol{m}}$ is the maximum likelihood solution and

$$\boldsymbol{C}_{pm} = \left(\boldsymbol{G}^T \boldsymbol{C}_d^{-1} \boldsymbol{G} + \boldsymbol{C}_m^{-1}\right)^{-1} \tag{4.13}$$

is the posterior model covariance. Together $\widetilde{\boldsymbol{m}}$ and $\boldsymbol{C}_{pm}$ define $p(\boldsymbol{m}|\boldsymbol{d})$, the full solution to the posed minimization problem in Equation 4.11. The model variance can be propagated into any quantity of interest using

$$\boldsymbol{C}_A = \boldsymbol{A}\boldsymbol{C}_{pm}\boldsymbol{A}^T, \tag{4.14}$$

if there exists a linear relationship ($\boldsymbol{A}$) between it and $\boldsymbol{m}$. Using Equation 4.14 the posterior model variance can be projected into predictions of the magnetic field.

In Earth and Space physics, we are seldom in possession of a prior model distribution.

Without $p(\boldsymbol{m})$ the cost function and maximum likelihood solution reduces to

$$\begin{aligned} \Phi(\boldsymbol{m}) &= (\boldsymbol{d} - \boldsymbol{G}\boldsymbol{m})^T \boldsymbol{C}_d^{-1} (\boldsymbol{d} - \boldsymbol{G}\boldsymbol{m}) \\ \widetilde{\boldsymbol{m}} &= \left(\boldsymbol{G}^T \boldsymbol{C}_d^{-1} \boldsymbol{G}\right)^{-1} \boldsymbol{G}^T \boldsymbol{C}_d^{-1} \boldsymbol{d}. \end{aligned} \tag{4.15}$$

However, inverse problems are often challenging because they are both under-determined, possess a null space, and ill-conditioned so that solutions of the type in Equation 4.15 are unstable in the presence of noise. Therefore, it is common to stabilize the solution by means of regularization. Formally, this involves a modification to the objective function by adding a term to minimize some aspect of the model,

$$\Phi(\boldsymbol{m}) = (\boldsymbol{d} - \boldsymbol{G}\boldsymbol{m})^T \boldsymbol{C}_d^{-1} (\boldsymbol{d} - \boldsymbol{G}\boldsymbol{m}) + \alpha \boldsymbol{m}^T \boldsymbol{R} \boldsymbol{m}. \tag{4.16}$$

Here, $\boldsymbol{R}$ is the roughening matrix describing some metric of the model parameters while α controls the trade-off between the data-driven solution and the imposed model constraint. Following the approach for deriving Equation 4.12 the regularized least squares solution is

$$\widetilde{\boldsymbol{m}} = \left(\boldsymbol{G}^T \boldsymbol{G} + \lambda \boldsymbol{R}\right)^{-1} \boldsymbol{G}^T \boldsymbol{d}, \tag{4.17}$$

where $\lambda = \alpha^2$.

One of the more simple methods to prevent overfitting with regularization is by minimizing the squared norm of the model parameters. This means that $\boldsymbol{R} = \boldsymbol{I}$ and the regularized solution takes the form

$$\widetilde{\boldsymbol{m}} = \left(\boldsymbol{G}^T \boldsymbol{G} + \lambda \boldsymbol{I}\right)^{-1} \boldsymbol{G}^T \boldsymbol{d}, \tag{4.18}$$

where $\boldsymbol{I}$ is an identity matrix. This is known as zeroth-order Tikhonov regularization. However, a more general expression may be written as

$$\widetilde{\boldsymbol{m}} = \left(\boldsymbol{G}^T \boldsymbol{G} + \lambda \boldsymbol{L}^T \boldsymbol{L}\right)^{-1} \boldsymbol{G}^T \boldsymbol{d}. \tag{4.19}$$

Here $\boldsymbol{R} = \boldsymbol{L}^T \boldsymbol{L}$ and $\boldsymbol{L}$ describes the linear relation between the model parameters. In higher-order Tikhonov regularization $\boldsymbol{L}$ would be a matrix taking the numerical difference between model parameters allowing for the minimization of gradients and thereby the retrieval of a smoother solution.

An alternative to zeroth order Tikhonov regularization is truncated Singular Value Decomposition (SVD). Here the design matrix $\boldsymbol{G}$ is factored into

$$\boldsymbol{G} = \boldsymbol{U}\boldsymbol{S}\boldsymbol{V}^T, \tag{4.20}$$

where $\boldsymbol{U}$ and $\boldsymbol{V}$ are square matrices spanning the data and model space, respectively, while $\boldsymbol{S}$ is a diagonal matrix of singular values. SVD is conceptually similar to an eigenvalue decomposition. That means singular values close to zero provide effectively no additional information about the system. Therefore, truncating the series of singular values can help stabilize the solution.

There are pros and cons with both Tikhonov regularization and truncated SVD. However, Tikhonov regularization is more straightforward for higher-order regularization, i.e. when more information about the structure of the solution is known. It is possible to implement higher-order regularization using SVD by using generalized SVD. In the work presented in this thesis, we have used Tikhonov regularization and will, therefore, focus on solutions in the form of Equations 4.17.

Regardless of implementation, regularization requires tuning of a hyper-parameter. For Tikhonov regularization, it is the parameter λ. There are several techniques for determining the optimal regularization parameter, but there is no universal technique. The reader is referred to Bauer and Lukas [2011] for a detailed review of different techniques. In the work presented in this thesis, we have employed both the L-curve [Hansen, 1992] and generalized cross-validation [e.g. Aster et al., 2013]. Furthermore, it is possible to design a cost function with more than one regularization term, thus requiring the optimization of multiple hyperparameters. This is not straightforward but has been addressed by Belge et al. [2002] who extended the L-curve technique to multiple parameters. In Paper IV we present a technique for determining a relationship between multiple regularization parameters effectively reducing the number of parameters needed to be determined allowing for the use of conventional approaches like the L-curve and generalized cross-validation.

A conceptual understanding of Bayes' theorem is extremely important. However, the human intuition of probabilities is seldom very good [Harari, 2015]. In our field, ionospheric physics, there is a tendency to only provide a single solution, the mode of $p(\boldsymbol{m}|\boldsymbol{d})$. This is a shortcoming that by its rectification will elevate our community's understanding of the applied modeling technique and the usefulness of results. A result without uncertainty means nothing.

4.2 Spatial scales

No matter which modeling technique is employed, deriving an ionospheric equivalent current from ground magnetic perturbation has inherent practical limitations. One key

factor is the decreasing strength of the magnetic field as the distance from the source current increases. The rate of decrease is dictated by the spatial dimensions of the magnetic field structure. This becomes clear when expressing the magnetic field in terms of SHs, Equation 4.2. For an external source, the downward continuation of the magnetic field from the ionosphere to Earth's surface is proportional to $(R_E/R_I)^{n-1}$. Here, R_E and R_I are the distances from Earth's center to the surface and the ionosphere, respectively, while n is the SH degree.

Large-scale magnetic perturbations, e.g. created by the auroral electrojets, spanning multiple degrees of latitude and/or longitude, correspond to lower values of n. Conversely, small-scale features are associated with higher values of n. Therefore, the magnitude of the magnetic perturbation from a small-scale feature drops off faster with distance to the source current, than that of large-scale features. The distance between the observed ground magnetic field and its ionospheric source current is approximately 110 km. As a result, it is in practice not possible to resolve spatial structures smaller than 110 km in the magnetic perturbation field generated by ionospheric currents [Gjerloev et al., 2011; Laundal et al., 2021; Madelaire et al., 2023; Untiedt and Baumjohann, 1993].

In a theoretical scenario featuring perfect measurements, ample data coverage, no numerical instabilities, and limitless computational resources, it would be possible to resolve all spatial scales. However, in practice, we face a couple of limitations. First, the measurement uncertainty of an instrument determines what signal can be observed. The signal-to-noise ratio (SNR) quantifies when a signal is too weak to be observed, relative to the background noise/measurement uncertainty. An SNR above 1 signifies that the instrument is sensitive enough to measure the signal. Oppositely, a signal can not be observed if the SNR is below 1. Therefore, SNR equal 1 is referred to as the noise floor as it is the separation between observable and unobservable signals. Figure 4.2 shows the magnitude of magnetic perturbation, at the ionosphere, required to exceed the noise floor of various instruments. Ground magnetometers are often considered to have an uncertainty of 1 nT or less [Gjerloev, 2012]. The solid blue line illustrate the case of a ground magnetometer with 1 nT uncertainty. We see that a magnetic structure in the ionosphere with a spatial scale of 200 km can not be observed by a ground magnetometer if the magnetic perturbation is 30 nT or lower at ionospheric altitude. Following this logic, it is possible to observe structures of 80 km, but the magnetic perturbation at the ionosphere has to be larger than approximately 5000 nT to exceed the noise floor of the ground magnetometer.

Analysis based on magnetic field perturbations requires subtraction of the ambient field in a pre-processing step. This could be the core and lithospheric magnetic fields. Su-

permag (https://supermag.jhuapl.edu/) is a popular web service for downloading magnetic perturbation measurements from ground magnetometers. The Supermag post-processing [Gjerloev, 2012] can result in uncertainty larger than 1 nT [Gjerloev, 2012; Waters et al., 2015]. The blue dotted line in Figure 4.2 shows the result of increasing the uncertainty to 10 nT. Keep in mind that this is a combined uncertainty containing both the measurement uncertainty and the potential error resulting from pre-processing. We will simply refer to this combined uncertainty as measurement uncertainty for simplicity. By increasing the uncertainty the noise-floor changes from approximately 900 to 10,000 nT when attempting to observe 100 km structures.

Figure 4.2 also shows this spatial scale to noise relation for EZIE which conceptually is like a magnetometer located at 85 km altitude. The NASA-funded satellite mission EZIE (see Section 3.5.1) aims to remotely sense magnetic perturbations in the mesosphere, located about 35 km below the ionospheric source current. The solid, dotted, and dashed lines (orange) show the noise floor for measurement uncertainties of 1, 10, and 100 nT, respectively. When the uncertainty is 100 nT a ground magnetometer with 1 nT uncertainty will be better at observing perturbation from structures larger than approximately 115 km. However, EZIE, with an uncertainty of about 100 nT, will be better for measuring perturbation from structures smaller than approximately 115 km. This statement does not factor in the implication of spatial coverage which we will discuss now.

The second practical limitation is the spacing between measurements. For context, Figure 4.3 summarizes the minimum distance between a ground magnetometer station and any other station. The figure is based on the ground magnetometer stations available from SuperMAG (https://supermag.jhuapl.edu/). Importantly, not all these stations are operational simultaneously. For latitudes above 60°, approximately 40 of the 160 stations are within 100 km of another station. If they were placed in a grid it would be 500×800 km, approximately the size of Denmark. Denmark is pretty small.

Given these conditions, it is evident that the achievable spatial resolution based on ground magnetometer data is fundamentally limited by the distribution of the stations. There are several strategies for improving the resolution. One option involves combining different types of measurements, such as done in AMIE and Lompe (Section **??**). Another seemingly straightforward solution is to populate a grid with ground magnetometers using a 100×100 km grid spacing; achieving this between latitudes 65° and 75° would require approximately 1,500 stations. This is not feasible due to oceans, lakes, mountains, and urban areas. Even on a smaller scale like North America or Fennoscandia, this is impractical as such stations are costly.

One potential workaround could be the use of low-precision, budget-friendly magnetometers to augment existing networks in regions like Fennoscandia or North America. Pairing these low-precision devices with pre-existing high-precision ground magnetometers could enhance spatial resolution. Another avenue to explore is conducting measurements closer to the source current, like EZIE. The radial distance, as well as the temporal and spatial separation between its measurements, allows for the resolution of mesoscale features (Paper IV).

As part of its public outreach, the EZIE team is developing an affordable magnetometer kit expected to cost a couple hundred US dollars. The instrument is not fully developed but will provide 3D magnetic field measurements with approximately 20 nT uncertainty. The collected data will be uploaded to a server and processed using the SuperMAG algorithm [Gjerloev, 2012]. Such instruments could serve as an effective proof-of-concept for filling the large gaps that exist in current ground magnetometer arrays, thereby facilitating a higher level of spatial resolution in ionospheric current system reconstruction.

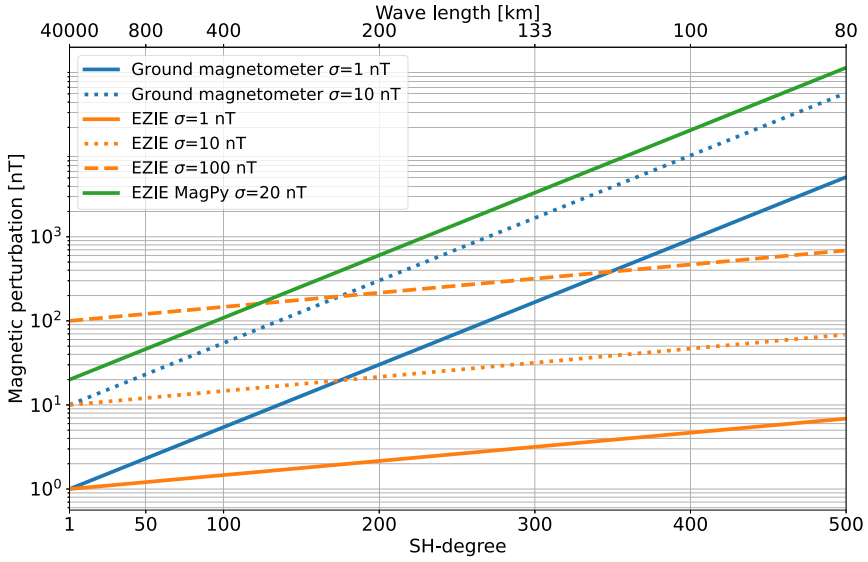

Figure 4.2: An illustration of the noise floor as a function of spatial scale-size. Here, we show the required magnetic perturbation, at ionospheric altitude, necessary to exceed the noise floor for different magnetometers and levels of measurement uncertainty. The blue solid and dotted lines indicate ground-based magnetometer stations with 1 and 10 nT measurement uncertainty, respectively. The orange solid, dotted, and dashed lines indicate measurements of the magnetic field at 85 km altitude derived by EZIE with 1, 10, and 100 nT uncertainty, respectively. The green line indicates the low-precision magnetometer being developed by the EZIE outreach program with (estimated) 20 nT uncertainty.

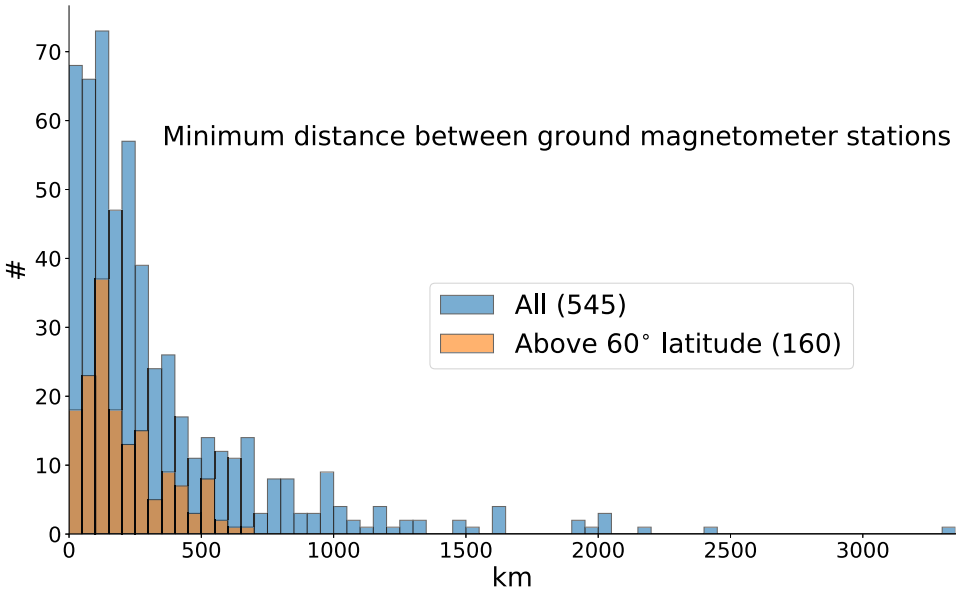

Figure 4.3: The distribution of the minimum distance from one ground magnetometer station to another over the Earth's surface in increments of 50 km. The coordinates for the ground magnetometers were provided by SuperMAG and include all magnetometers, both past and present.

4.2.1 Synthetic example: Augmenting pre-existing ground magnetometer arrays with low-precision measurements

In this section, we will explore the idea of augmenting a pre-existing high-precision ground magnetometer array with cheaper low-precision magnetometers. Synthetic magnetic field perturbation are generated based on an MHD simulation. The synthetic data is used to reconstruct the DF ionospheric current using the SECS technique (Section 4.1.2) by solving the linear inverse problem with zeroth-order Tikhonov regularization (Section 4.1.3). The reconstruction is done for various configurations of high- and low-precision measurements. Qualitative and quantitative comparisons are made based on the reconstruction and spatial resolution estimates, respectively. In addition, we take the opportunity to address the issue of edge effects when applying the SECS technique.

Here we provide a brief introduction to the quantification of spatial resolution based on the method presented in Paper IV. By inserting the forward problem (Equation 4.8) into the regularized least squares solution (Equation 4.18) we derive a relation between $\boldsymbol{m}$ and $\widetilde{\boldsymbol{m}}$, the truth and estimated solution:

$$\widetilde{\boldsymbol{m}} = \left(\boldsymbol{G}^T \boldsymbol{C}_d^{-1} \boldsymbol{G} + \lambda \boldsymbol{I}\right)^{-1} \boldsymbol{G}^T \boldsymbol{C}_d^{-1} \boldsymbol{G} \boldsymbol{m} = \boldsymbol{R}_m \boldsymbol{m}. \tag{4.21}$$

The model resolution matrix, $\boldsymbol{R}_m$, describes how well $\boldsymbol{m}$ can be resolved based on the available information, i.e. measurement location, measurement uncertainty, prior information/regularization, and the relation between the measured quantity and the system being modeled. The columns of $\boldsymbol{R}_m$ are point-spread functions (PSFs) describing how a single parameter of $\boldsymbol{m}$ is smeared out when projected through $\boldsymbol{R}_m$. By the quantification of the PSF's spatial extent, we can estimate the spatial resolution.

The synthetic data is based on the MHD simulation used to create synthetic data for the EZIE satellite mission [Laundal et al., 2021]. The RE-developed Magnetosphere-Ionosphere Coupler/Solver (REMIX) [Merkin and Lyon, 2010] is used to account for the MI coupling. However, some discrepancy in the magnetic field perturbation occurs when carrying out the Biot-Savart integral using the available tools and it is not possible to decompose the ionospheric current into its DF and CF parts. We therefore go through the exercise of creating a Lompe [Laundal et al., 2022] model based on the FACs, conductance, and potential electric field output from REMIX. The Lompe model is created on a cubed sphere grid down to approximately 60° latitude with a grid spacing of 55 km. The majority of the model is based on the FAC and conductance while the electric field is included below 65° latitude to help with edge effects. Furthermore, the solution is regularized slightly with zeroth-order Tikhonov regularization.

Figure 4.4a shows the radial magnetic field perturbation at ionospheric altitude, produced by the Lompe model. Overlain is an outline of the grid for the synthetic magnetic field data. Figure 4.4b shows the close-up of the overlain grid, in Figure 4.4a. Figure 4.5 compares the ionospheric currents and magnetic field perturbation produced by the Lompe model in more detail. Figure 4.5a-c shows the full, CF, and DF ionospheric current, respectively. Figures 4.5d-f show the eastward, northward, and upward components of the magnetic field at ionospheric altitude overlain with the DF current. Figures 4.5g-i show the less structured ground magnetic field. In the following examples, the synthetic data is created by sub-sampling the magnetic field (Figures 4.5g-i) while adding Gaussian noise.

Before testing various configurations of high- and low-precision measurements, we wanted to validate the SECS technique's ability to reproduce the truth (Figure 4.5d-i). Figure 4.6 summarizes the least squares solution (Equation 4.12) when synthetic data is placed on a 100×100 km grid. The DF SECS is also placed on a 100×100 km grid offset by half a grid cell from that of the synthetic data. Figures 4.6a-c show the reconstructed magnetic field at ionospheric altitude overlain with an equivalent ionospheric current. Figures 4.6d-f shows the reconstructed ground magnetic field. A comparison between Figures 4.5d-i and 4.6 shows that the ground magnetic field is reproduced very well while there are severe edge effects at ionospheric altitude. The issue stems from the influence of

electric currents outside the modeling grid (Figure 4.4a). The distant currents contribute to the measured magnetic field and map into the overhead DF SECS. The edge effects can be removed using regularization.

Figure 4.7 summarize the regularized solution (Equation 4.18) when λ is determined using the L-curve (Section 4.1.3). However, the regularized solution comes at the cost to the resolution which is evident when compared to the truth (Figure 4.5). Quantitatively, the spatial resolution increased from 100 to 300 km when applying regularization.

Figure 4.8 explores the possibility of placing layers of DF elementary currents outside the original grid to compensate for the contribution by distant electric currents. By gradually increasing the amount of DF elementary current layers while solving the regularized inverse problem, we determined that 5 layers are sufficient to account for the effect of distant currents while minimizing the effect of regularization of the spatial resolution. Effectively, the spatial resolution dropped back down to 100 km. A comparison of the model predictions using (Figure 4.8) and the truth (Figure 4.5d-i) suggests that this method works very well. In the following examples, we have applied 5 layers of DF elementary currents.

To emphasize the impact of the low-precision measurements on the spatial resolution, we used a grid with an 800×800 km spacing for the high-precision data. We tested four configurations where all contain high-precision measurements while only three contain low-precision measurements as illustrated by the black dots and blue crosses in Figure 4.9:

- Low-precision measurements on a 100×100 km grid (Figure 4.9b).
- Low-precision measurements are placed on the edge of the high-precision grid cells (800×800 km) with a 100 km spacing (Figure 4.9c).
- Low-precision measurements on a 400×400 km grid (Figure 4.9d).

Figure 4.9 compares the spatial resolution while also visualizing the position of the high- and low-precision measurements in each configuration as black dots and blue crosses, respectively. Figures 4.10 and 4.11 compare the reconstruction from the configuration highlighted in Figure 4.9a and 4.9c. From both the quantitative comparison of the spatial resolution and the qualitative comparison of the model predictions it is clear that augmenting pre-existing high-precision ground magnetometer arrays with low-precision units can drastically improve the efficacy of empirical models. We therefore highly recommend that this path is explored in the future. Sometimes quantity is better than quality.

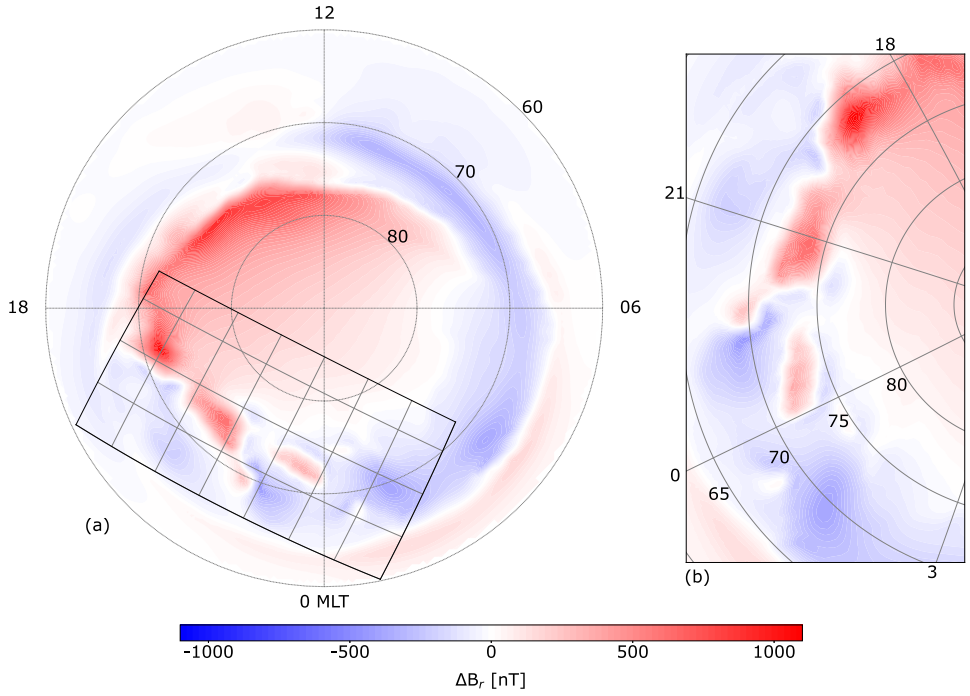

Figure 4.4: Overview of the synthetic data. Figure 4.4a shows the radial magnetic field component produced by the Lompe model at ionospheric altitude. An outline of the cubed sphere grid used for further analysis is overlain. Figure 4.4b shows a close-up of the outlined analysis grid in Figure 4.4a.

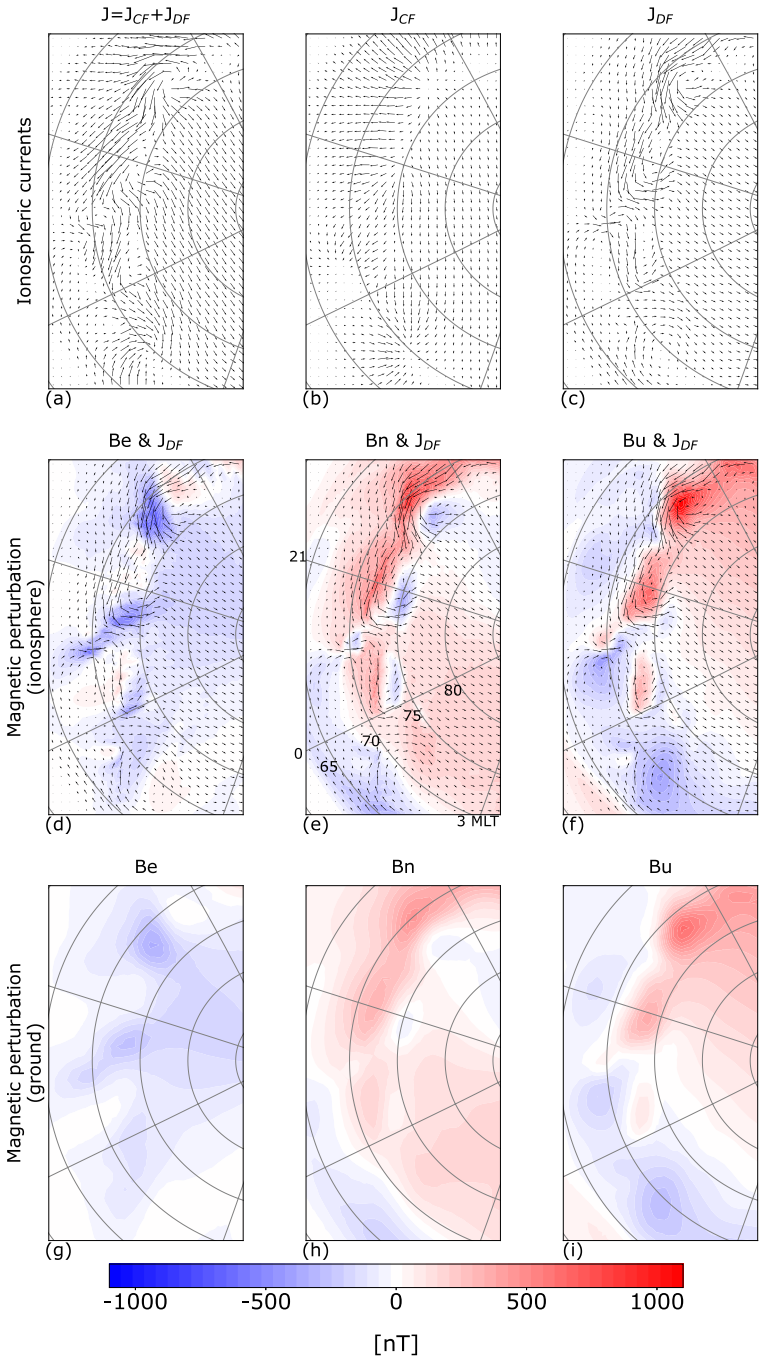

Figure 4.5: A summary of the synthetic data. Figures 4.5a-c show the full, CF and DF ionospheric electric current, respectively. Figures 4.5d-f show the eastward, northward, and upward magnetic field components at ionospheric altitude, respectively, with the DF current overlain. Figures 4.5g-i show the magnetic field perturbation on the ground.

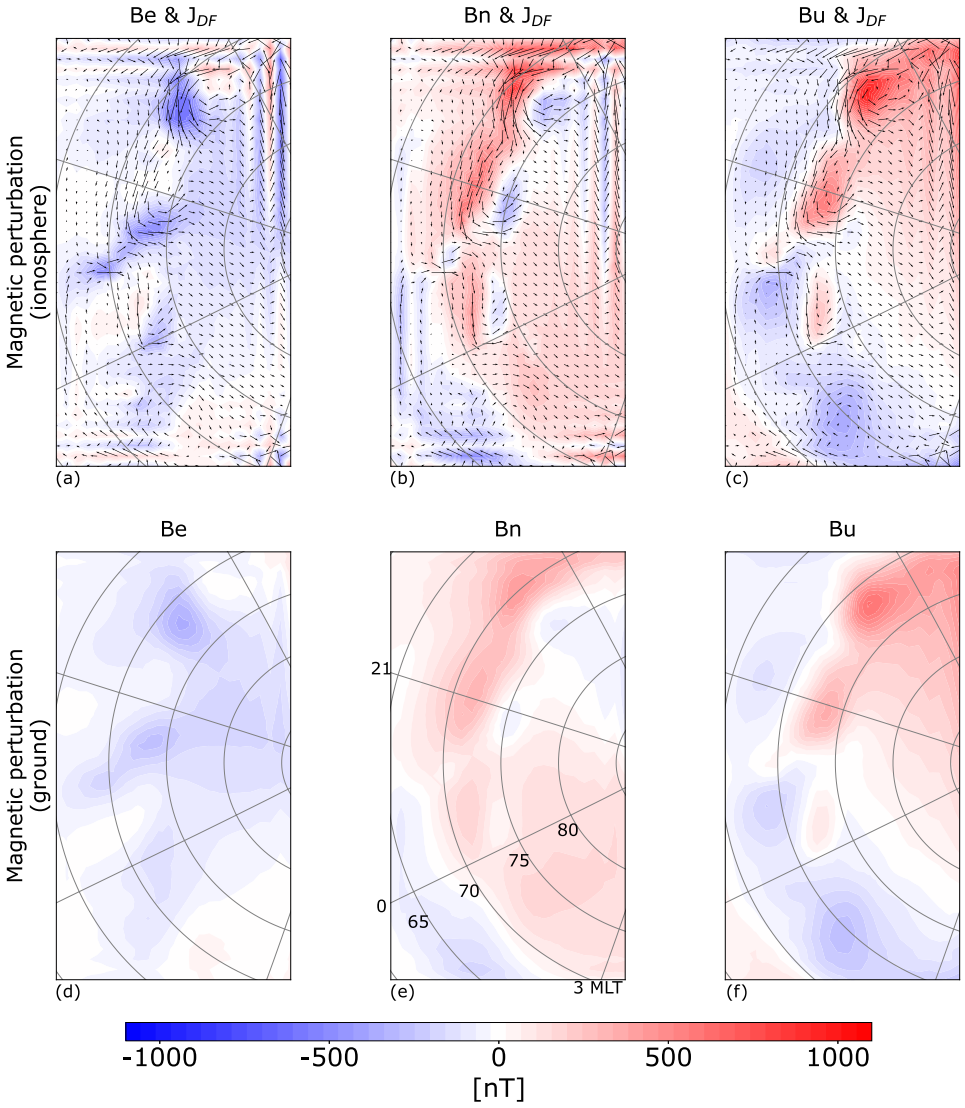

Figure 4.6: Summary of the inversion result using perfect synthetic data on a 100×100 km grid. Figures 4.6a-c show the reconstructed eastward, northward, and upward magnetic field components at ionospheric altitude, respectively, with the DF current overlain. Figures 4.6d-f shows the reconstructed ground magnetic perturbation.

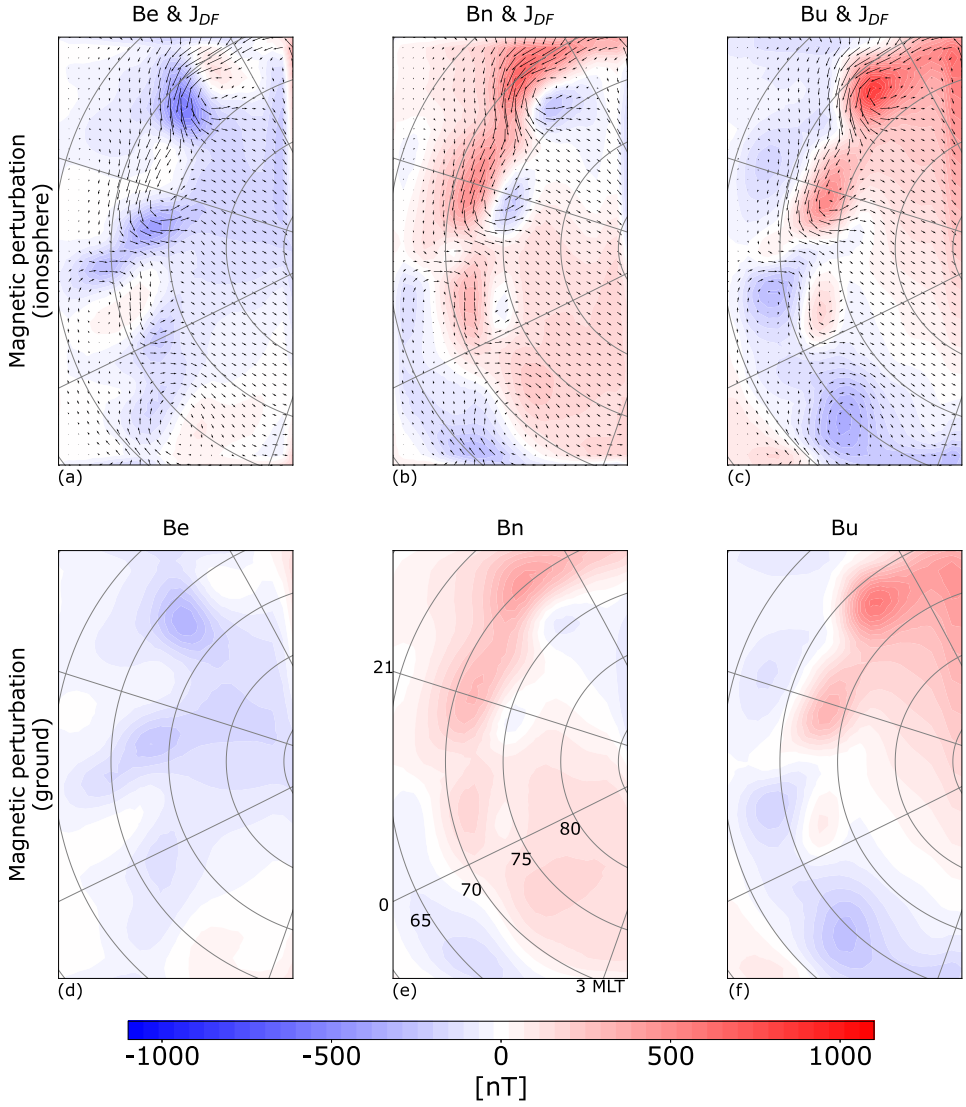

Figure 4.7: The same as Figure 4.6, but for the regularized solution.

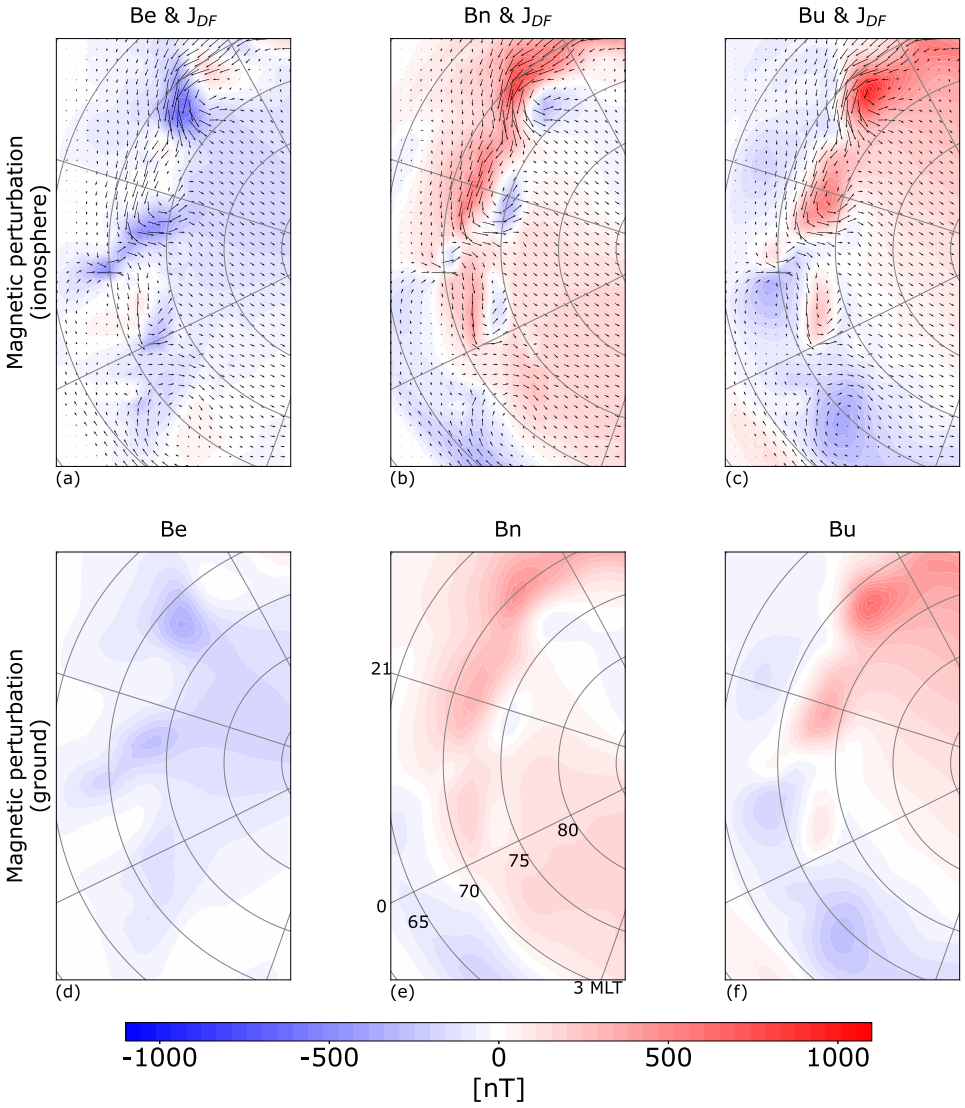

Figure 4.8: The same as Figure 4.6, but for the regularized solution including extra layers of DF elementary currents outside the original grid.

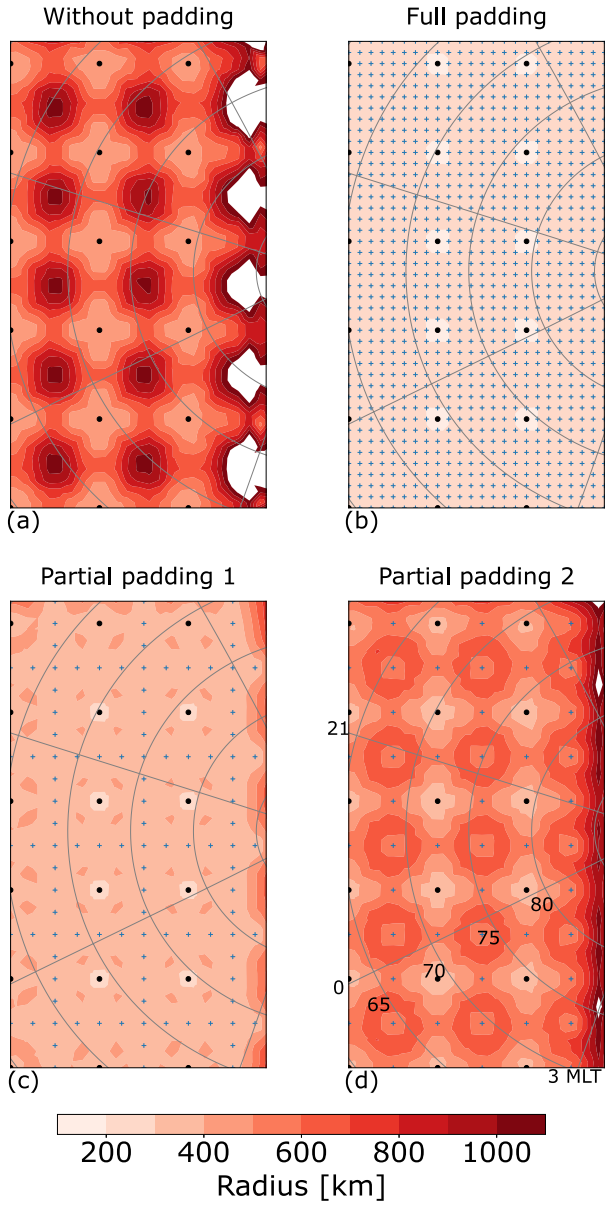

Figure 4.9: A comparison of the spatial resolution for various configurations of high- and low-precision synthetic data. The black dots and blue crosses illustrate the location of the high- and low-precision measurements.

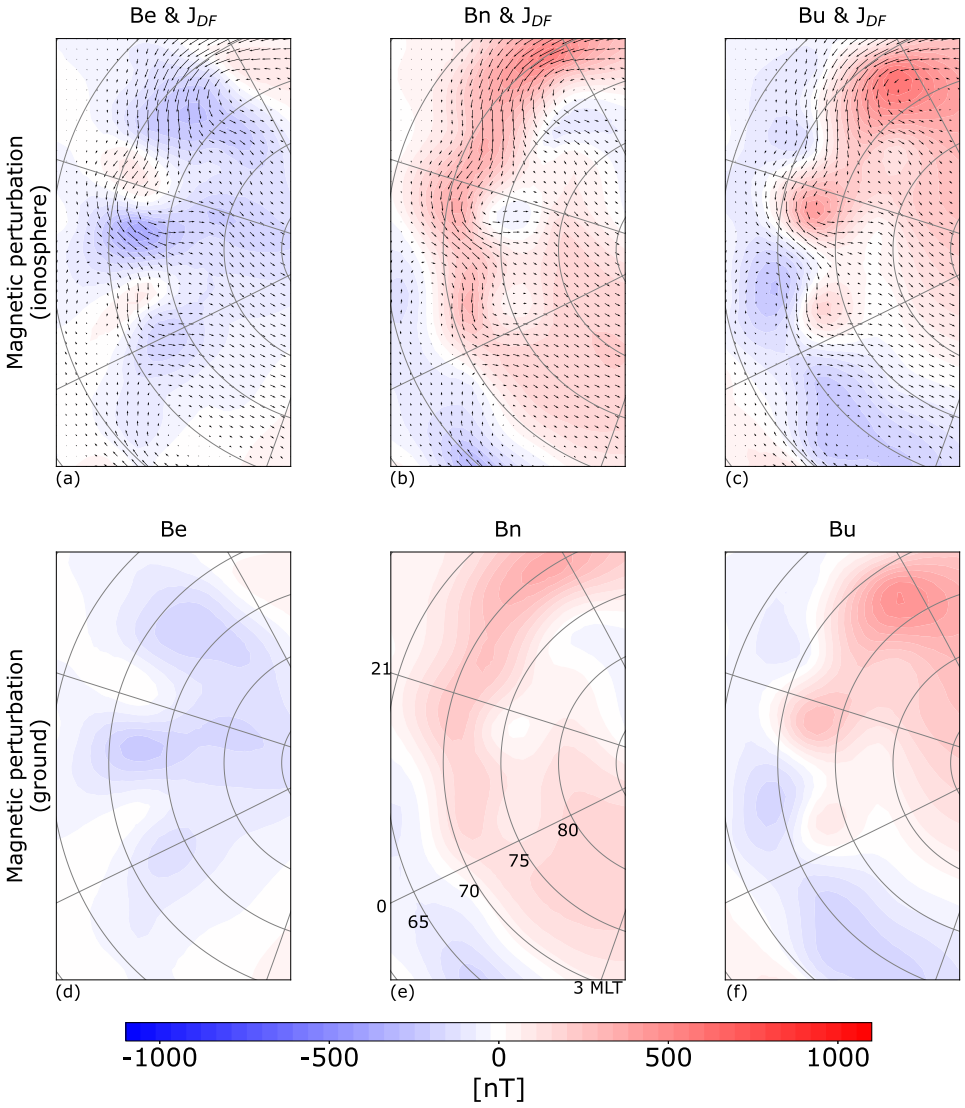

Figure 4.10: The same as Figure 4.8, but for synthetic data configuration illustrated in Figure 4.9a.

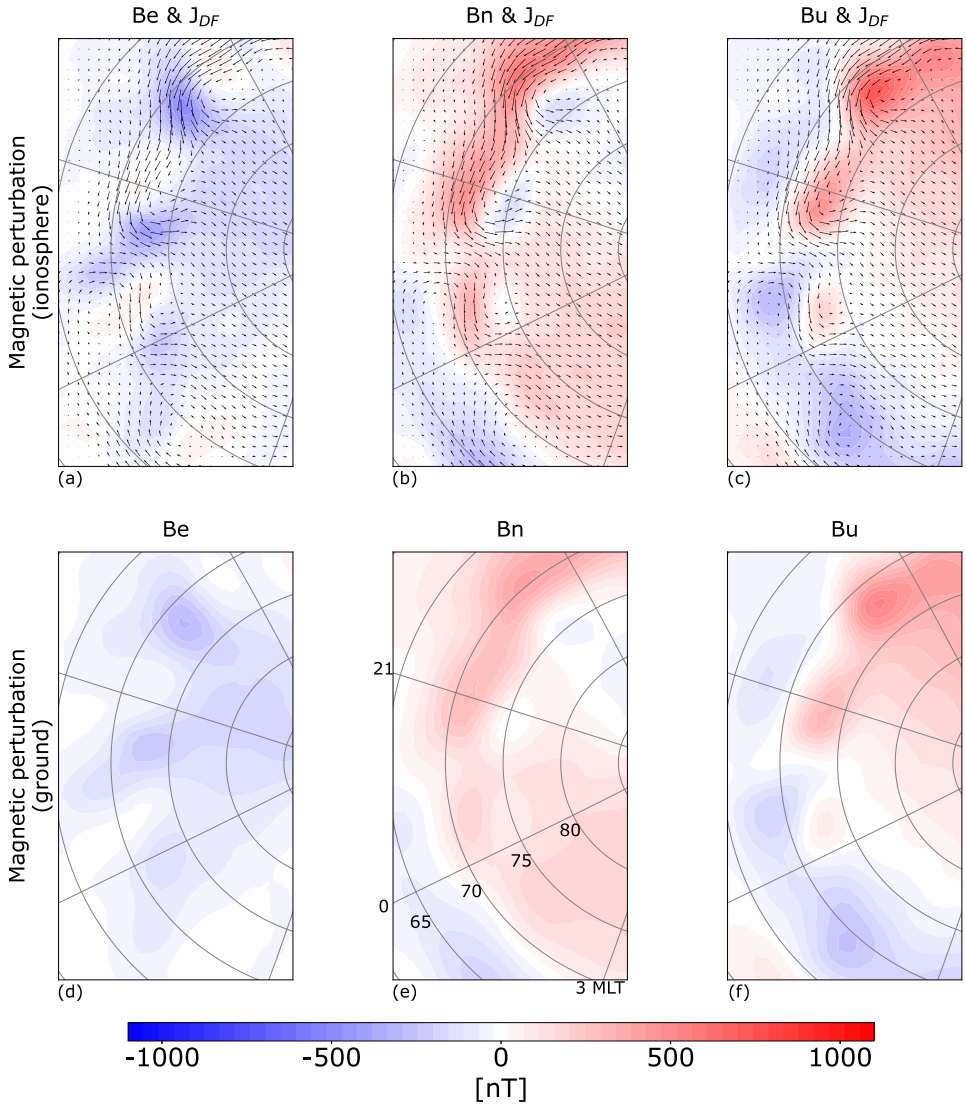

Figure 4.11: The same as Figure 4.8, but for synthetic data configuration illustrated in Figure 4.9c.

4.3 Contamination of the signal

Ground magnetic perturbation is a superposition of multiple sources, as discussed in Section 3.3.3. The largest contributor is typically the 3D ionospheric electric current. The magnetospheric currents produce large-scale perturbation of the magnetic field that mainly maps into the radial component at high latitudes. The strength of the perturbation can be well estimated based on magnetic field perturbation at low to mid-latitudes, e.g. Dst and SYM-H (Section 3.5). GICs can produce highly structured magnetic field perturbation, especially if the currents are induced close to the Earth's surface. Grayver et al. [2021] showed that the radial magnetic field component is significantly more affected by GICs than the horizontal component. They suggest only using the horizontal component unless GICs are accounted for in the applied modeling technique. In this simple way, ignoring the radial component, it is possible to minimize contamination from magnetospheric currents and GICs.

There are several publications presenting techniques that account for GICs. Juusola et al. [2020]; Walker et al. [2023] place a mirror current in the Earth's subsurface while using the SECS technique. The strength of the mirror current is defined by the depth at which the radial magnetic field perturbation from the two sources cancels. Pulkkinen et al. [2003] placed an additional DF SECS system in the Earth's subsurface. This is conceptually similar to the mirror current approach. However, the mirror current is directly linked to that of the ionosphere. Removing the linear relationship allows the two SECSs to change independently. The subsurface SECS is placed close to the surface, relative to the distance between the surface and the ionosphere. Conceptually, this seems like a good idea. However, in practice we solve regularized inverse problems, thus constraining some aspect of the model, typically the magnitude of the model norm. In this case, the most cost effective (see Equation 4.16) way to reconstruct small-scale structures is by using the subsurface SECS, while the ionospheric SECS more efficiently reconstructs large-scale structures. The choice of regularization parameter will, therefore, decide how much of the signal is assigned to the subsurface SECS and labeled GICs. The ambiguity of this approach makes it undesirable, in my opinion.

Grayver et al. [2021] presents a more advanced approach for accounting for GICs. They use a model of the 3D conductivity structure in the Earth's subsurface to create an impulse response function to temporal changes in the magnetic field. By their implementation in the SH technique, the GICs are co-estimated. Calculating the impulse response functions is computationally demanding, but need only be done once if the geometry of the inverse problem does not change. Interestingly, this makes the solution dependent on the history of the magnetic field. This technique was applied in the

development of the CHAOS-7 core field model [Finlay et al., 2020] to account for induced currents caused by temporal changes in the magnetic field. In Section 3.3.4 we will take a deeper look at the effects of a time-dependent magnetic field on the ionospheric current system. The technique presented by Grayver et al. [2021] seems to be very promising and breaks with the assumption of no GICs or a simplistic representation thereof. This technique has yet to be implemented for SECS and, therefore, no reference to its performance in regional data assimilation can be given.

Interpreting the equivalent ionospheric current as the DF part of the horizontal ionospheric current relies on the assumption of radial magnetic field lines. Magnetic perturbation from oblique FAC does not cancel completely with the CF ionospheric current below the ionosphere. Untiedt and Baumjohann [1993] discuss the interpretation of equivalent currents and the impact of non-radial magnetic field lines. They conclude that their contribution is insignificant, based on an example of a tilted magnetic field line (77°, where 90° is radial). However, when the quality of available data, computational resources, and modeling techniques improve, the impact of what previously was considered insignificant can change. Interpreting the equivalent current as the DF part of the horizontal ionospheric current might, therefore, be increasingly wrong when our ability to empirically model smaller and smaller spatial scales increases. Take for example the EZIE satellite mission that will produce measurements of the magnetic field at approximately 85 km altitude. Not only will the measurement geometry allow for a high spatial resolution, but the distance to the ionosphere will make smaller structures in the magnetic perturbation field stronger. In this way, the influence of tilted field lines might increase.

4.4 Modeling a time-dependent system

The SH and SECS techniques (see Sections 4.1.1-4.1.2), to the extent presented here, focus on modeling the ionospheric equivalent current system. Under ideal conditions, the retrieved equivalent current is the DF ionospheric horizontal current. That is, the combined DF current associated with both the ionosphere potential electric field ($\boldsymbol{E}_{pot}$), and the ionospheric induction electric field ($\boldsymbol{E}_{ind}$).

More holistic frameworks exist that link various types of measurements—like magnetic fields both above and below the ionosphere, conductance, and convection—to $\boldsymbol{E}_{pot}$ using ionospheric Ohm's law (Equation 3.2). Recall, Equation 3.2 only involves the assumption of quasi steady-state. However, in these techniques the system is assumed to be fully in steady-state, thus neglecting $\boldsymbol{E}_{ind}$. This approach is applied in the Assimilative

Mapping of Ionospheric Electrodynamics (AMIE) technique using spherical cap harmonics [Richmond and Kamide, 1988] and Local Mapping of Polar Ionospheric Electrodynamics (Lompe) using SECS [Hovland et al., 2022; Laundal et al., 2022]. Estimating $\boldsymbol{E}_{pot}$ allows for the decomposition of the associated electric current into its CF/DF and Hall/Pedersen components. Recall, that we used Lompe to create Figures 3.6-3.7 where the steady-state horizontal current was decomposed.

Despite advances in empirical modeling of ionospheric electrodynamics, the assumption of steady-state remains a limitation, especially when considering the dynamic nature of the ionospheric current system, see Section 3.3.4. Our desire to understand the complexities of the system, Paper I-II, and our future ability to resolve mesoscale structures, Paper III, necessitates the development of techniques that can capture the complexities of $\boldsymbol{E}_{ind}$. Paper IV presents a novel approach for estimating $\boldsymbol{E}_{ind}$ utilizing ground-based magnetic field measurements. This technique might bridge the gap between existing empirical modeling techniques and the time-dependent behavior of the ionospheric current system.

Technically, the assumption of steady-state is not required when utilizing the SH and SECS techniques. The SH technique is based on an expression of the magnetic scalar potential in the non-conductive region between the Earth's surface and the ionosphere. The SECS technique provides a linear relationship between an equivalent DF current and observed ground magnetic perturbation. The steady-state assumption is first applied when assuming $\boldsymbol{E}$ to be a potential electric field as done in AMIE and Lompe. Here, the assumption is necessary to combine measurements of various quantities. Whether or not SHs and SECSs are explicitly used to model $\boldsymbol{E}_{pot}$ they are frequently used to examine the temporal evolution of the ionospheric current system by modeling multiple consecutive time-steps independently. The subsequent empirical models are often interpreted in terms of steady-state making the assumption implicit, if not explicitly made prior to the analysis. Furthermore, the independent treatment of each time step can result in significant jumps/jitter in the perceived temporal evolution when comparing different time steps. By acknowledging the time-dependent nature of the ionospheric system we can utilize the difference between consecutive measurements to constrain the system's temporal evolution. Obtaining this information does not require extra work, it simply hides in plain sight waiting for its utilization.

Previous methodologies, such as those presented by [e.g. Takeda, 2008; Vanhamäki et al., 2005, 2006, 2007] have highlighted the local significance of $\boldsymbol{E}_{ind}$ and its potential to reach substantial fractions of the total electric field during dynamic events. The introduction of the new technique for modeling the ionospheric induction electric field could mark a significant step forward in ionospheric electrodynamics research. By acknowledging

the inductive components of the ionospheric electric field, future studies can develop a more complete understanding of the ionosphere's response to external drivers. This advancement opens the door to integrating the technique with existing empirical modeling techniques, such as AMIE and Lompe. The ability to co-estimate $\boldsymbol{E}_{pot}$ and $\boldsymbol{E}_{ind}$ will enhance our capability to predict and analyze the ionospheric behavior during both calm and dynamic conditions.

Chapter 5

Introduction to Papers

This chapter contains a summary of the four papers included in this thesis.

Paper I: Geomagnetic response to rapid increases in solar wind dynamic pressure: Event detection and large scale response

In this paper, we introduce a method that employs a random forest machine learning algorithm to detect discontinuities in the solar wind. We analyze in situ solar wind data from 1994 to 2019, identifying 3867 events characterized by rapid solar wind dynamic pressure increases. We observe these events to induce a positive perturbation in the horizontal geomagnetic field at low/mid latitudes, related to magnetospheric compression.

We conduct a superposed epoch analysis on the ground magnetic fields at low/mid-latitudes including the SMR index and utilize the PCN index to evaluate the high-latitude geomagnetic response. We find a dawn-dusk asymmetry at low/mid-latitudes and a notable dependence on the IMF orientation. Specifically, we discover that the dawn sector shows weaker magnetic perturbation, suggesting a difference in the ring current influence between dawn and dusk. During northward IMF conditions, an initial asymmetric geomagnetic response emerges, which then disappears after about 30 minutes. A similar asymmetry is found during southward IMF conditions. However, it quickly flips, making dawn experience the strongest perturbation, hinting at an amplification of the partial ring current.

Our analysis also reveals a noon-midnight asymmetry during southward IMF, with the

night side experiencing the strongest perturbation. This finding implies a significant effect from the geomagnetic field's dipolarization in the near tail. Our study outlines the geomagnetic response's complexity and the critical role of event lists for comprehensive statistical analyses.

Paper II: Transient high latitude geomagnetic response to rapid increases in solar wind dynamic pressure

In this paper, we present an extensive analysis of the transient geomagnetic response at high latitudes in the northern hemisphere to rapid solar wind dynamic pressure increases. We carry out a superposed epoch analysis based on 2058 events from the list presented in Paper I, sorting them by IMF clock angle and dipole tilt. Our SH model of the geomagnetic perturbation field reveals transient current vortices, most evident during northward IMF conditions, and specifically during equinox and winter.

We differentiate between the PI and MI of the geomagnetic response. The PI precedes the low/mid-latitude response by 1–2 minutes with a rise time of 4–6 minutes, while the MI commences about 2 minutes after the low/mid-latitude response and has a longer rise time of 6–11 minutes. We detail the current vortices' movement, noting the dawnside vortex moves westward at approximately 5 km/s, and the duskside vortex remains relatively static. The asymmetric movement of the vortices contradicts current physical models of SCs.

We recreate the SMR index and find a significant MLT dependence in the contributing magnetic field measurements above 40° and below 10° magnetic latitude. The effect above 40° is attributable to high-latitude ionospheric electric currents. We suggest that below 10° magnetic latitude, the variations could be due to the distribution of event occurrence probability and the South Atlantic Magnetic Anomaly's effect on the equatorial electrojet.

Our findings provide new insights into the high-latitude geomagnetic response to solar wind pressure changes and the characteristics of the involved ionospheric currents.

Paper III: Spatial Resolution in Inverse Problems: The EZIE satellite mission

In this paper, we develop a method for assessing spatial resolution in ionospheric electrodynamics modeling using magnetic field measurements, with a focus on data from the upcoming EZIE cubesat mission.

We estimate the spatial resolution of the ionospheric current model parameters to be approximately 200-400 km in the cross-track direction and 100-300 km in the along-track direction. These estimates lie within the 100-500 km range required to answer the EZIE science questions. We demonstrate that incorporating just one ground magnetometer measurement can improve the spatial resolution locally by up to 200 km, specifically for the EZIE measurement configuration. We also introduce a technique that simplifies the regularization process of the inverse problem by merging two regularization parameters into one, thus enabling the straightforward application of the L-curve method to identify optimal regularization values.

Our findings stress the significance of comprehending the limitations and capabilities of inverse models to prevent false interpretations. The proposed method holds potential for wide application in ionospheric science, especially with the enhanced measurement capabilities anticipated from the EZIE mission.

Paper IV: Estimating the Induction Electric Field in the Ionosphere Using Ground Magnetometer Data

In this paper, we address the often-neglected component of ionospheric electric field models—the induction electric field. We introduce a new technique for estimating this component from ground magnetometer data.

We demonstrate the technique on synthetic and real data from SCs, illustrating how the induction electric field can make up a significant part of the total electric field during dynamic ionospheric events. We find that including the induction electric field in Joule heating calculations can lead to local changes of tens of percent, despite a modest global increase. The energy dissipation due to the induction electric field during dynamic events is currently not accounted for in existing models, emphasizing its critical role in furthering empirical modeling capabilities in our community.

We emphasize the potential for integrating this method with empirical modeling techniques such as AMIE and Lompe, potentially enabling the co-estimation of the potential and induction electric fields in future studies for a more complete depiction of ionospheric dynamics.

Bibliography

P. Alken, E. Thébault, C. D. Beggan, H. Amit, J. Aubert, J. Baerenzung, T. N. Bondar, W. J. Brown, S. Califf, A. Chambodut, A. Chulliat, G. A. Cox, C. C. Finlay, A. Fournier, N. Gillet, A. Grayver, M. D. Hammer, M. Holschneider, L. Huder, G. Hulot, T. Jager, C. Kloss, M. Korte, W. Kuang, A. Kuvshinov, B. Langlais, J.-M. Léger, V. Lesur, P. W. Livermore, F. J. Lowes, S. Macmillan, W. Magnes, M. Mandea, S. Marsal, J. Matzka, M. C. Metman, T. Minami, A. Morschhauser, J. E. Mound, M. Nair, S. Nakano, N. Olsen, F. J. Pavón-Carrasco, V. G. Petrov, G. Ropp, M. Rother, T. J. Sabaka, S. Sanchez, D. Saturnino, N. R. Schnepf, X. Shen, C. Stolle, A. Tangborn, L. Tøffner-Clausen, H. Toh, J. M. Torta, J. Varner, F. Vervelidou, P. Vigneron, I. Wardinski, J. Wicht, A. Woods, Y. Yang, Z. Zeren, and B. Zhou. International geomagnetic reference field: the thirteenth generation. *Earth, Planets and Space*, 73(1):49, Feb 2021. ISSN 1880-5981. doi: 10.1186/s40623-020-01288-x. URL https://doi.org/10.1186/s40623-020-01288-x.

O. Amm. Direct determination of the local ionospheric hall conductance distribution from two-dimensional electric and magnetic field data: Application of the method using models of typical ionospheric electrodynamic situations. *Journal of Geophysical Research: Space Physics*, 100(A11):21473–21488, 1995. doi: https://doi.org/10.1029/95JA02213. URL https://agupubs.onlinelibrary.wiley.com/doi/abs/10.1029/95JA02213.

O. Amm. Ionospheric elementary current systems in spherical coordinates and their application. *Journal of geomagnetism and geoelectricity*, 49(7):947–955, 1997. doi: 10.5636/jgg.49.947.

O. Amm, H. Opgenoorth, and A. Viljanen. Ground-based magnetometer arrays in space research: A brief review. In *EGU General Assembly Conference Abstracts*, EGU General Assembly Conference Abstracts, page 4889, May 2010.

T. Araki. *A Physical Model of the Geomagnetic Sudden Commencement*, pages 183–200. American Geophysical Union (AGU), 1994. ISBN 9781118663943. doi: https://doi.org/10.1029/GM081p0183.

R. C. Aster, B. Borchers, and C. H. Thurber. *Parameter Estimation and Inverse Problems*. Academic Press, Boston, second edition edition, 2013. ISBN 978-0-12-385048-5. doi: https://doi.org/10.1016/B978-0-12-385048-5.00001-X. URL https://www.sciencedirect.com/science/article/pii/B978012385048500001X.

D. N. Baker, E. Daly, I. Daglis, J. G. Kappenman, and M. Panasyuk. Effects of space weather on technology infrastructure. *Space Weather*, 2(2), 2004. doi: https://doi.org/10.1029/2003SW000044. URL https://agupubs.onlinelibrary.wiley.com/doi/abs/10.1029/2003SW000044.

F. Bauer and M. A. Lukas. Comparing parameter choice methods for regularization of ill-posed problems. *Mathematics and Computers in Simulation*, 81(9):1795–1841, 2011. ISSN 0378-4754. doi: https://doi.org/10.1016/j.matcom.2011.01.016. URL https://www.sciencedirect.com/science/article/pii/S0378475411000607.

W. Baumjohann and R. A. Treumann. *Basic Space Plasma Physics*. IMPERIAL COLLEGE PRESS, revised edition, 2012. doi: 10.1142/p850. URL https://www.worldscientific.com/doi/abs/10.1142/p850.

M. Belge, M. E. Kilmer, and E. L. Miller. Efficient determination of multiple regularization parameters in a generalized l-curve framework. *Inverse Problems*, 18(4):1161, jul 2002. doi: 10.1088/0266-5611/18/4/314. URL https://dx.doi.org/10.1088/0266-5611/18/4/314.

C. Bertucci, F. Duru, N. Edberg, M. Fraenz, C. Martinecz, K. Szego, and O. Vaisberg. The induced magnetospheres of mars, venus, and titan. *Space Science Reviews*, 162(1):113–171, Dec 2011. ISSN 1572-9672. doi: 10.1007/s11214-011-9845-1. URL https://doi.org/10.1007/s11214-011-9845-1.

D. H. Boteler. Geomagnetically induced currents: present knowledge and future research. *IEEE Transactions on Power Delivery*, 9(1):50–58, 1994. doi: 10.1109/61.277679.

A. Brekke. *Physics of the Upper Polar Atmosphere*. Springer Berlin, 2015. ISBN 978-3-642-43890-5. doi: https://doi.org/10.1007/978-3-642-27401-5.

S. Brooks, A. Gelman, G. Jones, and X. L. Meng. *Handbook of Markov Chain Monte Carlo*. CRC press, 2011.

J. Burt and B. Smith. Deep space climate observatory: The dscovr mission. In *2012 IEEE Aerospace Conference*, pages 1–13, 2012. doi: 10.1109/AERO.2012.6187025.

E. Camporeale, A. Carè, and J. E. Borovsky. Classification of solar wind with machine learning. *Journal of Geophysical Research: Space Physics*, 122(11):10,910–

10,920, 2017. doi: https://doi.org/10.1002/2017JA024383. URL https://agupubs.onlinelibrary.wiley.com/doi/abs/10.1002/2017JA024383.

S. Chapman and J. Bartels. *Geomagnetism*, volume 2, chapter 17. Oxford University Press, 1940. doi: 10.2307/3606494.

S. Chapman and V. C. A. Ferraro. A new theory of magnetic storms. *Nature*, 126 (3169):129–130, Jul 1930. ISSN 1476-4687. doi: 10.1038/126129a0. URL https://doi.org/10.1038/126129a0.

S. W. H. Cowley and M. Lockwood. Excitation and decay of solar wind-driven flows in the magnetosphere-ionosphere system. *Annales Geophysicae*, 10(1-2), 1992.

J. Curto, T. Araki, and L. Alberca. Evolution of the concept of sudden storm commencements and their operative identification. *Earth, Planets, and Space*, 59, 11 2007. doi: 10.1186/BF03352059.

P. A. Dalin, G. N. Zastenker, K. I. Paularena, and J. D. Richardson. A survey of large, rapid solar wind dynamic pressure changes observed by interball-1 and imp 8. *Annales Geophysicae*, 20(3):293–299, 2002. doi: 10.5194/angeo-20-293-2002. URL https://angeo.copernicus.org/articles/20/293/2002/.

M. Decotte, K. M. Laundal, S. M. Hatch, and J. P. Reistad. Auroral oval morphology: Dawn-dusk asymmetry partially induced by earth's rotation. *Journal of Geophysical Research: Space Physics*, 128(6):e2023JA031345, 2023. doi: https://doi.org/10.1029/2023JA031345. URL https://agupubs.onlinelibrary.wiley.com/doi/abs/10.1029/2023JA031345. e2023JA031345 2023JA031345.

A. J. Dessler and E. N. Parker. Hydromagnetic theory of geomagnetic storms. *Journal of Geophysical Research (1896-1977)*, 64(12):2239–2252, 1959. doi: https://doi.org/10.1029/JZ064i012p02239. URL https://agupubs.onlinelibrary.wiley.com/doi/abs/10.1029/JZ064i012p02239.

A. P. Dimmock, L. Rosenqvist, J.-O. Hall, A. Viljanen, E. Yordanova, I. Honkonen, M. André, and E. C. Sjöberg. The gic and geomagnetic response over fennoscandia to the 7–8 september 2017 geomagnetic storm. *Space Weather*, 17(7):989–1010, 2019. doi: https://doi.org/10.1029/2018SW002132. URL https://agupubs.onlinelibrary.wiley.com/doi/abs/10.1029/2018SW002132.

V. Domingo, B. Fleck, and A. I. Poland. Soho: The solar and heliospheric observatory. *Space Science Reviews*, 72(1):81–84, Apr 1995. ISSN 1572-9672. doi: 10.1007/BF00768758. URL https://doi.org/10.1007/BF00768758.

J. Dreher. On the self-consistent description of dynamic magnetosphere-ionosphere coupling phenomena with resolved ionosphere. *Journal of Geophysical Research: Space Physics*, 102(A1):85–94, 1997. doi: https://doi.org/10.1029/96JA02800. URL https://agupubs.onlinelibrary.wiley.com/doi/abs/10.1029/96JA02800.

J. W. Dungey. Interplanetary magnetic field and the auroral zones. *Phys. Rev. Lett.*, 6: 47–48, Jan 1961. doi: 10.1103/PhysRevLett.6.47. URL https://link.aps.org/doi/10.1103/PhysRevLett.6.47.

R. Elhawary, K. M. Laundal, J. P. Reistad, M. Madelaire, and A. Ohma. Substorm impact on dayside ionospheric currents. *Geophysical Research Letters*, 50 (14):e2023GL104800, 2023. doi: https://doi.org/10.1029/2023GL104800. URL https://agupubs.onlinelibrary.wiley.com/doi/abs/10.1029/2023GL104800. e2023GL104800 2023GL104800.

P. Ellis and D. Southwood. Reflection of alfvén waves by non-uniform ionospheres. *Planetary and Space Science*, 31(1):107–117, 1983. ISSN 0032-0633. doi: https://doi.org/10.1016/0032-0633(83)90035-1. URL https://www.sciencedirect.com/science/article/pii/0032063383900351.

M. Faraday. V. experimental researches in electricity. *Philosophical Transactions of the Royal Society of London*, 122:125–162, 1832. doi: 10.1098/rstl.1832.0006. URL https://royalsocietypublishing.org/doi/abs/10.1098/rstl.1832.0006.

C. C. Finlay, C. Kloss, N. Olsen, M. D. Hammer, L. Tøffner-Clausen, A. Grayver, and A. Kuvshinov. The chaos-7 geomagnetic field model and observed changes in the south atlantic anomaly. *Earth, Planets and Space*, 72(1):156, Oct 2020. ISSN 1880-5981. doi: 10.1186/s40623-020-01252-9. URL https://doi.org/10.1186/s40623-020-01252-9.

E. Friis-Christensen and J. Wilhjelm. Polar cap currents for different directions of the interplanetary magnetic field in the y-z plane. *Journal of Geophysical Research (1896-1977)*, 80(10):1248–1260, 1975. doi: https://doi.org/10.1029/JA080i010p01248. URL https://agupubs.onlinelibrary.wiley.com/doi/abs/10.1029/JA080i010p01248.

E. Friis-Christensen, M. A. McHenry, C. R. Clauer, and S. Vennerstrøm. Ionospheric traveling convection vortices observed near the polar cleft: A triggered response to sudden changes in the solar wind. *Geophysical Research Letters*, 15(3):253–256, 1988. doi: https://doi.org/10.1029/GL015i003p00253.

S. Fujita, T. Tanaka, T. Kikuchi, K. Fujimoto, K. Hosokawa, and M. Itonaga. A numerical simulation of the geomagnetic sudden commencement: 1. generation of the field-

aligned current associated with the preliminary impulse. *Journal of Geophysical Research: Space Physics*, 108(A12), 2003a. doi: https://doi.org/10.1029/2002JA009407.

S. Fujita, T. Tanaka, T. Kikuchi, K. Fujimoto, and M. Itonaga. A numerical simulation of the geomagnetic sudden commencement: 2. plasma processes in the main impulse. *Journal of Geophysical Research: Space Physics*, 108(A12), 2003b. doi: https://doi.org/10.1029/2002JA009763.

N. Fukushima. Equivalence in ground geomagnetic effect of chapman-vestine's and birkeland-alfven's electric current systems for polar magnetic storms. *Rep. Ionosphere Space Res. Jap. 23: 219-27(1969).*, 1 1969. URL https://www.osti.gov/biblio/4755464.

N. Fukushima. Generalized theorem for no ground magnetic effect of vertical currents connected with Pedersen currents in the uniform-conductivity ionosphere. *Report of Ionosphere and Space Research in Japan*, 30(1-2):35–40, June 1976.

C. F. Gauss. *Allgemeine Theorie des Erdmagnetismus*, pages 119–193. Springer Berlin Heidelberg, Berlin, Heidelberg, 1877. ISBN 978-3-642-49319-5. doi: 10.1007/978-3-642-49319-5_5. URL https://doi.org/10.1007/978-3-642-49319-5_5.

A. Gelman, J. B. Carlin, H. S. Stern, and D. B. Rubin. *Bayesian Data Analysis*. Chapman and Hall/CRC, 2nd ed. edition, 2004.

J. W. Gjerloev. The supermag data processing technique. *Journal of Geophysical Research: Space Physics*, 117(A9), 2012. doi: 10.1029/2012JA017683.

J. W. Gjerloev, S. Ohtani, T. Iijima, B. Anderson, J. Slavin, and G. Le. Characteristics of the terrestrial field-aligned current system. *Annales Geophysicae*, 29(10):1713–1729, 2011. doi: 10.5194/angeo-29-1713-2011. URL https://angeo.copernicus.org/articles/29/1713/2011/.

K. H. Glassmeier and C. Heppner. Traveling magnetospheric convection twin vortices: Another case study, global characteristics, and a model. *Journal of Geophysical Research: Space Physics*, 97(A4):3977–3992, 1992. doi: https://doi.org/10.1029/91JA02464.

K. H. Glassmeier, M. Hönisch, and J. Untiedt. Ground-based and satellite observations of traveling magnetospheric convection twin vortices. *Journal of Geophysical Research: Space Physics*, 94(A3):2520–2528, 1989. doi: https://doi.org/10.1029/JA094iA03p02520. URL https://agupubs.onlinelibrary.wiley.com/doi/abs/10.1029/JA094iA03p02520.

T. I. Gombosi. *Physics of the Space Environment*. Cambridge Atmospheric and Space Science Series. Cambridge University Press, 1998. doi: 10.1017/CBO9780511529474.

A. V. Grayver, A. Kuvshinov, and D. Werthmüller. Time-domain modeling of three-dimensional earth's and planetary electromagnetic induction effect in ground and satellite observations. *Journal of Geophysical Research: Space Physics*, 126(3):e2020JA028672, 2021. doi: https://doi.org/10.1029/2020JA028672. URL https://agupubs.onlinelibrary.wiley.com/doi/abs/10.1029/2020JA028672. e2020JA028672 2020JA028672.

S. Haaland and J. Gjerloev. On the relation between asymmetries in the ring current and magnetopause current. *Journal of Geophysical Research: Space Physics*, 118 (12):7593–7604, 2013. doi: https://doi.org/10.1002/2013JA019345. URL https://agupubs.onlinelibrary.wiley.com/doi/abs/10.1002/2013JA019345.

S. E. Haaland, G. Paschmann, M. Förster, J. M. Quinn, R. B. Torbert, C. E. McIlwain, H. Vaith, P. A. Puhl-Quinn, and C. A. Kletzing. High-latitude plasma convection from cluster edi measurements: method and imf-dependence. *Annales Geophysicae*, 25(1): 239–253, 2007. doi: 10.5194/angeo-25-239-2007. URL https://angeo.copernicus.org/articles/25/239/2007/.

G. V. Haines. Spherical cap harmonic analysis. *Journal of Geophysical Research: Solid Earth*, 90(B3):2583–2591, 1985. doi: https://doi.org/10.1029/JB090iB03p02583. URL https://agupubs.onlinelibrary.wiley.com/doi/abs/10.1029/JB090iB03p02583.

P. C. Hansen. Analysis of discrete ill-posed problems by means of the l-curve. *SIAM Review*, 34(4):561–580, 1992. doi: 10.1137/1034115. URL https://doi.org/10.1137/1034115.

Y. N. Harari. *Sapiens: A Brief History of Humankind*. HarperCollins, 2015. ISBN 9780062316103. URL https://books.google.no/books?id=FmyBAwAAQBAJ.

J. P. Heppner and N. C. Maynard. Empirical high-latitude electric field models. *Journal of Geophysical Research: Space Physics*, 92(A5):4467–4489, 1987. doi: https://doi.org/10.1029/JA092iA05p04467. URL https://agupubs.onlinelibrary.wiley.com/doi/abs/10.1029/JA092iA05p04467.

M. Hesse and P. A. Cassak. Magnetic reconnection in the space sciences: Past, present, and future. *Journal of Geophysical Research: Space Physics*, 125 (2):e2018JA025935, 2020. doi: https://doi.org/10.1029/2018JA025935. URL https://agupubs.onlinelibrary.wiley.com/doi/abs/10.1029/2018JA025935. e2018JA025935 2018JA025935.

M. Hesse, J. Birn, and R. A. Hoffman. On the mapping of ionospheric convection into the magnetosphere. *Journal of Geophysical Research: Space Physics*, 102(A5): 9543–9551, 1997. doi: https://doi.org/10.1029/96JA03999. URL https://agupubs.onlinelibrary.wiley.com/doi/abs/10.1029/96JA03999.

A. Ø. Hovland, K. M. Laundal, J. P. Reistad, S. M. Hatch, S. J. Walker, M. Madelaire, and A. Ohma. The lompe code: A python toolbox for ionospheric data analysis. *Frontiers in Astronomy and Space Sciences*, 9, 2022. ISSN 2296-987X. doi: 10.3389/fspas.2022.1025823. URL https://www.frontiersin.org/articles/10.3389/fspas.2022.1025823.

W. Hughes. *The Magnetopause, Magnetotail, and Magnetic Reconnection*. Cambridge University Press, Cambridge, 1995. doi: 10.1017/9781139878296.010.

T. Iyemori, M. Takeda, M. Nose, and H. Toh. Mid-latitude geomagnetic indices asy and sym for 2009 (provisional). *Internal Report of Data Analysis Center for Geomagnetism and Space Magnetism, Kyoto University, Japan*, 2010.

L. Juusola, H. Vanhamäki, A. Viljanen, and M. Smirnov. Induced currents due to 3d ground conductivity play a major role in the interpretation of geomagnetic variations. *Annales Geophysicae*, 38(5):983–998, 2020. doi: 10.5194/angeo-38-983-2020. URL https://angeo.copernicus.org/articles/38/983/2020/.

K. A. Keller, M. Hesse, M. Kuznetsova, L. Rastätter, T. Moretto, T. I. Gombosi, and D. L. DeZeeuw. Global mhd modeling of the impact of a solar wind pressure change. *Journal of Geophysical Research: Space Physics*, 107(A7):SMP 21–1–SMP 21–8, 2002. doi: https://doi.org/10.1029/2001JA000060.

M. C. Kelley. *The Earth's Ionosphere (second edition)*. Academic Press, 2009. ISBN 978-0-12-404013-7. doi: https://doi.org/10.1016/B978-0-12-404013-7.50007-1. URL https://www.sciencedirect.com/science/article/pii/B9780124040137500071.

J. W. Kern. Analysis of polar magnetic storms. *Journal of geomagnetism and geoelectricity*, 18(2):125–131, 1966. doi: 10.5636/jgg.18.125.

O. Khabarova and G. Zastenker. Sharp changes of solar wind ion flux and density within and outside current sheets. *Solar Physics*, 270(1):311–329, May 2011. ISSN 1573-093X. doi: 10.1007/s11207-011-9719-4. URL https://doi.org/10.1007/s11207-011-9719-4.

O. Khabarova, O. Malandraki, H. Malova, R. Kislov, A. Greco, R. Bruno, O. Pezzi, S. Servidio, G. Li, W. Matthaeus, J. Le Roux, N. E. Engelbrecht, F. Pecora, L. Zelenyi, V. Obridko, and V. Kuznetsov. Current sheets, plasmoids and flux ropes in the

heliosphere. *Space Science Reviews*, 217(3), Mar 2021. ISSN 1572-9672. doi: 10.1007/s11214-021-00814-x. URL https://doi.org/10.1007/s11214-021-00814-x.

M. G. Kivelson and D. J. Southwood. Ionospheric traveling vortex generation by solar wind buffeting of the magnetosphere. *Journal of Geophysical Research: Space Physics*, 96(A2):1661–1667, 1991. doi: https://doi.org/10.1029/90JA01805.

M. J. Kosch, O. Amm, and M. W. J. Scourfield. A plasma vortex revisited: The importance of including ionospheric conductivity measurements. *Journal of Geophysical Research: Space Physics*, 105(A11):24889–24898, 2000. doi: https://doi.org/10.1029/2000JA900102. URL https://agupubs.onlinelibrary.wiley.com/doi/abs/10.1029/2000JA900102.

K. R. Lang. *The Sun from Space*. Astronomy and Astrophysics Library. Springer Berlin, 2009. ISBN 978-3-540-76952-1. doi: 10.1007/978-3-540-76953-8.

K. M. Laundal, J. W. Gjerloev, N. Østgaard, J. P. Reistad, S. Haaland, K. Snekvik, P. Tenfjord, S. Ohtani, and S. E. Milan. The impact of sunlight on high-latitude equivalent currents. *Journal of Geophysical Research: Space Physics*, 121(3):2715–2726, 2016. doi: https://doi.org/10.1002/2015JA022236. URL https://agupubs.onlinelibrary.wiley.com/doi/abs/10.1002/2015JA022236.

K. M. Laundal, J. H. Yee, V. G. Merkin, J. W. Gjerloev, H. Vanhamäki, J. P. Reistad, M. Madelaire, K. Sorathia, and P. J. Espy. Electrojet estimates from mesospheric magnetic field measurements. *Journal of Geophysical Research: Space Physics*, 126(5):e2020JA028644, 2021. doi: https://doi.org/10.1029/2020JA028644. URL https://agupubs.onlinelibrary.wiley.com/doi/abs/10.1029/2020JA028644. e2020JA028644 2020JA028644.

K. M. Laundal, J. P. Reistad, S. M. Hatch, M. Madelaire, S. Walker, A. Hovland, A. Ohma, V. Merkin, and K. Sorathia. Local mapping of polar ionospheric electrodynamics. *Journal of Geophysical Research: Space Physics*, 127, 05 2022. doi: 10.1029/2022JA030356.

W. Lowrie. *Geomagnetism and paleomagnetism*, page 281–362. Cambridge University Press, 2 edition, 2007. doi: 10.1017/CBO9780511807107.006.

H. Lühr, C. Xiong, N. Olsen, and G. Le. Near-earth magnetic field effects of large-scale magnetospheric currents. *Space Science Reviews*, 206(1):521–545, Mar 2017. ISSN 1572-9672. doi: 10.1007/s11214-016-0267-y. URL https://doi.org/10.1007/s11214-016-0267-y.

D. Lummerzheim, M. H. Rees, J. D. Craven, and L. A. Frank. Ionospheric conductances derived from de-1 auroral images. *Journal of Atmospheric and Terrestrial Physics*, 53(3):281–292, 1991. ISSN 0021-9169. doi: https://doi.org/10.1016/0021-9169(91)90112-K. URL https://www.sciencedirect.com/science/article/pii/002191699190112K. Ionospheric Signatures of Magnetospheric Phenomena.

K. A. Lynch, E. McManus, J. Gutow, M. Burleigh, and M. Zettergren. An ionospheric conductance gradient driver for subauroral picket fence visible signatures near steve events. *Journal of Geophysical Research: Space Physics*, 127 (12):e2022JA030863, 2022. doi: https://doi.org/10.1029/2022JA030863. URL https://agupubs.onlinelibrary.wiley.com/doi/abs/10.1029/2022JA030863. e2022JA030863 2022JA030863.

M. Madelaire, K. M. Laundal, J. P. Reistad, S. M. Hatch, and A. Ohma. Transient high latitude geomagnetic response to rapid increases in solar wind dynamic pressure. *Frontiers in Astronomy and Space Sciences*, 9, 2022a. ISSN 2296-987X. doi: 10.3389/fspas.2022.953954. URL https://www.frontiersin.org/articles/10.3389/fspas.2022.953954.

M. Madelaire, K. M. Laundal, J. P. Reistad, S. M. Hatch, A. Ohma, and S. Haaland. Geomagnetic response to rapid increases in solar wind dynamic pressure: Event detection and large scale response. *Frontiers in Astronomy and Space Sciences*, 9, 2022b. ISSN 2296-987X. doi: 10.3389/fspas.2022.904620. URL https://www.frontiersin.org/article/10.3389/fspas.2022.904620.

M. Madelaire, K. Laundal, J. Gjerloev, S. Hatch, J. Reistad, H. Vanhamäki, C. Waters, A. Ohma, R. Mesquita, and V. Merkin. Spatial resolution in inverse problems: The ezie satellite mission. *Journal of Geophysical Research: Space Physics*, 128(5):e2023JA031394, 2023. doi: https://doi.org/10.1029/2023JA031394. URL https://agupubs.onlinelibrary.wiley.com/doi/abs/10.1029/2023JA031394. e2023JA031394 2023JA031394.

B. Mailyan, C. Munteanu, and S. Haaland. What is the best method to calculate the solar wind propagation delay? *Annales Geophysicae*, 26(8):2383–2394, 2008. doi: 10.5194/angeo-26-2383-2008. URL https://angeo.copernicus.org/articles/26/2383/2008/.

D. J. McComas, S. J. Bame, B. L. Barraclough, W. C. Feldman, H. O. Funsten, J. T. Gosling, P. Riley, R. Skoug, A. Balogh, R. Forsyth, B. E. Goldstein, and M. Neugebauer. Ulysses' return to the slow solar wind. *Geophysical Research Letters*, 25(1):1–4, 1998. doi: https://doi.org/10.1029/97GL03444. URL https://agupubs.onlinelibrary.wiley.com/doi/abs/10.1029/97GL03444.

D. J. McComas, B. L. Barraclough, H. O. Funsten, J. T. Gosling, E. Santiago-Muñoz, R. M. Skoug, B. E. Goldstein, M. Neugebauer, P. Riley, and A. Balogh. Solar wind observations over ulysses' first full polar orbit. *Journal of Geophysical Research: Space Physics*, 105(A5):10419–10433, 2000. doi: https://doi.org/10.1029/1999JA000383. URL https://agupubs.onlinelibrary.wiley.com/doi/abs/10.1029/1999JA000383.

A. J. McKay and K. A. Whaler. The electric field in northern England and southern Scotland:implications for geomagnetically induced currents. *Geophysical Journal International*, 167(2):613–625, 11 2006. ISSN 0956-540X. doi: 10.1111/j.1365-246X.2006.03128.x. URL https://doi.org/10.1111/j.1365-246X.2006.03128.x.

V. G. Merkin and J. G. Lyon. Effects of the low-latitude ionospheric boundary condition on the global magnetosphere. *Journal of Geophysical Research: Space Physics*, 115 (A10), 2010. doi: https://doi.org/10.1029/2010JA015461. URL https://agupubs.onlinelibrary.wiley.com/doi/abs/10.1029/2010JA015461.

M. Moldwin. *An Introduction to Space Weather*. Cambridge University Press, 2008. doi: 10.1017/CBO9780511801365.

S. Nakamura, Y. Ebihara, S. Fujita, T. Goto, N. Yamada, S. Watari, and Y. Omura. Time domain simulation of geomagnetically induced current (gic) flowing in 500-kv power grid in japan including a three-dimensional ground inhomogeneity. *Space Weather*, 16(12):1946–1959, 2018. doi: https://doi.org/10.1029/2018SW002004. URL https://agupubs.onlinelibrary.wiley.com/doi/abs/10.1029/2018SW002004.

P. T. Newell and J. W. Gjerloev. Supermag-based partial ring current indices. *Journal of Geophysical Research: Space Physics*, 117(A5), 2012. doi: https://doi.org/10.1029/2012JA017586. URL https://agupubs.onlinelibrary.wiley.com/doi/abs/10.1029/2012JA017586.

S. Olbert, G. L. Siscoe, and V. M. Vasyliunas. A simple derivation of the dessler-parker-sckopke relation. *Journal of Geophysical Research (1896-1977)*, 73(3):1115–1116, 1968. doi: https://doi.org/10.1029/JA073i003p01115. URL https://agupubs.onlinelibrary.wiley.com/doi/abs/10.1029/JA073i003p01115.

D. Oliveira. A study of interplanetary shock geoeffectiveness controlled by impact angles using simulations and observations. *Doctoral Dissertations*, 2015. URL https://scholars.unh.edu/dissertation/2205.

N. Olsen and C. Stolle. Satellite geomagnetism. *Annual Review of Earth and Planetary Sciences*, 40(1):441–465, 2012. doi: 10.1146/annurev-earth-042711-105540. URL https://doi.org/10.1146/annurev-earth-042711-105540.

E. N. Parker. Dynamics of the Interplanetary Gas and Magnetic Fields. *Astrophysical Journal*, 128:664, Nov. 1958. doi: 10.1086/146579.

W. D. Parkinson and F. W. Jones. The geomagnetic coast effect. *Reviews of Geophysics*, 17(8):1999–2015, 1979. doi: https://doi.org/10.1029/RG017i008p01999. URL https://agupubs.onlinelibrary.wiley.com/doi/abs/10.1029/RG017i008p01999.

E. D. Pettigrew, S. G. Shepherd, and J. M. Ruohoniemi. Climatological patterns of high-latitude convection in the northern and southern hemispheres: Dipole tilt dependencies and interhemispheric comparisons. *Journal of Geophysical Research: Space Physics*, 115(A7), 2010. doi: https://doi.org/10.1029/2009JA014956. URL https://agupubs.onlinelibrary.wiley.com/doi/abs/10.1029/2009JA014956.

R. Pirjola. Review on the calculation of surface electric and magnetic fields and of geomagnetically induced currents in ground-based technological systems. *Surveys in Geophysics*, 23(1):71–90, Jan 2002. ISSN 1573-0956. doi: 10.1023/A:1014816009303. URL https://doi.org/10.1023/A:1014816009303.

A. Pulkkinen, O. Amm, A. Viljanen, and B. w. group. Separation of the geomagnetic variation field on the ground into external and internal parts using the spherical elementary current system method. *Earth, Planets and Space*, 55(3):117–129, Mar 2003. ISSN 1880-5981. doi: 10.1186/BF03351739. URL https://doi.org/10.1186/BF03351739.

A. Pulkkinen, E. Bernabeu, A. Thomson, A. Viljanen, R. Pirjola, D. Boteler, J. Eichner, P. J. Cilliers, D. Welling, N. P. Savani, R. S. Weigel, J. J. Love, C. Balch, C. M. Ngwira, G. Crowley, A. Schultz, R. Kataoka, B. Anderson, D. Fugate, J. J. Simpson, and M. MacAlester. Geomagnetically induced currents: Science, engineering, and applications readiness. *Space Weather*, 15(7):828–856, 2017. doi: https://doi.org/10.1002/2016SW001501. URL https://agupubs.onlinelibrary.wiley.com/doi/abs/10.1002/2016SW001501.

A. D. Richmond and Y. Kamide. Mapping electrodynamic features of the high-latitude ionosphere from localized observations: Technique. *Journal of Geophysical Research*, 93(A6):5741–5759, 1988. ISSN 0148-0227. doi: 10.1029/JA093iA06p05741. URL https://doi.org/10.1029/JA093iA06p05741.

A. J. Ridley. Estimations of the uncertainty in timing the relationship between magnetospheric and solar wind processes. *Journal of Atmospheric and Solar-Terrestrial Physics*, 62(9):757–771, 2000. ISSN 1364-6826. doi: https://doi.org/10.1016/S1364-6826(00)00057-2. URL https://www.sciencedirect.com/science/article/pii/S1364682600000572.

C. T. Russel. *A Brief History of Solar-Terrestrial Physics*. Cambridge University Press, Cambridge, 1995. doi: 10.1017/9781139878296.002.

T. J. Sabaka, G. Hulot, and N. Olsen. *Mathematical Properties Relevant to Geomagnetic Field Modeling*. Springer, 2010. doi: 10.1007/978-3-642-27793-1_17-2.

C. J. Schrijver, K. Kauristie, A. D. Aylward, C. M. Denardini, S. E. Gibson, A. Glover, N. Gopalswamy, M. Grande, M. Hapgood, D. Heynderickx, N. Jakowski, V. V. Kalegaev, G. Lapenta, J. A. Linker, S. Liu, C. H. Mandrini, I. R. Mann, T. Nagatsuma, D. Nandy, T. Obara, T. Paul O'Brien, T. Onsager, H. J. Opgenoorth, M. Terkildsen, C. E. Valladares, and N. Vilmer. Understanding space weather to shield society: A global road map for 2015–2025 commissioned by cospar and ilws. *Advances in Space Research*, 55(12):2745–2807, 2015. ISSN 0273-1177. doi: https://doi.org/10.1016/j.asr.2015.03.023. URL https://www.sciencedirect.com/science/article/pii/S0273117715002252.

G. Schubert. *Treatise on Geophysics*, volume 2. 01 2015. ISBN 9780444538024.

R. Schwenn. *Large-Scale Structure of the Interplanetary Medium*, pages 99–181. Springer Berlin Heidelberg, Berlin, Heidelberg, 1990. ISBN 978-3-642-75361-9. doi: 10.1007/978-3-642-75361-9_3. URL https://doi.org/10.1007/978-3-642-75361-9_3.

R. Schwenn. Space weather: The solar perspective. *Living Reviews in Solar Physics*, 3 (1), Dec 2006. ISSN 1614-4961. doi: 10.12942/lrsp-2006-2. URL https://doi.org/10.12942/lrsp-2006-2.

N. Sckopke. A general relation between the energy of trapped particles and the disturbance field near the earth. *Journal of Geophysical Research (1896-1977)*, 71 (13):3125–3130, 1966. doi: https://doi.org/10.1029/JZ071i013p03125. URL https://agupubs.onlinelibrary.wiley.com/doi/abs/10.1029/JZ071i013p03125.

C. Shen, Y. Y. Yang, Z. J. Rong, X. Li, M. Dunlop, C. M. Carr, Z. X. Liu, D. N. Baker, Z. Q. Chen, Y. Ji, and G. Zeng. Direct calculation of the ring current distribution and magnetic structure seen by cluster during geomagnetic storms. *Journal of Geophysical Research: Space Physics*, 119(4):2458–2465, 2014. doi: https://doi.org/10.1002/2013JA019460. URL https://agupubs.onlinelibrary.wiley.com/doi/abs/10.1002/2013JA019460.

X. Shi, D. Lin, W. Wang, J. B. H. Baker, J. M. Weygand, M. D. Hartinger, V. G. Merkin, J. M. Ruohoniemi, K. Pham, H. Wu, V. Angelopoulos, K. A. McWilliams, N. Nishitani, and S. G. Shepherd. Geospace concussion: Global reversal of ionospheric vertical plasma drift in response to a sudden commencement. *Geophysical Research Letters*, 49(19):e2022GL100014, 2022. doi: https://doi.org/10.1029/

2022GL100014. URL https://agupubs.onlinelibrary.wiley.com/doi/abs/10.1029/2022GL100014. e2022GL100014 2022GL100014.

D. G. Sibeck. A model for the transient magnetospheric response to sudden solar wind dynamic pressure variations. *Journal of Geophysical Research: Space Physics*, 95(A4): 3755–3771, 1990. doi: https://doi.org/10.1029/JA095iA04p03755.

P. Song and V. M. Vasyliūnas. *Inductive-Dynamic Coupling of the Ionosphere With the Thermosphere and the Magnetosphere*, chapter 17, pages 201–215. American Geophysical Union (AGU), 2014. ISBN 9781118704417. doi: https://doi.org/10.1002/9781118704417.ch17. URL https://agupubs.onlinelibrary.wiley.com/doi/abs/10.1002/9781118704417.ch17.

P. Stauning and O. A. Troshichev. Polar cap convection and pc index during sudden changes in solar wind dynamic pressure. *Journal of Geophysical Research: Space Physics*, 113(A8), 2008. doi: https://doi.org/10.1029/2007JA012783. URL https://agupubs.onlinelibrary.wiley.com/doi/abs/10.1029/2007JA012783.

E. C. Stone, A. M. Frandsen, R. A. Mewaldt, E. R. Christian, D. Margolies, J. F. Ormes, and F. Snow. The advanced composition explorer. *Space Science Reviews*, 86(1):1–22, Jul 1998. ISSN 1572-9672. doi: 10.1023/A:1005082526237. URL https://doi.org/10.1023/A:1005082526237.

M. Sugiura. Hourly values of equatorial dst for the igy. *Ann. Int. Geophys. Yr.*, 35, 1964.

M. Sugiura and T. Kamel. Equatorial dst index 1957-1986. *IAGA Bulletin*, 40, 1991.

M. Takeda. Effects of the induction electric field on ionospheric current systems driven by field-aligned currents of magnetospheric origin. *Journal of Geophysical Research: Space Physics*, 113(A1), 2008. doi: https://doi.org/10.1029/2007JA012662. URL https://agupubs.onlinelibrary.wiley.com/doi/abs/10.1029/2007JA012662.

T. Tamao. The structure of three-dimensional hydromagnetic waves in a uniform cold plasma. *Journal of geomagnetism and geoelectricity*, 16(2):89–114, 1964. doi: 10.5636/jgg.16.89.

T. Tamao. Direct contribution of oblique field-aligned currents to ground magnetic fields. *Journal of Geophysical Research: Space Physics*, 91(A1):183–189, 1986. doi: https://doi.org/10.1029/JA091iA01p00183. URL https://agupubs.onlinelibrary.wiley.com/doi/abs/10.1029/JA091iA01p00183.

T. Tanaka, Y. Ebihara, M. Watanabe, M. Den, S. Fujita, T. Kikuchi, K. K. Hashimoto, and R. Kataoka. Reproduction of ground magnetic variations during the sc and the

substorm from the global simulation and biot-savart's law. *Journal of Geophysical Research: Space Physics*, 125(2):e2019JA027172, 2020. doi: https://doi.org/10.1029/2019JA027172. URL https://agupubs.onlinelibrary.wiley.com/doi/abs/10.1029/2019JA027172. e2019JA027172 2019JA027172.

A. Tarantola. *Inverse Problem Theory and Methods for Model Parameter Estimation*. Society for Industrial and Applied Mathematics, 2005. doi: 10.1137/1.9780898717921. URL https://epubs.siam.org/doi/abs/10.1137/1.9780898717921.

M. Temmer. Space weather: the solar perspective. *Living Reviews in Solar Physics*, 18(1), Jun 2021. ISSN 1614-4961. doi: 10.1007/s41116-021-00030-3. URL https://doi.org/10.1007/s41116-021-00030-3.

J. M. Torta. Modelling by spherical cap harmonic analysis: A literature review. *Surveys in Geophysics*, 41(2):201–247, Mar 2020. ISSN 1573-0956. doi: 10.1007/s10712-019-09576-2. URL https://doi.org/10.1007/s10712-019-09576-2.

J. Tu, P. Song, and V. M. Vasyliūnas. Inductive-dynamic magnetosphere-ionosphere coupling via mhd waves. *Journal of Geophysical Research: Space Physics*, 119(1):530–547, 2014. doi: https://doi.org/10.1002/2013JA018982. URL https://agupubs.onlinelibrary.wiley.com/doi/abs/10.1002/2013JA018982.

J. Untiedt and W. Baumjohann. Studies of polar current systems using the ims scandinavian magnetometer array. *Space Science Reviews*, 63(3):245–390, Sep 1993. ISSN 1572-9672. doi: 10.1007/BF00750770. URL https://doi.org/10.1007/BF00750770.

H. Vanhamäki and L. Juusola. *Introduction to Spherical Elementary Current Systems*, pages 5–33. Springer International Publishing, Cham, 2020. ISBN 978-3-030-26732-2. doi: 10.1007/978-3-030-26732-2_2. URL https://doi.org/10.1007/978-3-030-26732-2_2.

H. Vanhamäki, A. Viljanen, and O. Amm. Induction effects on ionospheric electric and magnetic fields. *Annales Geophysicae*, 23(5):1735–1746, 2005. doi: 10.5194/angeo-23-1735-2005. URL https://angeo.copernicus.org/articles/23/1735/2005/.

H. Vanhamäki, O. Amm, and A. Viljanen. New method for solving inductive electric fields in the non-uniformly conducting ionosphere. *Annales Geophysicae*, 24(10):2573–2582, 2006. doi: 10.5194/angeo-24-2573-2006. URL https://angeo.copernicus.org/articles/24/2573/2006/.

H. Vanhamäki, O. Amm, and A. Viljanen. Role of inductive electric fields and currents in dynamical ionospheric situations. *Annales Geophysicae*, 25(2):437–455, 2007. doi:

10.5194/angeo-25-437-2007. URL https://angeo.copernicus.org/articles/25/437/2007/.

V. M. Vasyliunas. Mathematical models of magnetospheric convection and its coupling to the ionosphere. In B. M. McCormac, editor, *Particles and Fields in the Magnetosphere*, pages 60–71, Dordrecht, 1970. Springer Netherlands. ISBN 978-94-010-3284-1.

S. Walker, K. Laundal, J. Reistad, A. Ohma, and S. Hatch. Statistical temporal variations in the auroral electrojet estimated with ground magnetometers in fennoscandia. *Space Weather*, 21(1):e2022SW003305, 2023. doi: https://doi.org/10.1029/2022SW003305. URL https://agupubs.onlinelibrary.wiley.com/doi/abs/10.1029/2022SW003305. e2022SW003305 2022SW003305.

C. L. Waters, J. W. Gjerloev, M. Dupont, and R. J. Barnes. Global maps of ground magnetometer data. *Journal of Geophysical Research: Space Physics*, 120(11):9651–9660, 2015. doi: https://doi.org/10.1002/2015JA021596. URL https://agupubs.onlinelibrary.wiley.com/doi/abs/10.1002/2015JA021596.

P. Weidelt. The Inverse Problem of Geomagnetic Induction. *Geophysical Journal International*, 35(1-3):379–379, 12 1973. ISSN 0956-540X. doi: 10.1093/gji/35.1.379. URL https://doi.org/10.1093/gji/35.1.379.

D. R. Weimer. Improved ionospheric electrodynamic models and application to calculating joule heating rates. *Journal of Geophysical Research: Space Physics*, 110 (A5), 2005. doi: https://doi.org/10.1029/2004JA010884. URL https://agupubs.onlinelibrary.wiley.com/doi/abs/10.1029/2004JA010884.

D. R. Weimer, D. M. Ober, N. C. Maynard, M. R. Collier, D. J. McComas, N. F. Ness, C. W. Smith, and J. Watermann. Predicting interplanetary magnetic field (imf) propagation delay times using the minimum variance technique. *Journal of Geophysical Research: Space Physics*, 108(A1), 2003. doi: https://doi.org/10.1029/2002JA009405. URL https://agupubs.onlinelibrary.wiley.com/doi/abs/10.1029/2002JA009405.

J. M. Weygand, O. Amm, A. Viljanen, V. Angelopoulos, D. Murr, M. J. Engebretson, H. Gleisner, and I. Mann. Application and validation of the spherical elementary currents systems technique for deriving ionospheric equivalent currents with the north american and greenland ground magnetometer arrays. *Journal of Geophysical Research: Space Physics*, 116(A3), 2011. doi: https://doi.org/10.1029/2010JA016177. URL https://agupubs.onlinelibrary.wiley.com/doi/abs/10.1029/2010JA016177.

J. M. Weygand, M. J. Engebretson, V. A. Pilipenko, E. S. Steinmetz, M. B. Moldwin, M. G. Connors, Y. Nishimura, L. R. Lyons, C. T. Russell, S. Ohtani, and J. Gjerloev. Secs analysis of nighttime magnetic perturbation events observed in arctic canada. *Journal of Geophysical Research: Space Physics*, 126(11):e2021JA029839, 2021. doi: https://doi.org/10.1029/2021JA029839. URL https://agupubs.onlinelibrary.wiley.com/doi/abs/10.1029/2021JA029839. e2021JA029839 2021JA029839.

A. N. Willer. Pcn index, 2021.

L. B. Wilson III, A. L. Brosius, N. Gopalswamy, T. Nieves-Chinchilla, A. Szabo, K. Hurley, T. Phan, J. C. Kasper, N. Lugaz, I. G. Richardson, C. H. K. Chen, D. Verscharen, R. T. Wicks, and J. M. TenBarge. A quarter century of wind spacecraft discoveries. *Reviews of Geophysics*, 59(2):e2020RG000714, 2021. doi: https://doi.org/10.1029/2020RG000714. URL https://agupubs.onlinelibrary.wiley.com/doi/abs/10.1029/2020RG000714. e2020RG000714 2020RG000714.

J. H. Yee, J. Gjerloev, D. Wu, and M. J. Schwartz. First application of the zeeman technique to remotely measure auroral electrojet intensity from space. *Geophysical Research Letters*, 44(20):10,134–10,139, 2017. doi: https://doi.org/10.1002/2017GL074909. URL https://agupubs.onlinelibrary.wiley.com/doi/abs/10.1002/2017GL074909.

J. H. Yee, J. Gjerloev, and D. Wu. *Remote Sensing of Magnetic Fields Induced by Electrojets From Space*, chapter 21, pages 451–468. American Geophysical Union (AGU), 2021. ISBN 9781119815631. doi: https://doi.org/10.1002/9781119815631.ch21. URL https://agupubs.onlinelibrary.wiley.com/doi/abs/10.1002/9781119815631.ch21.

Y. I. Yermolaev and V. V. Stupin. Helium abundance and dynamics in different types of solar wind streams: The prognoz 7 observations. *Journal of Geophysical Research: Space Physics*, 102(A2):2125–2136, 1997. doi: https://doi.org/10.1029/96JA01635. URL https://agupubs.onlinelibrary.wiley.com/doi/abs/10.1029/96JA01635.

Y. I. Yermolaev, N. S. Nikolaeva, I. G. Lodkina, and M. Y. Yermolaev. Catalog of large-scale solar wind phenomena during 1976–2000. *Cosmic Research*, 47(2), Apr 2009. ISSN 1608-3075. doi: 10.1134/S0010952509020014. URL https://doi.org/10.1134/S0010952509020014.

A. Yoshikawa and M. Itonaga. The nature of reflection and mode conversion of mhd waves in the inductive ionosphere: Multistep mode conversion between divergent and rotational electric fields. *Journal of Geophysical Research: Space Physics*, 105 (A5):10565–10584, 2000. doi: https://doi.org/10.1029/1999JA000159. URL https://agupubs.onlinelibrary.wiley.com/doi/abs/10.1029/1999JA000159.

E. G. Zweibel and M. Yamada. Magnetic reconnection in astrophysical and laboratory plasmas. *Annual Review of Astronomy and Astrophysics*, 47(1):291–332, 2009. doi: 10.1146/annurev-astro-082708-101726. URL https://doi.org/10.1146/annurev-astro-082708-101726.

Chapter 6

Scientific results

Article I

6.1 Geomagnetic Response to Rapid Increases in Solar Wind Dynamic Pressure: Event Detection and Large Scale Response

M. Madelaire, K.M. Laundal, J.P. Reistad, S.M. Hatch, A. Ohma, S. Haaland

Fronteirsin in Astronomy and Space Sciences, Vol. 9, doi:10.3389/fspas.2022.904620, 2022

frontiers | Frontiers in Astronomy and Space Sciences

ORIGINAL RESEARCH
published: 05 May 2022
doi: 10.3389/fspas.2022.904620

Geomagnetic Response to Rapid Increases in Solar Wind Dynamic Pressure: Event Detection and Large Scale Response

Michael Madelaire[1], Karl M. Laundal[1], Jone P. Reistad[1], Spencer M. Hatch[1], Anders Ohma[1] and Stein Haaland[1,2]*

[1]Birkeland Centre for Space Science, Bergen, Norway, [2]Max Planck Institute for Solar System Research, Göttingen, Germany

Discontinuities in the solar wind trigger a variety of processes in the magnetosphere-ionosphere system. A rapid increase in solar wind dynamic pressure causes compression of the magnetosphere. This manifests itself as a positive perturbation of the horizontal ground magnetic field at low/mid latitudes. In this study we present a method for detecting these discontinuities *in situ* solar wind data by using the random forest machine learning algorithm. Each detected event is propagated to Earth and its arrival time is aligned with a corresponding response in the low latitude ground magnetic field. A list of 3,867 events, detected between 1994 and 2019, is presented. We use the list in a superposed epoch analysis of the low/mid latitude response in the ground magnetic field at different local times, and of the high latitude response using the Polar Cap index. A dawn-dusk asymmetry is found at low/mid latitudes with weaker positive perturbations at dawn compared to any other local time sector. This suggests a stronger ring current contribution at dawn assuming the magnetopause contribution to be uniform. During northward IMF the initial response is asymmetric, but returns to symmetry after 30 min. During southward IMF the low/mid latitude response decays rapidly in all local sectors except dawn. After around 30 min the asymmetry has flipped such that the strongest positive perturbation is at dawn. This suggests an amplification of the partial ring current. In addition, a noon-midnight asymmetry is observed during southward IMF with the strongest positive perturbation on the night side suggesting a significant contribution from dipolarization of the geomagnetic field in the near tail. The complex geomagnetic response to rapid increases in solar wind dynamic pressure demonstrates a need for further statistical analyses. Event lists, such as the one presented here, are critical components in such studies.

Keywords: solar wind dynamic pressure, rapid pressure increase, magnetospheric compression, sudden commencement, machine learning, superposed epoch analysis, ring current asymmetry

OPEN ACCESS

Edited by:
Olga V. Khabarova, Institute of Terrestrial Magnetism Ionosphere and Radio Wave Propagation (RAS), Russia

Reviewed by:
Zdenek Nemecek, Charles University, Czechia
Vladimir Parkhomov, Baikal State University, Russia

****Correspondence:***
Michael Madelaire
michael.madelaire@uib.no

Specialty section:
This article was submitted to Space Physics, a section of the journal Frontiers in Astronomy and Space Sciences

Received: *25 March 2022*
Accepted: *08 April 2022*
Published: *05 May 2022*

Citation:
Madelaire M, Laundal KM, Reistad JP, Hatch SM, Ohma A and Haaland S (2022) Geomagnetic Response to Rapid Increases in Solar Wind Dynamic Pressure: Event Detection and Large Scale Response. Front. Astron. Space Sci. 9:904620. doi: 10.3389/fspas.2022.904620

1 INTRODUCTION

The solar wind flows radially outward from the Sun, populating the interplanetary space and carrying with it the Sun's magnetic field referred to as the Interplanetary Magnetic Field (IMF). The magnetosphere-ionosphere-thermosphere system is heavily dependent on conditions in the solar

wind and IMF. Understanding this complex system is a difficult task. Natural phenomena in the solar wind can perturb the entire system. Studying their characteristics in combination with those of the perturbed system may result in a deeper understanding of the dynamic system and its dependencies.

In this study we focus on rapid increases in solar wind dynamic pressure P_d. This type of event can have various origins. The best known of these are coronal mass ejections, a large and sudden release of plasma from the Sun. The ejecta is referred to as interplanetary coronal mass ejection when propagating through interplanetary space and can form an interplanetary shock (IS). Another well known origin is a stream interaction region which occurs in the rarefaction zone of two solar wind streams. However, ISs (of the forward type) rarely evolve in these rarefaction zones before they have passed Earth and are therefore seldom observed at Earth (Smith and Wolfe, 1976). A detailed description of ISs is given by Oliveira and Samsonov (2018).

Rapid changes in P_d can occur without the formation of a shock. In their examination of such solar wind structures Dalin et al. (2002a) found that the majority of cases occurred due to increases in solar wind number density and not solar wind speed. Additionally, they found that their occurrence rate was independent of solar cycle, unlike ISs (Oliveira and Samsonov, 2018).

Rapid increases in P_d are linked to Sudden Commencements (SC). The term SC comes from storm sudden commencement which is a pressure-induced magnetic perturbation on ground that precedes a geomagnetic storm. However, it was suspected that the phenomena could occur without being followed by a storm and thus SC was termed. In addition, the term sudden impulse was coined after the discovery of a characteristic perturbation in the H-component later shown to be caused by the same mechanism as the SC. We will use the term SC as a general expression for both storm sudden commencement and sudden impulse as suggested by Curto et al. (2007).

Following Araki (1994), we divide the ground response D_{sc} into a low-latitude (DL) and high-latitude (DP) response:

$$\begin{aligned} D_{sc} &= DL + DP \\ DP &= DP_{PI} + DP_{MI} \end{aligned} \tag{1}$$

DL is thought to be a direct effect of magnetospheric compression which increases the magnetic flux density resulting in a positive perturbation of the horizontal magnetic field. DP is connected to vortices in the high latitude ionosphere. The vortices occur in two pairs; the first is the preliminary impulse PI and the second is the main impulse MI.

Describing these contributions and the parameters they depend on requires a large set of events to facilitate analysis of multiple sub-sets with a statistically meaningful size. This study will focus on finding suitable events and on analysis of the magnetospheric contribution. The ionospheric contribution will be addressed in a later study.

Several statistical studies of the geospace response to ISs have been made (Russell et al., 1994a,b; Russell and Ginskey, 1995). It was found that an increase in the horizontal magnetic field due to compression of the magnetosphere, at 20° latitude, is expected to be around 18.4 nT/nPa$^{\frac{1}{2}}$ during northward IMF (Russell et al., 1994a) and 13.8 nT/nPa$^{\frac{1}{2}}$ (i.e., 25% lower) during southward IMF (Russell et al., 1994b). It was also found that the magnetic field perturbation is dependent on local time, being largest on the dayside and smallest at night. In their examination of the response at subauroral latitudes, Russell and Ginskey (1995) found that the PI lasted for ~1 min, and was followed by a steady increase over a 5-min period as a result of magnetospheric compression and the main impulse.

Our goal is to isolate the influence of dipole tilt and IMF orientation on SC development. None of the lists of events described in existing statistical studies of SCs are appropriate for our purposes, since to our knowledge these studies are tailored to ISs and/or the lists contain too few events to separate events into bins based on more than one environmental parameter without compromising the ability to yield statistically meaningful conclusions.

Before the use of *in situ* observations of solar wind plasma, lists of SC were made by inspection of observations from ground magnetometer stations. A historical overview of the study of SCs is given in Curto et al. (2007). Various lists from the early to mid-19th century are mentioned, one of which is still maintained and can be accessed at http://www.obsebre.es/en/rapid.

During the late 20th century *in situ* solar wind data became more common and the connection between SC and changes in P_d was made (Friis-Christensen et al., 1988). At the same time lists of various solar wind events were made, typically either through cumbersome manual inspection or through manual verification after applying an algorithm to the raw data. Two classic lists of interplanetary coronal mass ejections and stream interaction regions using the manual approach were presented by Richardson and Cane (1995) and Jian et al. (2006), respectively. A list of ISs was presented by Oliveira and Raeder (2015), containing 461 events spanning 1995–2013. The list is a compilation of four other lists combined with the authors own manually verified events detected by an algorithm. In addition, Boudouridis and Zesta (2021) recently presented an algorithm for automated detection of rapid pressure increases by fitting a logistic function to *in situ* solar wind data.

These lists are all based on measurements from the solar wind, and only a few provide the arrival time at Earth. We know only one analysis where the arrival time was determined based on ground magnetometers: Huang and Yumoto (2006) presented 160 instances of P_d enhancements between 1998 and 2005, and arrival times were determined based on a corresponding ground response. We use this concept when addressing arrival time in **Section 3.2**.

In **Section 2**, we describe the solar wind and magnetometer measurements that we use to derive our list. In **Section 3**, we describe our methodology for automated identification of rapid P_d increase via the random forest machine learning algorithm and the estimated arrival time at Earth. In **Section 4**, we discuss the resulting list of 3,867 events, which covers a 26-year period, and perform a superposed epoch analysis using various subsets of the event list to isolate the influence of controlling parameters. In **Sections 5** we discuss the implications of the event detection method, a seasonal dependence of the occurrence rate, and the

interpretation of a possible dawn-dusk ring current asymmetry. **Section 6** concludes the paper.

2 DATA

The aim of this study is two-fold; to create a list of rapid P_d increases leading to measurable magnetic ground perturbation, and to perform a statistical analysis of these magnetic ground perturbations. In order to achieve this, both *in situ* solar wind measurements and ground-based magnetic field measurements are required.

2.1 *In Situ* Solar Wind

In situ observations of the solar wind spanning 1994–2019 was provided by the Advanced Composition Explorer (ACE) and Wind missions. The two spacecraft measure solar wind plasma characteristics using the Solar Wind Experiment (SWE) (Ogilvie et al., 1995) and the Solar Wind Electron, Proton and Alpha Monitor (SWEPAM) (McComas et al., 1998). The IMF is measured using the Magnetic Fields Investigation (MFI) (Lepping et al., 1995) and magnetometer (MAG) (Smith et al., 1998) instruments. Plasma data with a temporal resolution of 3- and 64-s and IMF data with a temporal resolution of 3- and 16-s for ACE and Wind, respectively, was downloaded from the Coordinated Data Analysis Web (CDAWeb) at https://cdaweb.gsfc.nasa.gov/index.html/. All solar wind observations were up- or down-sampled to 1-min resolution after interpolating data gaps smaller than 4 min.

Measurements from Wind were provided in the GSE reference frame. A rotation into GSM was therefore carried out using the method described in Hapgood (1992). The GSM reference frame is preferred as it better describes coupling between the IMF and Earth's magnetic field.

2.2 Indices

The SYM-H index (Iyemori et al., 2010) at 1-min resolution was used for arrival time estimates of events. The SYM-H index is closely related to the ground magnetic perturbation due to the ring current and is strongly correlated with P_d enhancements (Burton et al., 1975). This index is accessible at https://omniweb.gsfc.nasa.gov.

For the superposed epoch analysis another ring current index was used: SMR (Newell and Gjerloev, 2012) is a ring current index provided by the SuperMAG web service (https://supermag.jhuapl.edu/), based on a much larger number of magnetometers than SYM-H. This is important for the study of asymmetry as it allows for a local time dependent index SMR LT which is provided in four 6-h wide sectors centered at midnight/dawn/noon/dusk (00/06/12/18). The high latitude response was investigated using the polar cap index PC for the northern hemisphere PCN. This index is based on the Thule magnetometer station on Greenland (Willer, 2021). It is accessible at https://omniweb.gsfc.nasa.gov. Both indices are provided in a 1-min resolution.

3 METHODS

In this section we introduce the method with which the list of rapid P_d increases is generated. The process is separated into two main steps. First an algorithm processes the *in situ* solar wind data to find events. Then the event is aligned with a corresponding response on ground. In this study an event refers to a step-like increase in P_d that provokes a measurable geomagnetic response on ground.

Section 3.1 focuses on detection of events, while **Section 3.2** describes how we match the detected events with a response measured by magnetometers on ground.

3.1 Event Detection

Detection of events is done using 120 min segments of *in situ* solar wind measurements of P_d as input into a machine learning algorithm. The algorithm is designed to classify whether or not a rapid pressure increase (an event) is present in these segments. The algorithm is based on a set of features determined from each segment.

The training data is described in **Section 3.1.1**, the features are explained in detail in **Section 3.1.2**, and an introduction to the random forest machine learning algorithm is given in **Section 3.1.3**.

3.1.1 Training Data

In this study we work with two classes: *events* and *non-events*. Our training data must contain examples of each of these classes.

The training data were compiled in two ways. The *events* were taken from a list of ISs provided by Oliveira and Raeder (2015). Initially, it consisted of 461 ISs. After removing events with data gaps 383 remained. In a second post-processing step the time of detection was corrected, typically not by more than a couple of minutes, to match the observed onset of the pressure jump.

The list of *non-events* is significantly longer with ~1700 entries. The first 700 were determined by randomly selecting a point on the P_d time series from either ACE or Wind. This point is referred to as an Evaluation Point (EP). We determined if the EP was located at the onset of a rapid P_d increase or not by visual inspection. Segments with large data gaps were discarded. It was also enforced that the EPs should be uniformly distributed in seven groups according to background levels: 0–2, 2–3, 3–4, 4–5, 5–6, 6–7 and above 7 nPa. This was done to include information about the spread in *non-events*. The last 1,000 entries were determined by manually inspecting a ±60 min window around randomly chosen EPs where the subsequent data-point experienced an increase of 0.4 nPa or more (resolution between each data-point is 1-min). This group represents situations with larger P_d variance around the EP than the first group.

3.1.2 Features

The algorithm is designed to predict if an EP is the onset of a rapid P_d increase. This is done by evaluating a set of features chosen to best describe the step-like behavior that we search for. We have chosen a total of five features. All features are determined on a

relative scale such that events can be compared independent of the background level and size of the jump. The features are:

3.1.2.1 Slope

The gradient in the pressure jump. This is estimated by the slope of a linear regression fit based on the EP and the following two data-points. To facilitate intercomparison of events the resulting slope was divided by the largest of the three data-points. This feature is highly sensitive to data gaps and so if any of these three data-points were missing the EP was discarded.

3.1.2.2 Maximum Prior Difference

The difference between the minimum and maximum value in the 60-min interval prior to the EP. This was calculated using normalized data with mean and standard deviation determined from a ±60 min window around the EP.

3.1.2.3 Relative Increase

The relative increase from before to after the EP. This is a percentage increase between the maximum 60 min prior to and the median between 3 and 8 min after the EP.

3.1.2.4 PCA_5 and PCA_{20}

The last two features are based on a principal component analysis of the P_d measurements in the *events* from the training data. The first principal component shows a very clear step-like behavior (see **Figure 1**). The features, PCA_5 and PCA_{20}, are defined as the dot product between a candidate event and the first principal component, using time windows that are ±5 and ±20 min, respectively. When calculating the dot product, we fill in data gaps by interpolation and extrapolation.

The features are conceptually illustrated in **Figure 1**. In the top row the three first principal components in the *events* training dataset are shown. The first component has a step-like increase between epoch 0 and 2 and explains 88.57% of the variance. The second and third principal components also experience rapid increases at epoch 0 followed by a decay. These two components explain only 4.93 and 1.8% of the variance and could be related to pressure increases that last for only a short duration. The bottom row of **Figure 1** shows an example event observed by ACE. Superimposed are the features when the EP is located at the onset of the jump. The calculated linear fit from which the slope is determined is illustrated in orange. The minimum and maximum prior to the EP is indicated by the blue lines, over the range from which they were determined. The median after the EP, used to calculate the percentage increase, is shown as a red line.

An active check for data gaps is only carried out during calculation of the slope. For the rest of the features, EPs were only discarded if the entire time series used for calculating a metric was missing.

The 5D space spanned by the features, commonly referred to as feature space, is illustrated for the training data in **Figure 2**. *Events* are shown in blue while the first part of *non-events* are

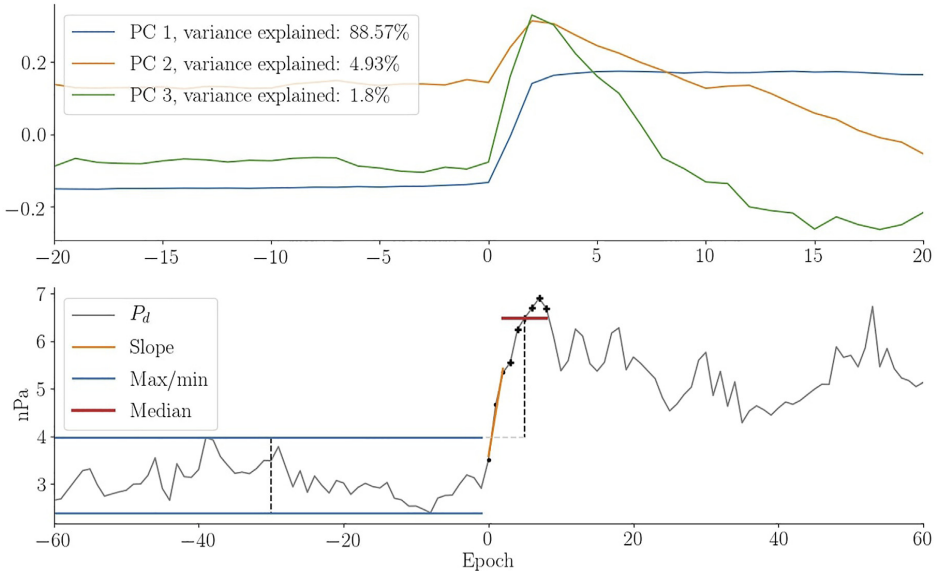

FIGURE 1 | Illustration of the features used in the random forest algorithm. The top panel shows the first three principal components as a result of a PCA analysis of the data used in *events*. The bottom panel shows the slope in orange, the minimum and maximum before onset in blue and the median after onset in red. The P_d time series itself is an event observed May 8, 1998 at 09:20 by ACE.

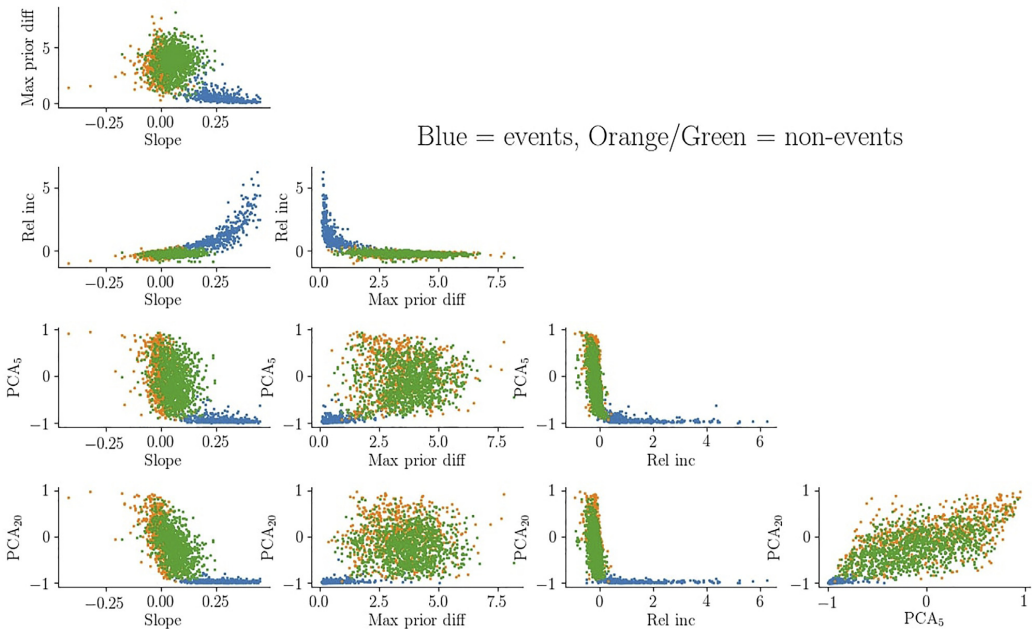

FIGURE 2 | Distribution of *events* and *non-events* with respect to the features described in **Section 3.1.2**. The blue dots illustrate *events* while the orange and green dots are *non-events*. Data in *non-events* associated with more quiet conditions are orange while the ones associated with more active conditions are green.

shown in orange and the last part in green. It is evident that the features provide a clear distinction between the two classes which is crucial for the success of the algorithm.

3.1.3 Random Forest

To separate between events and non-events we employ the random forest machine learning algorithm, a variation of the well-known supervised algorithm called decision tree. Training data are used to set up a series of binary questions (yes/no) with the purpose of separating data belonging to different classes. These binary questions are the basis for classifying events after training. If a decision tree is used in a bootstrapping format it is referred to as a random forest (Ho, 1995).

The random forest algorithm works by training a series of decision trees on individual data sets sampled from the training data. Each decision tree can then provide a classification when asked to predict the class of a potential event. In this way numerous decision trees can be used to calculate the probability that a given EP belongs to a particular class. Potential events are commonly assigned to whichever class has the highest probability. We used a stricter criteria by enforcing that 90% of all decision trees have to agree before a potential event can be classified as an *event*.

In practice the Python implementation by scikit-learn was used. In most practical implementations certain parameter choices have to be made (e.g., the number of decision trees, the maximum depth etc.). A complete description of the method used for selecting these parameters as well as illustrative plots is given in appendix.

3.1.4 Event Merging

Multiple EPs close to a P_d increase can be classified as *events*. In this scenario the EP with the highest classification probability was kept. During highly disturbed times multiple discontinuous P_d structures may appear resulting in events being very close in time. A minimum spacing of 1 h between events was enforced with the first come first serve principle. Events were detected with both ACE and Wind. When two events with similar arrival time estimates (discussed in the following section) arose ACE was prioritized and the Wind event discarded.

3.2 Arrival Time

Our definition of arrival is when information about magnetospheric compression has propagated to Earth and is observed in SYM-H. Estimation of arrival time at Earth is done in three main steps.

Initially, arrival time at Earth was crudely estimated by propagating the events to the magnetopause, assumed to be located at 10 R_E along the Sun-Earth line, using the spacecraft's x coordinate and the measured solar wind velocity. The distribution of the normalized SYM-H responses is shown in **Figure 5A** for this step. Each response is normalized for better comparison as

background level and jump size can vary. It is clear that the alignment is quite poor resulting in a gradual increase starting several minutes prior to epoch zero. This is because we do not take into account the location of the magnetopause given the preexisting solar wind conditions or the orientation of the solar wind structure (Weimer et al., 2003; Mailyan et al., 2008). In addition, the delay between impact with the magnetopause and observing a response on ground is not trivial, resulting in additional uncertainty.

A comprehensive correction of the initial arrival time estimate was done using a correlation analysis between P_d and SYM-H. **Figure 3** showcases an example of the analysis. In the first row we show a ±10 min window of P_d (blue line) around the time of detection along with a ±40 min window of SYM-H (red line) around the crudely estimated arrival time. The second row shows the correlation resulting from sliding P_d over SYM-H. In the third row the slope from a fit between $\sqrt{P_d}$ and SYM-H is illustrated by a thin grey line while the product between the slope and correlation is shown in black. The blue dot indicates the maximum of the curve while ensuring that the correlation (second row) is above 0.6 and the slope (grey line in third row) is above 6 nT/nPa$^{\frac{1}{2}}$. If no lag fulfills these two criteria the event is discarded. These two thresholds were set low to accommodate differences in rise time between SYM-H and P_d. The fourth panel shows the result of using the blue dot from the third panel as the new arrival time. The improvement to the superposed SYM-H response after applying this correction is clearly seen in **Figure 5B**.

Figure 3 suggests that the arrival time for all events can be shifted ±30 min. However, a custom threshold is determined for each event as a combination of uncertainty in the propagation ε_1 and the magnetospheric-ionospheric coupling ε_2. Ridley (2000) investigated the uncertainty in using various propagation techniques and found propagation along the Sun-Earth line had an average uncertainty of $\varepsilon_{\text{mean}} = 0.219D_{YZ} + 1.63$ min when the spacecraft's euclidean distance D_{YZ} to the Sun-Earth line is given in Earth radii. We used a slightly more conservative estimate to allow for scenarios outside the norm by defining $\varepsilon_1 = 2\varepsilon_{\text{mean}}$. An additional delay due to propagation through the magnetosphere and rise time of the response was accounted for by setting $\varepsilon_2 = 10$ min. The maximum allowed correction of any event is thus $[-\varepsilon_1, \varepsilon_1 + \varepsilon_2]$ which is a function of the spacecraft position. ACE and Wind have a maximum D_{YZ} around 50 and 100 Earth radii leading to an ε_1 of around 20–45 min, respectively.

The step-like increase in P_d is often more rapid than the SYM-H response. It is therefore clear that their correlation can exhibit a maximum somewhere between the SYM-H onset and the following plateau. In order to ensure the best possible alignment we perform a minor correction to the result of the correlation analysis using an algorithm to estimate the onset and plateau of the SYM-H response and then change the arrival time estimate to match that of the estimated onset.

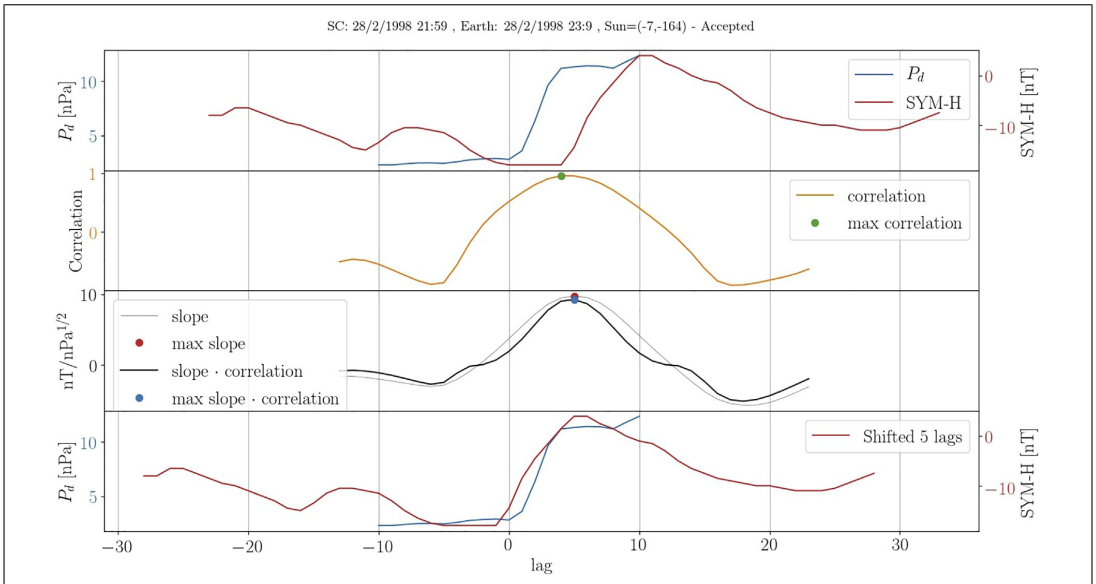

FIGURE 3 | Example of the correlation analysis on event detected by ACE at 22 UT the February 28, 1998. The first panel shows P_d increase as observed by ACE along with SYM-H after around the event's initial arrival time estimate. The second panel shows the correlation when sliding P_d over SYM-H in the first panel. The third panel shows the slope from a linear fit between SYM-H and $\sqrt{P_d}$ and the product of the slope and correlation. The fourth panel repeats the first panel when correcting the arrival time using the lag indicated by the blue dot in the third panel.

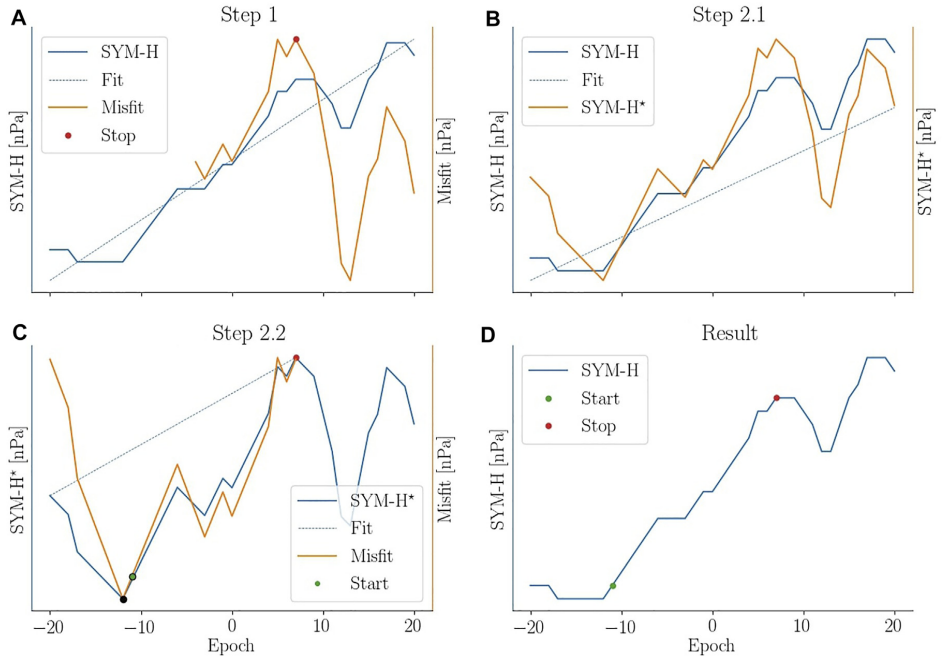

FIGURE 4 | Example of algorithm used to find the onset of the response in SYM-H. In **(A)** the peak of the response is found. In **(B)** the SYM-H response is detrended. In **(C)** the onset if located. **(D)** shows the estimated onset and peak of the SYM-H response.

The algorithm for finding the onset is divided into two steps as illustrated in **Figure 4**. The first step, **Figures 4A**, is to determine when the increase begins to plateau. First a linear fit (dashed blue) to the SYM-H (blue) is made. Then the misfit (orange) between the two is determined. The end of the rise time (red dot) is then determined as the maximum misfit after epoch −5.

The second step is separated into two sub-steps for illustration. First, **Figure 4B**, the SYM-H time series is detrended (indicated by the asterisk) by subtracting a linear fit (dashed blue) to the first 15 min from the entire time series. The next part, **Figures 4C**, is done on the detrended time series (blue). Epoch −20 and the red dot from 4a are connected by a straight line (dashed blue). From this the misfit (orange) between the detrended SYM-H and the linear fit is determined. The onset of the SYM-H response is then determined as the first misfit value, going from right to left, that falls below the 5% quantile of the misfit. Here two point fulfill the requirement, but the rightmost (green) is chosen. It is easy to tell from **Figure 4D** that the onset is not aligned with epoch 0. Using the newly determined onset the estimated arrival time is shifted accordingly.

The effect of this last response correction is evident when comparing **Figures 5B,C**. The onset is no longer observed as a gradual increase prior to epoch 0. The 90% confidence interval after onset has however become broader which makes sense given the varying rise time between events.

4 RESULTS

This section presents the results of the study. The first part will focus on the list of events while the second part will showcase a superposed epoch analysis of the low and high latitude geomagnetic response to rapid increases in P_d as observed in various indices.

4.1 Event List

The event detection algorithm described in **Section 3** was applied to the *Pd* series in a sliding window fashion evaluating all data points as potential events. The resulting event list contains 3,867 rapid increases in P_d between the year 1994 and 2019. A detailed description of the method used to make the list is given in **Section 3**. It is important to reiterate that the focus of this study is rapid increases in P_d regardless of origin.

Classifications by the event detection algorithm are made entirely based on P_d measurements. It is therefore interesting to see how the events in the list are characterized with respect to other solar wind parameters and thus how they distinguish themselves from other space weather phenomena. A summary of various solar wind parameters, before and after onset, is given in **Figure 6**. The statistics in **Figures 6B–F** were calculated from two 12-min windows offset 3 min to either side of the P_d onset. The median is shown for most variables. The exceptions are

downstream P_d, the solar wind velocity and number density, for which the maximum is shown.

The number of detected events per year is shown in **Figure 6A** along with the monthly sunspot number downloaded from SILSO World Data center at http://www.sidc.be/silso/. The ratio between events detected at solar max (cycle 23) and solar min (between cycle 23 and 24) for our list is ~2.2 while it is ~5.5 for the IS list in Oliveira and Raeder (2015). Our events are determined solely on P_d and don't necessarily uphold the Rankine-Hugoniot jump conditions. Dalin et al. (2002a) found the occurrence rate of pressure increases that are not shocks to be independent of the solar cycle. The difference in solar cycle dependence between the two lists is therefore consistent with our list containing non-shock events.

Figure 6B shows the IMF clock angle given as

$$\theta_c = \arctan2\,(B_Y, B_Z) \tag{2}$$

where B_Y and B_Z are the IMF components in the Y and Z (GSM) direction. The angle is thus 0° for purely northward IMF

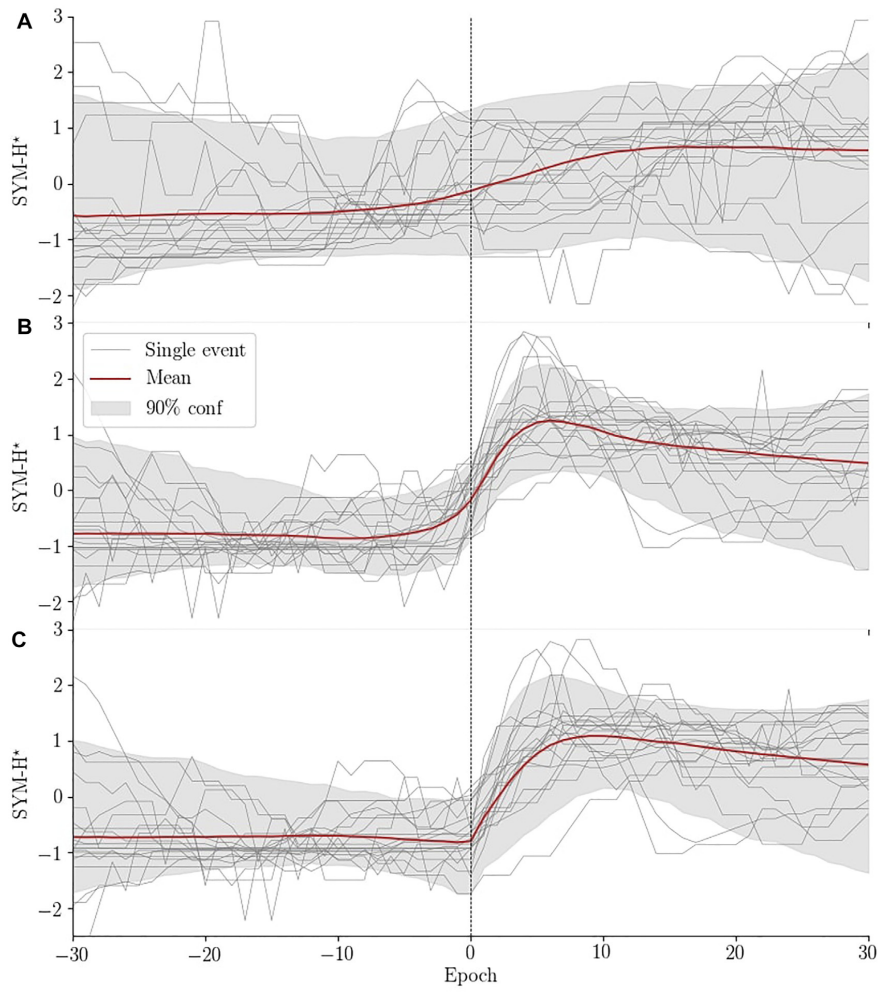

FIGURE 5 | Comparison of normalized superposed SYM-H before any arrival time correction **(A)**, after correlation analysis **(B)** and after aligning the onset of the SYM-H response **(C)**. The shaded area illustrates the 90% confidence interval, the grey lines are 20 randomly selected events and the red lines are the mean of the distribution. Each event has been normalized, indicated by the asterisk in the axis label, in order to improve comparison between events.

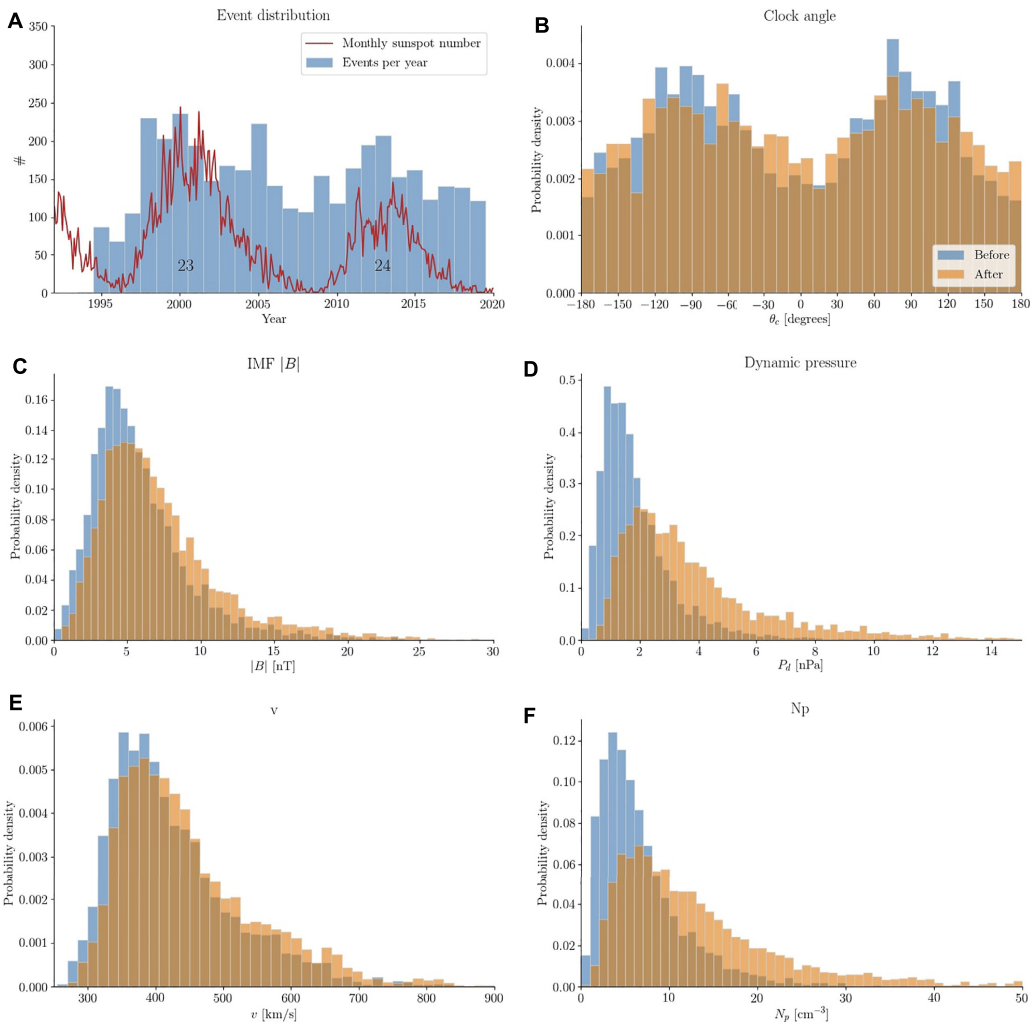

FIGURE 6 | Summary of statistics related to the event list. **(A)** shows the number of events detected for individual years along with the monthly sunspot number. **(B–F)** show statistics of the upstream (orange) and downstream (blue) IMF clock angle, IMF magnitude, solar wind dynamic pressure, solar wind bulk velocity and ion number density.

and ±180° for purely southward IMF. The distribution is bimodal illustrating a statistically dominant B_Y component. The distribution after onset has slightly broadened. It is tempting to suggest from this figure that θ_c for individual events is similar before and after onset, but that is far from the case. Only 40% (61%) of events stay within ±22.5 (±45) degrees of the pre-onset clock angle.

The IMF magnitude, **Figure 6C**, has a mode around 4nT prior to onset which increases to 5 nT afterwards. Similarly, the mode of the P_d distribution, **Figure 6D**, changes from 1.1 to 2 nPa while the spread also is significantly increased as shown by the heavy tail. Note that the distribution shown in the figure is truncated at 15 nPa leaving 98 events outside. **Figures 6E,F** are distributions of solar wind bulk velocity and ion number density. Their modes are 365 km/s and 3.5 cm^{-3} before onset, and 380 kms/s and 6 cm^{-3} after. It is evident that the P_d increases are generally caused by rapid changes in solar wind ion number density consistent with Dalin et al. (2002a) who found their events to

be either slow shocks or rotational discontinuities. Khabarova and Zastenker (2011) confirms that rapid increases in P_d are often caused by abrupt changes in ion number density. They likewise found that these types of event are not associated with coronal mass ejections, stream interaction regions and ISs, but are highly correlated with crossings of the heliospheric current sheet. It has later been shown that bends and kinks in the heliospheric current sheet can result in small magnetic islands that are related to ULF-variations in ion number density and IMF (Khabarova et al., 2021).

There are differences between our list and previously published IS lists. Oliveira and Samsonov (2018) have reviewed ISs and their characteristics (e.g., orientation, shock speed). Studies of ISs often investigate the importance of orientation as frontal impacts tend to be more geoeffective than those with a high inclination (Takeuchi et al., 2002; Oliveira et al., 2015; Oliveira and Raeder, 2015; Selvakumaran et al., 2016). The angle between the shock normal and Sun-Earth line can be determined as

$$\theta_{X_n} = cos^{-1}(n_x) \tag{3}$$

where n_x is the component along the Sun-Earth line of the shock normal. Here $\theta_{X_n} = 180$ and 90 is parallel and perpendicular to the Sun-Earth line, respectively. Calculating θ_{X_n} requires an estimate of the shock normal which can be determined as described by Schwartz (1998) if the assumption of coplanarity holds. This is based on the Rankine-Hugoniot jump conditions and assumes that the normal to the shock plane and magnetic field on either side of the shock lie in the same plane. The convention is to point the shock normal into the unshocked medium, commonly making n_x negative. **Figure 7** compares the distributions of estimates of θ_{X_n} between our event list (blue) and that of Oliveira and Raeder (2015) (orange). The orange distribution has a mean of ~145 and is skewed towards more frontal angles. The blue distribution illustrates the result when the assumption of coplanarity does not hold for a majority of the events and should not be considered credible. The shock normal often has its dominating component in the Y or Z direction (GSM) leading to an estimated orientation parallel to the Sun-Earth line. Estimates of orientation for rapid P_d increases that are not IS are best achieved using timing analysis with multiple spacecrafts. Such analyses were carried out by Richardson and Paularena (1998); Dalin et al. (2002b); Riazantseva et al. (2003). They found that solar wind plasma structures tend to be oriented with an angle between frontal and the Parker spiral and are thus slightly skewed towards dusk.

Figure 7 underlines that the majority of events in our list are not IS and thus comparisons to IS studies should be done with caution. We do not attempt to distinguish between events that are IS and events that are not, although a comparison of the effectiveness between shocks and non-shocks would be interesting.

4.2 Superposed Epoch Analysis

Our motivation for creating the event list is to provide the necessary data for a statistical analysis of the geospace response to rapid increases in P_d. In the following we showcase how the event list can be used in a superposed epoch analysis of the response for different angles of IMF clock angle and dipole tilt. Dipole tilt, θ_d, will also be referred to as season and is positive when the dipole axis points towards the Sun in the northern hemisphere.

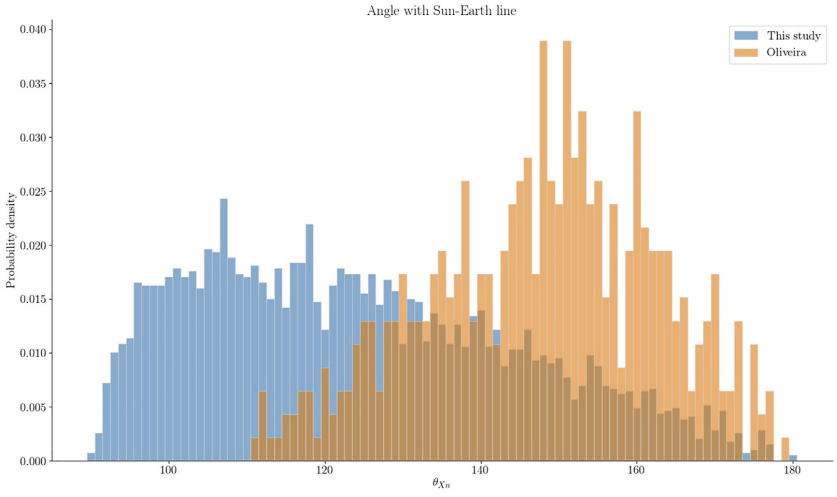

FIGURE 7 | Comparison of θ_{X_n} estimates between the events found in this study (blue) and those presented in Oliveira and Raeder (2015) (orange) under the assumption of coplanarity (Schwartz, 1998). A shock is aligned with the Sun-Earth line if $\theta_{X_n} = 180°$ and perpendicular when $\theta_{X_n} = 90°$. The assumption of coplanarity does not hold for a majority of the events in this study and the estimates (blue) should not be considered credible.

4.2.1 Event Groups

The effect of θ_c and θ_d can be studied by separating the event list into groups. From **Figure 6B** it is evident that the IMF is more prone to be oriented east/west than north/south and we therefore use slightly uneven angular ranges to achieve an approximately equal amount of events in each group. Additionally, the clock angle can change drastically from before ($\theta_{c,b}$) to after ($\theta_{c,a}$) onset. This can make the interpretation of the effect of the rapid pressure increase difficult as it has to be separated from the effect of changing IMF orientation. For this reason we impose constraints on either side of the onset.

All 3,867 events can be represented in a 3D space, **Q**, spanned by θ_d, $\theta_{c,b}$ and $\theta_{c,a}$. The following criteria were imposed to group the events by dipole tilt and IMF orientation:

$$\begin{aligned}
&\text{Summer} : \mathbf{Q} \cap (\ 13° < \theta_d\ ) \\
&\text{Equinox} : \mathbf{Q} \cap (\ -13° < \theta_d < 13°\ ) \\
&\text{Winter} \ : \mathbf{Q} \cap (\ \theta_d < -13°\ ) \\
&\mathrm{B}_Z+ \ : \mathbf{Q} \cap (\ -55° < \theta_{c,a} < 55°\ ) \cap (\ -55° < \theta_{c,b} < 55°\ ) \\
&\mathrm{B}_Y+ \ : \mathbf{Q} \cap (\ 55° < \theta_{c,a} < 125°\ ) \cap (\ 55° < \theta_{c,b} < 125°\ ) \\
&\mathrm{B}_Z- \ : \mathbf{Q} \cap (\ 125° < \theta_{c,a} < -125°\ ) \cap (\ 125° < \theta_{c,b} < -125°\ ) \\
&\mathrm{B}_Y- \ : \mathbf{Q} \cap (\ -125° < \theta_{c,a} < -55°\ ) \cap (\ -125° < \theta_{c,b} < -55°\ )
\end{aligned} \tag{4}$$

Table 1 summarizes the number of events in the different groups. Only 2058 events were used in the analysis due to the criterion on both $\theta_{c,a}$ and $\theta_{c,b}$, **Eq. 4**.

The clock angle distributions of these 2058 events are shown in **Figure 8**. Here the grey and colored bars illustrate the distributions prior to and after onset, respectively, and each grey circle signifies 10 events. Comparing the occurrence rate of $\mathrm{B}_Y\pm$ events show a higher rate of B_Y+ events during summer than during winter.

4.2.2 Low Latitude Geomagnetic Response

The general expectation of the low/mid latitude geomagnetic response to a rapid increase in P_d is a positive step-like perturbation of the horizontal magnetic field. To the first order this can be thought of as uniform and caused by compression of the magnetosphere. Magnetic indices such as SYM-H describe this well. However, the response is a superposition of multiple magnetospheric sources where the primary contributors are the magnetopause and ring current. The ring current is known to be asymmetric (Walsh et al., 2014; Ganushkina et al., 2015; Lühr et al., 2017) and responds near instantaneously to rapid increases in P_d (Shi et al., 2005). It is therefore no surprise that the low latitude magnetic perturbation would be local time dependent.

TABLE 1 | Summary of the amount of event in each group after imposing the criteria in **Eq. 4**.

	Summer	Equinox	Winter	Sum
B_Z+	175	251	125	551
B_Y+	181	209	114	504
B_Z-	181	207	125	513
B_Y-	145	229	116	490
Sum	682	896	480	2058

Using numerous magnetometer stations between ±50° latitude (Newell and Gjerloev, 2012) produced a local time ring current index called SMR that is provided for midnight, dawn, noon and dusk. **Figure 9** summarizes the results of a superposed epoch analysis of SMR with respect to the groups defined in **Section 4.2.1**. The results are generated by scaling the SMR time series for each event by $\Delta\sqrt{P_d}$ and subtracting a baseline value before onset. The ensemble of these time series constitutes a distribution at all epochs from which the mean is determined. The blue/orange/green/red lines are the mean for the SMR index at midnight/dawn/noon/dusk. The black line is the mean of the global SMR index while the dashed black lines are its 25% and 75% percentiles, respectively.

4.2.2.1 Dawn-Dusk Asymmetries

It is clear that the response depends on local time. The initial peak at dawn is consistently lower than in any other sector. Two of the main contributors to ring current indices are the magnetopause and ring current (Haaland and Gjerloev, 2013) and according to Araki (1977) the main contribution to DL is the magnetopause current. The magnetopause current generates a positive perturbation while the ring current generates a negative. Assuming the magnetopause current's contribution to be symmetric with respect to local time, the asymmetry originates from the ring current. Under this assumption the dawnside ring current must generate a stronger magnetic perturbation compared to any other sector.

Several studies report that the ring current is strongest at dusk (Newell and Gjerloev, 2012; Walsh et al., 2014; Ganushkina et al., 2015; Lühr et al., 2017). Studies on ring current asymmetry tend to investigate the effect during the main/recovery phase of geomagnetic storms. In that scenario the asymmetric ring current is caused by an intensification of the partial ring current. However what we are interested in is the initial response, the sudden commencement, which occurs before the main phase of the geomagnetic storm and evolves on a timescale of minutes while the storm evolves on a timescale of hours and days.

Ring current asymmetry is highly dependent on the geomagnetic disturbance level (Le et al., 2004). The majority of events used in this study (81%) experience SYM-H above −30 nT before onset, which is considered quiet. It is therefore interesting that Zhang et al. (2011) found higher current density on the dawn side when investigating the local time distribution of the ring current using Cluster.

Following the argumentation presented by Shi et al. (2005) an azimuthal electric field is induced (Faraday's law) as a result of magnetospheric compression when the solar wind pressure enhancement impinges on the magnetosphere. This causes a near instantaneous adiabatic energization of ring current particles. Under the assumption that the ring current is strongest at dawn during geomagnetic quiet times, a rapid increase in P_d results in a larger negative perturbation at dawn and therefore accounts for the consistently weaker response observed in **Figure 9**. However, one must keep in mind that there are other sources of perturbation. A more thorough analysis that includes contributions from field aligned currents has to be made.

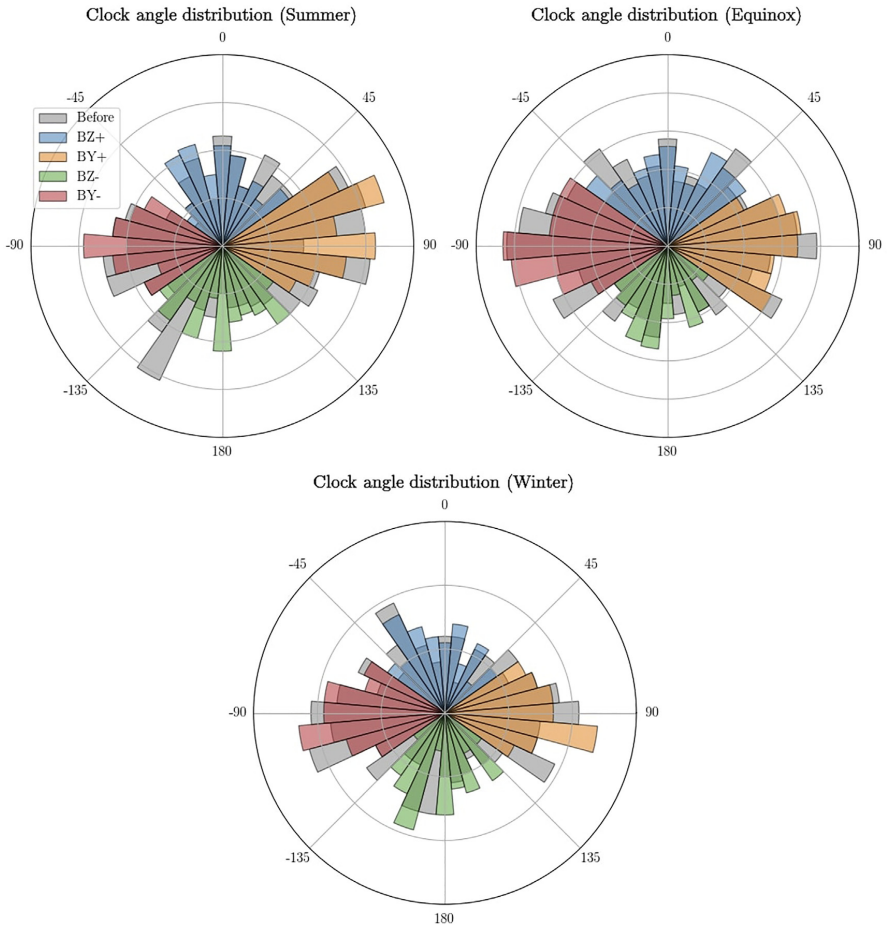

FIGURE 8 | Polar histograms of the IMF clock angle distribution in each of the 12 groups. The grey bars indicate the distribution before the increase in P_d while the colored bars indicate the distribution after. Each circle represents 10 events.

4.2.2.2 Decay

The trend following the initial step-like increase exhibits different behavior with respect to local time and clock angle. In all scenarios the trend at dawn is slightly positive or constant while the opposite is true for all local time sectors. During northward IMF all local time sectors appear to converge towards symmetry. However, during southward IMF the decay at noon/dusk/midnight is much more rapid resulting in the perturbation to reduce below the baseline prior to onset. This is in agreement with the higher probability of geomagnetic storms occurring during southward IMF. The ring current asymmetry remains strong, but has changed from being dominating at dawn to dominating at dusk.

4.2.2.3 Noon-Midnight Differences

We see a noon-midnight asymmetry during southward IMF as the response in SMR-00 tends to be stronger than SMR-12 (and the other sectors). A similar result was found in case studies by Lee and Lyons (2004). They observed dipolarization of the geomagnetic field at geosynchronous orbit consistent with a reduction of the cross-tail current which will result in a positive perturbation of the horizontal magnetic field. This effect was not found for events during northward IMF. It is likely a result of acceleration of already Earthward moving plasma in the tail as part of the Dungey cycle. Boudouridis et al. (2004) found that compression of the magnetosphere enhances reconnection in the tail and increases magnetospheric convection.

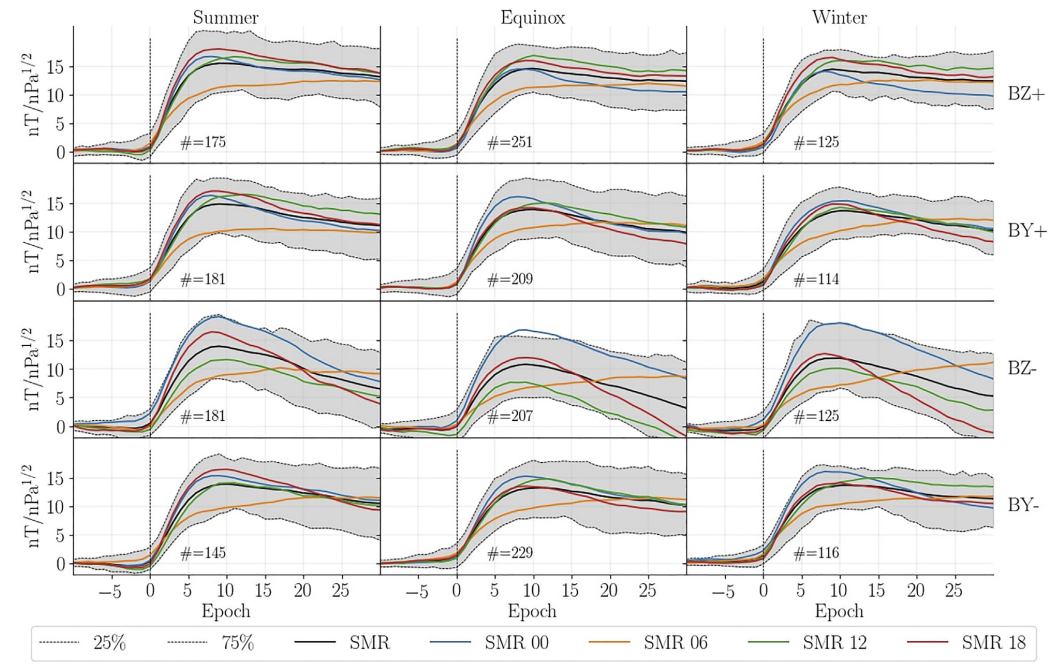

FIGURE 9 | Superposed epoch analysis of the low/mid latitude response to rapid increases in P_d using the SMR index. The solid lines indicate the mean of SMR and its local time components. The dashed grey lines indicate the 25 and 75% percentile. The SMR time series for each event has been scaled with respect to the increase in $\sqrt{P_d}$ and a baseline prior to onset subtracted. The number in each window indicates the number of events in each group.

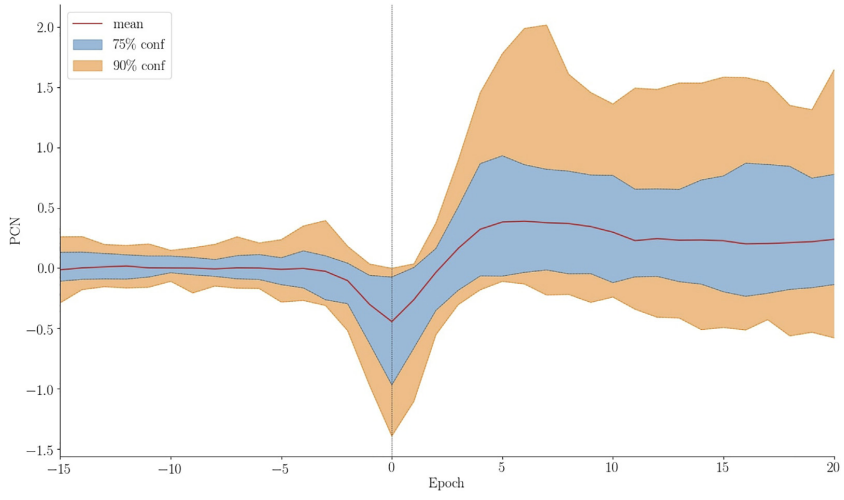

FIGURE 10 | Superposed epoch analysis of the high latitude response to rapid increases in P_d during Northward IMF and negative dipole tilt using the PCN index. The analysis is based on 90 events each of which were aligned with respect to the peak of the PI and shifted to a common baseline to improve comparison. The red line shows the mean and the blue and orange shade indicates the 75 and 90% confidence interval.

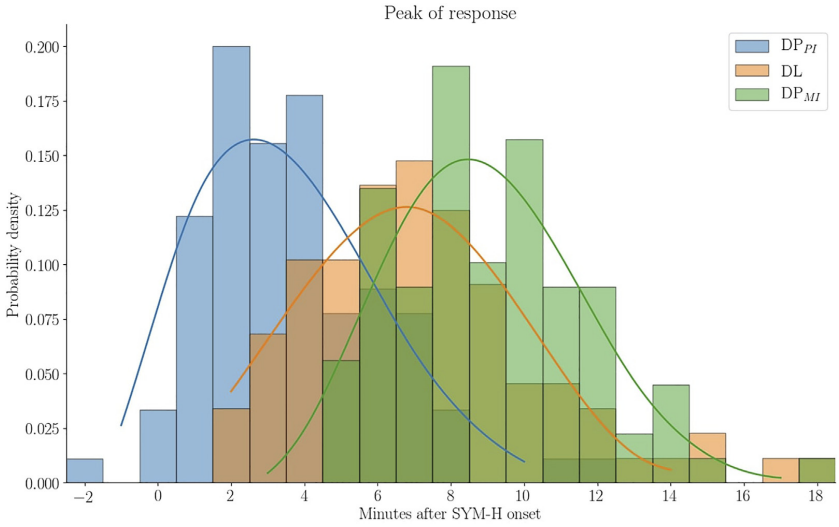

FIGURE 11 | Distribution of when the peak in DL (low latitude), DP_{PI} (high latitude preliminary impulse) and DP_{MI} (high latitude main impulse) occur relative to onset in SYM-H (epoch 0) for northward IMF during negative dipole tilt. Cubic splines are fitted and superposed to help distinguish the distributions in areas of overlap.

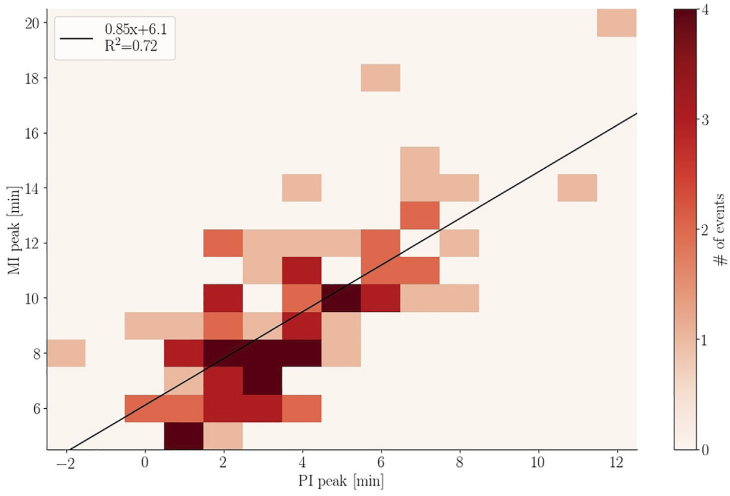

FIGURE 12 | Regression analysis of the DP_{PI} and DP_{MI} distribution in **Figure 11**.

4.2.3 High Latitude Response

The high latitude transient response following a rapid increase in P_d, earlier mentioned as DP, is caused by two sets of anti-sunward moving convection vortices, referred to as PI and MI (Araki, 1994). In previous studies a connection between PI/MI and the PC index were made (Lukianova, 2003; Huang, 2005; Stauning and Troshichev, 2008). PC indicates the antisunward convection in the polar cap by trying to quantify transpolar currents. All studies found that the PI and MI resulted in a negative and positive excursion of the PC index, respectively. Huang (2005) also found the magnitude of variation in PC caused by changes in IMF and substorms to be much greater

than that of the pressure enhancement. For this reason we limit ourselves to the group for northward IMF during winter, which is when the background convection is weakest. We manually determine the peak of PI and MI by inspecting the PCN time series for each event. Events with noisy time series or that were otherwise difficult to interpret were discarded, leaving 90 events.

Figure 10 is a superposed epoch analysis of the PCN when realigning the time series with the PI peak. For better comparison a baseline value prior to epoch 0 has been removed. We find that the average PI amplitude is 0.44 mV/m. If alignment is done with the MI peak its average is found to be 0.50 mV/m. This is lower than results from Huang (2005), but in agreement with results by Stauning and Troshichev (2008). The average value of the MI peak cannot be read directly from **Figure 10** as the PI alignment does not ensure alignment of MI.

Figure 11 shows the time of the peak of each response relative to the onset in SYM-H. The superposed lines are spline fits to help visualize the overlapping distributions. We find that the PI peaks around 2–3 min after onset while the low latitude response takes 6–7 min and the MI peak occur around 8–10 min after onset.

A regression analysis is performed between each of the distributions in **Figure 11**. The analysis between PI and MI, **Figure 12**, shows a strong relationship (R^2 = 0.72) between when the two responses peak. From the intercept we see that the average time between the PI and MI peak is ~6 min. The analysis between DL and PI/MI indicates a low level of correlation between low and high latitude response with R^2 = 0.29 and 0.32.

5 DISCUSSION

Event detection is highly relevant in space weather research. Certain events (e.g., coronal mass ejection, solar flare, stream interaction region etc.) can have a large impact on satellites and the electrical infrastructure on ground. Event detection and forecasting is the first step in handling a potential problem such that precautionary measures can be taken. Machine learning is used frequently as a means to find connections not immediately obvious as well as to remove human bias. A review of its role in space weather was given by Camporeale (2019).

The event detection approach used in this paper was designed to be as objective as possible. Nevertheless, we used a supervised algorithm meaning it is "taught" what is and is not an event. These definitions are based on the training data which is to some extent subjective. One could take an unsupervised approach in which the training data does not include a list of the varies classes and the algorithm will have to define them itself. However, this is far more complex: More data would be required as the algorithm needs to discover classes autonomously. Including variables other than P_d would introduce more difficulty as rapid pressure increases might be split into multiple subclasses. Borovsky et al. (2019) used the unsupervised algorithm self organizing maps to analyze 10 years of ACE data leading to four classes of solar wind instead of the general two; slow and fast solar wind. One of these classes was ejecta which is related to coronal mass ejections and thereby rapid P_d increases. In the future the majority of classification might be done in a similar fashion, but for the task at hand it is a much too complex tool and the supervised approach seems to be a fair middle ground.

The *non-event* class contain everything that are not pressure increases. It is therefore likely that the 1700 entries do not account for all scenarios the algorithm will encounter and the outcome will therefore be unpredictable. This is one of the drawbacks when having to create training data. We tried to combat this potential problem by only accepting classifications of type *event* if 90% of the decision trees agreed.

Features in the training data were selected based on a comparison of numerous potential features and boiled down to the five presented here. The optimal features should be robust such that they do not depend heavily on single data-points or one risks discarding events unnecessarily. Our first feature, the slope, depends on 3 data-points and carries a lot of weight. An alternative to this could be to fit a logistic function as done by Boudouridis and Zesta (2021). The slope could be extracted from the fit and would therefore depend on a larger range of data and making it more robust when facing missing data.

The correlation analysis is a crucial part of creating the list of events as it ensures a measurable response on ground. However, when comparing two (or more) events it is important that they are aligned correctly in time; otherwise the statistics extracted when superposing multiple events will exhibit higher variance than necessary. The question is, what is the reference point that should be used for alignment? The rise time of the SYM-H response is around 2–10 min (Takeuchi et al., 2002). The exact number depends on the solar wind velocity since it dictates how much time is required for the discontinuity to pass Earth relative to the time of impact. The orientation of the discontinuity is another large factor in the variation of rise time. One extreme case with a 30 min rise time is analyzed in Takeuchi et al. (2002). We decided on using the onset of the SYM-H response as reference. Unfortunately, the precision of the correlation analysis also suffers from the variation in SYM-H rise times.

In the initial step of the superposed epoch analysis 12, groups were created based on dipole tilt and IMF clock angle, see **Section 4.2.1**. Unsurprisingly, there are more events around equinox than summer/winter as the dipole tilt range is larger. It is however curious that the occurrence rate is larger during summer compared to winter. The average ratio between summer and winter is ~1.4.

The reason for this asymmetry is still not clear, but we have ruled out two possible mechanisms: 1) Huang and Yumoto (2006) studied hemispheric asymmetry during rapid P_d increases and found a significant variation between hemispheres when comparing magnetic perturbation at low latitudes. They concluded that the perturbation is stronger in the summer hemisphere than in the winter hemisphere. Coincidentally, SYM-H is based on six stations where the majority are located in the northern hemisphere. However, the higher occurrence rate during positive dipole tilt is present prior to the correlation

analysis. It is also present when evaluating ACE and Wind data separately. When evaluating the individual years the ratio between summer and winter sometimes go below 1, but on average is ~1.3. We therefore find it unlikely that it is caused by data gaps. 2) Due to the eccentricity of Earth's orbit there will be a few percent more data with positive dipole tilt. Calculating the occurrence probability by normalizing the occurrence rate with the amount of data available does change the seasonal difference slightly, but not enough to be eliminated. One might suspect that it is related to solar cycles, but it is present when evaluating data from solar cycle 23 and 24 individually. We suspected it might be related to heliographic latitude. When repeating the analysis using latitude (heliographic inertial coordinates) we found a smaller difference between seasons. It was no surprise as the min/max in the latitude of Earth's orbit does not overlap with the extremes in dipole tilt (summer/winter). The cause of this seasonal difference is still not clear, but we are satisfied that it is unrelated to the method with which the events were detected and propagated to Earth.

In the superposed epoch analysis we observed a dawn-dusk asymmetry in the low latitude response. Contrary to our expectation the weakest positive perturbation was observed at dawn. Under the assumption of a uniform positive perturbation from the magnetopause current the asymmetry was caused by currents in the inner magnetosphere. Plasma in the ring current is energized instantaneously by magnetospheric compression (Shi et al., 2005). In this scenario the dawn-dusk asymmetry could be caused by a pre-existing asymmetry in the ring current plasma population. Using Cluster measurement between 4–4.5 Earth radii, Zhang et al. (2011) found significantly stronger current densities on the dawn side during quiet conditions (Dst>-30 nT) which corresponds to the pre-onset conditions for 81% of our events. It is important to keep in mind that the result came from using the SMR index. It is therefore relevant to discuss the different sources that contribute to the index. The ground magnetometers used span ±50° latitude. According to Haaland and Gjerloev (2013) the ring, magnetopause, and tail currents all contribute to the SMR index. However, Kikuchi et al. (2001) found contributions by field aligned currents and ionospheric currents at low/mid latitudes with a local time dependence. Reality is rarely as simple as the assumption we make, and a more thorough analysis of the constituents of the SMR index is therefore needed such that we can understand the origin of the observed dawn-dusk asymmetry.

6 CONCLUSION

Rapid increases in solar wind dynamic pressure result in the transient magnetospheric-ionosperic phenomena called sudden commencement, which is sometimes followed by a geomagnetic storm. In this study we develop a new method for automatic detection of these events in solar wind data. The events are propagated to Earth and paired with a corresponding response in ground magnetometers. We also use the list to conduct a superposed epoch analysis of the geomagnetic response to solar wind pressure increases. The main results are:

1. A list of 3,867 rapid pressure increases detected by ACE and Wind, between 1994–2019, including estimates of their arrival at Earth. The event list can be accessed at doi.org/10.5281/zenodo.6243103.
2. There is a clear dawn-dusk asymmetry in SMR following a compression of the magnetosphere for all seasons and IMF orientations. We suggest that an asymmetric ring current (stronger at dawn) results in weaker positive magnetic perturbation at dawn. This asymmetry is very short lived. Little asymmetry is observed after 30 min during northward IMF. During southward IMF the asymmetry changes from dawn to dusk within 30 min of the initial response in SYM-H.
3. A noon-midnight asymmetry is observed in the low latitude response for southward IMF. We believe it to be caused by dipolarization of the geomagnetic field as observed at geosynchonous orbit by Lee and Lyons (2004).
4. The geomagnetic response does not appear to have any significant dependence on IMF B_Y and dipole tilt and thus the main dependency is on IMF BZ.
5. The superposed epoch analysis of the PCN index for northward IMF during winter shows the average preliminary impulse (PI) causes a negative excursion of 0.44 mV/m from the baseline while the average main impulse (MI) causes a positive excursion of 0.50 mV/m from the baseline. The rise time of the low latitude response is approximately 7 min while the average PI (MI) peak occurs around 2 (8) min after the onset at low latitude. A regression analysis of the PI and MI response showed that their rise times are highly correlated, and that they differ by on average 6 min. A very low correlation between the low latitude response and PI/MI was found.

The purpose of creating this list was to provide the information for a statistical analysis. In the future we intend to conduct a more thorough analysis of the response by utilizing spherical harmonic modelling of the ground magnetic field perturbations. This would greatly increase the information extracted from the high latitude response compared to the PCN index analysis presented in this paper.

DATA AVAILABILITY STATEMENT

The datasets presented in this study can be found in online repositories. The names of the repository/repositories and accession number(s) can be found in the article/**Supplementary Material**.

AUTHOR CONTRIBUTIONS

MM is the primary author and developed the event detection algorithm and carried out the superposed epoch analysis. KML and JPR helped set up the overall structure of the manuscript. All co-authors contributed to the discussions and provided editorial

comment thus contributing to the article and approved the submitted version.

FUNDING

This work was funded by the Research Council of Norway (RCN) under contract 300844/F50. KML and JPR were also funded by the RCN under contract 223252/F50. KML and SMH were also funded by the Trond Mohn Foundation.

SUPPLEMENTARY MATERIAL

The Supplementary Material for this article can be found online at: https://www.frontiersin.org/articles/10.3389/fspas.2022.904620/full#supplementary-material

REFERENCES

Araki, T. (1994). A Physical Model of the Geomagnetic Sudden Commencement. *Geophys. Monogr. Ser.* 81, 183–200. doi:10.1029/GM081p0183

Araki, T. (1977). Global Structure of Geomagnetic Sudden Commencements. *Planet. Space Sci.* 25, 373–384. doi:10.1016/0032-0633(77)90053-8

Borovsky, J. E., Denton, M. H., and Smith, C. W. (2019). Some properties of the solar wind turbulence at 1 au statistically examined in the different types of solar wind plasma. *J. Geophys. Res. Space Phys.* 124, 2406–2424. doi:10.1029/2019JA026580

Boudouridis, A., and Zesta, E. (2021). Automated Technique for the Detection of Step-like Solar Wind Dynamic Pressure Changes: Application to the Response of the Transpolar Potential to Solar Wind Dynamic Pressure Fronts. *J. Geophys. Res. Space Phys.* 126, e2021JA029198. doi:10.1029/2021JA029198

Boudouridis, A., Zesta, E., Lyons, L. R., Anderson, P. C., and Lummerzheim, D. (2004). Magnetospheric Reconnection Driven by Solar Wind Pressure Fronts. *Ann. Geophys.* 22, 1367–1378. doi:10.5194/angeo-22-1367-2004

Burton, R. K., McPherron, R. L., and Russell, C. T. (1975). An Empirical Relationship between Interplanetary Conditions andDst. *J. Geophys. Res.* 80, 4204–4214. doi:10.1029/JA080i031p04204

Camporeale, E. (2019). The challenge of Machine Learning in Space Weather: Nowcasting and Forecasting. *Space Weather* 17, 1166–1207. doi:10.1029/2018SW002061

Curto, J. J., Araki, T., and Alberca, L. F. (2007). Evolution of the Concept of Sudden Storm Commencements and Their Operative Identification. *Earth Planet. Sp* 59, i–xii. doi:10.1186/BF03352059

Dalin, P. A., Zastenker, G. N., Paularena, K. I., and Richardson, J. D. (2002a). A Survey of Large, Rapid Solar Wind Dynamic Pressure Changes Observed by Interball-1 and Imp 8. *Ann. Geophys.* 20, 293–299. doi:10.5194/angeo-20-293-2002

Dalin, P. A., Zastenker, G. N., and Richardson, J. D. (2002b). Orientation of Middle-Scale Structures in the Solar Wind Plasma. *Cosmic Res.* 40, 319–323. doi:10.1023/a:1019838226629

Friis-Christensen, E., McHenry, M. A., Clauer, C. R., and Vennerstrøm, S. (1988). Ionospheric Traveling Convection Vortices Observed Near the Polar Cleft: A Triggered Response to Sudden Changes in the Solar Wind. *Geophys. Res. Lett.* 15, 253–256. doi:10.1029/GL015i003p00253

Ganushkina, N. Y., Liemohn, M. W., Dubyagin, S., Daglis, I. A., Dandouras, I., De Zeeuw, D. L., et al. (2015). Defining and Resolving Current Systems in Geospace. *Ann. Geophys.* 33, 1369–1402. doi:10.5194/angeo-33-1369-2015

Haaland, S., and Gjerloev, J. (2013). On the Relation between Asymmetries in the Ring Current and Magnetopause Current. *J. Geophys. Res. Space Phys.* 118, 7593–7604. doi:10.1002/2013JA019345

Hapgood, M. A. (1992). Space Physics Coordinate Transformations: A User Guide. *Planet. Space Sci.* 40, 711–717. doi:10.1016/0032-0633(92)90012-D

Huang, C.-S. (2005). Variations of Polar Cap index in Response to Solar Wind Changes and Magnetospheric Substorms. *J. Geophys. Res.* 110, 10616. doi:10.1029/2004JA010616

Huang, C.-S., and Yumoto, K. (2006). Quantification and Hemispheric Asymmetry of Low-Latitude Geomagnetic Disturbances Caused by Solar Wind Pressure Enhancements. *J. Geophys. Res.* 111, 11831. doi:10.1029/2006JA011831

Iyemori, T., Takeda, M., Nose, M., and Toh, H. (2010). "Mid-latitude Geomagnetic Indices Asy and Sym for 2009 (Provisional)," in *Internal Report of Data Analysis Center for Geomagnetism and Space Magnetism* (Japan: Kyoto University).

Jian, L., Russell, C. T., Luhmann, J. G., and Skoug, R. M. (2006). Properties of Stream Interactions at One AU during 1995 - 2004. *Sol. Phys.* 239, 337–392. doi:10.1007/s11207-006-0132-3

Khabarova, O., Malandraki, O., Malova, H., Kislov, R., Greco, A., Bruno, R., et al. (2021). Current Sheets, Plasmoids and Flux Ropes in the Heliosphere. *Space Sci. Rev.* 217. doi:10.1007/s11214-021-00814-x

Khabarova, O., and Zastenker, G. (2011). Sharp Changes of Solar Wind Ion Flux and Density within and outside Current Sheets. *Sol. Phys.* 270, 311–329. doi:10.1007/s11207-011-9719-4

Kikuchi, T., Tsunomura, S., Hashimoto, K., and Nozaki, K. (2001). Field-aligned Current Effects on Midlatitude Geomagnetic Sudden Commencements. *J. Geophys. Res.* 106, 15555–15565. doi:10.1029/2001JA900030

Kuhn, M., and Johnson, K. (2013). Remedies for Severe Class Imbalance. *Appl. Predictive Model.* 2013, 419–443. doi:10.1007/978-1-4614-6849-3_16

Le, G., Russell, C. T., and Takahashi, K. (2004). Morphology of the Ring Current Derived from Magnetic Field Observations. *Ann. Geophys.* 22, 1267–1295. doi:10.5194/angeo-22-1267-2004

Lee, D.-Y., and Lyons, L. R. (2004). Geosynchronous Magnetic Field Response to Solar Wind Dynamic Pressure Pulse. *J. Geophys. Res.* 109, 10076. doi:10.1029/2003JA010076

Lepping, R. P., Acūna, M. H., Burlaga, L. F., Farrell, W. M., Slavin, J. A., Schatten, K. H., et al. (1995). The Wind Magnetic Field Investigation. *Space Sci. Rev.* 71, 207–229. doi:10.1007/BF00751330

Lühr, H., Xiong, C., Olsen, N., and Le, G. (2017). Near-earth Magnetic Field Effects of Large-Scale Magnetospheric Currents. *Space Sci. Rev.* 206, 521–545. doi:10.1007/s11214-016-0267-y

Lukianova, R. (2003). Magnetospheric Response to Sudden Changes in Solar Wind Dynamic Pressure Inferred from Polar Cap index. *J. Geophys. Res.* 108. doi:10.1029/2002JA009790

Mailyan, B., Munteanu, C., and Haaland, S. (2008). What Is the Best Method to Calculate the Solar Wind Propagation Delay? *Ann. Geophys.* 26, 2383–2394. doi:10.5194/angeo-26-2383-2008

McComas, D. J., Bame, S. J., Barker, P., Feldman, W. C., Phillips, J. L., Riley, P., et al. (1998). Solar Wind Electron Proton Alpha Monitor (Swepam) for the Advanced Composition Explorer. *Space Sci. Rev.* 86, 563–612. doi:10.1007/978-94-011-4762-0_20

Newell, P. T., and Gjerloev, J. W. (2012). Supermag-based Partial Ring Current Indices. *J. Geophys. Res.* 117, a–n. doi:10.1029/2012JA017586

Ogilvie, K. W., Chornay, D. J., Fritzenreiter, R. J., Hunsaker, F., Keller, J., Lobell, J., et al. (1995). Swe, a Comprehensive Plasma Instrument for the Wind Spacecraft. *Space Sci. Rev.* 71, 55–77. doi:10.1007/BF00751326

Oliveira, D. M., and Raeder, J. (2015). Impact Angle Control of Interplanetary Shock Geoeffectiveness: A Statistical Study. *J. Geophys. Res. Space Phys.* 120, 4313–4323. doi:10.1002/2015JA021147

Oliveira, D. M., Raeder, J., Tsurutani, B. T., and Gjerloev, J. W. (2015). Effects of Interplanetary Shock Inclinations on Nightside Auroral Power Intensity. *Braz. J. Phys.* 46, 97–104. doi:10.1007/s13538-015-0389-9

Oliveira, D. M., and Samsonov, A. A. (2018). Geoeffectiveness of Interplanetary Shocks Controlled by Impact Angles: A Review. *Adv. Space Res.* 61, 1–44. doi:10.1016/j.asr.2017.10.006

Riazantseva, M. O., Dalin, P. A., Zastenker, G. N., and Richardson, J. (2003). Orientation of Sharp Fronts of the Solar Wind Plasma. *Cosmic Res.* 41, 382–391. doi:10.1023/a:1025061711391

Richardson, I. G., and Cane, H. V. (1995). Regions of Abnormally Low Proton Temperature in the Solar Wind (1965-1991) and Their Association with Ejecta. *J. Geophys. Res.* 100, 23397–23412. doi:10.1029/95JA02684

Richardson, J. D., and Paularena, K. I. (1998). The Orientation of Plasma Structure in the Solar Wind. *Geophys. Res. Lett.* 25, 2097–2100. doi:10.1029/98GL01520

Ridley, A. J. (2000). Estimations of the Uncertainty in Timing the Relationship between Magnetospheric and Solar Wind Processes. *J. Atmos. Solar-Terrestrial Phys.* 62, 757–771. doi:10.1016/S1364-6826(00)00057-2

Russell, C. T., Ginskey, M., and Petrinec, S. M. (1994b). Sudden Impulses at Low Latitude Stations: Steady State Response for Southward Interplanetary Magnetic Field. *J. Geophys. Res.* 99, 13403–13408. doi:10.1029/94JA00549

Russell, C. T., Ginskey, M., and Petrinec, S. M. (1994a). Sudden Impulses at Low-Latitude Stations: Steady State Response for Northward Interplanetary Magnetic Field. *J. Geophys. Res.* 99, 253–261. doi:10.1029/93JA02288

Russell, C. T., and Ginskey, M. (1995). Sudden Impulses at Subauroral Latitudes: Response for Northward Interplanetary Magnetic Field. *J. Geophys. Res.* 100, 23695–23702. doi:10.1029/95JA02495

Schwartz, E. (1998). Doriot Anthony Dwyer, Flute. *Am. Music* 16, 249–270. doi:10.2307/3052576

Selvakumaran, R., Veenadhari, B., Ebihara, Y., Kumar, S., and Prasad, D. S. V. V. D. (2017). The role of interplanetary shock orientation on sc/si rise time and geoeffectiveness. *Adv. Space Res.* 59, 1425–1434. doi:10.1016/j.asr.2016.12.010

Shi, Y., Zesta, E., Lyons, L. R., Boudouridis, A., Yumoto, K., and Kitamura, K. (2005). Effect of Solar Wind Pressure Enhancements on Storm Time Ring Current Asymmetry. *J. Geophys. Res.* 110, 11019. doi:10.1029/2005JA011019

Smith, C. W., L'Heureux, J., Ness, N. F., Acuña, M. H., Burlaga, L. F., and Scheifele, J. (1998). The Ace Magnetic fields experiment. *Space Sci. Rev.* 86, 613–632. doi:10.1023/A:1005092216668

Smith, E. J., and Wolfe, J. H. (1976). Observations of interaction regions and corotating shocks between one and five au: Pioneers 10 and 11. *Geophys. Res. Lett.* 3, 137–140. doi:10.1029/GL003i003p00137

Stauning, P., and Troshichev, O. A. (2008). Polar Cap Convection and Pc index during Sudden Changes in Solar Wind Dynamic Pressure. *J. Geophys. Res.* 113, a–n. doi:10.1029/2007JA012783

Takeuchi, T., Russell, C. T., and Araki, T. (2002). Effect of the Orientation of Interplanetary Shock on the Geomagnetic Sudden Commencement. *J. Geophys. Res.* 107, 6–1. doi:10.1029/2002JA009597

Tin Kam Ho, T. H. (1995). Random Decision Forests. *Proc. 3rd Int. Conf. Document Anal. Recognition* 1, 278–282. doi:10.1109/ICDAR.1995.598994

Walsh, A. P., Haaland, S., Forsyth, C., Keesee, A. M., Kissinger, J., Li, K., et al. (2014). Dawn-dusk Asymmetries in the Coupled Solar Wind-Magnetosphere-Ionosphere System: a Review. *Ann. Geophys.* 32, 705–737. doi:10.5194/angeo-32-705-2014

Weimer, D. R., Ober, D. M., Maynard, N. C., Collier, M. R., McComas, D. J., Ness, N. F., et al. (2003). Predicting Interplanetary Magnetic Field (Imf) Propagation Delay Times Using the Minimum Variance Technique. *J. Geophys. Res.* 108. doi:10.1029/2002JA009405

[Dataset] Willer, A. N. (2021). The Polar Cap North (PCN) index (Definitive) [Data Set]. *PCN index*. doi:10.11581/DTU:00000057

Zhang, Q.-H., Dunlop, M. W., Lockwood, M., Holme, R., Kamide, Y., Baumjohann, W., et al. (2011). The Distribution of the Ring Current: Cluster Observations. *Ann. Geophys.* 29, 1655–1662. doi:10.5194/angeo-29-1655-2011

Conflict of Interest: The authors declare that the research was conducted in the absence of any commercial or financial relationships that could be construed as a potential conflict of interest.

Publisher's Note: All claims expressed in this article are solely those of the authors and do not necessarily represent those of their affiliated organizations or those of the publisher, the editors, and the reviewers. Any product that may be evaluated in this article, or claim that may be made by its manufacturer, is not guaranteed or endorsed by the publisher.

Article II

6.2 Transient high latitude geomagnetic response to rapid increases in solar wind dynamic pressure

M. Madelaire, K.M. Laundal, J.P. Reistad, S.M. Hatch, A. Ohma

Fronteirsin in Astronomy and Space Sciences, Vol. 9, doi: 10.3389/fspas.2022.953954, 2022

frontiers | Frontiers in Astronomy and Space Sciences

TYPE Original Research
PUBLISHED 16 August 2022
DOI 10.3389/fspas.2022.953954

OPEN ACCESS

EDITED BY
Daniel Okoh,
National Space Research and Development Agency, Nigeria

REVIEWED BY
Vivian Otugo,
Rivers State University, Nigeria
Patrick Essien,
University of Cape Coast, Ghana

*CORRESPONDENCE
Michael Madelaire,
michael.madelaire@uib.no

SPECIALTY SECTION
This article was submitted to Space Physics, a section of the journal Frontiers in Astronomy and Space Sciences

RECEIVED 26 May 2022
ACCEPTED 05 July 2022
PUBLISHED 16 August 2022

CITATION
Madelaire M, Laundal KM, Reistad JP, Hatch SM and Ohma A (2022), Transient high latitude geomagnetic response to rapid increases in solar wind dynamic pressure.
Front. Astron. Space Sci. 9:953954.
doi: 10.3389/fspas.2022.953954

Transient high latitude geomagnetic response to rapid increases in solar wind dynamic pressure

Michael Madelaire*, Karl M. Laundal, Jone P. Reistad, Spencer M. Hatch and Anders Ohma

Birkeland Centre for Space Science, Bergen, Norway

Rapid changes in solar wind dynamic pressure can produce a transient geomagnetic response in the high latitude ionosphere. In this study we carry out a superposed epoch analysis of the geomagnetic response based on 2,058 events. The events are divided into 12 groups based on interplanetary magnetic field clock angle and dipole tilt and the magnetic perturbation field is modeled using spherical harmonics. We find that the high latitude transient current vortices associated with a sudden commencement are most clearly observed when the interplanetary magnetic field is northward during equinox and winter in the northern hemisphere. The high latitude geomagnetic response during northward interplanetary magnetic field is decomposed into a preliminary and main impulse. The preliminary impulse onset is 1–2 min prior to the onset of the low/mid latitude geomagnetic response and its rise time is 4–6 min. The main impulse onset is around 2 min after the low/mid latitude geomagnetic response and has a rise time of 6–11 min. When examining the change relative to pre-onset conditions a coherent transient geomagnetic response emerges for all IMF clock and dipole tilt angles. The current vortex associated with the main impulse on the dawnside appears at (9.3 ± 0.5 mlt, $64.8^{\circ} \pm 1.5^{\circ}$ mlat) and moves westward with a velocity of 5 ± 1.4 km/s. The vortex on the duskside appears at (15.3 ± 0.9 mlt, $65.8^{\circ} \pm 2.5^{\circ}$ mlat) and does not move significantly. In addition, the models were used to recreate the SMR index showing a significant mlt dependence on the magnetic perturbation above 40° mlat and below 10° mlat. The former is thought to be caused by high latitude ionospheric currents. The latter is potentially a combination of the event occurrence probability being skewed toward certain UT ranges for large dipole tilt angles and a UT dependence of the equatorial electrojet magnitude caused by the south atlantic magnetic anomaly.

KEYWORDS

solar wind dynamic pressure, rapid pressure increase, magnetospheric compression, sudden commencement, high latitude ionosphere, superposed epoch analysis, transient current vortex

1 Introduction

A (Storm) Sudden Commencement (SC) occurs when a rapid increase in solar wind dynamic pressure (P_d) impinges on our magnetosphere. These events are interesting as they allow us to observe a perturbation of the system and the subsequent transient response that unfolds in the following 10 s of minutes. In this study we focus on the geomagnetic response as observed from ground magnetometers and define SC as independent of whether or not it is followed by a geomagnetic storm as suggested by Curto et al. (2007).

SCs were initially thought to be associated with flux transfer events, but their connection to rapid changes in P_d was later shown in two case studies (Friis-Christensen et al., 1988; Glassmeier et al., 1989). In each study ground magnetometers were used to infer the ionospheric equivalent current which revealed transient current vortices.

A few years later Sibeck (1990), Kivelson and Southwood (1991) and Glassmeier and Heppner (1992) published theories on a mechanism that generates transient ionospheric current vortices. They all suggested that a shear flow close to the magnetopause or low-latitude boundary layer would give rise to Field Aligned Currents (FACs) that map to the ionosphere. However, they disagreed on the expected response. Sibeck (1990) and Kivelson and Southwood (1991) argue that the arrival of the solar wind pressure structure will launch a compression wave in the magnetosphere. This wave is faster than the solar wind in the magnetosheath and results in an expansion followed by a contraction of the magnetopause and thus two sets of twin vortices are created. Glassmeier and Heppner (1992) argues that a pressure pulse will create two sets of twin vortices while a single pressure increase/decrease will only result in a single set of twin vortices. Alternatively, it was suggested by Araki (1994), building on Tamao (1964), that the compression wave undergoes a mode conversion to a transverse mode inside the magnetosphere where gradients in Alfvenic speeds are large. Beside the theory of the underlying mechanism Araki (1994) presented a model of the expected response, D_{sc}, which was decomposed into two parts.

$$D_{sc} = DL + DP \tag{1}$$

DL refers to a step-like increase in the horizontal magnetic field component at low/mid latitudes due to an increased magnetopause current. DP refers to the ionospheric response dominant at high latitudes and is itself composed of two parts.

$$DP = DP_{PI} + DP_{MI} \tag{2}$$

The preliminary impulse PI and main impulse MI both refer to two sets of twin transient high latitude ionospheric current vortices generated during the SC (Araki, 1994). The PI is the first set of current vortices that are generated on the dayside i.e. one at pre-noon and another at post-noon. The electric current in the pre-noon vortex flows anti-clockwise while the current in the post-noon vortex is clockwise, i.e., similar to the NBZ current vortices generated during northward IMF due to lobe reconnection (Cowley and Lockwood, 1992). The MI is the second set of vortices, also generated at pre- and post-noon, however, the current flows opposite to that of the PI vortices, i.e., similar to that of the region 1/region 2 (R1/R2) current vortices (Cowley and Lockwood, 1992).

Our goal is to determine the influence of environmental parameters, such as Interplanetary Magnetic Field (IMF) clock angle and dipole tilt, on the development of the high latitude geomagnetic response to rapid increases in P_d. Due to the lack of data (events) in previous studies it has not been possible to carry out statistical studies on more than one environmental parameter without compromising the statistical integrity.

Many case studies of SCs have been conducted, e.g., Lam and Rodger (2001) tested the physical model presented by Araki (1994) against a single event. They found good correspondence between predictions and observations at high latitudes on the dayside while the predictions were less reliable at low latitudes and at night. Moretto et al. (2000) modeled the high latitude ionospheric response and resolved both growth and decay of current vortices, however, their propagation did not agree with Araki (1994), thus questioning the validity of the physical models with respect to real events. They noted that the shock normal was not parallel to the Sun-Earth line and might therefore result in an asymmetric geospace response which Araki (1994) did not take into account.

It is difficult to find instances where sensors are aligned optimally in the solar wind, magnetosheath, magnetosphere and on ground such that a full picture of the geospace response can be observed. Magnetohydrodynamic (MHD) simulations are therefore a very powerful tool as they provide a controlled environment where everything can be observed. Many studies have utilized MHD simulations in attempts to understand both the magnetospheric origin and the ionospheric response during rapid increases of P_d (Slinker et al., 1999; Keller et al., 2002; Fujita et al., 2003a,b, 2005; Ridley et al., 2006; Samsonov et al., 2010; Samsonov and Sibeck, 2013; Shi et al., 2014; Welling et al., 2021). These studies differ in several aspects. The MHD code used varies and in some cases the solar wind parameters uphold the Rankine-Hugoniot jump conditions and other times they do not. Some studies model common pressure changes while others model Carrington-like events. With these variabilities it is understandable that the resulting conclusions as to the magnetospheric origin also vary. Some studies agree with Araki (1994) that the magnetospheric vortices are generated inside the magnetosphere while others conclude that they are generated at the magnetopause. The studies conducted by Samsonov et al. (2010); Samsonov and Sibeck (2013) stand out as they do not agree with any of the preexisting theories. They suggest that the initial compression wave reflects on an inner boundary, probably the ionosphere, resulting in a sunward moving wave which by interacting with the anti-sunward flow creates a shear.

10.3389/fspas.2022.953954

Russell et al. (1994a,b) and Russell and Ginskey (1995) present statistical studies of the geomagnetic response at low/mid latitudes during northward and southward IMF conditions. They found the geomagnetic response to be 18.4 nT/nPa$^{1/2}$ during northward IMF while it is 13.8 nT/nPa$^{1/2}$ (25% less) during southward IMF. Stauning and Troshichev (2008), Huang (2005) and Madelaire et al. (2022) carried out statistical studies of the transient high latitude response using the PCN index (World Data Center For Geomagnetism, Copenhagen, 2019), i.e., the Northern Polar Cap and refers to an index based on a single ground magnetometer station (Thule) close to the northern magnetic pole that attempts to quantify anti-sunward plasma convection in the polar cap. They found that the DP_{PI} and DP_{MI} corresponds to a negative and positive excursion in the PCN index, respectively. Madelaire et al. (2022) showed that the DP_{PI} and DP_{MI} peaked around 3 and 9 min after onset of the DL response. In addition, Stauning and Troshichev (2008) created maps of the equivalent ionospheric current using ground magnetometers showing the creation and decay of ionospheric current vortices, however, no environmental parameters were taken into account.

In this paper we carry out a superposed epoch analysis of the transient high latitude geomagnetic response using the list of rapid pressure increases presented by Madelaire et al. (2022). In Section 2, we describe the list of events and ground magnetometer data utilized to carry out the analysis. In Section 3, we describe the modeling technique employed in our superposed epoch analysis as well as how equivalent ionospheric currents are retrieved. In Section 4, we discuss the modeled transient high latitude geomagnetic response. In Section 5, we discuss the high latitude impact on low/mid latitude geomagnetic perturbations and the differences between our results and the physical models. Section 6 concludes the paper.

2 Data

The statistical analysis presented here is based on a list of 3,867 rapid increases in P_d presented by Madelaire et al. (2022). The Earth arrival time of each event is based on a correlation analysis between P_d and the SYM-H index. The moment P_d and SYM-H begin to increase are both referred to as onset. The onset is the common reference point used to combine data from multiple events. The events are divided into 12 groups based on IMF clock angle and dipole tilt, and are identical to those defined by Madelaire et al. (2022). Dipole tilt, θ_d, is separated into three groups and IMF clock angle, θ_c, into four groups which when combined make 12 groups. Dipole tilt is positive when the northern hemisphere points toward the Sun and the three associated groups are referred to as season. Equation 3 summarize the criteria used,

$$\begin{array}{lcl}
\text{Summer} & : & (13^\circ < \theta_d) \\
\text{Equinox} & : & (-13^\circ < \theta_d < 13^\circ) \\
\text{Winter} & : & (\theta_d < -13^\circ) \\
B_Z+ & : & (-55^\circ < \theta_{c,a} < 55^\circ) \cap (-55^\circ < \theta_{c,b} < 55^\circ) \\
B_Y+ & : & (55^\circ < \theta_{c,a} < 125^\circ) \cap (55^\circ < \theta_{c,b} < 125^\circ) \\
B_Z- & : & (125^\circ < \theta_{c,a} < -125^\circ) \cap (125^\circ < \theta_{c,b} < -125^\circ) \\
B_Y- & : & (-125^\circ < \theta_{c,a} < -55^\circ) \cap (-125^\circ < \theta_{c,b} < -55^\circ),
\end{array} \tag{3}$$

where $\theta_{c,b}$ and $\theta_{c,a}$ refer to the IMF clock angle before and after the rapid increase in P_d. After imposing these event selection criteria the list of events is reduced to 2058. Supplementary Table S1 in the supplementary materials summarizes the number of events in each group.

The focus of our analysis is the ground magnetic perturbation associated with the identified events. Superposing multiple events allows for global coverage of the geomagnetic response. Measurements of the magnetic perturbation field are provided by the SuperMAG web service (https://supermag.jhuapl.edu/). It is given in a local magnetic coordinate system, assumed to be aligned with the Earth's main field, with a 1-min temporal resolution (Gjerloev, 2012). We further processed the data by rotating it into geocentric coordinates using the CHAOS-7.2 model (Finlay et al., 2020) and then into Quasi-Dipole (QD) coordinates. The QD reference frame is height dependent and maps along field lines; it is therefore useful when studying phenomena at a specific height such as ionospheric currents (Laundal and Richmond, 2017). Only data from the northern hemisphere is used in this study as data coverage in the southern hemisphere is sparse, especially at high latitudes.

3 Methods

The main purpose of the list of rapid P_d increases published in Madelaire et al. (2022) was to facilitate a superposed epoch analysis of SCs. Madelaire et al. (2022) presented such an analysis based on geomagnetic indices, which is difficult at high latitude since the complexity of the polar ionospheric current can hardly be summarized in a single index. In this study we aim to represent ground magnetometer data in terms of a spherical harmonic (SH) expansion and then calculate the equivalent horizontal currents and FACs. This section will provide a summary of SHs, how the inverse problem is solved and finally how equivalent currents are calculated.

3.1 Spherical harmonics

If the divergence and curl of a vector field are zero it can be fully described by a scalar potential field which will satisfy Laplace's equation. It can be argued that this is true for the magnetic field measured on ground. A rigorous presentation of

this is given in Chapman and Bartels (1940). The magnetic potential field can be expanded in terms of spherical harmonic:

$$V(r,\theta,\phi) = a\sum_{n=1}^{\infty}\sum_{m=0}^{n}\left(\left[g_n^m\cos(m\phi) + h_n^m\sin(m\phi)\right]\left(\frac{a}{r}\right)^{n+1} + \left[q_n^m\cos(m\phi) + s_n^m\sin(m\phi)\right]\left(\frac{r}{a}\right)^{n}\right)P_n^m(\cos(\theta)) \quad (4)$$

where a is the reference radius, r is radius, θ co-latitude, ϕ longitude, (g_n^m, h_n^m) are the SH coefficients related to the internal field, (q_n^m, s_n^m) are the SH coefficients related to the external field, $P_n^m(\cos(\theta))$ are Schmidt quasi-normalized Legendre functions, and n and m are the SH-degree and -order, respectively.

3.2 Inverse problem

The magnetic field components are easily retrieved by evaluating the negative derivative of the potential. This presents a linear relationship between magnetic field observations and the SH coefficients that can be expressed in matrix format as

$$\boldsymbol{d} = \boldsymbol{G}\boldsymbol{m} \quad (5)$$

where $\boldsymbol{d}$ and $\boldsymbol{m}$ contain observations and SH coefficients, respectively,

$$\boldsymbol{d} = \left[\boldsymbol{B_r}, \boldsymbol{B_\theta}, \boldsymbol{B_\phi}\right]^T, \quad \boldsymbol{m} = \left[g_1^0, q_1^0, g_1^1, h_1^1, \ldots, q_n^m, s_n^m\right]^T \quad (6)$$

while $\boldsymbol{G}$, the data kernel, describes the linear relation between the two.

The inverse problem, to isolate $\boldsymbol{m}$ in Eq. 5, can conveniently be solved using a least squares approach where the 2-norm of the data misfit is minimized. Depending on the nature of the observations this approach can be prone to overfitting. In this study the inversion method is modified with a combination of iterative reweighting and Tikhonov regularization. The resulting objective function becomes

$$\Phi(\boldsymbol{m}) = (\boldsymbol{d} - \boldsymbol{G}\boldsymbol{m})^T\boldsymbol{W}(\boldsymbol{d} - \boldsymbol{G}\boldsymbol{m}) + \alpha^2\boldsymbol{m}^T\boldsymbol{L}^T\boldsymbol{L}\boldsymbol{m} \quad (7)$$

where $\boldsymbol{W}$ are data weights, α is the regularization parameter determining the trade-off between minimizing data misfit and the model norm, and $\boldsymbol{L}$ describes the nature of the regularization. When minimizing the model 2-norm $\boldsymbol{L}^T\boldsymbol{L}$ is a diagonal matrix and commonly the identity matrix. A minimum in Φ can be found by imposing $\frac{\partial}{\partial \boldsymbol{m}}\Phi(\boldsymbol{m}) = 0$ on Eq. 7 and isolating for $\boldsymbol{m}$.

$$\boldsymbol{m} = \left(\boldsymbol{G}^T\boldsymbol{W}\boldsymbol{G} + \alpha^2\boldsymbol{L}^T\boldsymbol{L}\right)^{-1}\boldsymbol{G}^T\boldsymbol{W}\boldsymbol{d} \quad (8)$$

Here $\boldsymbol{W}$ is decomposed into $\boldsymbol{W} = \boldsymbol{W}_d \circ \boldsymbol{W}_r$ where $\boldsymbol{W}_d$ and $\boldsymbol{W}_r$ refer to weights related to data coverage and iterative reweighting, respectively.

The iterative reweighted scheme used in this study applies Huber weights (Constable, 1988; Huber and Ronchetti, 2009) that are iteratively updated until the maximum percentage change of the model 2-norm between the previous and current iteration is equal to or less than 0.01% (Aster et al., 2013b). The weights based on data coverage are unchanging throughout the iterations and used to reduce spatial bias. They are determined as the inverse of the amount of observations in each cell of an equal area grid.

The Tikhonov regularization scheme applied here assumes $\boldsymbol{R} = \boldsymbol{L}^T\boldsymbol{L}$ to be diagonal. The values that populate the diagonal of $\boldsymbol{R}$ is based on the Lowes-Mauersberger power spectrum (Sabaka et al., 2014) for internal $W_n^i(r)$ and external $W_n^e(r)$ sources, Eq. 9, evaluated at ionospheric heights. Due to a dependence on height relative to the reference height and SH degree, the external field and higher harmonic terms will be dampened more severely than the internal field and lower harmonic terms, respectively.

$$W_n^i(r) = R_i(n)\sum_{m=0}^{n}\left[\left(g_n^m\right)^2 + \left(h_n^m\right)^2\right], \quad R_i(n) = (n+1)\left(\frac{a}{r}\right)^{2n+4}$$
$$W_n^e(r) = R_e(n)\sum_{m=0}^{n}\left[\left(q_n^m\right)^2 + \left(s_n^m\right)^2\right], \quad R_e(n) = n\left(\frac{r}{a}\right)^{2n-2} \quad (9)$$

Applying regularization necessitates choosing a value for the regularization parameter. This is done automatically for each epoch using Generalized Cross-Validation (GCV) (Aster et al., 2013a) to ensure reproducibility and reduce human bias. The optimal value for the regularization parameter can be found by solving the inverse problem, Eq. 8, for a series of α-values and evaluate the GCV score, Eq. 10 where N is the number of observations. The optimal value of α is related to the lowest GCV score. As this approach can be computational very heavy, we implemented a simple steepest descent algorithm to minimize unnecessary computations.

$$GCV(\alpha^2) = \frac{N}{\mathrm{Tr}[\boldsymbol{I} - \boldsymbol{G}\boldsymbol{G}^{-\alpha}]^2}\sum_{k=1}^{N}\left[(\boldsymbol{d} - \boldsymbol{G}\boldsymbol{m})^T\boldsymbol{W}(\boldsymbol{d} - \boldsymbol{G}\boldsymbol{m})\right]_k$$
$$\boldsymbol{G}^{-\alpha} = \left(\boldsymbol{G}^T\boldsymbol{W}\boldsymbol{G} + \alpha^2\boldsymbol{L}^T\boldsymbol{L}\right)^{-1}\boldsymbol{G}^T\boldsymbol{W} \quad (10)$$

In addition to reducing the model 2-norm the inverse problem is constrained by truncating the SH-degree at 40 resulting in 1,680 model parameters. The model is further constrained by 1) using only $n - m$ odd terms which enforces hemispheric symmetry. 2) truncating the SH-order at 3 under the assumption that the east/west gradient is more smooth than the north/south gradient (Laundal et al., 2016). As a result of these two constraints the amount of model parameters is reduced to 272.The combination of iterative reweighting and Tikhonov regularization has been sketched out in Algorithm 1.In order to evaluate the variance in the model solutions a bootstrapping approach was taken. The inverse problem for each group of events was repeated 50 times while resampling the events going into the solution with replacement. Predictions from the various model realizations thus provide a variance estimate.

10.3389/fspas.2022.953954

Algorithm 1. Inversion scheme.

```
generate_required_data();    # G, d, R, W
for all α do
  reset_weights();    # Preparing for a new run.
  while conv ≥ threshold do
    if iteration > 1 then
      calculate_weights();    # Based on the initial inversion.
    end if
    solve_inv_problem();
    if iteration == 1 then
      calculate_sigma();    # Used to calculate Huber weights.
    end if
    if iteration > 1 then
      calculate_convergence();    # Check if the solution has converged
    end if
  end while
  calculate_gcv();    # Done for all α.
end for
find_min_gcv();    # Determine the optimal regularization parameter.
```

3.3 Equivalent currents

The equivalent horizontal ionospheric current (EHIC) can similarly be represented by a scalar potential (Laundal et al., 2016) and therefore expressed in terms of the same SH coefficients as in Eq. 4.

$$\Psi = \frac{a}{\mu_0}\sum_{n,m}\frac{2n+1}{n+1}\left(\frac{a+h}{a}\right)^n P_n^m(cos(\theta))\left[q_n^m\, cos(m\phi) + s_n^m\, sin(m\phi)\right] \tag{11}$$

Here h is the height with respect to a where the potential is evaluated. It is important to point out that Eq. 11 is the current potential expressed by the external magnetic field and h is therefore set to 110 km.

Evaluating the horizontal gradient of Ψ gives the EHIC.

$$\boldsymbol{j}_\perp = \hat{\boldsymbol{r}} \times \nabla\Psi \tag{12}$$

Where $\hat{\boldsymbol{r}}$ is a unit vector in the radial direction. The magnetic perturbation as a result of the ionospheric Hall current can be set equal to $\mathbf{j}_\perp$ if the magnetic field lines are assumed to be radial and the conductance uniform (Fukushima, 1969, 1976). Additionally, following Amm et al. (2002) an expression for the FACs can be written as

$$j_\parallel = \beta^{-1}\left[\nabla \times \boldsymbol{j}_\perp\right]_r \tag{13}$$

where β is the Hall and Pedersen conductance ratio and assumed to be constant. Equation 13 can be written in terms of Ψ by applying the relation from equation 34 in Sabaka et al. (2014).

$$j_\parallel = \frac{n(n+1)}{\beta r^2}\Psi \tag{14}$$

β is still unknown and will later be assumed to be 1 resulting in what we will refer to as equivalent field aligned currents (EFACs). Thus providing estimates of the EHIC and EFAC in terms of SH coefficients.

4 Results

A rapid increase in P_d can cause a SC which is commonly decomposed into two main parts; the low/mid and high latitude geomagnetic response, Eq. 1, with varying spatial and temporal scales. Madelaire et al. (2022) carried out a superposed epoch analysis of the SMR and PCN index in order to examine these geomagnetic responses. In this study we carry out a superposed epoch analysis using SH modeling. With this approach we create a continuous model, in space, based on multiple events allowing us to estimate magnetic field perturbations and ionospheric equivalent currents. In this section we 1) present model results prior to onset to illustrate the methods ability to recreate IMF and dipole tilt dependent current patterns and 2) examine incoherent and coherent high latitude ionospheric responses and the dependence on IMF orientation and dipole tilt.

4.1 Prior patterns

This study builds on the premise that a superposed epoch analysis using a spherical harmonic modeling technique is capable of robustly reproducing the underlying pattern common for a majority of events in a group. As an initial assessment Figure 1 shows the mean and standard deviation of the external radial magnetic field perturbation B_r across all 50 model realizations at epoch −5 (5 min prior to onset) for all 12 event groups above 50° mlat (magnetic latitude). The figure is divided into three rows indicating dipole tilt and four columns indicating IMF clock angle. The magnitude of the model predictions vary significantly across groups and the maps have therefore been given individual colorbars. The number in the upper right corner of each map indicate the maximum of their respective colorbars, in units of nT.

Maps of the mean are in good agreement with previous studies on current patterns and their dependency on IMF clock angle and dipole tilt (Cowley and Lockwood, 1992; Pettigrew et al., 2010; Weimer, 2013; Laundal et al., 2018). Predictions during summer are of higher magnitude than equinox and winter mainly as a result of variations in sunlight-induced conductivity and auroral precipitation with decreasing dipole tilt (Moen and Brekke, 1993; Liou et al., 2001). During B_Z+ there are strong NBZ currents and overall stronger currents on the duskside as a result of co-rotation (Förster et al., 2017). During B_Z-region 1 and 2 (R1/R2) currents are strong as a result of reconnection on both day and nightside giving rise to a two-cell current pattern. During B_Y± conditions the dawn and dusk cells become more circular or crescent as a result of the dayside reconnection geometry, giving rise to alternate current paths.

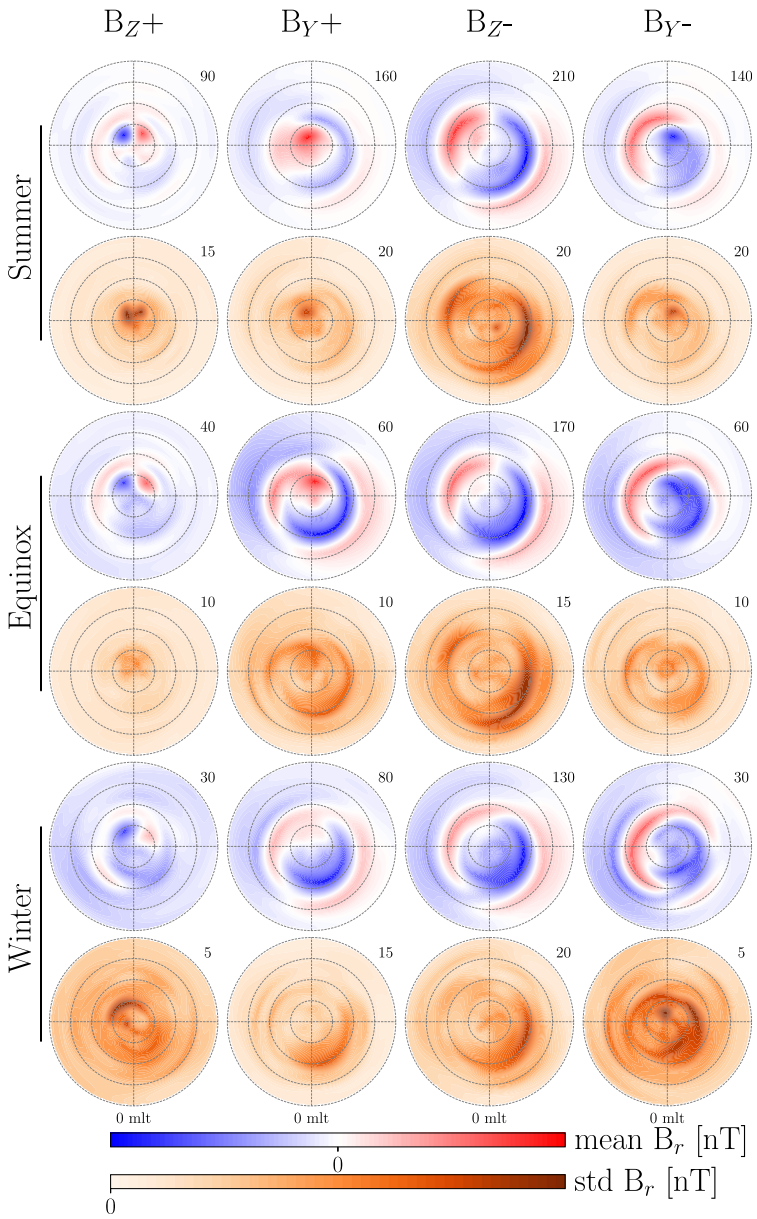

FIGURE 1
Illustration of the average model and its variation 5 min prior to onset. Each map shows either the mean or standard deviation of B_r as predicted by the 50 model realizations. The number in the upper right corner of each map indicates the magnitude of the colorbars for that specific map in units of nT. The columns and rows indicate the IMF clock and dipole tilt angle, respectively.

10.3389/fspas.2022.953954

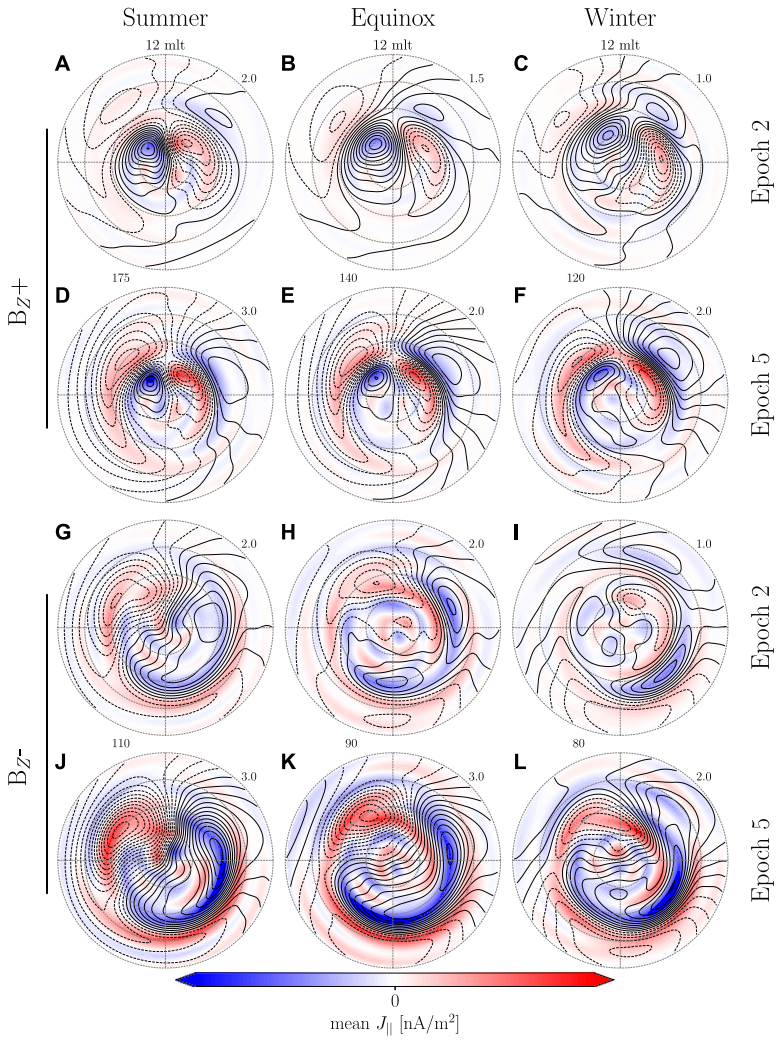

FIGURE 2
Maps of EHIC and EFAC 5 min before and after onset for the B_Z groups. The colored contour indicates EFACs while Ψ is shown by the black equipotential lines. Each set of figures is described by the two numbers written between them. The first indicates the step size of Ψ in kA while the second indicates the maximum of their unique colorbar.

Variation between model realizations is generally low, but can become large near the edges of current cells as a result of a varying latitudinal extent of the cells. The variations might be reduced if the magnitude of the IMF and increase in P_d was taken into account when creating the event groups.

4.2 High latitude geomagnetic response

The geomagnetic response is divided in two, Eq. 1. DP is further divided into PI (preliminary impulse) and MI (main impulse), Eq. 2, representing two sets of transient convection vortices. The resulting magnetic perturbation is superimposed

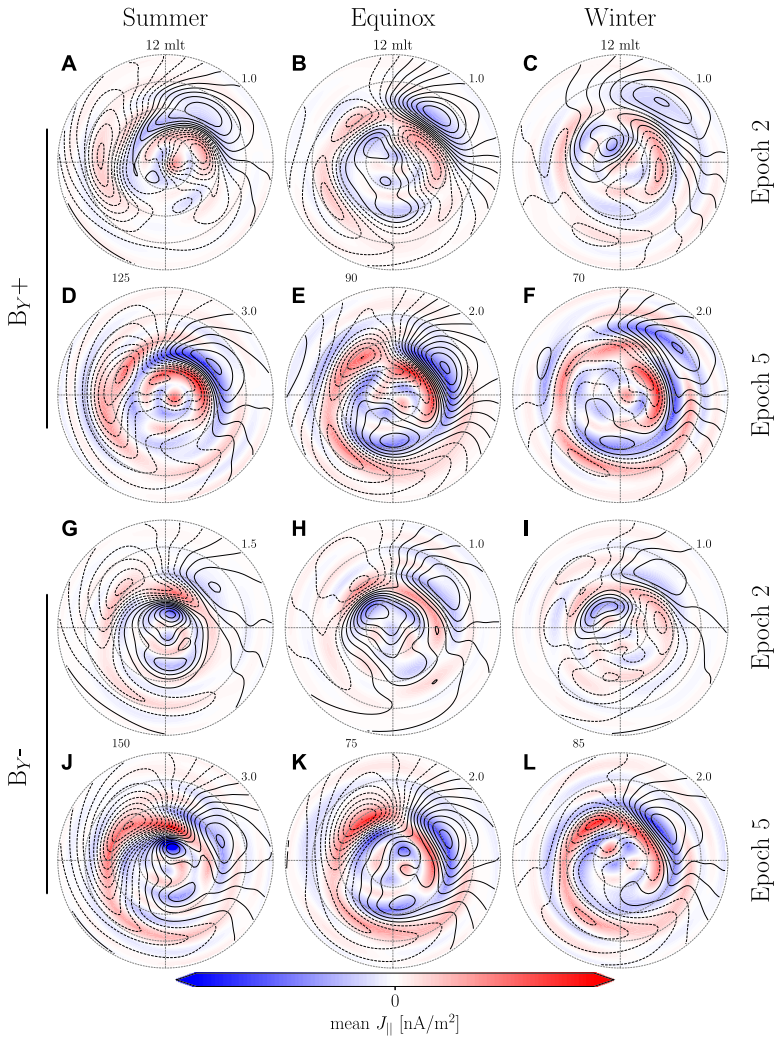

FIGURE 3
Similar to Figure 2, but for B_Y dominated IMF.

on the pre-existing perturbation magnetic field shown in Figure 1. The signal from these transient convection vortices will in most cases be overshadowed by the dominant pre-existing signal. Figures 2, 3 show Ψ, Eq. 11, and EFACs (equivalent field aligned currents), Eq. 14, at epoch −5 and 5 (5 min before and after onset). The colored contours are EFACs, where red (blue) indicate an upward (downward) FAC, and Ψ is illustrated in terms of equipotential lines.

B_Z+ models during equinox (Figures 2B,E) and winter (Figures 2C,F) show clear differences before and after onset. After onset the area around the NBZ currents intensifies and the current vortices extend towards the nightside. These vortices are confined by a second set of current vortices on their equatorward edge that have opposite orientation. The orientation, spatial extent and temporal evolution of these two set of current vortices are in agreement with previous case studies (Friis-Christensen et al., 1988; Moretto et al.,

10.3389/fspas.2022.953954

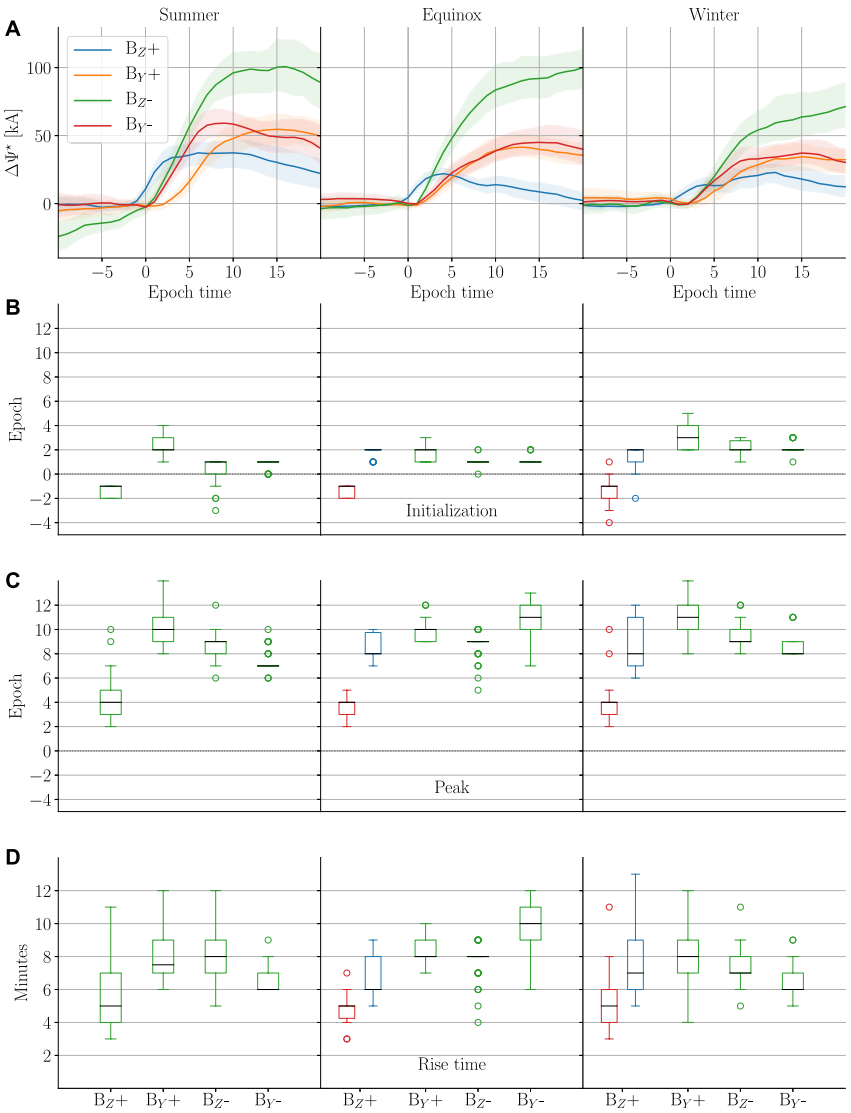

FIGURE 4
(A) Time series of $\Delta\Psi$ for all 12 groups. The mean and 90% confidence interval across all 50 mode realizations is shown as a solid line and a shaded area, respectively. The time series was set to zero with respect to when the response initiates indicated by the asterisk on the y-axis. **(B–D)** Summary of statistics related to Figure 4A shown as box plots. **(B)** shows the epoch at which response initiates for the 12 groups. **(C)** shows when the $\Delta\Psi$ time series peaks. **(D)** shows the rise time [difference between **(A** and **B)**]. During equinox and winter B_Z+ is given by two (red and blue) boxplots which are related to a decomposition illustrated in Figure 5.

2000), statistical studies (Stauning and Troshichev, 2008) and MHD simulation studies (Slinker et al., 1999; Keller et al., 2002; Fujita et al., 2003a,b, 2005; Ridley et al., 2006; Samsonov et al., 2010; Samsonov and Sibeck, 2013; Shi et al., 2014; Welling et al., 2021). For all other event groups the general magnitude increases, but no transient response is observed (Figures 2A,D,G–L and

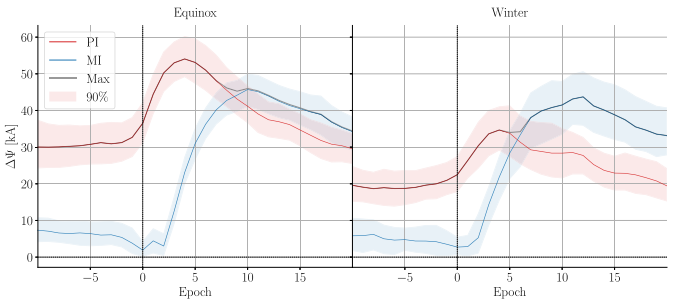

FIGURE 5
Decomposition ΔΨ for B_Z+ during equinox and winter into PI and MI.

Figures 3A–L). One factor that could play a role in the lack of a transient response is the increased dayside reconnection which enhances the preexisting convection pattern. The lack of a visible transient response is likely due to stronger pre-existing convection as a result of dayside reconnection.

4.2.1 Incoherent ionospheric response

In this section we attempt to look past the pre-existing magnetic field in order to examine the temporal evolution of the transient ionospheric response. This is more easily achieved by summarizing it by a single parameter. Here we use ΔΨ, the maximum difference in the current potential given by Eq. 11. Under normal circumstances the potential will be bi-modal with the global min/max coinciding with the current pattern allowing for easy determination of the maximum difference. Changes to the system will often manifest themselves as an increase or decrease in ΔΨ making it convenient for an analysis of the temporal evolution. Figure 4A shows the mean ΔΨ across all model realizations along with the 90% confidence interval. The time series was set to zero with respect to when the response initiates. The time at which the response initiates was determined using the rise time algorithm described by Madelaire et al. (2022). The algorithm also provides the peak (when the time series begins to plateau) allowing for the rise time to be determined.

The shape, size and temporal evolution changes significantly with IMF clock angle and dipole tilt. In the rest of this section we take a closer look at the characteristics of Figure 4A.

4.2.1.1 Initialization

The epoch at which ΔΨ, in Figure 4A, begins to increase is illustrated as box plots in Figure 4B. The red and blue box plots relate to a decomposition done later in this section and the reader should disregard the blue box plot for now. The signal initiates around epoch 1–3 for all event groups except for B_Z+ groups where the initialization occurs around epoch −2 to −1.

Determining ΔΨ is normally easy due to the bi-modal nature of Ψ. However, when multiple cells of similar magnitude grow and decay, as is the case for B_Z+ during equinox and winter, the global min/max will jump around thus making the current method invalid. In these two cases we observed an increase in and around the NBZ cells, consistent with the PI (preliminary impulse), followed by an increase at 65°–75° mlat similar to R1/R2 starting on the dayside, consistent with the MI. We constrained the area within which ΔΨ was computed so as to separate the PI and MI. The PI was isolated by evaluating Ψ above 72° mlat and between 6 and 18 mlt (magnetic local time). The MI was isolated by evaluating Ψ between 65° and 80° mlat. Separate constraints were applied to the dawn and dusk cell due to an asymmetric response which will be further discussed in Section 4.2.2. At dusk Ψ was evaluated between 12 and 18 mlt while dawn was constrained to 6–12 mlt until epoch 5 whereafter it was relaxed to 0–12 mlt. The result of hard-coding where Ψ was evaluated allows for the separation of the two responses as shown in Figure 5. Here the mean PI (MI) is shown in red (blue) with a 90% confidence interval, and the maximum of the two is shown in black. We have labeled the two time series PI and MI as the current vortices observed correspond to the expected orientation and location of the convection vortices associated with PI and MI.

Returning to Figure 4B the PI (MI) is shown with red (blue) box plots. The PI values fit very well with those determined for B_Z+ during summer where the response near the NBZ cells is dominant. The MI initialization fits very well with the initialization of ΔΨ for all other IMF clock angles. One might question why there is no PI for non-B_Z+ groups. This is likely because the PI occurs poleward of the global min/max where ΔΨ is evaluated and its magnitude is not large enough to shift their location.

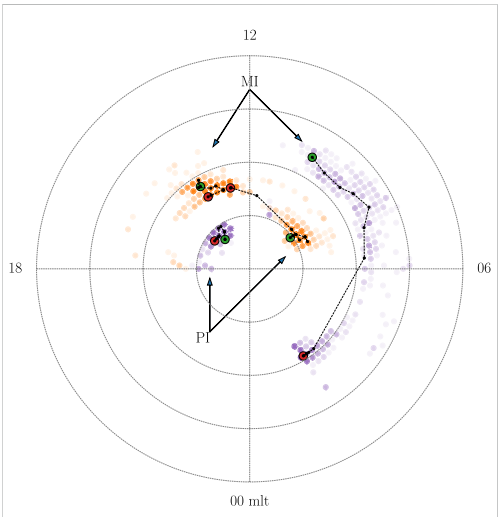

FIGURE 6
Illustration of the PI and MI current vortex centers resulting from the decomposition of ΔΨ during B_Z+ Winter in Figure 5. The poleward (equatorward) purple/orange dots indicate convection cell centers for PI (MI) across all 50 model realizations between epochs −2–8 (0–10). The black lines indicated the average path of the convection cell where the green and red dots indicate the start and end, respectively.

4.2.1.2 Peak and rise time

The peak and rise time of ΔΨ are shown in Figures 4C,D. For B_Z+ the peak occurs around epoch 4 while for all other IMF conditions it occurs around epoch 7–11. The difference is not surprising considering how clearly the PI can be observed during B_Z+. The results are consistent with the superposed epoch analysis of the PCN index conducted by Madelaire et al. (2022). The rise time for the PI is around 5 min while it is 6–10 min for the MI. When comparing Figures 4B–D, the largest source of variation in rise time is from the peak determination. This is consistent with Takeuchi et al. (2002) who studied the rise time of the low/mid latitude geomagnetic response and found it to be around 2–10 min with one event reaching 30 min, presumably due to a highly inclined shock normal.

4.2.1.3 Magnitude and decay

The average increase in P_d across event groups is of similar size, one might therefore assume that the magnitude of the geomagnetic response would be of similar magnitude across all IMF groups in a particular season. Comparing ΔΨ within the individual seasons shows B_Z-to have a magnitude around 2 (3) times larger than B_Y± (B_Z+). The solar wind-magnetosphere coupling efficiency is highly dependent on the IMF clock angle (Newell et al., 2007) and it is therefore no surprise that ΔΨ is significantly larger for B_Z-due to dayside reconnection.

The ΔΨ ratio between summer and winter is ~1.8 for all IMF clock angles. The ratio of the PI for B_Z+ is 2.4 indicating a much higher seasonal dependence. Samsonov et al. (2010) studied the effects of an interplanetary shock using a MHD simulation and concluded that the PI was associated with lobe reconnection. If this finding is true the larger variation in the PI can be controlled partly by dipole tilt as it has a large impact on the lobe coupling efficiency (Reistad et al., 2019).

Similar to the magnitude, the decay is IMF clock angle dependent. The decay during B_Z+ is quicker compared to other event groups. The B_Y± groups plateau or decay slowly while B_Z-plateau or trend upwards. The longer lived response for B_Y± and B_Z-is most probably a consequence of increased dayside reconnection brought on by the new pressure balance.

4.2.2 Northward IMF case

In Section 4.2.1 we examined the ionospheric response to rapid increases in P_d and found dependencies on both IMF clock angle and dipole tilt. Here we examine the temporal evolution using the model during B_Z+ as the transient event is strongest relative to the background for these environmental conditions.

The decomposition of ΔΨ in Figure 5 illustrates the magnitude of PI and MI along with their temporal extent. The decomposition was made by evaluating the local min/max of Ψ. The positions used in that calculation can be visualized to show how the cells move and the variation between model realizations. Figure 6 shows the location of the current potential min/max in orange/purple dots. Superimposed is the average path where the green (red) dots indicate the beginning (end). The PI is shown from epoch −2–10 and the MI is shown from 0 to 15. It is clear that the center of the PI current vortices and the MI vortex at dusk do not move much. However, the MI at dawn moves from around 10 to 6.5 mlt between epoch 2–8 (6 min) at 67° mlat leading to a westward velocity of 6.3 km/s. This is similar in size to the estimates of 3–5 km/s by Friis-Christensen et al. (1988) and 5 km/s by Slinker et al. (1999). After epoch 8 the center jumps from 6 to 2 mlt as the current vortex weakens and becomes indistinguishable from the pre-existing feature on the night side.

Figures 7, 8 show maps of EHIC and EFAC superimposed. Here model predictions are shown with 1–min resolution spanning epoch −1–6 and then with 2–min resolution from epoch 6–14. Before onset there is a set of NBZ cells with centers located around (9 mlt, 80° mlat) and (14 mlt, 82° mlat). There appears to be virtually no westward electrojet, while there is an eastward electrojet, possibly due to co-rotation (Förster et al., 2017). On the nightside there are 2 cells located around (1 mlt, 75° mlat)

10.3389/fspas.2022.953954

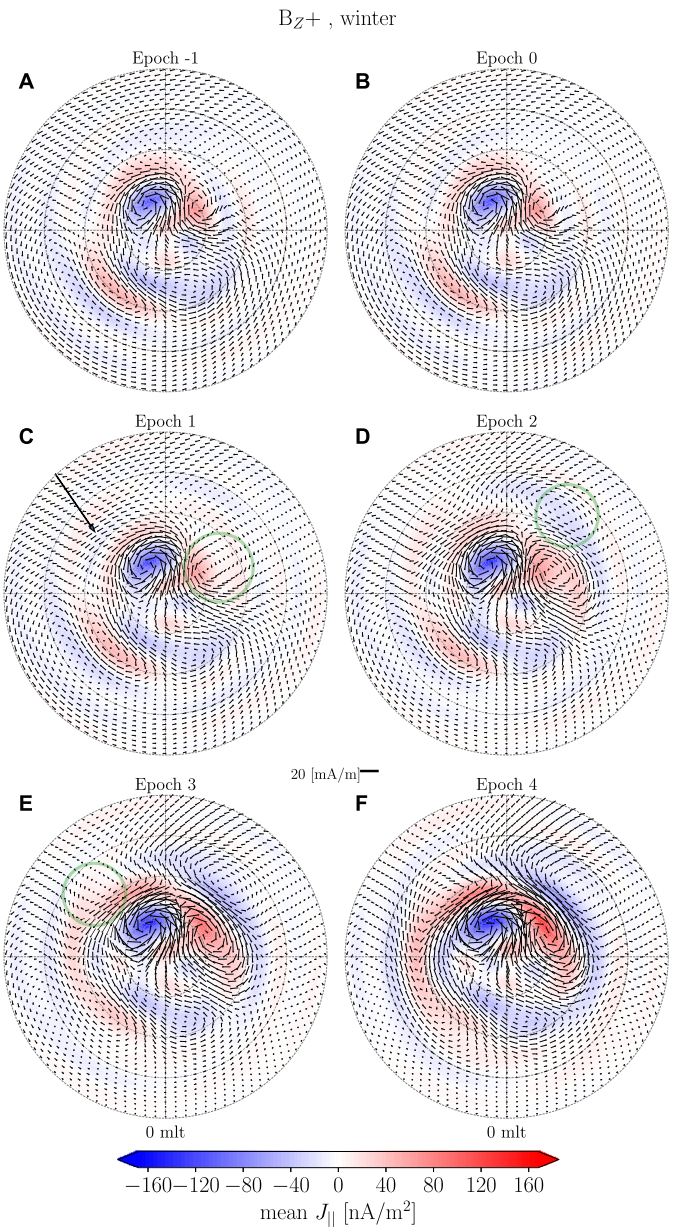

FIGURE 7
Maps of B_Z+ during Winter from epoch –1–4. The contours and arrows indicated EFACs and EHICs, respectively.

10.3389/fspas.2022.953954

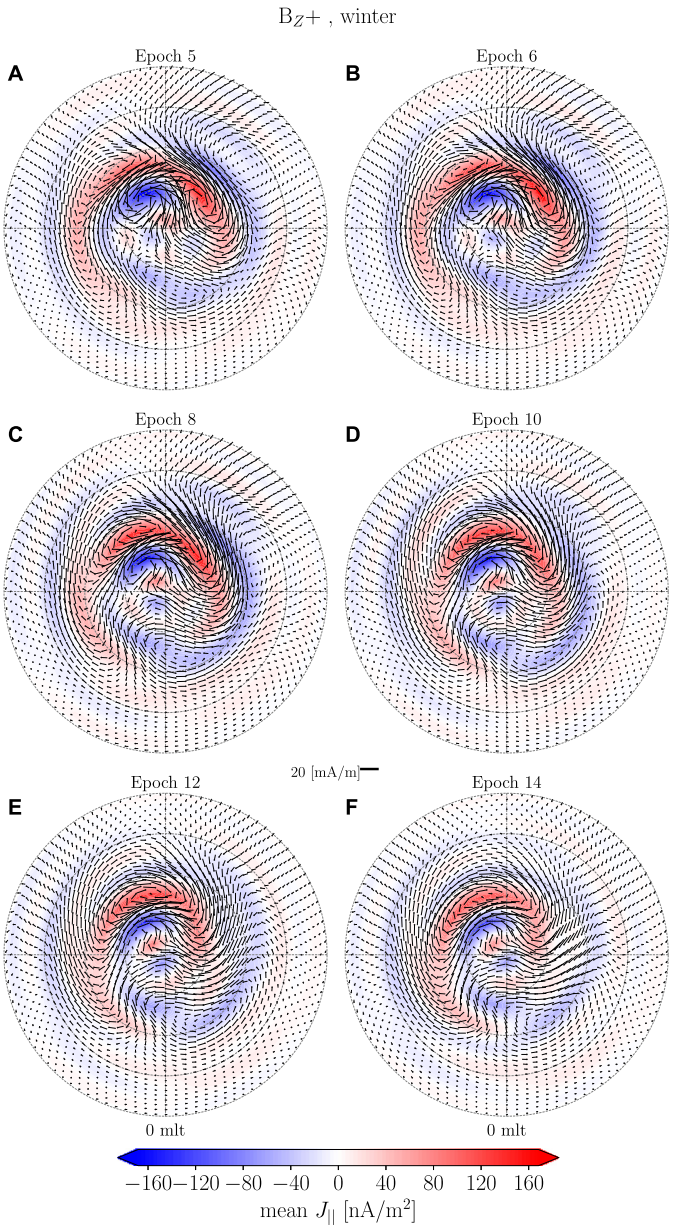

FIGURE 8
Maps of B_Z+ during Winter from epoch 5–14. The contours and arrows indicated EFACs and EHICs, respectively.

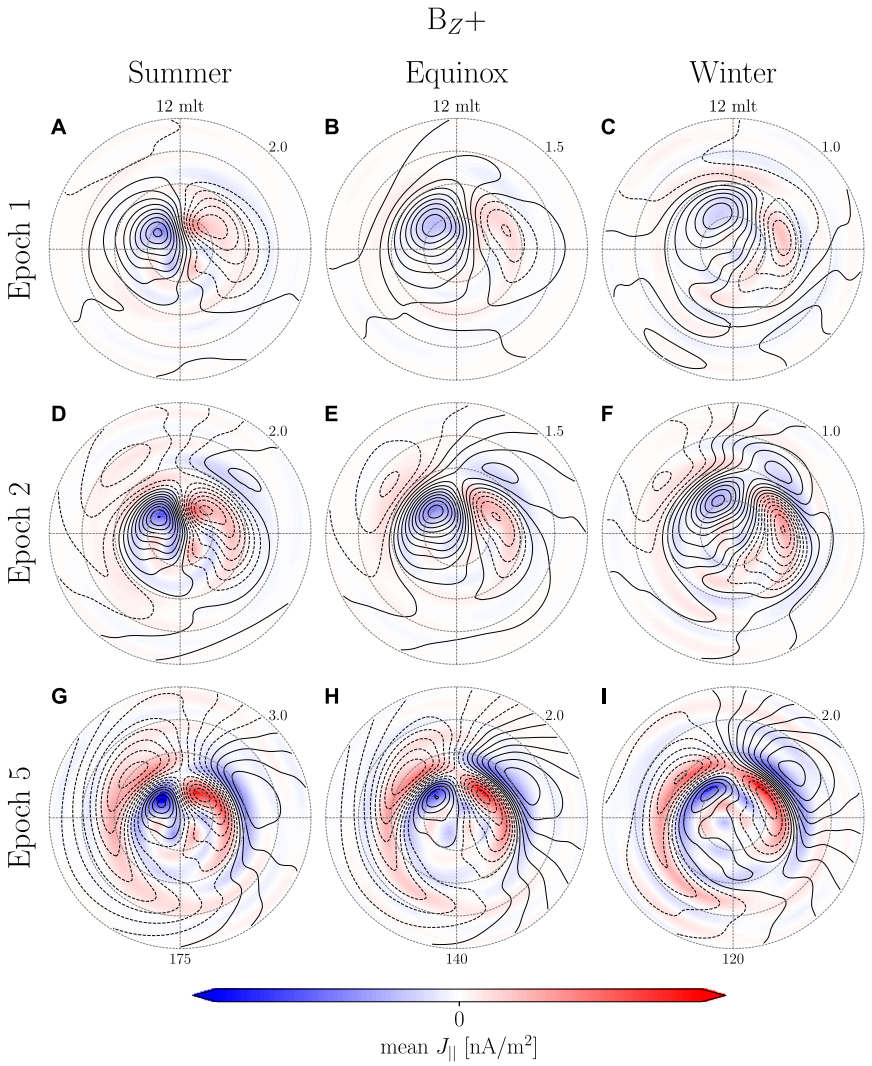

FIGURE 9
Relative change from epoch −2 to epoch 1, 2, and 5 for B_Z+. The blue/red contour illustrates EFAC while the black contour is Ψ. Each column represents a specific dipole tilt range and the number at the bottom of each column is the maximum value of the associated colorbar in units nA/m^2. The number in the top right of each map is the step size of the black contour in kA.

and (21 mlt, 70° mlat) and are likely related to nightside reconnection.

There is no apparent difference when comparing epochs −1 and 0 (Figures 7A,B). One minute after onset, Figures 7A,C small intensification is observed at pre- and post-noon around 65°–80° mlat as indicated by the annotations. Two minutes after onset, Figure 7D, the equatorward boundary of the pre-noon structure has moved poleward to 70° mlat and merged with the pre-existing NBZ cell with its center located around (8 mlt, 78° mlat). Additionally, a current vortex with opposite orientation has appeared at (10 mlt, 65° mlat). At post-noon we see a general intensification of the pre-existing current

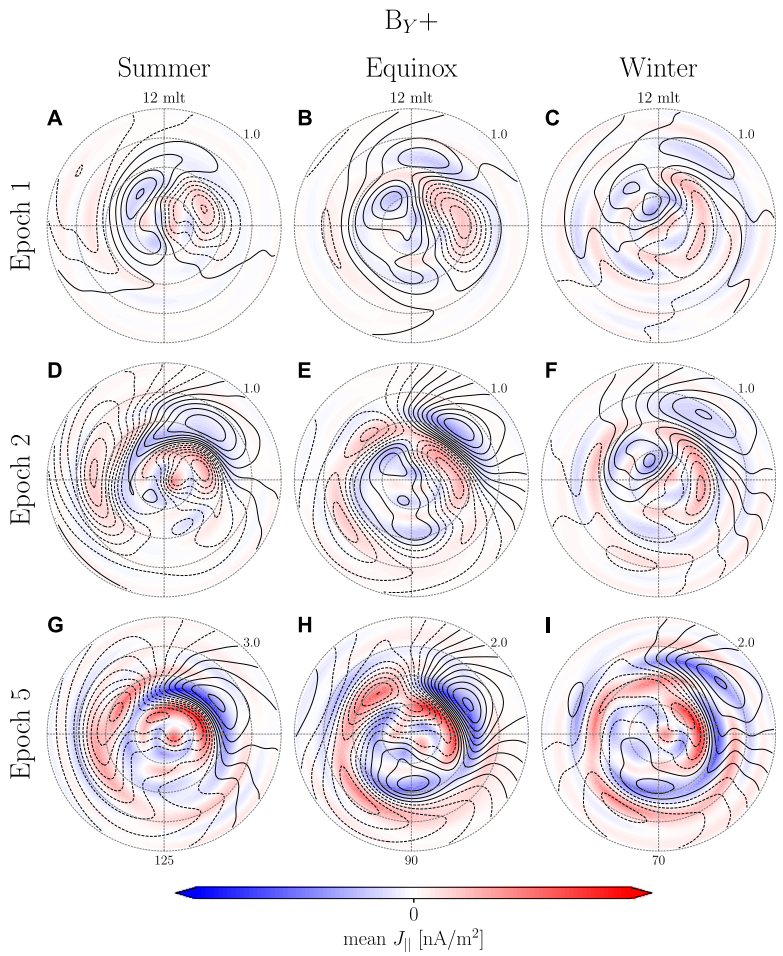

FIGURE 10
Similar to Figure 9, but for B_Y+.

pattern. It is possible that the pre-existing eastward electrojet obscures the PI which therefore is manifested as a general increase of the pre-existing current pattern. Between epoch 3 and 4, Figures 7E,F, the PI current vortices intensify, move poleward and start draping towards the nightside while their centers do not move. At dawn the MI current vortices intensifies, extending toward the night side while its center moves 1–2 MLT westward. At dusk the center of the MI current vortex appears and as it intensifies it moves poleward, from (15 mlt, 65° mlat) to (15 mlt, 70° mlat), and merges with the pre-existing nightside current vortex. Between epoch 5 and 6, Figures 8A,B, the PI cell intensifies while their equatorward extent decrease. At the same time the MI also intensifies and the center of the dawnside vortex moves westward. The duskside MI current vortex becomes more well defined and moves poleward. Between epoch 8 and 10, Figures 8C,D, the PI decreases in intensity and at dawn the PI vortex merges with the MI vortex at dusk. The center of the MI vortex at dawn moves westward and becomes less well defined. At dusk the MI cell intensifies and moves slightly westward towards the noon meridian. Between epoch 12 and 14, Figures

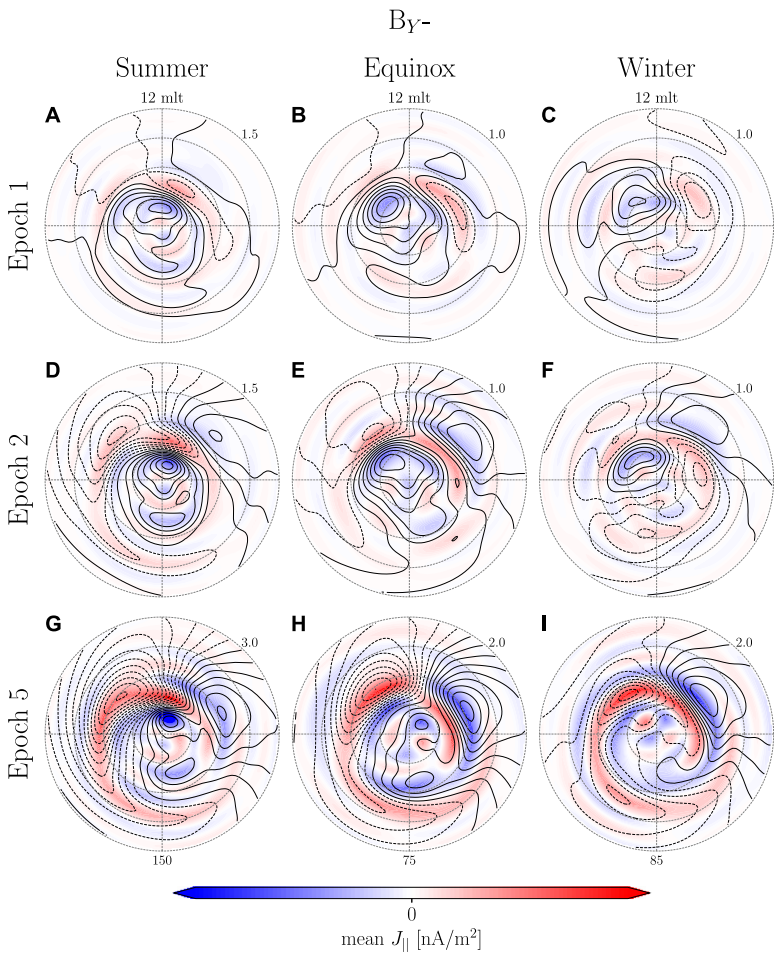

FIGURE 11
Similar to Figure 9, but for B_Y-.

8E,F, the PI response continues to decrease in strength. The MI response slowly disappears at dawn while it remains strong at dusk.

In our examination of the B_Z+ during winter a transient high latitude geomagnetic response was observed and will be discussed further in Section 5.

4.2.3 Coherent ionospheric response

Despite the lack of a visible transient response in a majority of the event groups it might very well still be there, hidden under a more dominant current pattern. A weak transient signal can be examined by evaluating the relative change as long as the contribution from the change of the transient signal is larger than that of the background signal.

In Figures 2E,F the MI-associated current vortices appears to extend far equatorward. This, to some extent, is an artifact caused by how DL geomagnetic response maps into the horizontal magnetic field at subauroral latitudes, mainly the north/south component, resulting in what appears to be large scale east/west aligned ionospheric current. We remove this effect by approximating the magnetic perturbation from magnetospheric sources as an

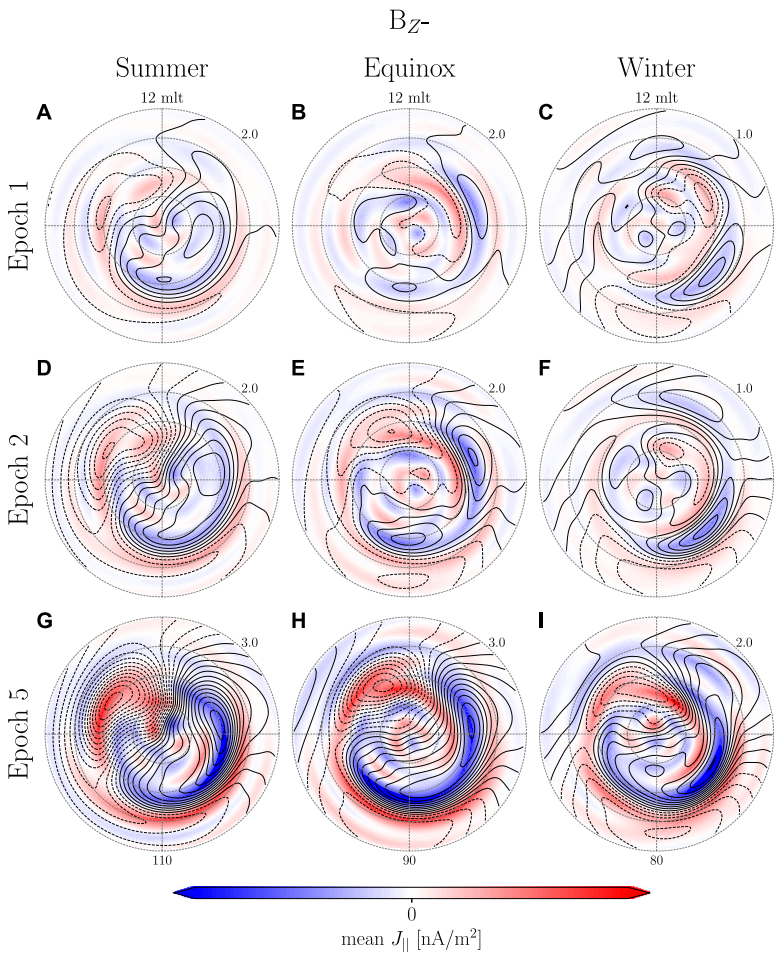

FIGURE 12
Similar to Figure 9, but for B$_Z$-.

external dipole field. The external dipole field can be seen as uniform magnetic field in $\hat{z}$,

$$B_m = B_r \sin(\theta) - B_\theta \cos(\theta), \tag{15}$$

which except for a sign difference is the same as the SH expansion of the external magnetic field to degree 1 and order 0. B_m is determined at each epoch as the average of 1,000 model predictions at 30° mlat that are evenly spaced in mlt. The effect of the magnetospheric compression is then isolated by subtracting a baseline prior to onset. Finally, a corrected SH model is created,

$$q_1^{0*} = q_1^0 + B_m. \tag{16}$$

Figures 9–12 shows the relative change from epoch −2 to epoch 1, 2 and 5 using the corrected model for B$_Z$+, B$_Y$+, B$_Y$- and B$_Z$-, respectively. Each column represents a season and the rows different epochs i.e., each column pertains to one of the 12 groups. The number below the maps in the last rows indicate the maximum value of the colorbar for that group in nA/m^2. The number in the upper right corner of each map is the step size of the black contour in kA.

When comparing B_Z+ between Figure 9 to Figure 2A–F it is clear that the transient high latitude response shows very little dipole tilt dependence. At epoch 1 (Figure 9A–C) only the PI is present. At epoch 2 (Figure 9D–F) the MI starts forming around 60°–65° mlat. At epoch 5 (Figure 9G–I) both PI and MI increase in magnitude and the center of the MI vortex at post-noon has moves poleward by 5° mlat while the vortex at pre-noon moves westward.

The B_Y± groups at epoch 1 (Figures 10A–C and Figure 11A–C) show PI current vortices. They are not as well defined when comparing with B_Z+, but there does not appear to be any favoring of one vortex over the other as might be expected when comparing B_Y+ and B_Y-. At epoch 2 (Figures 10D–F and Figures 11D–F) the PI moves slightly poleward as the MI forms on its equatorward edge. In some cases, Figures 10D, 11D,E, one of the PI vortices disappear or merge with one of the MI vortices. This might be attributed to the model's spatial resolution, the fact that we are looking at a relative change or the combination of northward and southward IMF in B_Y± groups causing higher variation between events close to the pole. At epoch 5 (Figures 10G–I, 11G–I) the PI is almost completely gone and the MI is well defined with the exception of B_Y+ winter where no clear MI current vortex appear on the dusk side. Under these environmental conditions it is also only the MI vortex on the dawnside that moves toward the nightside.

The current potential for B_Z- at epoch 1 (Figures 12A–C) is highly variable, i.e. many local min/max, and it is therefore difficult to associate any of the structures to PI or MI. During summer (Figures 12A,D,G) the current pattern is very similar to the expected current pattern during southward IMF (Laundal et al., 2018). The center of the 2 cells are shifted towards the dayside indicating some similarity to the MI current vortices. During equinox and winter current vortices appear on the night side at epoch 1 and increase in strength at epoch 2 (Figures 12B,C,E,F). At epoch 2 during equinox (Figure 12E) two MI associated vortices appear on the dayside; one on the dawnside and another very close to noon on the duskside. At epoch 5 (Figure 12H) the dawnside MI vortex merges with that on the nightside. The same can be observed during winter, however, the post-noon current vortex first appears at epoch 5 (Figure 12I). Common for all B_Z-groups is a general lack of the PI current vortices and a very strong nightside geomagnetic response possibly associated with dipolarization of the tail magnetic field as observed by Lee and Lyons (2004).

5 Discussion

In our examination of the transient high latitude response we looked closely at the model for northward IMF during winter as these are the conditions under which the transient response is strongest relative to the background. The model shows vortices that evolve on a minute time scale. The spatial extent of the vortices vary with time, however, the center of the vortices tend not to move except for the MI-associated vortex on the dawnside which moves westward with an estimated velocity of 6.3 km/s. The shock impact angle is surprisingly not one of the factors controlling the motion of the MI-associated vortices at dawn and dusk. Our reasoning is as follows. Madelaire et al. (2022) argued that the majority of the events in their list of rapid increases in P_d are not interplanetary shock. It is therefore likely that our results represent an average impact angle that is skewed toward dusk, in agreement with the statistical survey of rapid solar wind pressure changes presented by Dalin et al. (2002). In contrast the case study of Moretto et al. (2000), which used the AMIE technique to model the ionospheric response of an inclined shock arriving first at the dawn side, also found that the MI-associated convection vortex at dusk did not move, while that at dawn did. If the impact angle controlled which vortex convects toward the nightside, the response of the vortices reported by Moretto et al. (2000) would presumably be opposite the observed response; that is, the dusk vortex would have moved toward the nightside while the dawn vortex remained stationary. Existing simulation-based studies of interplanetary shocks unfortunately do not lend much insight (Slinker et al., 1999; Keller et al., 2002; Fujita et al., 2003a,b; Ridley et al., 2006; Samsonov et al., 2010; Welling et al., 2021): while they universally show a symmetric ionospheric response across the noon-midnight meridian with both MI cells moving anti sunward, all have been carried out with an interplanetary shock aligned with the Sun-Earth line.

5.1 Coherent high-latitude response

A coherent transient high latitude geomagnetic response is observed for all groups when examining the relative change with respect to epoch −2 (Figures 9–12). When comparing different groups we find the EFAC magnitude and PI current vortices to be more dominant during B_Z+ likely due to a higher contribution from lobe reconnection. During B_Z-there is a general lack of PI and the MI is poorly resolved due to a significant enhancement of the pre-existing current pattern. The appearance of MI current vortices during B_Z+ and B_Y± is very consistent. We estimate the westward velocity of the dawnside associated MI current vortex based on epoch 2–5 (Figures 9–11) to be between 3.6 and 7.8 km/s with a mean of 5 km/s and a standard deviation of 1.4 km/s. The initial appearance of the MI current vortex on the dawnside occurs at (9.3 ± 0.5 mlt, 64.8° ± 1.5° mlat) while it on the duskside occurs at (15.3 ± 0.9 mlt, 65.8° ± 2.5° mlat) with the majority of the mlt variation caused by Figure 11D.

The SH model is a global representation of the magnetic potential. It is important to understand the benefits and shortcomings of the method such that results can be interpreted in the correct context and improvements or

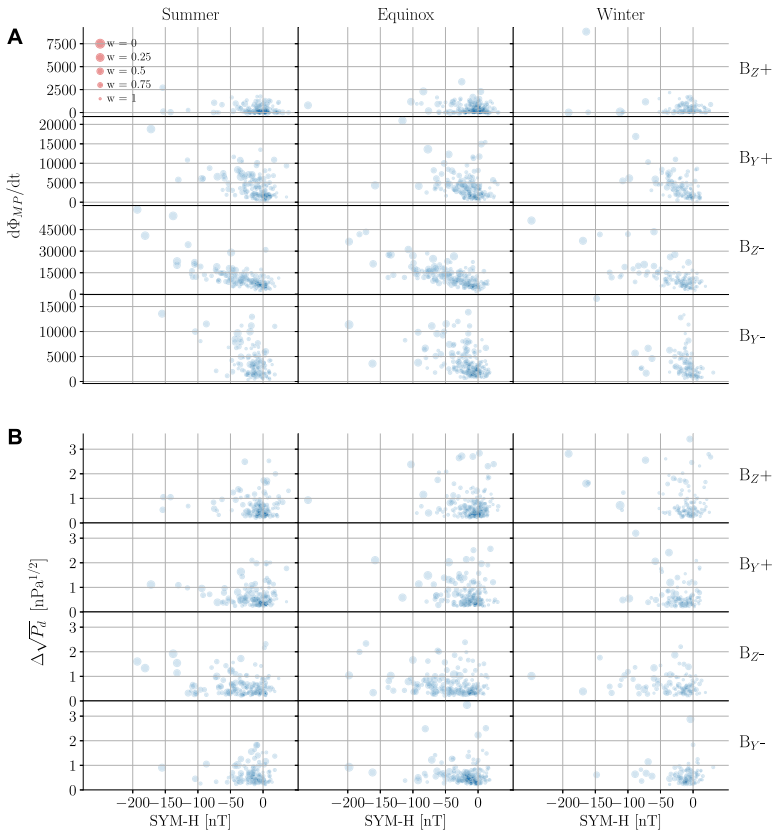

FIGURE 13
Huber weights at epoch 5 for each event. In **(A)** illustrated as function of the Newell coupling function and SYM-H before onset and in **(B)** as function $\Delta\sqrt{P_d}$ and SYM-H before onset. Each dot indicates an event and the size of each dot illustrates the weight of each event. A large (small) dot indicates an event that is weighted low (high).

alternatives might be proposed. The spatial resolution of any modeling method will partly depend on data coverage. When using ground magnetometers the data coverage is seldom uniform and the spatial resolution is highly dependent on the area with the lowest data density. By combining multiple events, as done here, we can achieve much denser data coverage resulting in a better spatial resolution. Combining multiple events generates inconsistencies as observations that are spatially very close can vary significantly. The variation is reduced by only combining events thought to be of similar nature. The model will inevitably be an average highlighting features common for all the events. We have tried to quantify the variation in our model using bootstrapping (Figure 1), but in order to understand how and why events vary from the average they need to be analyzed individually. The spherical elementary current system technique (Amm et al., 2002) is ideal for analyzing single events as it is not globally defined and can take advantage of the regions with dense data coverage. This method is implemented by Laundal et al. (2022); they combine magnetic perturbation and convection measurements from space and ground with conductance measurements via ionospheric Ohm's law to significantly improve data coverage and information retrieved. This will be a very useful tool when the EZIE satellite mission (Laundal et al., 2021) launches in the near future providing measurements of the magnetic field in the mesosphere. In the future we intend to carry out a regional analysis of events to study their variation in more detail.

10.3389/fspas.2022.953954

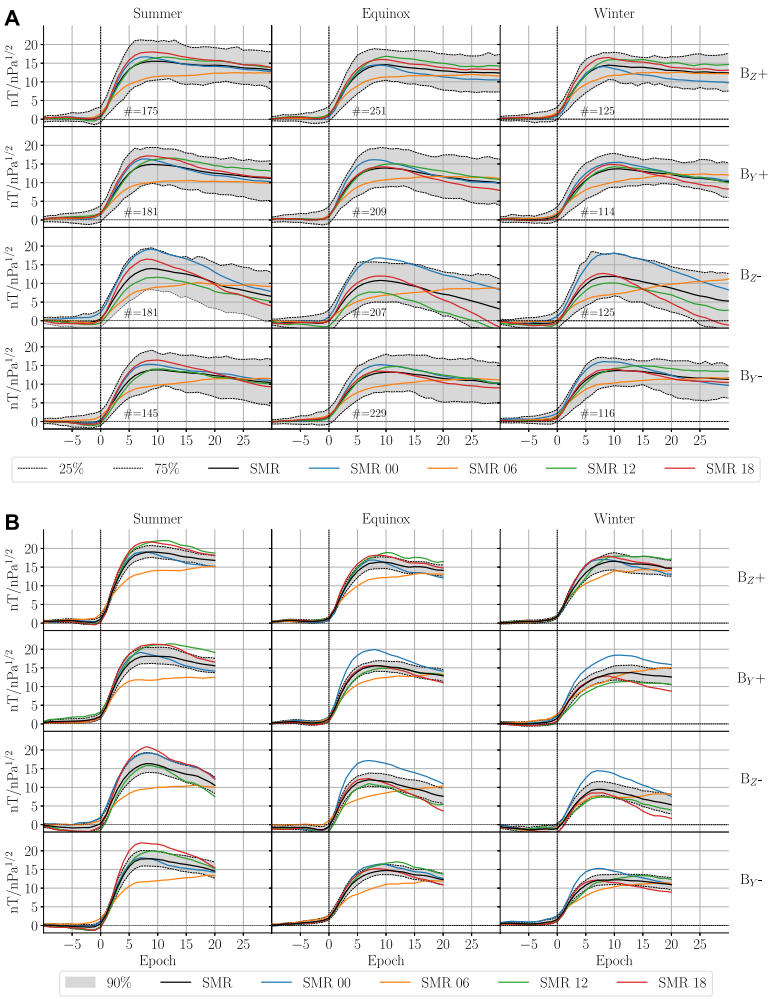

FIGURE 14
Comparison between the superposed epoch analysis of the SMR index by Madelaire et al. (2022) and the recreated SMR index from the SH models. **(A)** Similar to Figure 9 of (Madelaire et al., 2022). **(B)** The recreated SMR index where the solid lines indicate the mean of SMR and its local time components. The gray area indicates a 90% confidence interval of the global SMR. The SMR time series for each model realization has been scaled with respect to the median increase in $\sqrt{P_d}$ and a baseline prior to onset subtracted.

5.2 Huber weights

A superposed epoch analysis assumes a certain level of comparability between events which we in practice achieve by imposing criteria on IMF clock angle and dipole tilt. It is obvious that there will be differences between events and at times so much so that individual events can be considered outliers. When solving the inverse problem the imposed spatial relationship, inherent in SHs, will force the solution toward the typical event and thereby automatically reduce the relative importance of certain data. Adding iterative reweighting allows for a fine tuning of the fit as the influence of outliers are weighed down and the inversion repeated. The term outliers is often used synonymously with measurement errors, but here refer to events behaving differently from the majority. In practice, the outliers are

10.3389/fspas.2022.953954

weighed down using Huber weights which are determined as part of the iterative procedure.

The Huber weights can be used to analyze how consistent the data selection is and if outliers are correlated with certain environmental parameters. Figure 13 visualizes the average Huber weight for each event using data-points above 50° mlat with respect to certain environmental parameters. Each dot represents an event and the size of the dot indicates the weight of that specific event illustrated by the scale of red dots in the upper left corner; a large (small) dot indicates an event that has been weighed low (high) in the inversion. Figures 13A,B show how the weight relates to the Newell coupling function (Newell et al., 2007) before onset, the SYM-H index before onset and $\Delta\sqrt{P_d}$. It is clear that events with a SYM-H value below −50 nT are generally weighed very low. From Figure 13A we find that the Newell coupling function also can be used to separate between events that are weighted high and low in event groups with southward IMF ($B_Y\pm$ and B_Z-). Figure 13B, on the other hand, shows that $\Delta\sqrt{P_d}$ does not play a large role in whether or not an event deviates from the norm.

These figures are not intended to be employed in determining which parameters to use for grouping events, but are rather an illustration of how information about individual events can be extracted from a superposed epoch analysis. Additionally, they serve as an illustration of how data selection occurs prior to and during the modeling process.

5.3 Low/mid latitude geomagnetic response

A benefit of a global model is the possibility of examining the high latitude impact on low/mid latitude perturbations. Changes in $\sqrt{P_d}$ have previously been related linearly to changes in the Dst index (Burton et al., 1975) as a result of magnetospheric compression. This is best observed at low/mid latitudes as equatorial and subauroral/polar latitudes experience additional effects from electrojets (Sugiura, 1964; Sugiura and Kamel, 1991).

Russell et al. (1994a) did a statistical analysis of the linear relationship during interplanetary shocks and found the slope to be 18.4 nT/nPa$^{1/2}$ at Earth's surface which includes a 50% markup due to ground induced currents. This estimate was given for northward IMF and should be reduced by 25% (13.8 nT/nPa$^{1/2}$) during southward IMF (Russell et al., 1994b). The superposed epoch analysis by Madelaire et al. (2022) was based on the SMR index and found the average relationship to be around 15 nT/nPa$^{1/2}$ during northward IMF and around 12 nT/nPa$^{1/2}$ for southward IMF. Additionally, Madelaire et al. (2022) found a dawn-dusk asymmetry in the SMR index as well as a noon-midnight asymmetry for southward IMF.

The SH models are essentially a weighted average of the events in each group expressed in terms of SH surface waves. Their performance can be compared to the results of Madelaire et al. (2022) by testing if they can recreate their results. The results of the superposed epoch analysis of the SMR index by Madelaire et al. (2022) is reproduced in Figure 14A to facilitate comparison later. The SMR index

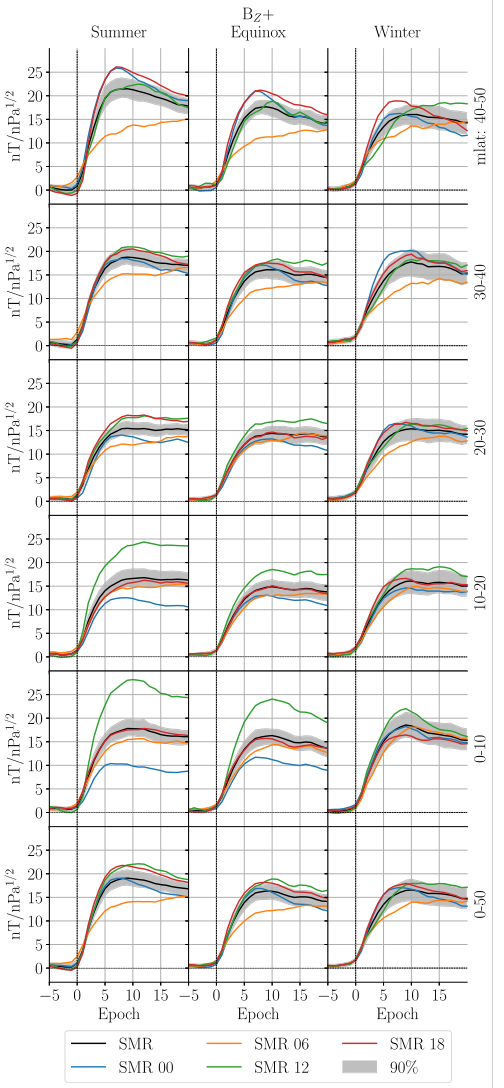

FIGURE 15
A latitudinal profile of the reproduced SMR for B_Z+ during all seasons. The first five rows show contributions from five latitudinal regions between 0° and 50° mlat. The last row shows SMR for the entire latitudinal region which is identical to row 1 of Figure 14B.

was recreated using the SH models; the northward component of the magnetic field perturbations are calculated using the internal and external model for each of the 50 realizations between the equator and 50° mlat. The model predictions are made at the same location as the data that went into the models. A latitudinal correction similar to that of the SMR index was applied (Newell and Gjerloev, 2012). The model predictions from each realization are scaled with the median of $\Delta\sqrt{P_d}$ for the events used in that particular realization. The median is used as there are a few very strong events biasing the mean. A common value for $\Delta\sqrt{P_d}$ is 0.6 $nPa^{1/2}$. The average is then calculated in four local time sectors to replicate SMR 00/06/12/18. Finally, the global SMR index is determined as the average of the four local time indices.

The recreated SMR index is shown in Figure 14B. The expected step-like increase is reproduced. The magnitudes of SMR range from 12 to 19 $nT/nPa^{1/2}$ which is slightly larger than the averages provided in Figure 14A. The dawn-dusk difference is also reproduced which is most pronounced during summer. Comparing Figures 14A,B suggests that the SH models are sufficient to reproduce the expected geomagnetic response observed on ground which is an indication that the modeling scheme performs well.

The latitudinal profile of the recreated SMR for B_Z+ is shown in Figure 15. The first 5 rows show 5 latitude bands between 0° and 50° mlat. The last row is identical to the first row of Figure 14B for more easy comparison. It is clear that the dawn-dusk asymmetry is most pronounced between 40° and 50° mlat. This suggests it is an ionospheric source and not magnetospheric, given its small spatial extent. A recent study (Zhou and Lühr, 2022) investigated SCs with an immediate and strong activation of the westward electrojet. However, they concluded that it required southward IMF preceding the SC. The lower magnitude at dawn between 40° and 50° mlat could reflect the ionospheric vortices generated at high latitude. The seasonal dependence would then be a result of seasonal variations in conductance varying the strength of the high latitude currents and thus the latitudinal extent of their magnetic perturbation.

In the region closest to the equator, 0°–10° mlat, a noon-midnight asymmetry is observed which is present for all IMF clock angles (only B_Z+ shown). The geomagnetic response on the dayside (nightside) tends to be stronger (weaker) than at dawn and dusk. The small latitudinal and longitudinal extent of the dayside/nightside (SMR 12/00) enhancement suggests an ionospheric source. A seasonal dependence is observed as the asymmetry almost disappears during winter. There are several possible explanations for this; Kikuchi (1986); Kikuchi et al. (2001); Kikuchi (2014) proposed that the potential difference at high latitude would be transported toward the equator in an Earth-ionosphere waveguide. In this frame the increased equatorial perturbation is caused by Cowling conductivity. However, Tu and Song (2019) argued against this idea as the waveguide should transport the electric field with the speed of light and the observed delay between high and low latitude is in the order of minutes. Movement of the Sq foci is thought to be responsible for the semiannual variation of the equatorial electrojet (Tarpley, 1973). The seasonal variation is not a modulation of the magnitude, but rather a latitudinal shift along with the Sq foci. Unfortunately, we are not able to test this hypothesis with our model as they are only based on data from the northern hemisphere. It is also possible that there is no hemispheric asymmetry and the seasonal variation is an artifact caused by the event occurrence probability being skewed toward a certain UT range for different dipole tilt angles due to the offset between the geomagnetic and geographic poles. Specifically, events are more likely to occur between 0 and 12 (12–24) UT for positive (negative) dipole tilt. Trivedi et al. (2005) showed that the magnetic perturbation due to SCs measured close to the south atlantic magnetic anomaly are stronger than elsewhere. It is therefore possible that the dipole tilt dependence of the magnetic perturbation at equator latitude simply is due to longitudinal variations in the equatorial electrojet.

It is clear that the geomagnetic response between 10° and 40° mlat is very similar while magnetometer observations between 0°–10° and 40°–50° mlat are under high influence of ionospheric sources. This consideration was taken into account in the development of the Dst index (Sugiura, 1964; Sugiura and Kamel, 1991) and it is therefore curious that it is not taken into account in the SYM-H and SMR index (Iyemori et al., 2010; Newell and Gjerloev, 2012). We do not attempt to understand the origin of the contamination pointed out here as that should be done in a future study using data directly from the magnetometer stations and not our SH models.

6 Conclusion

In this study we carried out a superposed epoch analysis of the transient high latitude geomagnetic response in the northern hemisphere to rapid increases in solar wind dynamic pressure using spherical harmonics. The analysis is based on the list of rapid solar wind pressure increases presented by Madelaire et al. (2022). A total of 2058 events were separated into 12 groups, Supplementary Table S1, based on IMF clock angle and dipole tilt. We found:

1. An incoherent geomagnetic response for a majority of the groups due to a dominant background signal; only during B_Z+ equinox and winter was the transient response visible.
2. A coherent geomagnetic response showing the development of current vortices associated with PI and/or MI of the sudden commencement was observed for all groups when evaluating the relative change with respect to epoch −2.
3. The PI (MI) onset occurs ~2 min before (after) the SYM-H defined onset and the rise time is 4–6 (6–11) min.

4. The pre-noon current vortex associated with the MI initially appears at (9.3 ± 0.5 mlt, 64.8° ± 1.5° mlat) and moves westward with a velocity of 5 ± 1.4 km/s until it reaches ~6 mlt. Here it remains while it slowly decays and a new steady state current pattern emerges.
5. The post-noon current vortex associated with the MI initially appears at (15.3 ± 0.9 mlt, 65.8° ± 2.5° mlat) and does not move towards the nightside which is inconsistent with previously published models and MHD simulations.
6. The high latitude impact on the low/mid latitude perturbation results in significant contamination of the SMR index due to the inclusion of observations from 0° to 10° mlat and 40°–50° mlat.

The purpose of the study was to create a climatological analysis of the transient high latitude geomagnetic response. In the future we intend to examine how individual events in the 12 groups differ from each other and what the controlling environmental factors are.

Data availability statement

Publicly available datasets were analyzed in this study. This data can be found here: Event list (doi. org/10.5281/zenodo.6243103), Ground magnetic perturbation from SuperMAG.

Author contributions

MM is the primary author and carried out the analysis. KML and JPR helped set up the overall structure of the manuscript. All co-authors contributed to the discussions and provided editorial comment thus contributing to the article and approved the submitted version.

Funding

This work was funded by the Research Council of Norway (RCN) under contract 223252/F50. KL and JR were also funded by the RCN under contract 300844/F50. KL and SH were also funded by the Trond Mohn Foundation.

Conflict of interest

The authors declare that the research was conducted in the absence of any commercial or financial relationships that could be construed as a potential conflict of interest.

Publisher's note

Supplementary material

The Supplementary Material for this article can be found online at: https://www.frontiersin.org/articles/10.3389/fspas.2022.953954/full#supplementary-material

References

Amm, O., Engebretson, M. J., Hughes, T., Newitt, L., Viljanen, A., and Watermann, J. (2002). A traveling convection vortex event study: Instantaneous ionospheric equivalent currents, estimation of field-aligned currents, and the role of induced currents. *J. Geophys. Res.* 107, 1334. SIA 1–1–SIA 1–11. doi:10.1029/2002JA009472

Araki, T. (1994). A physical model of the geomagnetic sudden commencement (American geophysical union (AGU)). *Sol. Wind Sources Magnetos. Ultra-Low-Frequency Waves,Geophysical Monogr. Ser.*, 183–200. doi:10.1029/GM081p0183

Aster, R. C., Borchers, B., and Thurber, C. H. (2013a). "Chapter four - tikhonov regularization," in *Parameter estimation and inverse problems*. Editors R. C. Aster, B. Borchers, and C. H. Thurber. Second Edition (Boston: Academic Press), 93–127. Second edition edn. doi:10.1016/B978-0-12-385048-5.00004-5

Aster, R. C., Borchers, B., and Thurber, C. H. (2013b). "Chapter two - linear regression," in *Parameter estimation and inverse problems*. Editors R. C. Aster, B. Borchers, and C. H. Thurber. Second Edition (Boston: Academic Press), 25–54. Second edition edn. doi:10.1016/B978-0-12-385048-5.00004-5

Burton, R. K., McPherron, R. L., and Russell, C. T. (1975). An empirical relationship between interplanetary conditions and dst. *J. Geophys. Res.* 80 (1896-1977), 4204–4214. doi:10.1029/JA080i031p04204

Chapman, S., and Bartels, J. (1940). *Geomagnetism*, 2. Oxford University Press. chap. 17. doi:10.2307/3606494

Constable, C. G. (1988). Parameter estimation in non-Gaussian noise. *Geophys. J. Int.* 94, 131–142. doi:10.1111/j.1365-246X.1988.tb03433.x

Cowley, S. W. H., and Lockwood, M. (1992). Excitation and decay of solar wind-driven flows in the magnetosphere-ionosphere system. *Ann. Geophys.* 10.

Curto, J., Araki, T., and Alberca, L. (2007). Evolution of the concept of sudden storm commencements and their operative identification. *Earth Planets Space* 59–xii. doi:10.1186/BF03352059

Dalin, P. A., Zastenker, G. N., and Richardson, J. D. (2002). Orientation of middle-scale structures in the solar wind plasma. *Cosmic Res.* 40, 319–323. doi:10.1023/a:1019838226629

Finlay, C. C., Kloss, C., Olsen, N., Hammer, M. D., Toffner-Clausen, L., Grayver, A., et al. (2020). The chaos-7 geomagnetic field model and observed changes in the south atlantic anomaly. *Earth Planets Space* 72, 156. doi:10.1186/s40623-020-01252-9

Förster, M., Doornbos, E., and Haaland, S. (2017). The role of the upper atmosphere for dawn-dusk differences in the coupled magnetosphere-ionosphere-thermosphere system. *Dawn-Dusk Asymmetries Planet. Plasma Environments,Geophysical Monogr. Ser.* 10, 125–141. American Geophysical Union (AGU)), chap. doi:10.1002/9781119216346.ch10

Friis-Christensen, E., McHenry, M. A., Clauer, C. R., and Vennerstrøm, S. (1988). Ionospheric traveling convection vortices observed near the polar cleft: A triggered

response to sudden changes in the solar wind. *Geophys. Res. Lett.* 15, 253–256. doi:10.1029/GL015i003p00253

Fujita, S., Tanaka, T., Kikuchi, T., Fujimoto, K., Hosokawa, K., and Itonaga, M. (2003a). A numerical simulation of the geomagnetic sudden commencement: 1. Generation of the field-aligned current associated with the preliminary impulse. *J. Geophys. Res.* 108, 1416. doi:10.1029/2002JA009407

Fujita, S., Tanaka, T., Kikuchi, T., Fujimoto, K., and Itonaga, M. (2003b). A numerical simulation of the geomagnetic sudden commencement: 2. Plasma processes in the main impulse. *J. Geophys. Res.* 108, 1417. doi:10.1029/2002JA009763

Fujita, S., Tanaka, T., and Motoba, T. (2005). A numerical simulation of the geomagnetic sudden commencement: 3. A sudden commencement in the magnetosphere-ionosphere compound system. *J. Geophys. Res.* 110, A11203. doi:10.1029/2005JA011055

Fukushima, N. (1969). Equivalence in ground geomagnetic effect of chapman-vestine's and birkeland-alfven's electric current systems for polar magnetic storms. *Rep. Ionos. Space Res. Jap.* 23 (1969), 219–227.

Fukushima, N. (1976). Generalized theorem for no ground magnetic effect of vertical currents connected with Pedersen currents in the uniform-conductivity ionosphere. *Rep. Ionos. Space Res. Jpn.* 30, 35–40.

Gjerloev, J. W. (2012). The supermag data processing technique. *J. Geophys. Res.* 117. doi:10.1029/2012JA017683

Glassmeier, K. H., and Heppner, C. (1992). Traveling magnetospheric convection twin vortices: Another case study, global characteristics, and a model. *J. Geophys. Res.* 97, 3977. doi:10.1029/91JA02464

Glassmeier, K. H., Hönisch, M., and Untiedt, J. (1989). Ground-based and satellite observations of traveling magnetospheric convection twin vortices. *J. Geophys. Res.* 94, 2520. doi:10.1029/JA094iA03p02520

Huang, C.-S. (2005). Variations of polar cap index in response to solar wind changes and magnetospheric substorms. *J. Geophys. Res.* 110, A01203. doi:10.1029/2004JA010616

Huber, P., and Ronchetti, E. (2009). *Robust Stat.* 78. doi:10.2307/2287149

Iyemori, T., Takeda, M., Nose, M., and Toh, H. (2010). *Internal report of data analysis center for geomagnetism and space magnetism*. Japan: Kyoto University.Mid-latitude geomagnetic indices asy and sym for 2009 (provisional)

Keller, K. A., Hesse, M., Kuznetsova, M., Rastätter, L., Moretto, T., Gombosi, T. I., et al. (2002). Global mhd modeling of the impact of a solar wind pressure change. *J. Geophys. Res.* 107, 1126. SMP 21–1–SMP 21–8. doi:10.1029/2001JA000060

Kikuchi, T. (1986). Evidence of transmission of polar electric fields to the low latitude at times of geomagnetic sudden commencements. *J. Geophys. Res.* 91, 3101. doi:10.1029/JA091iA03p03101

Kikuchi, T. (2014). Transmission line model for the near-instantaneous transmission of the ionospheric electric field and currents to the equator. *J. Geophys. Res. Space Phys.* 119, 1131–1156. doi:10.1002/2013JA019515

Kikuchi, T., Tsunomura, S., Hashimoto, K., and Nozaki, K. (2001). Field-aligned current effects on midlatitude geomagnetic sudden commencements. *J. Geophys. Res.* 106, 15555–15565. doi:10.1029/2001JA900030

Kivelson, M. G., and Southwood, D. J. (1991). Ionospheric traveling vortex generation by solar wind buffeting of the magnetosphere. *J. Geophys. Res.* 96, 1661–1667. doi:10.1029/90JA01805

Lam, M. M., and Rodger, A. S. (2001). A case study test of araki's physical model of geomagnetic sudden commencement. *J. Geophys. Res.* 106, 13135–13144. doi:10.1029/2000JA900134

Laundal, K. M., Finlay, C. C., Olsen, N., and Reistad, J. P. (2018). Solar wind and seasonal influence on ionospheric currents from swarm and champ measurements. *J. Geophys. Res. Space Phys.* 123, 4402–4429. doi:10.1029/2018JA025387

Laundal, K. M., Gjerloev, J. W., Østgaard, N., Reistad, J. P., Haaland, S., Snekvik, K., et al. (2016). The impact of sunlight on high-latitude equivalent currents. *J. Geophys. Res. Space Phys.* 121, 2715–2726. doi:10.1002/2015JA022236

Laundal, K. M., Reistad, J. P., Hatch, S. M., Madelaire, M., Walker, S., Hovland, A., et al. (2022). Local mapping of polar ionospheric electrodynamics. *JGR. Space Phys.* 127. doi:10.1029/2022JA030356

Laundal, K. M., and Richmond, A. (2017). Magnetic coordinate systems. *Space Sci. Rev.* 206, 27–59. doi:10.1007/s11214-016-0275-y

Laundal, K. M., Yee, J. H., Merkin, V. G., Gjerloev, J. W., Vanhamäki, H., Reistad, J. P., et al. (2021). Electrojet estimates from mesospheric magnetic field measurements. *JGR. Space Phys.* 126, e2020JA028644. doi:10.1029/2020ja028644

Lee, D.-Y., and Lyons, L. R. (2004). Geosynchronous magnetic field response to solar wind dynamic pressure pulse. *J. Geophys. Res.* 109, A04201. doi:10.1029/2003JA010076

Liou, K., Newell, P. T., and Meng, C.-I. (2001). Seasonal effects on auroral particle acceleration and precipitation. *J. Geophys. Res.* 106, 5531–5542. doi:10.1029/1999JA000391

Madelaire, M., Laundal, K. M., Reistad, J. P., Hatch, S. M., Ohma, A., Haaland, S., et al. (2022). Geomagnetic response to rapid increases in solar wind dynamic pressure: Event detection and large scale response. *Front. Astron. Space Sci.* 9. doi:10.3389/fspas.2022.904620

Moen, J., and Brekke, A. (1993). The solar flux influence on quiet time conductances in the auroral ionosphere. *Geophys. Res. Lett.* 20, 971–974. doi:10.1029/92GL02109

Moretto, T., Ridley, A. J., Engebretson, M. J., and Rasmussen, O. (2000). High-latitude ionospheric response to a sudden impulse event during northward imf conditions. *J. Geophys. Res.* 105, 2521–2531. doi:10.1029/1999JA900475

Newell, P. T., and Gjerloev, J. W. (2012). Supermag-based partial ring current indices. *J. Geophys. Res.* 117, n/a. doi:10.1029/2012JA017586

Newell, P. T., Sotirelis, T., Liou, K., Meng, C.-I., and Rich, F. J. (2007). A nearly universal solar wind-magnetosphere coupling function inferred from 10 magnetospheric state variables. *J. Geophys. Res.* 112, n/a. doi:10.1029/2006JA012015

Pettigrew, E. D., Shepherd, S. G., and Ruohoniemi, J. M. (2010). Climatological patterns of high-latitude convection in the northern and southern hemispheres: Dipole tilt dependencies and interhemispheric comparisons. *J. Geophys. Res.* 115. doi:10.1029/2009JA014956

Reistad, J. P., Laundal, K. M., Østgaard, N., Ohma, A., Thomas, E. G., Haaland, S., et al. (2019). Separation and quantification of ionospheric convection sources: 2. The dipole tilt angle influence on reverse convection cells during northward imf. *JGR. Space Phys.* 124, 6182–6194. doi:10.1029/2019JA026641

Ridley, A. J., De Zeeuw, D. L., Manchester, W. B., and Hansen, K. C. (2006). The magnetospheric and ionospheric response to a very strong interplanetary shock and coronal mass ejection. *Adv. Space Res.* 38, 263–272. doi:10.1016/j.asr.2006.06.010

Russell, C. T., Ginskey, M., and Petrinec, S. M. (1994b). Sudden impulses at low latitude stations: Steady state response for southward interplanetary magnetic field. *J. Geophys. Res.* 99, 13403. doi:10.1029/94JA00549

Russell, C. T., Ginskey, M., and Petrinec, S. M. (1994a). Sudden impulses at low-latitude stations: Steady state response for northward interplanetary magnetic field. *J. Geophys. Res.* 99, 253. doi:10.1029/93JA02288

Russell, C. T., and Ginskey, M. (1995). Sudden impulses at subauroral latitudes: Response for northward interplanetary magnetic field. *J. Geophys. Res.* 100, 23695. doi:10.1029/95JA02495

Sabaka, T. J., Hulot, G., and Olsen, N. (2014). Mathematical properties relevant to geomagnetic field modeling. *Handb. Geomathematics*, 1–37. Springer. doi:10.1007/978-3-642-27793-1_17-2

Samsonov, A. A., and Sibeck, D. G. (2013). Large-scale flow vortices following a magnetospheric sudden impulse. *J. Geophys. Res. Space Phys.* 118, 3055–3064. doi:10.1002/jgra.50329

Samsonov, A. A., Sibeck, D. G., and Yu, Y. (2010). Transient changes in magnetospheric-ionospheric currents caused by the passage of an interplanetary shock: Northward interplanetary magnetic field case. *J. Geophys. Res.* 115. doi:10.1029/2009JA014751

Shi, Q. Q., Hartinger, M. D., Angelopoulos, V., Tian, A. M., Fu, S. Y., Zong, Q.-G., et al. (2014). Solar wind pressure pulse-driven magnetospheric vortices and their global consequences. *J. Geophys. Res. Space Phys.* 119, 4274–4280. doi:10.1002/2013JA019551

Sibeck, D. G. (1990). A model for the transient magnetospheric response to sudden solar wind dynamic pressure variations. *J. Geophys. Res.* 95, 3755. doi:10.1029/JA095iA04p03755

Slinker, S. P., Fedder, J. A., Hughes, W. J., and Lyon, J. G. (1999). Response of the ionosphere to a density pulse in the solar wind: Simulation of traveling convection vortices. *Geophys. Res. Lett.* 26, 3549–3552. doi:10.1029/1999GL010688

Stauning, P., and Troshichev, O. A. (2008). Polar cap convection and pc index during sudden changes in solar wind dynamic pressure. *J. Geophys. Res.* 113. doi:10.1029/2007JA012783

Sugiura, M. (1964). Hourly values of equatorial dst for the igy. *Ann. Int. Geophys. Yr.* 35.

Sugiura, M., and Kamel, T. (1991). Equatorial dst index 1957-1986. *IAGA Bull.* 40.

Takeuchi, T., Russell, C. T., and Araki, T. (2002). Effect of the orientation of interplanetary shock on the geomagnetic sudden commencement. *J. Geophys. Res.* 107, SMP 6-1–SMP 6-10. SMP 6–1–SMP 6–10. doi:10.1029/2002JA009597

Tamao, T. (1964). *A hydromagnetic interpretation of geomagnetic ssc**, 18. Japan. Rept. Ionosphere Space Res.

Tarpley, J. D. (1973). Seasonal movement of the sq current foci and related effects in the equatorial electrojet. *J. Atmos. Terr. Phys.* 35, 1063–1071. doi:10.1016/0021-9169(73)90005-6

Trivedi, N. B., Abdu, M. A., Pathan, B. M., Dutra, S. L. G., Schuch, N. J., Santos, J. C., et al. (2005). Amplitude enhancement of events in the South Atlantic anomaly region. *J. Atmos. Sol. Terr. Phys.Space Geophys.* 67, 1751–1760. doi:10.1016/j.jastp.2005.03.010

Tu, J., and Song, P. (2019). On the momentum transfer from polar to equatorial ionosphere. *JGR. Space Phys.* 124, 6064–6073. doi:10.1029/2019JA026760

Weimer, D. R. (2013). An empirical model of ground-level geomagnetic perturbations. *Space weather.* 11, 107–120. doi:10.1002/swe.20030

Welling, D. T., Love, J. J., Rigler, E. J., Oliveira, D. M., Komar, C. M., Morley, S. K., et al. (2021). Numerical simulations of the geospace response to the arrival of an idealized perfect interplanetary coronal mass ejection. *Space weather.* 19, e2020SW002489. doi:10.1029/2020SW002489

World Data Center For Geomagnetism, Copenhagen (2019). The Polar Cap North (PCN) index (definitive). *DTU Space, Geomagnetism.* doi:10.11581/DTU:00000057

Zhou, Y.-L., and Lühr, H. (2022). Initial response of nightside auroral currents to a sudden commencement: Observations of electrojet and substorm onset. *JGR. Space Phys.* 127, e2021JA030050. doi:10.1029/2021ja030050

Article III

6.3 Spatial Resolution in Inverse Problems: The EZIE satellite mission

M. Madelaire, K. Laundal, J. Gjerloev, S. Hatch, J. Reistad, H. Vanhamäki, C. Waters, A. Ohma, R. Mesquita and V. Merkin

Journal of Geophysical Research: Space Physics, Vol. 128, doi:10.1029/2023JA031394, 2023

JGR Space Physics

RESEARCH ARTICLE
10.1029/2023JA031394

Spatial Resolution in Inverse Problems: The EZIE Satellite Mission

Michael Madelaire[1], Karl Laundal[1], Jesper Gjerloev[1,2], Spencer Hatch[1], Jone Reistad[1], Heikki Vanhamäki[3], Colin Waters[4], Anders Ohma[1], Rafael Mesquita[2], and Viacheslav Merkin[2]

[1]Birkeland Centre for Space Science, University of Bergen, Bergen, Norway, [2]Johns Hopkins University Applied Physics Laboratory, Laural, MD, USA, [3]Space Physics and Astronomy Research Unit, University of Oulu, Oulu, Finland, [4]School of Mathematical and Physical Sciences, University of Newcastle, Callaghan, NSW, Australia

Key Points:

- A method for quantifying spatial resolution in inverse problems is presented
- We show that adding a ground magnetometer to a reconstruction based on Electrojet Zeeman Imaging Explorer satellite measurements improves accuracy locally and globally
- A method for reducing model complexity by combining regularization parameters is presented

Correspondence to:

M. Madelaire,
michael.madelaire@uib.no

Citation:

Madelaire, M., Laundal, K., Gjerloev, J., Hatch, S., Reistad, J., Vanhamäki, H., et al. (2023). Spatial resolution in inverse problems: The EZIE satellite mission. *Journal of Geophysical Research: Space Physics*, *128*, e2023JA031394. https://doi.org/10.1029/2023JA031394

Received 8 FEB 2023
Accepted 13 MAY 2023

Abstract Inverse modeling has become one of the primary methods for studying ionospheric electrodynamics, especially when using magnetic field measurements from below the ionosphere. We present a method for quantifying the spatial resolution in an inverse model for non-uniformly sampled spatial data. This method provides a tool for assessing if a model can resolve the physical phenomena of interest. We quantify the spatial resolution for the Spherical Elementary Current System basis functions to model the ionospheric dynamics. Our results apply to models with spatially confined model parameters, unlike spherical harmonics where the model parameters describe the amplitude of global surface functions. The method is demonstrated for the upcoming Electrojet Zeeman Imaging Explorer cubesat mission which will provide spatially distributed remote sensing measurements of the magnetic field in the mesosphere. We show that, including measurements from a single ground magnetometer can significantly improve the spatial resolution. However, the impact of including a ground magnetometer depends on the relative position of the station with respect to the mesospheric measurements. In addition, a method for reducing two regularization parameters to one is presented. Reducing the amount of regularization parameters simplifies the optimization problem and facilitates a fair comparison between the models with and without a ground magnetometer.

1. Introduction

Historically, ground magnetometers have played a key role in the study of ionospheric electrodynamics (Amm et al., 2010) as observations of the ground magnetic perturbation allow for the determination of an equivalent horizontal ionospheric electrical current (Friis-Christensen et al., 1988). It is now common to use inverse modeling techniques to create regional and global estimates of such currents (Laundal et al., 2022; Madelaire et al., 2022; Richmond & Kamide, 1988). While the techniques used are very useful tools, it is sometimes forgotten that the resulting model depends on a series of choices made prior to solving the inverse problem. If these choices alter, then the conclusions drawn might change. It is therefore crucial that we, as a community, understand the limitations of our models to avoid drawing false conclusions and improve the methods with which we analyze data.

The solution to an inverse problem is inherently probabilistic. Regardless of the method, for example, least squares or a Monte-Carlo Markov-Chain algorithm, the solution is the most probable, that is, other solutions of similar probability are likely to exist. The distribution of these solutions is the posterior model distribution. Analyzing the spread of the posterior model distribution quantifies how prior information about the model and measurement uncertainties propagate into the solution, referred to as model variance. Furthermore, the underlying assumptions in the physical model can be a source of uncertainty. Juusola et al. (2020) showed how accounting for ground induced currents can impact the estimated ionospheric currents and their uncertainties. In addition to model variance, spatial resolution is an important attribute that can be addressed. It is determined by multiple factors:

1. The spatial distance between model parameters, assuming they are locally defined, unlike spherical harmonics where the model parameters describe global surface functions;
2. The spatial distance between observations and in the case of magnetic fields the distance between the measurement and source current;
3. The choice of regularization parameters.

Regarding the second factor, ground magnetometers are ∼110 km from the ionospheric current responsible for the observed magnetic perturbation. As measurements are obtained from increasing distance from the source current its strength decreases, but this decrease is faster for small scale sizes resulting in a smoothing of the magnetic field with increasing distance (Laundal et al., 2021). This concept plays a large role in the spatial scales that can be resolved for example, by ground magnetometers. Regarding the third and perhaps least intuitive factor, it is common to perform zeroth order Tikhonov regularization or truncated singular value decomposition when an inverse problem is ill-posed. As the level of regularization increases the spatial resolution degrades. In other words, one should keep in mind when working with a regularized solution that the resulting spatial resolution will be affected by the choice of regularization parameter. The issue of choosing a regularization parameter can be addressed by using techniques such as the L-curve (Hansen, 1992). Bauer and Lukas (2011) provide a comprehensive comparison of different techniques. However, determining the right value of the regularization parameter is significantly more difficult when there is more than one.

Both model variance and spatial resolution are important attributes to evaluate. The former can be examined by determining the posterior model covariance (Cousins et al., 2015; Matsuo et al., 2015; Richmond & Kamide, 1988). Information about measurement uncertainty and prior information about the solution can be propagated through the inverse problem and provide the variance and covariance of the model parameters. The latter, to the knowledge of the authors, has not been explored in terms of the Spherical Elementary Current Technique (Spherical Elementary Current System [SECS]) (Amm & Viljanen, 1999). However, several studies have been reported from the tomography community (Gustavsson, 1998; Pascual-Marqui, 1999; Ren & Kalscheuer, 2020). Spatial resolution of a model parameter is often quantified by analyzing the spatial extent of its point-spread function (PSF). These functions are determined by the design of the inverse problem and can be analyzed without experimental data.

It is important to understand the spatial resolution with which a model can resolve structures. In one scenario, we may be looking for small scale structures in the model predictions to validate the existence of certain physical phenomena. A lack of such structures can only be considered significant if the model resolution implies that they should be detectable. It can be tempting to think of the spatial resolution purely as a function of the spatial distance between measurements, that is, the Nyquist sampling frequency. This would be applicable if a simple interpolation scheme was used on a series of measurements of a single magnetic field component. However, in an inversion scheme, for example, the SECS technique, the interpolation of the magnetic field is based on physics, that is, the existence of an equivalent current that can produce the observed magnetic field. Measurement uncertainty and the inclusion of prior information add to the complexity of the problem. The spatial resolution based on the Nyquist sampling frequency should therefore only be considered a lower limit.

As measurement techniques improve and provide increasingly spatial dense observations it becomes crucial to analyze the spatial resolution. Dense observations make it possible to resolve small scale features which provides opportunities to test hypotheses and perform new analyses. An example is the NASA satellite mission Electrojet Zeeman Imaging Explorer (EZIE) (Laundal et al., 2021; Yee et al., 2021) scheduled to launch late 2024 or early 2025. It will provide measurements of the magnetic field perturbation at mesospheric heights (∼80 km). In order to answer the science questions posed by the mission, the reconstruction of the ionospheric horizontal electric current needs to be achieved on mesoscales (100–500 km).

In this study, we address the question of spatial resolution using EZIE as an example and introduce ground magnetometer measurements to understand how these additional data affect the model. We present a method for determining a relationship between the two regularization parameters controlling the zeroth and first-order Tikhonov regularization applied in this study. Combining the two parameters facilitates choosing suitable parameter values. Section 2 describes the design of our inverse problem an previous existing work on spatial resolution, and explains how we calculate spatial resolution. Section 3 presents the method used to combine and determine the two regularization parameters. Section 4 compares model predictions, spatial resolution, and model variance with and without the inclusion of a ground magnetometer. Sections 5 and 6 discusses the results and concludes the study, respectively.

2. Spatial Resolution

The term resolution refers to the accuracy with which something can be observed/measured (e.g., grid resolution, temporal/spatial resolution of measurements). The aim of this study is to quantify the accuracy with which the

spatial structure of the ionospheric current can be resolved that is, answering the question: What is the smallest spatial scale our model can resolve? We refer to this as *spatial resolution*.

2.1. The Inverse Problem

The EZIE satellite mission (Laundal et al., 2021; Yee et al., 2021) consists of three cubesats flying in a pearls-on-a-string formation and will image the magnetic structure of the ionosphere. Each satellite will have four sensors pointing toward Earth measuring oxygen thermal emissions in a push-broom configuration. The EZIE technique is based on the Zeeman splitting of the 118 GHz oxygen emission. The result of this technique is the ambient magnetic field in the mesosphere (Yee et al., 2017, 2021). This novel method of measuring the magnetic field results in an unprecedented spatial resolution close to the source current (∼80 km altitude) compared to ground magnetometers (∼0 km altitude).

Laundal et al. (2021) showed how the magnetic perturbation observed by an EZIE satellite could be used to retrieve an equivalent ionospheric electric current using the SECS technique (Amm & Viljanen, 1999; Amm et al., 2002). The synthetic data used by Laundal et al. (2021) were based on the Gamera (MHD) model (Sorathia et al., 2020; Zhang et al., 2019). Magnetic field perturbations were determined using the Magnetosphere-Ionosphere Coupler/Solver code (Merkin & Lyon, 2010) rewritten for Gamera. The magnetic field perturbations are used together with a main field model and an atmospheric model to simulate mesospheric O_2 microwave emissions. A realistic model of the EZIE instrument performance (including various noise sources and uncertainties) was then used, together with the emissions, to generate realistic measurements. Finally, an inversion, explained in detail by Yee et al. (2021), was computed to retrieve simulated magnetic field measurements with realistic noise. Since that paper was published the viewing angle of the four sensors has been changed resulting in a new synthetic data set that will be used here. This new data set was produced in the same way as before and contains 3D vector magnetic field perturbations, along the satellite's four tracks. The measurements are provided with 3-s cadence in agreement with the EZIE integration time. Furthermore, the variance of each component along with the covariance between the three vector components is included.

Figure 1 is a snapshot of the radial magnetic field perturbation (ΔB_r) in the northern polar hemisphere from the MHD simulation used to generate the synthetic data set. The dotted lines represent the four tracks along which the satellite's four sensors measure the magnetic field. The black square is the boundary of the grid used in the inverse problem and the solid blue/orange/green/red lines, inside the black square, indicate the part of the satellite trajectory used in the inversion. The grid has been extended beyond the region where data are provided for illustration purposes. Model predictions outside the region of data are subject to extrapolation. It is outside the scope of this study to determine how far it is safe to extrapolate.

The forward problem can be written as

$$\boldsymbol{d} = \boldsymbol{G}\boldsymbol{m}, \tag{1}$$

where $\boldsymbol{d}$ is a column vector with measurements of the magnetic field components (ΔB_r, ΔB_θ, ΔB_ϕ), $\boldsymbol{m}$ is a column vector with model parameters that scale the strength of the divergence-free current field around each SECS pole and $\boldsymbol{G}$ is a matrix containing the linear relationship between $\boldsymbol{d}$ and $\boldsymbol{m}$, often referred to as the design matrix. An estimate of $\boldsymbol{m}$ can be written in terms of a regularized least squares solution (Aster et al., 2013; Neumaier, 1998; Tikhonov & Arsenin, 1977)

$$\begin{aligned} \tilde{\boldsymbol{m}} &= \boldsymbol{G}^{\dagger}\boldsymbol{d} = \left(\boldsymbol{G}^T\boldsymbol{C}_d^{-1}\boldsymbol{G} + \boldsymbol{C}_m^{-1}\right)^{-1}\boldsymbol{G}^T\boldsymbol{C}_d^{-1}\boldsymbol{d} \\ \boldsymbol{C}_m^{-1} &= \lambda_1\boldsymbol{I} + \lambda_2\boldsymbol{L}^T\boldsymbol{L}. \end{aligned} \tag{2}$$

The column vector $\boldsymbol{m}$ is the true model while $\tilde{\boldsymbol{m}}$ is the estimated model. Here $\boldsymbol{G}^{\dagger}$ is the generalized inverse of $\boldsymbol{G}$, $\boldsymbol{C}_d$ is the data covariance matrix, and $\boldsymbol{C}_m$ is the prior model covariance matrix. This inverse problem is ill-posed due to the spatial distribution of measurements and the amount of measurements compared to model parameters. Therefore, regularization is required to stabilize the solution. We employ a regularization scheme similar to Laundal et al. (2021); $\lambda_1\boldsymbol{I}$ minimizes the 2-norm of the model while $\lambda_2\boldsymbol{L}^T\boldsymbol{L}$ smooths the gradients of the SECS amplitudes in the magnetic east/west direction. Both λ_1 and λ_2 are regularization parameters to be determined, $\boldsymbol{I}$ is the identity matrix, and $\boldsymbol{L}$ describes the finite difference calculation of east/west gradients. The stability of

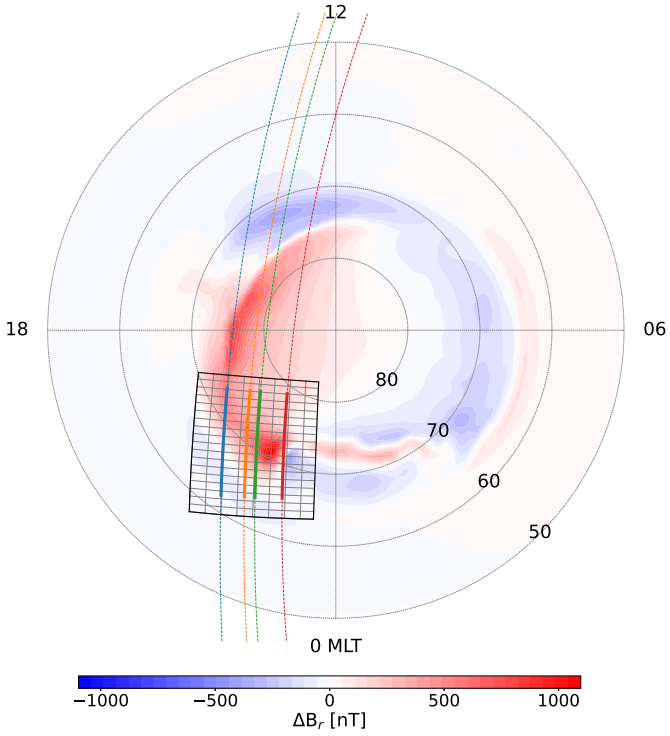

Figure 1. Illustration of ΔB_r (80 km altitude) in the northern polar hemisphere from an MHD simulation (Gamera (Sorathia et al., 2020; Zhang et al., 2019)). A crossing by one of the Electrojet Zeeman Imaging Explorer satellites is overlain and the foot points (80 km altitude) of its four sensors are indicated by the dotted lines. The black square is the boundary of the grid used in the inverse problem to reconstruct the equivalent ionospheric horizontal electric current. The gray grid is a coarse version of the cubed sphere grid on which the model is defined (Laundal et al., 2021). The solid colored lines show where the data used in our inverse problem is located. The point of the figure is to give an overview of the geometry of the inverse problem before we zoom in on the black square.

the model is challenged by the spatial separation between the four measurement tracks. The east/west gradient smoothing is included to stabilize the model between the tracks by assuming that current structures typically are aligned east/west. However, the solution is still data driven as there is no hard boundary on the possible gradients.

The variance of the model parameters and the covariance, as a result of measurement uncertainty and $\boldsymbol{C}_m$, is contained in the posterior model covariance matrix (Aster et al., 2013)

$$\boldsymbol{C}_{pm} = \left(\boldsymbol{G}^T \boldsymbol{C}_d^{-1} \boldsymbol{G} + \boldsymbol{C}_m^{-1}\right)^{-1}. \tag{3}$$

It is important to recognize that this is not an uncertainty related to how well the model reproduces the truth, but an uncertainty in the model parameters based on the information provided. As such, the posterior model covariance will decrease as the importance of regularization is increased. The uncertainty described by $\boldsymbol{C}_{pm}$ can be projected into any other quantity of interest, as long as there exists a linear relationship with the model. The posterior data covariance matrix can be written as

$$\boldsymbol{C}_{pd} = \boldsymbol{A}\boldsymbol{C}_{pm}\boldsymbol{A}^T, \tag{4}$$

which can be used to examine how variance in the model is reflected in predictions of the magnetic field.

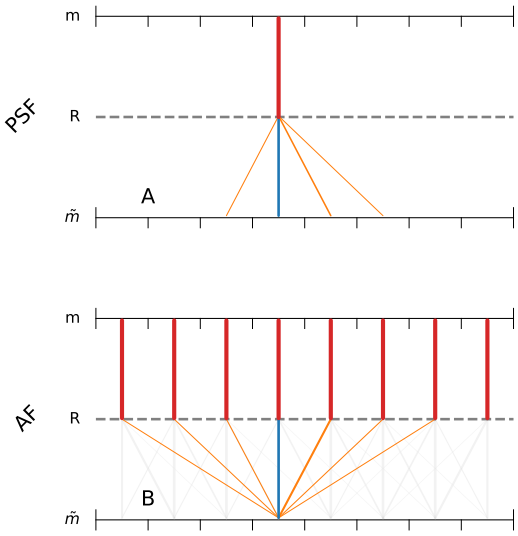

Figure 2. A conceptual illustration of averaging functions (AFs) and point-spread functions (PSFs). Imagine $\boldsymbol{R}$ to be a filter through which light passes. $\boldsymbol{m}$ is the light source and $\tilde{\boldsymbol{m}}$ is the observed pattern after the light passes through $\boldsymbol{R}$. Panel (a)illustrates how light from a single point source spreads after passing through $\boldsymbol{R}$, that is, a PSF. Panel (b) illustrates how the light observed at one location is a linear combination of multiple point sources, that is, an AF. The point of this figure is to provide a conceptual idea of AFs and PSFs before and after we introduce 2D versions and discuss how to derive information from them.

2.2. Quantifying Spatial Resolution

The subject of spatial resolution has been explored extensively in the tomography community; magnetotellurics, seismology, electroencephalograms, etc. (Gustavsson, 1998; Pascual-Marqui, 1999; Ren & Kalscheuer, 2020). Although the scientific topics vary from medicine to geophysics, the underlying inverse problem is often similar. In tomography, the model parameters, for example, conductivity, tend to be the quantity of interest. If a 5×5 grid is used then there are 25 unknown conductivity values. In our inverse problem, the model parameters are similarly defined on a grid and represent the amplitude of the divergence-free current associated with the individual SECS poles. Therefore, the methods for quantifying spatial resolution in tomography are applicable here. In this study, spatial resolution refers to the ability of the inverse problem to resolve a model parameter, that is, the strength of the divergence-free current in a single cell of the model grid.

The true model, $\boldsymbol{m}$, can be directly related to the estimated model, $\tilde{\boldsymbol{m}}$, by combining Equations 1 and 2

$$\tilde{\boldsymbol{m}} = \boldsymbol{G}^{\dagger}\boldsymbol{G}\boldsymbol{m} = \boldsymbol{R}\boldsymbol{m}. \tag{5}$$

The model resolution matrix, $\boldsymbol{R}$, describes how well the model parameters are resolved in the estimated model. If $\boldsymbol{R}$ is the identity matrix $\tilde{\boldsymbol{m}}$ is perfectly resolved, that is, $\tilde{\boldsymbol{m}} = \boldsymbol{m}$. However, for regularized solutions, it is more common that $\boldsymbol{R}$ contains non-zero off-diagonal elements suggesting that the model parameters are not perfectly resolved. The level to which the individual model parameters are resolved can be determined by examining the rows and columns of $\boldsymbol{R}$. The rows are referred to as averaging functions (AFs) and columns as PSFs. Miller and Routh (2007), Oldenborger and Routh (2009), and Ren and Kalscheuer (2020) provide an overview of these concepts. Here we attempt to give a conceptual illustration of AFs and PSFs by viewing $\boldsymbol{R}$ as a filter through which light passes. Figure 2a illustrates how a single point source is spread out as it passes through $\boldsymbol{R}$. This is a PSF and is equivalent to evaluating Equation 5 when $\boldsymbol{m}$ is a δ-function. Figure 2b shows how a single value of $\tilde{\boldsymbol{m}}$ is a linear combination of multiple point sources. This linear combination is the AF and is important for understanding the interpolation between different spatial locations.

Various approaches for quantifying spatial resolution have previously been presented. Tarantola and Valette (1982) suggested using the posterior model covariance matrix, Barmin et al. (2001), An (2012), and Chiao et al. (2014) suggested using AFs, and Miller and Routh (2007) and Oldenborger and Routh (2009) suggested using PSFs. However, as pointed out by Oldenborger and Routh (2009), several studies, including some cited here, confuse the terms AF and PSF. This is understandable as the AFs and PSFs can be identical if the inverse problem is not regularized or if truncated SVD was used (Oldenborger & Routh, 2009). Miller and Routh (2007) studied the resolving capabilities of AFs and PSFs and concluded that PSFs were better suited for determining spatial resolution. For this reason, we use the PSF when quantifying spatial resolution.

Figure 3 shows the absolute PSF for the model parameter located at the cyan dot on a map similar to Figure 1. Contrary to the conceptual illustration of a PSF in Figure 2, the PSFs are not limited to positive values as the model parameters can be negative. We therefore take the absolute value of the PSF before quantifying the spatial resolution. The figure also illustrates how PSFs are elongated in the east/west direction when constraints are placed on the smoothness of the east/west gradients. On the bottom and to the right of the map we show the projection of the PSF onto one axis. The projection is the sum over the PSF in a specific direction and can be thought of as a marginal distribution. In addition, Figure 3 summarizes the result of three methods for quantifying spatial resolution. Barmin et al. (2001) and An (2012) suggested quantifying the spread by fitting an appropriate function to the PSF. Two ellipses indicating a non-linear fit of a 2D Gaussian function. The innermost is the Full Width Half Maximum (FWHM) (2.335σ) while the outermost is $\pm 3\sigma$, where σ is the standard deviation of the fitted Gaussian distribution. The FWHM of the marginal distributions is shown as an orange shaded area overlain the

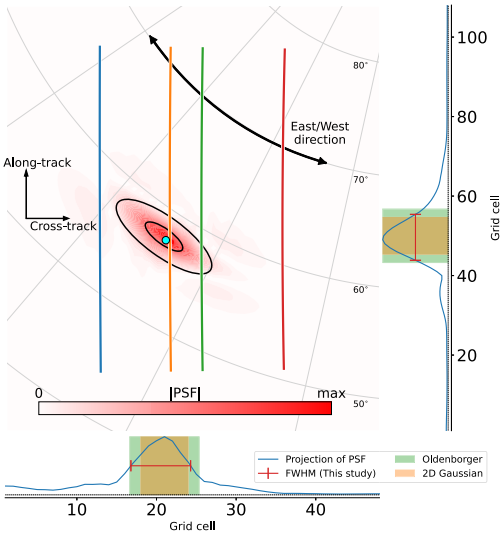

Figure 3. Illustration of a point-spread function (PSF) and a comparison of three ways to quantify spatial resolution. The map is a close-up of the black square in Figure 1 and the contour is the absolute of the PSF associated with the model parameter located at the cyan dot. The four colored vertical lines indicate the foot points of the satellite's four sensors and the black ellipses represent a non-linear fit of a 2D Gaussian function. The graphs on the bottom and the right-hand side are projections of the PSF. The green shaded area reflects the result of using the spread metric suggested by Oldenborger and Routh (2009), under the assumption that the PSF is Gaussian. The orange shaded area is the Full Width Half Maximum (FWHM) of the marginal distribution of the 2D Gaussian fit. The red line is the FWHM of the projection of the PSF which we use to quantify spatial resolution. The point of this figure is to help visualize a PSF and provide a platform on which methods for quantifying spatial resolution can be compared.

projected PSF. The FWHM is the minimum distance between two impulses for them to be distinguished from each other. This method is informative as it provides the rotation of the PSF. The downside is its complexity as it requires a non-linear fit which when automated can result in substantial errors.

Oldenborger and Routh (2009) presented a spread metric, similar to Miller and Routh (2007), based on the definition of variance using the squared PSF as a probability mass function. To translate the spread metric into the FWHM one must assume some known distribution. We assumed the PSF to be Gaussian, requiring a scaling of the spread metric by $\sqrt{2}$, the result is illustrated as a green-shaded area. We quantify spatial resolution as the FWHM of the projected PSF, shown on the axis of Figure 3. This is done by locating the first point, on either side of the maximum, to fall below 50% of the maximum. Linear interpolation between the point above and below 50% of the maximum is used to estimate the FWHM. The results are shown as red lines spanning the projected PSF. The spatial resolution estimates are provided in the cross- and along-track directions as these reflect the geometry of the EZIE measurements.

3. Combining Regularization Parameters

We are interested in quantifying spatial resolution to better understand the performance of a model. Similarly, we are interested in how combining measurements from different sources affects spatial resolution, for example, EZIE and ground magnetometer measurements. When comparing the resolution of two models it is crucial that the regularization parameters are determined objectively. It is tempting to tune them manually until the model predictions look "right," but these parameters have a direct impact on the spatial resolution and model variance and should be chosen with care. If not, one might under- or over-regularize resulting in a scenario where the results are not reproducible since values were chosen subjectively. This is where methods such as the L-curve (Hansen, 1992) come into play. The L-curve allows a trade-off between minimizing the data misfit and the part of the cost function controlled by the regularization. However, the L-curve is commonly applied to problems with a single regularization parameter and we have two. Therefore, we present an approach to determine a relationship between λ_1 and λ_2, referred to as the λ-relation, allowing the use of the L-curve for a single regularization parameter.

The λ-relation is based on $\boldsymbol{R}$. The AFs (rows of $\boldsymbol{R}$) describe the linear relationship between $\tilde{\boldsymbol{m}}$ and $\boldsymbol{m}$. The AF of a model parameter spatially close to a measurement will be sparse as that model parameter only will depend on other model parameters close to itself. The AF of a model parameter far away from measurements will depend on a much larger group of model parameters as those close to it also are poorly constrained by data. When the east/west gradients are smoothed, controlled by λ_2, the model parameters between the measurements, for example, the green and red data track, will become less dependent on the model parameters in their immediate vicinity and more dependent on those close to measurements. In other words, for moderate values of λ_2 the AF between the data tracks becomes more sparse. If the gradient smoothing is increased the dependence will not only be on the model parameters around the nearest measurements but also on those close to measurements on other data tracks (following a path of equal latitude). At this point, the AF becomes less sparse. We find that the models perform best when the model parameters between data tracks mainly depend on the nearest measurements. Achieving this coincides with the sparsest AF, that is, the linear relationship that depends on the least amount of other model parameters.

Figure 4 is a conceptual illustration of how we determine the λ-relation. Figure 4a is a map of the Hoyer index (Hoyer, 2004) over the AFs for a specific λ_1 and λ_2. The Hoyer index,

$$\text{information} = \frac{\sqrt{n} - \frac{\|\text{AF}\|_1}{\|\text{AF}\|_2}}{\sqrt{n} - 1}, \tag{6}$$

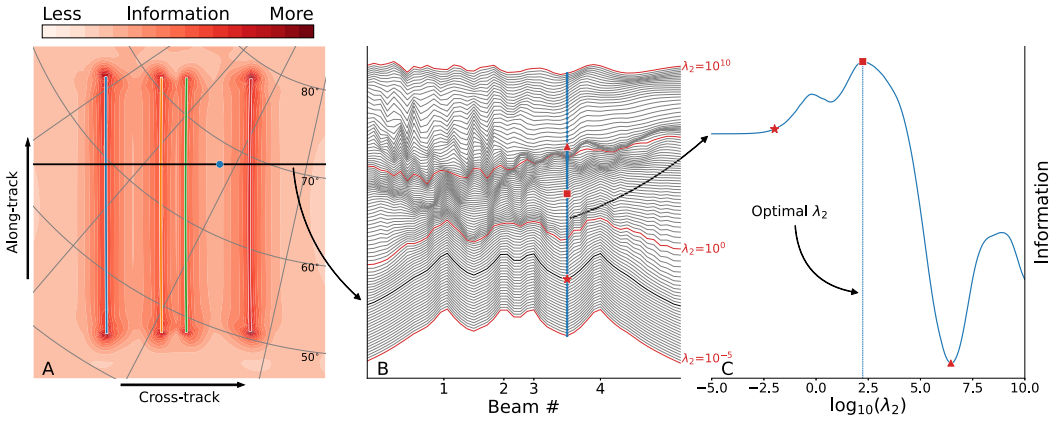

Figure 4. Conceptual illustration of how the λ-relation is determined. Panel (a) shows the Hoyer index of the averaging functions for a specific λ_1 and λ_2. Panel (b) shows how the cross-section in panel (a) changes with λ_2, while keeping λ_1 constant. Panel (c) shows how the Hoyer index changes as a function of λ_2 for the model parameters furthest away from data. The point of this figure is to provide a conceptual idea of how the "optimal" λ_2 is determined for a given λ_1.

is the normalized ratio of the 1- and 2-norm making it well suited for quantifying information/sparsity/entropy (Hurley & Rickard, 2008). Here n is the size of the AF (the number of model parameters). Areas with high information reflect sparse AFs while areas with low information reflect denser AFs. Figure 4b shows a movie of how a cross-section of the map in Figure 4a changes if λ_1 is kept constant and λ_2 is varied. When λ_2 is small, that is, little to no gradient smoothing, there is a big difference between the information contained in the AFs close to and further away from measurements. However, as λ_2 increases the relative difference between the information contained in the AFs decreases. We are specifically interested in how information in the AF belonging to the model parameter furthest away from data changes as a function of λ_2. This model parameter is located halfway between the green and red track and its position on the cross-section is illustrated by a blue dot and line in Figures 4a and 4b, respectively. Figure 4c shows how the information in that AF changes as a function of λ_2. Initially, when λ_2 increases there is little to no change. At around $\log_{10}(\lambda_2) = -2$ (red star) the information starts to increase. Then, around $\log_{10}(\lambda_2) = 2.5$ (red square) the information is maximized and starts to decrease. This means that for the specific λ_1 used to create Figure 4 we have found the λ_2 that maximizes the information used to determine the model parameter furthest away from measurements.

By repeating the process summarized in Figure 4 for a series of λ_1 values a λ-relation can be generated as illustrated in Figure 5. For each value of λ_1 the λ_2 value that maximizes information is selected. In addition, we select the surrounding nine λ_2 that have the next highest information. This is done to help provide the B-spline fit, used to make the λ-relation continuous, information about the gradient. The λ-relation is shown for both cases explored in Section 5, that is, with and without a ground magnetometer.

It is now possible to solve the inverse problem repeatedly while changing λ_1, using the λ-relation to determine λ_2, to create an L-curve from which the "optimal" pair of λ_1 and λ_2 can be determined. The L-curve does have some difficulties. The best trade-off is found in the "knee." There have been many suggestions on how to determine this point, some of which are discussed by Hansen et al. (2007). We use the Kneedle algorithm (Satopaa et al., 2011), via. the python implementation (Arvai, 2020), that is designed to find the point of largest curvature. Figure 6 shows the L-curve. The knee has been marked by a black dot from which λ_1 and λ_2 can be determined. These are the λ_1 and λ_2 values used to create the models examined in Section 5.

4. Results

In this section, we compare model predictions, spatial resolution, and model variance when solving the inverse problem with synthetic measurements from EZIE with and without a single ground magnetometer. The ground magnetometer was included by adding two 3D vector measurements assuming a 1-min cadence, which

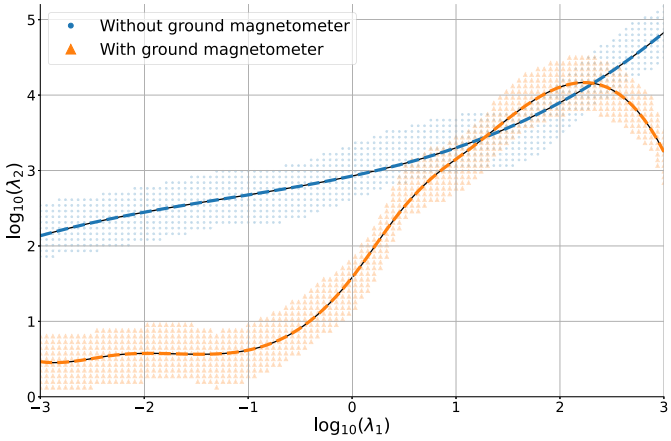

Figure 5. The λ-relations for the two models using Electrojet Zeeman Imaging Explorer data with (orange) and without (blue) an additional ground magnetometer. The dots show the 10 λ_2 that result in the highest Hoyer index for each λ_1. The dashed lines are B-spline fits to make the λ-relation continuous. The purpose of this figure is to explain how we go from the figure to a continuous λ-relation.

approximately corresponds to the temporal span of the EZIE measurements used. The two ground magnetometer measurements are taken directly from the MHD simulation, thus reflecting the truth. Their uncertainty is assumed to be 1 nT, which is 2–3 orders of magnitude lower than the EZIE measurements.

EZIE and ground magnetometers both provide measurements below the ionosphere, which means they are only affected by the divergence-free part of the ionospheric electric current. Therefore, these measurements are easily combined in an inversion. Figure 7 compares the truth (MHD, first column), to the predictions from two models: one based only on EZIE measurements (second column), and one that also includes a single ground magnetometer (third column). Each row refers to one of the magnetic field components (ΔB_r, ΔB_θ, and ΔB_ϕ). The gray arrows illustrate the divergence-free ionospheric electric current, from the MHD, responsible for the magnetic

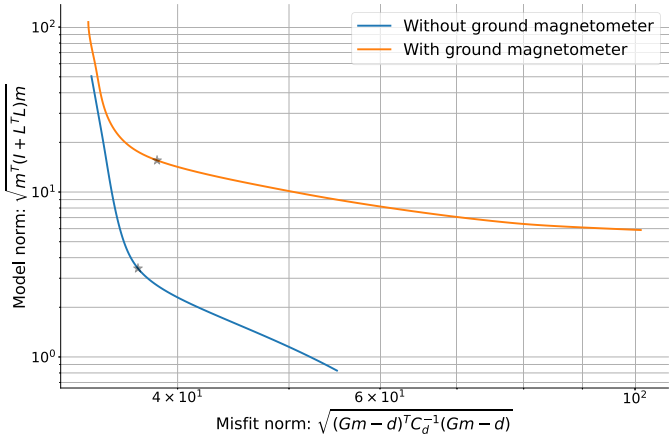

Figure 6. L-curve for the two models after testing numerous pairs of λ_1 and λ_2. The black dot indicates the best trade-off and was determined using the Kneedle algorithm (Satopaa et al., 2011). The point of this figure is to show how both regularization parameters are easily determined using the classic L-curve after having determined the λ-relation.

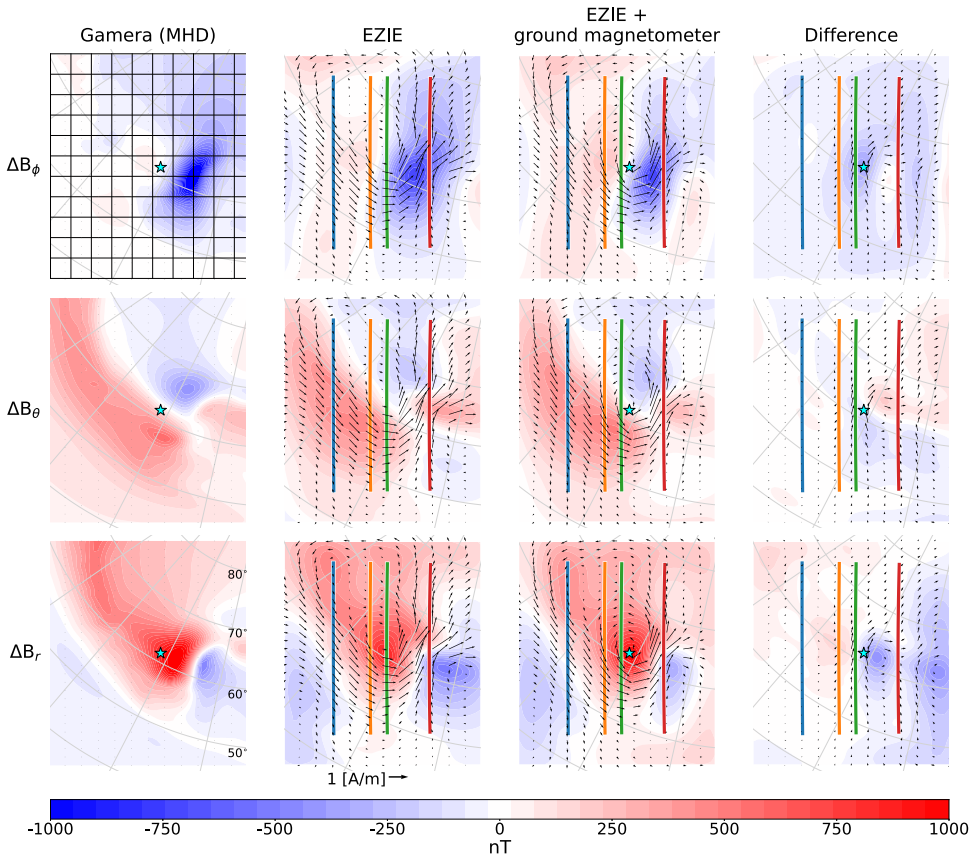

Figure 7. Comparison of the truth (MHD), first column, the model predictions based on Electrojet Zeeman Imaging Explorer measurements, second column, and model predictions after including the ground magnetometer, third column. The difference between the two models is shown in the fourth column, calculated by subtracting the third column from the second. The ground magnetometer's location is marked by a star. Each row shows a contour of one of the three magnetic field components $(\Delta B_\phi, \Delta B_\theta, \Delta B_r)$. The gray arrows show the divergence-free current from the MHD, while the black arrows show the equivalent ionospheric current determined from the models. The point of this figure is to show how well the models reproduce the truth.

perturbation below the ionosphere while the black arrows illustrate the equivalent ionospheric electric current as produced by the models. The four vertical lines (blue/orange/green/red) indicate the location of the EZIE measurements at 80 km altitude while the cyan star marks the location of the ground magnetometer.

Both the magnetic perturbation and ionospheric current are reconstructed rather well by both models. Outside the regions of data, the models perform worse which is no surprise as they are simply extrapolating. Between the green and red data tracks the MHD shows a current vortex that is better resolved in the model that includes a ground magnetometer. The difference between the two models is shown in the fourth column of Figure 7, calculated by subtracting the third column from the second. The difference is most prominent near the ground magnetometer. However, such qualitative comparisons do not provide details of the inherent properties of the models. Quantifying spatial resolution and model variance can provide an idea of how trustworthy the features in Figure 7 are and what physical phenomena can be resolved.

The first column of Figure 8 shows the spatial resolution in the cross- and along-track directions for the model based only on EZIE measurements, calculated as described in Section 2.2. The black background is visible when

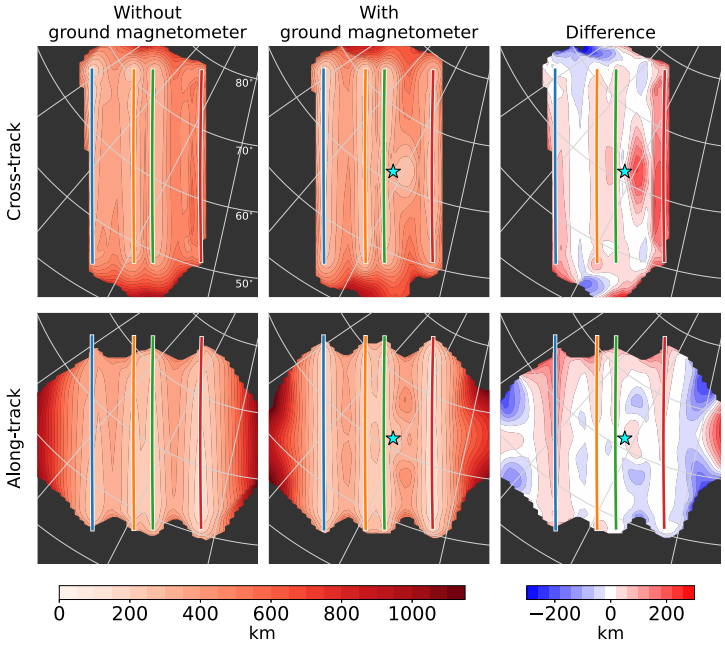

Figure 8. Comparison of the spatial resolutions in both cross- and along-track directions before and after including a single ground magnetometer. The difference, in the third column, is calculated by subtracting the second column from the first. A positive value thus means that the spatial resolution improved after including the ground magnetometer. The point of this figure is to show how a single measurement with low uncertainty, for example, from a ground magnetometer, can lead to significant improvements in the spatial resolution.

the FWHM could not be determined. This occurs when it is not possible to find a point smaller than 50% of the maximum on either side of the maximum. We see that the cross-track resolution is around 200–400 km with the lowest values close to the data and the highest values located between tracks. Looking at the along-track resolution we find that it is slightly lower, around 100–300 km. The areas where the FWHM could not be determined change depending on the direction of the spatial resolution. We suggest only considering the spatial resolution determined at locations constrained by more than one data point. That is, any value outside the blue and red track should be ignored, as well as values too close to the beginning and end of the data tracks. The second column in Figure 8 shows the spatial resolution after introducing the ground magnetometer while the third column shows the difference. The second column was subtracted from the first which means that a positive value indicates that the resolution has improved after including the ground magnetometer.

The spatial resolution in the cross-track direction between the ground magnetometer and the red track has improved by up to ∼200 km. Oddly, little to no improvement is seen between the ground magnetometer and the green/orange track which could be an indication of the minimum scale size that a ground magnetometer can resolve due to its distance to the ionosphere. The spatial resolution in the along-track direction did not significantly change. However, symmetrically above and below the ground magnetometer, in the along-track direction, the spatial resolution degraded slightly. We attribute this to the elongation of the PSF toward the ground magnetometer due to its low measurement uncertainty. Additionally, the inclusion of the ground magnetometer has an indirect global impact on the spatial resolution. By including the ground magnetometer the amount of east/west gradient smoothing necessary to stabilize the model has decreased. As a result the PSFs become more circular. This deformation occurs in east/west and north/south which maps into the cross- and along-track directions differently depending on location. The changes in spatial resolution due to the deformation of the PSFs is most pronounced in the along-track direction close to the data tracks. The improvements in spatial resolution after inclusion of the

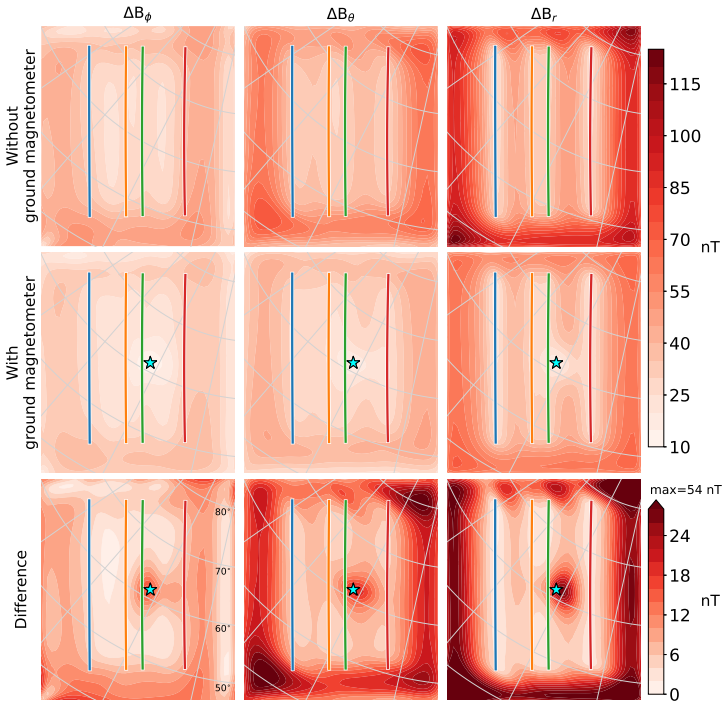

Figure 9. Comparison of the posterior data variance before and after including the ground magnetometer. The third row shows the difference between the first two rows, calculated by subtracting the second row from the first. The point is to show that even though the ground magnetometer mainly impacted the spatial resolution locally it affected the posterior data covariance both locally and globally.

ground magnetometer depends on the location and noise level of the ground magnetometer as well as the noise level and spatial separation between the EZIE measurements. It is therefore not possible to provide a single quantity to summarize the expected improvement when including ground magnetometer measurements.

Although the spatial resolution becomes worse in some areas after introducing the ground magnetometer, one should not conclude that the ground magnetometers have a negative impact on the model. This is clear when examining the posterior data covariance matrix, $\boldsymbol{C}_{pd}$. In Figure 9 the square root of the diagonal of $\boldsymbol{C}_{pd}$ is visualized when $\boldsymbol{A}$ (Equation 4) is the linear relationship between the model and the individual magnetic field components. The columns are ordered as ΔB_ϕ, ΔB_θ, and ΔB_r while the first two rows refer to the model with and without a ground magnetometer, respectively. Furthermore, the third row shows the difference between the models, calculated by subtracting the second row from the first. This implies that positive values are improvements due to the inclusion of the ground magnetometer. There are two clear differences. First, the variance decreases on a global level as the ground magnetometer measurements provide the model with additional information about the magnitude of the magnetic perturbation. Second, the variance is decreased in the area immediately around the ground magnetometer.

We did not find any substantial differences from the comparison of model predictions in Figure 7, except close to the current vortex after the introduction of the ground magnetometer. However, Figure 8 showed a clear improvement in spatial resolution. Figure 9 showed how the variance in the model prediction was reduced, both globally and locally. It should therefore be clear that examining attributes such as spatial resolution and model variance should be a more common practice as they contain crucial information regarding the design of the inverse problem and the performance of its solution.

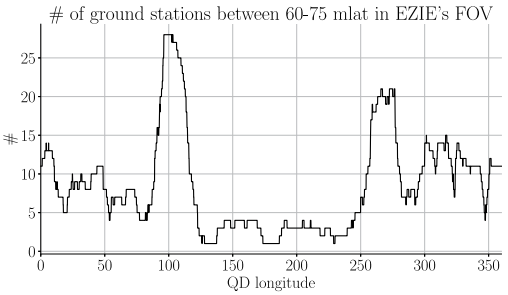

Figure 10. The estimated number of ground magnetometers in the Electrojet Zeeman Imaging Explorer field of view. This is based on the ground magnetometers available at SuperMag. The point of this figure is to show that the improvements, after including the ground magnetometer, shown in our study will be possible to achieve in every orbit and likely be better as many ground magnetometers will be available (the median is 7).

5. Discussion

In this study, we presented a method for quantifying spatial resolution when modeling ionospheric dynamics with SECS. Our method quantifies the spatial resolution of the model parameters, that is, the strength of the divergence-free current, by assessing the width of PSFs. This type of approach is called a resolution test (Aster et al., 2013). In general, the resolution test involves testing how the true model, $\boldsymbol{m}$, changes when passed through $\boldsymbol{R}$. The most common approach is to use a spike model, which we refer to as a δ-function, where only one model parameter is non-zero (Rawlinson & Spakman, 2016). Using a δ-function is in reality a special case. It would likewise be informative to test true models with different shapes, sizes, and/or gradients. However, it is not feasible to test all possible scenarios and we therefore only show resolution tests with the δ-function. In addition to the strength of the divergence-free current, we are also interested in the horizontal current and associated magnetic field that can be derived from the model parameters. The magnetic field has three components and the horizontal current two, totaling five quantities. To avoid confusion over six different spatial resolutions we have chosen to work specifically with those related directly to the model parameters. It is possible to examine the spatial resolution of the other quantities. However, this requires formulation of a structure, for example, in ΔB_r, in terms of a true model that can be passed through $\boldsymbol{R}$. The resulting model can be used to calculate model predictions that can be compared with the truth. The only issue is how to get the true model. One way, in case of synthetic data, could be to solve the inverse problem with a very high and even data coverage, along with no measurement noise. This would likely make the inverse problem well-posed and thus require virtually no regularization. The resulting model could be considered the truth.

It is tempting to think that an alternative to examining $\boldsymbol{R}$ is to test how well a model can reproduce a checkerboard pattern. The size of the tiles could be varied to find the smallest resolvable size. Although the method is intuitive and illustrative, Lévêque et al. (1993) showed it to be misleading as it might be possible to resolve small scale structures while large scale structures are poorly resolved.

We advocate for the use of spatial resolution and model variance to better understand the inherent properties of inverse problems. Spatial resolution is especially compelling as it does not require experimental data and can therefore play an important role when designing the inverse problem. We compared the spatial resolution of two models in Figure 8 and saw improvements when a single ground magnetometer was included. Figure 10 shows how many ground magnetometers will be in EZIE's field of view as a function of quasi-dipole longitude (Laundal & Richmond, 2017), in the northern hemisphere. Figure 10 is based on the ground magnetometers available from SuperMag (https://supermag.jhuapl.edu/). This assumes that the distance between the blue and red track is 1,000 km, the orbit is north/south and measurements are taken between 60° and 75° latitude. Based on the median of the distribution there will typically be around seven ground magnetometers in EZIE's field of view. Therefore, it seems natural to include ground magnetometers as they can provide valuable information. Likewise, the measurements by EZIE fit neatly into the SECS-based Lompe technique (Hovland et al., 2022; Laundal et al., 2022), that like AMIE Richmond and Kamide (1988) and AMGeO Collaboration (2019) combines multiple types of measurements to model the ionospheric electric field.

In this study ground magnetometer measurements were included to illustrate the value of using spatial resolution and model variance to compare and assess the performance of models. It is outside the scope of this study to analyze the implications of including multiple ground magnetometer stations. However, in a future study it would be interesting to carry out case studies for when the EZIE orbit intersects with certain ground magnetometer arrays, for example, North America, Greenland, and Fennoscandia.

Spatial resolution, model variance and regularization are related. The smallest spatial scale a model can resolve increases when the regularization is increased. It is therefore clear that the choice of regularization parameter is important. Figure 4 shows how the λ-relation is determined. The question is; what range of λ_1 and λ_2 should be tested? It can be a good idea to scale λ_1 by some quantity of $\boldsymbol{G}^T\boldsymbol{C}_d^{-1}\boldsymbol{G}$, for example, median of the diagonal,

such that $\lambda_1 = 1$ will have a significant impact. By scaling λ_1 in this way, we are almost certain to find the desired trade-off with $\lambda_1 \in [10^{-3}; 10^{3}]$. Unfortunately, determining a range for λ_2 is not as straightforward. It can be scaled in a similar fashion as λ_1, but since it controls gradient smoothing its magnitude does not have to be close to 1. The example shown here is well-behaved, such that the surface formed by λ_1, λ_2 and the Hoyer index has one clear maximum before the model solution becomes dominated by zonal structures. For this reason, it has not been necessary to define an upper threshold for λ_2. However, this can become relevant if the measurement geometry changes. The measurement geometry is not only determined by the viewing angle of the instruments, but also by where the measurements lie on the spherical surface and the declination of the tracks. Changing these aspects of the measurement geometry determines if λ_2, controlling east/west gradient smoothing, smooths structures cross-track direction, along-track direction or some direction in between. In addition, it is possible for the gradient smoothing to essentially loop around on itself, at higher latitudes. This is observed as an additional peak in the Hoyer index at large λ_2 values. By examining the PSF and/or model solution for this last peak it is easily concluded that it is undesirable. We therefore suggest that the localization error (Oldenborger & Routh, 2009) can be used to indicate the upper limit of λ_2. The localization error is determined by evaluating the Euclidean distance between the maximum of the δ-function and the PSF. Ideally, the two maxima should be at the same location. However, small deviations are likely to occur. By examining the localization error we found that a discontinuous increase occurs at large λ_2 values and the λ_2 at which it happens increases with λ_1. By locating the discontinuity a threshold after which λ_2 should not be increased further can be determined.

The λ-relation is defined based on how the AF of a specific model parameter behaves. If we chose another model parameter the relation would change. However, the geometry between the green and red track of Figure 4 is symmetric, and changing to a neighboring model parameter in the along-track direction would not lead to any significant change. This is not the case near the end of the data tracks. At the top of the red track, it is easy to find a measurement that does not have a counterpart on the green track if a path of equal latitude is followed. This is an issue because we have imposed prior information about how the structures are aligned (east/west) and thus with sufficient east/west gradient smoothing model parameters on such a path are subject to extrapolation and not interpolation. Therefore, it is wise to avoid determining the λ-relation based on model parameters that are not constrained by data on either side when λ_2 is increased.

The presented method for combining regularization parameters works well for the measurement geometry of EZIE. However, there are alternatives to tackling multiple regularization parameters. Belge et al. (2002) developed a method for creating an L-hypersurface allowing for the determination of any number of regularization parameters. Working in multiple dimensions tends to be computationally expensive and it can therefore be advantageous to try and reduce the dimensionality by using the λ-relation. It is also possible to consider these regularization parameters as model parameters and embrace the non-linearity of the problem. If so, a solution can be found using Monte-Carlo Markov-Chain algorithms. In these types of algorithms the posterior model distribution is explored by continuously solving the forward problem. However, with a large number of model parameters comes the curse of dimensionality which can make these algorithms impractical. It is especially difficult if the posterior model covariance turns out to be multi-modal. Alternatively, *model selection* (Akaike, 1974; Virtanen et al., 2018) can be used to determine an adequate level of model complexity. Here the grid resolution could be varied while calculating the likelihood of the associated solution, for example, using the Akaike Information Criterion or the Bayesian Information Criterion (Akaike, 1974; Burnham & Anderson, 2002). The solution that reproduces the observations best while keeping the model complexity low can then be selected. This could also be done with anisotropic grids to accommodate variations in data coverage and/or quality. Instead of using an anisotropic grid it is also possible to use spatially varying regularization parameters such that local variations of a regularization parameter does not affect the solution globally (Roininen et al., 2014). The approach for determining the λ-relation (Figure 4) was initially carried out for all cross-track locations to determine position dependent east/west smoothing. However, this was found to cause multi modality of the PSFs and thereby affect the spatial resolution estimation and was therefore not used.

The EZIE satellites will measure 118 GHz oxygen emission using the Microwave Electrojet Magnetogram (Yee et al., 2021). In the mesosphere, the foot point will be a few tens of km, but vary with viewing angle and the altitude of the satellite. Spatial scales small enough to vary within the MEM's field of view could lead to a higher measurement uncertainty. The MHD, shown in Figure 1, contain large-scale features. In the scenario where parts of the measurement track is co-located with structures small enough to affect measurement uncertainty the spatial resolution of the surrounding area could be affected.

6. Conclusion

In this study we have presented a method for quantifying spatial resolution, and illustrated this via an example in which the SECS technique (Amm et al., 2002) was employed to model the equivalent ionospheric current using synthetic measurements from one of the EZIE satellites (Laundal et al., 2021; Yee et al., 2021). The spatial resolution is found to be around 200–400 km in the cross-track direction and around 100–300 km in the along-track direction. This is sufficient to resolve mesoscale features (100–500 km), which is necessary to answer the science questions posed by the EZIE mission. In addition, we have compared the spatial resolution and model variance to another model which includes a single ground magnetometer. This comparison shows that the cross-track spatial resolution around the ground magnetometer improves. However, the comparison also illustrated that there are limitations to how small spatial scales the ground magnetometer can resolve. This is due to the ∼80 km distance between the peak 118 GHz thermal oxygen emission and the ground location. Comparison of the posterior data covariance of the two models shows how inclusion of the ground magnetometer reduces the variance locally and globally. We attribute this to a significantly lower uncertainty associated with the ground magnetometer measurements, thus providing a better constraint for the magnitude of the model parameters. We hope that by further developing the concept of spatial resolution to the ionospheric science community we improve the way that we analyze and draw conclusions based on inverse models.

Besides the quantification of spatial resolution and comparison of models, we have presented a method for combining two regularization parameters based on the model resolution matrix. This makes determining the trade-off between minimizing data misfit and the regularization term easier. Our method enables comparison between the two models, one with and one without a ground magnetometer, as the need to choose the regularization parameters by manual tuning is not needed. In particular, the method is highly efficient in scenarios where measurement geometry remains constant, for example, ground magnetometer arrays, as it does not depend on the actual measurement values, but rather the location and uncertainty of the measurements.

Data Availability Statement

The simulation dataset used in this study is available at Zenodo via https://doi.org/10.5281/zenodo.7823088 (Madelaire, 2023).

Acknowledgments
This work was funded by the Research Council of Norway (RCN) under Contract 223252/F50. KL and JR were also funded by the RCN under Contract 300844/F50. KL and SH were also funded by the Trond Mohn Foundation.

References

Akaike, H. (1974). A new look at the statistical model identification. *IEEE Transactions on Automatic Control*, *19*(6), 716–723. https://doi.org/10.1109/TAC.1974.1100705

AMGeO Collaboration. (2019). A collaborative data science platform for the geospace community: Assimilative mapping of geospace observations (AMGeO) v1.0.0. *Zenodo*. https://doi.org/10.5281/zenodo.3564914

Amm, O., Engebretson, M. J., Hughes, T., Newitt, L., Viljanen, A., & Watermann, J. (2002). A traveling convection vortex event study: Instantaneous ionospheric equivalent currents, estimation of field-aligned currents, and the role of induced currents. *Journal of Geophysical Research*, *107*(A11), SIA1-1–SIA1-11. https://doi.org/10.1029/2002JA009472

Amm, O., Opgenoorth, H., & Viljanen, A. (2010). Ground-based magnetometer arrays in space research: A brief review. In *Egu general assembly conference abstracts* (p. 4889).

Amm, O., & Viljanen, A. (1999). Ionospheric disturbance magnetic field continuation from the ground to the ionosphere using spherical elementary current systems. *Earth Planets and Space*, *51*(6), 431–440. https://doi.org/10.1186/BF03352247

An, M. (2012). A simple method for determining the spatial resolution of a general inverse problem. *Geophysical Journal International*, *191*(2), 849–864. https://doi.org/10.1111/j.1365-246X.2012.05661.x

Arvai, K. (2020). kneed. *Zenodo*. https://doi.org/10.5281/zenodo.6496267

Aster, R. C., Borchers, B., & Thurber, C. H. (2013). Chapter four - Tikhonov regularization. In R. C. Aster, B. Borchers, & C. H. Thurber (Eds.), *Parameter estimation and inverse problems* (2nd ed.), (pp. 93–127). Academic Press. https://doi.org/10.1016/B978-0-12-385048-5.00004-5

Barmin, M. P., Ritzwoller, M. H., & Levshin, A. L. (2001). A fast and reliable method for surface wave tomography. *Pure and Applied Geophysics*, *158*(8), 1351–1375. https://doi.org/10.1007/PL00001225

Bauer, F., & Lukas, M. A. (2011). Comparing parameter choice methods for regularization of ill-posed problems. *Mathematics and Computers in Simulation*, *81*(9), 1795–1841. https://doi.org/10.1016/j.matcom.2011.01.016

Belge, M., Kilmer, M. E., & Miller, E. L. (2002). Efficient determination of multiple regularization parameters in a generalized L-curve framework. *Inverse Problems*, *18*(4), 1161–1183. https://doi.org/10.1088/0266-5611/18/4/314

Burnham, K. P., & Anderson, D. R. (2002). *Model selection and multimodel inference*. Springer. https://doi.org/10.1007/b97636

Chiao, L.-Y., Chen, Y.-N., & Gung, Y. (2014). Constructing empirical resolution diagnostics for kriging and minimum curvature gridding. *Journal of Geophysical Research: Solid Earth*, *119*(5), 3939–3954. https://doi.org/10.1002/2013JB010364

Cousins, E. D. P., Matsuo, T., & Richmond, A. D. (2015). Mapping high-latitude ionospheric electrodynamics with superdarn and ampere. *Journal of Geophysical Research: Space Physics*, *120*(7), 5854–5870. https://doi.org/10.1002/2014JA020463

Friis-Christensen, E., McHenry, M. A., Clauer, C. R., & Vennerstrøm, S. (1988). Ionospheric traveling convection vortices observed near the polar cleft: A triggered response to sudden changes in the solar wind. *Geophysical Research Letters*, *15*(3), 253–256. https://doi.org/10.1029/GL015i003p00253

Gustavsson, B. (1998). Tomographic inversion for ALIS noise and resolution. *Journal of Geophysical Research*, *103*(A11), 26621–26632. https://doi.org/10.1029/98JA00678

Hansen, P. C. (1992). Analysis of discrete ill-posed problems by means of the L-curve. *SIAM Review*, *34*(4), 561–580. https://doi.org/10.1137/1034115

Hansen, P. C., Jensen, T. K., & Rodriguez, G. (2007). An adaptive pruning algorithm for the discrete L-curve criterion. *Journal of Computational and Applied Mathematics*, *198*(2), 483–492. https://doi.org/10.1016/j.cam.2005.09.026

Hovland, A. Ø., Laundal, K. M., Reistad, J. P., Hatch, S. M., Walker, S. J., Madelaire, M., & Ohma, A. (2022). The Lompe code: A python toolbox for ionospheric data analysis. *Frontiers in Astronomy and Space Sciences*, *9*, 1025823. https://doi.org/10.3389/fspas.2022.1025823

Hoyer, P. O. (2004). Non-negative matrix factorization with sparseness constraints. *Journal of Machine Learning Research*, *5*, 1457–1469.

Hurley, N. P., & Rickard, S. T. (2008). Comparing measures of sparsity. arXiv. https://doi.org/10.48550/ARXIV.0811.4706

Juusola, L., Vanhamäki, H., Viljanen, A., & Smirnov, M. (2020). Induced currents due to 3D ground conductivity play a major role in the interpretation of geomagnetic variations. *Annales Geophysicae*, *38*(5), 983–998. https://doi.org/10.5194/angeo-38-983-2020

Laundal, K. M., Reistad, J. P., Hatch, S. M., Madelaire, M., Walker, S., Hovland, A., et al. (2022). Local mapping of polar ionospheric electrodynamics. *Journal of Geophysical Research: Space Physics*, *127*(5), e2022JA030356. https://doi.org/10.1029/2022JA030356

Laundal, K. M., & Richmond, A. (2017). Magnetic coordinate systems. *Space Science Reviews*, *206*(1–4), 27–59. https://doi.org/10.1007/s11214-016-0275-y

Laundal, K. M., Yee, J. H., Merkin, V. G., Gjerloev, J. W., Vanhamäki, H., Reistad, J. P., et al. (2021). Electrojet estimates from mesospheric magnetic field measurements. *Journal of Geophysical Research: Space Physics*, *126*(5), e2020JA028644. https://doi.org/10.1029/2020JA028644

Lévêque, J.-J., Rivera, L., & Wittlinger, G. (1993). On the use of the checker-board test to assess the resolution of tomographic inversions. *Geophysical Journal International*, *115*(1), 313–318. https://doi.org/10.1111/j.1365-246X.1993.tb05605.x

Madelaire, M. (2023). Replication data for "spatial resolution in inverse problems: The EZIE satellite mission" [Dataset]. Zenodo. https://doi.org/10.5281/zenodo.7823088

Madelaire, M., Laundal, K. M., Reistad, J. P., Hatch, S. M., & Ohma, A. (2022). Transient high latitude geomagnetic response to rapid increases in solar wind dynamic pressure. *Frontiers in Astronomy and Space Sciences*, *9*, 953954. https://doi.org/10.3389/fspas.2022.953954

Matsuo, T., Knipp, D. J., Richmond, A. D., Kilcommons, L., & Anderson, B. J. (2015). Inverse procedure for high-latitude ionospheric electrodynamics: Analysis of satellite-borne magnetometer data. *Journal of Geophysical Research: Space Physics*, *120*(6), 5241–5251. https://doi.org/10.1002/2014JA020565

Merkin, V. G., & Lyon, J. G. (2010). Effects of the low-latitude ionospheric boundary condition on the global magnetosphere. *Journal of Geophysical Research*, *115*(A10), A10202. https://doi.org/10.1029/2010JA015461

Miller, C. R., & Routh, P. S. (2007). Resolution analysis of geophysical images: Comparison between point spread function and region of data influence measures. *Geophysical Prospecting*, *55*(6), 835–852. https://doi.org/10.1111/j.1365-2478.2007.00640.x

Neumaier, A. (1998). Solving ill-conditioned and singular linear systems: A tutorial on regularization. *SIAM Review*, *40*(3), 636–666. https://doi.org/10.1137/S0036144597321909

Oldenborger, G. A., & Routh, P. S. (2009). The point-spread function measure of resolution for the 3-D electrical resistivity experiment. *Geophysical Journal International*, *176*(2), 405–414. https://doi.org/10.1111/j.1365-246X.2008.04003.x

Pascual-Marqui, R. D. (1999). Review of methods for solving the EEG inverse problem.

Rawlinson, N., & Spakman, W. (2016). On the use of sensitivity tests in seismic tomography. *Geophysical Journal International*, *205*(2), 1221–1243. https://doi.org/10.1093/gji/ggw084

Ren, Z., & Kalscheuer, T. (2020). Uncertainty and resolution analysis of 2D and 3D inversion models computed from geophysical electromagnetic data. *Surveys in Geophysics*, *41*(1), 47–112. https://doi.org/10.1007/s10712-019-09567-3

Richmond, A. D., & Kamide, Y. (1988). Mapping electrodynamic features of the high-latitude ionosphere from localized observations: Technique. *Journal of Geophysical Research*, *93*(A6), 5741–5759. https://doi.org/10.1029/JA093iA06p05741

Roininen, L., Huttunen, J., & Lasanen, S. (2014). Whittle-Matérn priors for Bayesian statistical inversion with applications in electrical impedance tomography. *Inverse Problems and Imaging*, *8*(2), 561–586. https://doi.org/10.3934/ipi.2014.8.561

Satopaa, V., Albrecht, J., Irwin, D., & Raghavan, B. (2011). Finding a "kneedle" in a haystack: Detecting knee points in system behavior. In *2011 31st international conference on distributed computing systems workshops* (pp. 166–171). https://doi.org/10.1109/ICDCSW.2011.20

Sorathia, K. A., Merkin, V. G., Panov, E. V., Zhang, B., Lyon, J. G., Garretson, J., et al. (2020). Ballooning-interchange instability in the near-Earth plasma sheet and auroral beads: Global magnetospheric modeling at the limit of the MHD approximation. *Geophysical Research Letters*, *47*(14), e2020GL088227. https://doi.org/10.1029/2020GL088227

Tarantola, A., & Valette, B. (1982). Inverse problems = quest for information. *Journal of Geophysics*, *50*, 159–170.

Tikhonov, A. N., & Arsenin, V. Y. (1977). *Solutions of ill-posed problems*. John Wiley & Sons, V. H. Winston & Sons. (Translated from the Russian, Preface by translation editor Fritz John, Scripta Series in Mathematics).

Virtanen, I. I., Gustavsson, B., Aikio, A., Kero, A., Asamura, K., & Ogawa, Y. (2018). Electron energy spectrum and auroral power estimation from incoherent scatter radar measurements. *Journal of Geophysical Research: Space Physics*, *123*(8), 6865–6887. https://doi.org/10.1029/2018JA025636

Yee, J. H., Gjerloev, J., & Wu, D. (2021). Remote sensing of magnetic fields induced by electrojets from space. In *Upper atmosphere dynamics and energetics* (pp. 451–468). American Geophysical Union (AGU). https://doi.org/10.1002/9781119815631.ch21

Yee, J. H., Gjerloev, J., Wu, D., & Schwartz, M. J. (2017). First application of the Zeeman technique to remotely measure auroral electrojet intensity from space. *Geophysical Research Letters*, *44*(20), 10134–10139. https://doi.org/10.1002/2017GL074909

Zhang, B., Sorathia, K. A., Lyon, J. G., Merkin, V. G., Garretson, J. S., & Wiltberger, M. (2019). Gamera: A three-dimensional finite-volume MHD solver for non-orthogonal curvilinear geometries. *The Astrophysical Journal - Supplement Series*, *244*(1), 20. https://doi.org/10.3847/1538-4365/ab3a4c

Article IV

6.4 Estimating the Induction Electric Field in the Ionosphere Using Ground Magnetometer Data

M. Madelaire, K. Laundal, S. Hatch, H. Vanhamäki, J. Reistad, A. Ohma, V. Merkin and D. Lin

In review

Estimating the Ionospheric Induction Electric Field using Ground Magnetometers

Michael Madelaire[1], Karl Laundal[1], Spencer Hatch[1], Heikki Vanhamäki[2], Jone Reistad[1], Anders Ohma[1], Viacheslav Merkin[4], Dong Lin[3]

[1]Department of Physics and Technology, University of Bergen, Bergen, Norway
[2]Space Physics and Astronomy Research Unit, University of Oulu, Oulu, Finland
[3]High Altitude Observatory, National Center for Atmospheric Research, Boulder, CO, USA
[4]Applied Physics Laboratory, Johns Hopkins University, Laural, MD, USA

Key Points:

- A method for estimating the induction electric field using ground magnetometer measurements is presented.
- Locally, the induction electric field can constitute tens of percent of the total electric field, during the sudden commencement examined.
- The spatial pattern of ionospheric Joule heating is shown to be highly affected by the induction electric field, even during weak induction.

Corresponding author: Michael Madelaire, michael.madelaire@uib.no

Abstract
The ionospheric convection electric field is often assumed to be a potential field. This assumption is not always valid, especially when the ionosphere changes on short time scales $T \lesssim 5$ min. We present a technique for estimating the induction electric field using ground magnetometer measurements. The technique is demonstrated on real and simulated data for sudden increases in solar wind dynamic pressure of ∼1 and 10 nPa, respectively. For the real data, the ionospheric induction electric field is 0.15±0.015 mV/m, and the corresponding compressional flow is 2.5±0.3 m/s. For the simulated data, the induction electric field and compressional flow reach 3 mV/m and 50 m/s, respectively. The induction electric field can locally constitute tens of percent of the total electric field. Inclusion of the induction electric field increased the total Joule heating by 2.4%. Locally the Joule heating changed by tens of percent. This corresponds to energy dissipation that is not accounted for in existing models.

Plain Language Summary

In the study of ionospheric dynamics, it is often assumed that the ionospheric electric field is a potential field. This means the contribution from induction is neglected. The induction electric field is described by Faraday's law and relates to temporal changes in the magnetic field. This assumption only holds when the ionospheric dynamics change slowly. In this study, we present a technique for calculating the ionospheric induction electric field using measurements of the magnetic field on the ground. We demonstrate the technique on real and simulated data of a dynamic event, i.e. a sudden commencement. We find that the induction electric field, on a global scale, is small compared to the potential electric field. However, locally it can be relatively large. Similarly, the inclusion of the induction electric field increased the total energy dissipation, i.e. Joule heating, by only a couple of percent but resulted in local variations of tens of percent. Furthermore, we quantified and visualized the compression flow which is the compression and expansion of the magnetic field related to the temporal evolution of a dynamic ionospheric event.

1 Introduction

In this paper, we investigate the ionospheric induction electric field ($\boldsymbol{E}_{ind}$) using a new technique based on ground magnetometers. When studying ionospheric dynamics the ionospheric electric field ($\boldsymbol{E}$) is often assumed to be a potential field ($\boldsymbol{E}_{pot}$). This assumption can be very useful as it may simplify modeling efforts significantly. Techniques such as AMIE/AMGeO [Richmond and Kamide 1988]; [AMGeO Collaboration 2019] and Lompe [Laundal et al. 2022]; [Hovland et al. 2022] model $\boldsymbol{E}_{pot}$ by ignoring $\boldsymbol{E}_{ind}$ that otherwise is implied by Faraday's induction law ($\nabla \times \boldsymbol{E} = -\frac{\partial}{\partial t}\boldsymbol{B}$) [Faraday 1832]. Similarly, $\boldsymbol{E}_{ind}$ is almost always ignored in the ionospheric solvers used to account for the magnetosphere-ionosphere (MI) coupling in magnetohydrodynamic (MHD) simulations (e.g. Tanaka 2000; J. Lyon et al. 2004; Merkin and J. G. Lyon 2010. We present a technique for estimating $\boldsymbol{E}_{ind}$ based on measurements of ground magnetic perturbation. Essentially, allowing $\boldsymbol{E}_{ind}$ to be measured from ground.

Transient events (e.g. sudden commencements or substorm expansions) can result in large changes in the magnetic field ($\boldsymbol{B}$) on a timescale of seconds or minutes. When ignoring Faraday's law the mutual interaction between the electrostatic and inductive processes is neglected which can be important during dynamic events. Yoshikawa and Itonaga 2000 provide a detailed explanation of the inductive ionosphere, from an $\boldsymbol{E}$,$\boldsymbol{J}$ perspective [Vasyliūnas 2012]. It is well known that field-aligned currents (FACs) close through the ionosphere via a divergent Pedersen current, assuming the ionospheric conductance is uniform and the system is in steady state. When a magnetospheric driver is changed, e.g. the opening of a magnetic field line and subsequent anti-sunward con-

vection, the information is communicated via shear Alfvén waves. Bending a magnetic field line, in the conductive ionosphere, excites a flow of electrons perpendicular to the direction of the bend (i.e. Ampere's law) which constitutes a rotational electric field, i.e. $\boldsymbol{E}_{ind}$. Again, assuming uniform conductance, the flow of electrons is a divergent Hall current. Because the electrons are *frozen-in* they act to compress/expand magnetic flux, i.e. $\frac{\partial}{\partial t}\boldsymbol{B}$. We refer to this as *compression flow* ($\boldsymbol{E}_{ind}\times\boldsymbol{B}$). The compression flow is necessary to alter the distribution of magnetic flux to facilitate the ionospheric closure current carried by ions and a new steady state. In other words, in steady state and uniform conductance, the Pedersen current closing FACs only exist due to a pre-existing divergent Hall current. The rate of change in the ionosphere depends on the Pedersen conductance (Σ_P). Southwood and Kivelson 1991 derived a decay rate ($\gamma \propto \Sigma_P^{-1}$) describing the time it takes for the ionospheric current system to change. Additionally, Dreher 1997 simulated the MI coupling with inductive terms and showed that the time it takes a FAC to reach steady state varies with Σ_P.

Vanhamäki et al. 2005 investigated the inductive effect on the ionospheric electric field using realistic time-dependent three-dimensional models of the high latitude ionospheric current system. They found that ionospheric self-induction is locally important with $\boldsymbol{E}_{ind}$ reaching a few mV/m. Vanhamäki et al. 2006 presented a new technique for calculating $\boldsymbol{E}_{ind}$ in a non-uniform conducting ionosphere. The technique utilizes the Cartesian elementary current system technique and requires $\boldsymbol{E}_{pot}$ and Hall/Pedersen conductances as input. Vanhamäki et al. 2007 applied this technique to derive $\boldsymbol{E}_{ind}$ for a westward traveling surge, Ω-band, and intensifying electrojet. They found that $\boldsymbol{E}_{ind}$ can reach magnitudes of several tens of percent of the total electric field. Takeda 2008 simulated $\boldsymbol{E}_{ind}$ associated with FACs with periods of 60, 10, 4, and 1 min and found that $\boldsymbol{E}_{ind}$ had a non-negligible impact when the period of the FACs was 4 min or less.

In this study, we present a technique for estimating the ionospheric induction electric field based on ground magnetometer measurements represented with a spherical harmonic expansion, and present examples of the associated ionospheric plasma flow. This method of studying spatiotemporal variations in the magnetic field to infer compressional flow is analogous with studies of core flow using time-dependent models of Earth's main magnetic field (e.g. Finlay et al. 2020; Sabaka et al. 2020; Finlay et al. 2023). Spherical harmonic models of Earth's core magnetic field can provide information about changes in the motion of liquid metal in the outer core through estimates of secular variation. This information can be used as boundary conditions in models of Earth's dynamo [Schaeffer et al. 2016]. To the knowledge of the authors, it is the first time ground magnetometer measurements have been used to inform about the inductive component of the ionospheric electric field. However, Vanhamäki et al. 2013 solved Faraday's law based on the radial magnetic field to derive the induced electric field at Earth's surface.

In Section 2 we present a technique for deriving the ionospheric $\boldsymbol{E}_{ind}$ from ground magnetic field perturbations. A more thorough derivation is provided in the Supporting Information. In Section 3, the technique is demonstrated using synthetic data from a coupled geospace model presented by Shi et al. 2022 and real ground magnetometer measurements during sudden commencements (SCs). Section 4 discusses the results.

2 Technique

In this section, we describe how an estimate of the ionospheric induction electric field ($\boldsymbol{E}_{ind}$) can be derived from the temporal derivative of the radial magnetic field $\left(\frac{\partial}{\partial t}B_r\right)$ below the ionosphere. A more in-depth derivation is provided in the Supporting Information.

The ionospheric electric field ($\boldsymbol{E}$) can be decomposed into three scalar fields using the *alternative Helmholtz representation* [Sabaka et al. 2010],

$$\boldsymbol{E} = U\hat{\boldsymbol{r}} + \boldsymbol{\nabla}_S V - \hat{\boldsymbol{r}} \times \boldsymbol{\nabla}_S W. \tag{1}$$

Here $\hat{\boldsymbol{r}}$ is the radial unit vector and $\boldsymbol{\nabla}_S$ is the angular portion of the $\boldsymbol{\nabla}$ operator.

The curl of the ionospheric electric field ($\boldsymbol{\nabla} \times \boldsymbol{E}$) on a spherical shell can be described by $\frac{\partial}{\partial t} B_r$ on the shell according to Faraday's law. By inserting Equation 1 into Faraday's law $\frac{\partial}{\partial t} B_r$ can be expressed in terms of W,

$$\frac{\partial}{\partial t} B_r = \hat{\boldsymbol{r}} \boldsymbol{\nabla}^2 W. \tag{2}$$

The scalar field W can be represented with a Spherical Harmonic (SH) expansion,

$$W = \sum_{n=1}^{N} \sum_{m=0}^{n} \left[a_n^{m,W} \cos(m\phi) + b_n^{m,W} \sin(m\phi) \right] P_n^m \left(\cos(\theta) \right). \tag{3}$$

Here (θ, ϕ) are colatitude and longitude, (n, m) are the SH degree and order, ($a_n^{m,W}$, $b_n^{m,W}$) are the SH coefficients, and $P_n^m(\cos(\theta))$ is the Schmidt quasi normalized Legendre polynomial. The coefficients ($a_n^{m,W}$, $b_n^{m,W}$) are unknown, but can be expressed in terms of the SH coefficients ($\frac{\partial}{\partial t} a_n^{m,B}$, $\frac{\partial}{\partial t} b_n^{m,B}$) related to a SH expansion of $\frac{\partial}{\partial t} B_r$ following Sabaka et al. 2010,

$$\begin{aligned} a_n^{m,W} &= \frac{r^2}{n+1} \frac{\partial}{\partial t} a_n^{m,B} \\ b_n^{m,W} &= \frac{r^2}{n+1} \frac{\partial}{\partial t} b_n^{m,B}. \end{aligned} \tag{4}$$

In practice $a_n^{m,B}$ and $b_n^{m,B}$ can be determined by solving a linear inverse problem with magnetic field measurements on ground as input. The resulting SH coefficients should be determined using the ionosphere as their reference height. However, if the coefficients are determined with Earth's surface as their reference height they can simply be upward continued to the ionosphere. This detail is important as it defines the altitude of the spherical shell on which $\boldsymbol{E}_{ind}$ will be determined. Only the radial magnetic field component can be upward continued to the ionosphere because it is continuous across boundary layers, unlike the horizontal components.

The horizontal part of $\boldsymbol{E}_{ind}$ is given by the last term of Equation 1,

$$\boldsymbol{E}_{ind,h} = -\hat{\boldsymbol{r}} \times \boldsymbol{\nabla}_S W = -\hat{\boldsymbol{r}} \times \boldsymbol{\nabla} W. \tag{5}$$

In the ionosphere, where the field-aligned conductivity is high, the electric field maps along the magnetic field making $\boldsymbol{E} \cdot \boldsymbol{B} = 0$. This allows for the determination of $E_{ind,r}$. However, $\boldsymbol{E}_{pot}$ is typically unknown. By assuming radial magnetic field lines $E_{ind,r} = -E_{pot,r}$ and the compression flow is given as

$$\boldsymbol{v} = \frac{\boldsymbol{E}_{ind} \times \hat{\boldsymbol{b}}_r}{B}, \tag{6}$$

where $\hat{\boldsymbol{b}}_r = -\hat{\boldsymbol{r}}$ in the northern hemisphere.

Through the merger of the technique presented here and empirical modeling techniques of the ionospheric potential electric field like AMIE and Lompe $\boldsymbol{E}_{pot}$ and $\boldsymbol{E}_{ind}$ might be co-estimated. This will be the focus of future studies.

3 Results

Estimating the induction electric field ($\boldsymbol{E}_{ind}$) requires a SH model of $\frac{\partial}{\partial t} B_r$. In this section, we apply our method to two different cases of SCs. One model is based on ground magnetic perturbations from an MHD simulation while the other is based on real ground magnetometer measurements.

3.1 Synthetic data example

The synthetic data is based on an MHD simulation of an interplanetary shock carried out and analyzed by Shi et al. 2022. During this event, the solar wind dynamic pressure increases by approximately 10 nPa. The RE-developed Magnetosphere-Ionosphere Coupler/Solver (REMIX) [Merkin and J. G. Lyon 2010] is used to determine the ionospheric current and assumes that $\boldsymbol{\nabla} \times \boldsymbol{E} = 0$. The reader is referred to Shi et al. 2022 for further details regarding the simulation. The ground magnetic perturbation is determined by computing a Biot-Savart integral over the ionospheric currents, FACs, and magnetospheric currents on an equal area grid with a 0.5 degree latitudinal resolution down to 0° latitude. We represent the ground magnetic perturbation using SHs, where the SH coefficients ($a_n^{m,B}$, $b_n^{m,B}$) are determined by solving an inverse problem similar to Madelaire et al. 2022a with the SH expansion truncated at $n = 100$. The SH expansion is only done for external sources as the synthetic data does not include ground induction.

Figure 1 summarizes the technique for estimating $\boldsymbol{E}_{ind}$, using synthetic data of the preliminary impulse associated with a SC. Figure 1a shows $\frac{\partial}{\partial t} B_r$ on ground. Figure 1b shows a recreation of $\frac{\partial}{\partial t} B_r$ using a SH model based on ground magnetic perturbation. A comparison between Figures 1a-b shows that $\frac{\partial}{\partial t} B_r$ is reproduced well by the SH model. Figures 1c-d compare the estimated $\boldsymbol{E}_{ind}$ and the ionospheric potential electric field ($\boldsymbol{E}_{pot}$) from the MHD simulation. Comparison between $\boldsymbol{E}_{ind}$ and $\boldsymbol{E}_{pot}$ are done with respect to the first of the two subsequent timesteps used to determine $\frac{\partial}{\partial t} B_r$. We find that $\boldsymbol{E}_{ind}$ reaches up to 3 mV/m which locally can correspond to tens of percent of $\boldsymbol{E}$ ($\boldsymbol{E} = \boldsymbol{E}_{pot} + \boldsymbol{E}_{ind}$) in the high latitude ionosphere. Therefore, $\boldsymbol{E}_{ind}$ can have a significant regional impact. Figure 1e shows Joule heating associated with $\boldsymbol{E}_{pot}$ (i.e. $\Sigma_p E_{pot}^2$) which is a result of maintaining the steady state current system. Figure 1f shows the difference in Joule heating when including $\boldsymbol{E}_{ind}$, i.e. $\Sigma_P \left[E_{pot}^2 + 2(\boldsymbol{E}_{pot} \cdot \boldsymbol{E}_{ind}) + E_{ind}^2\right]$. The difference can locally be tens of percent, both positive and negative. However, the total Joule heating above 50 degrees latitude only increases by approximately 2.4%. The pins in Figures 1e-f illustrate the steady state convection and compression flow (Equation 6), respectively, where B is the magnitude of a dipole magnetic field. The dipole magnetic field is determined using the first SH degree of IGRF-12 [Thébault et al. 2015]. The flow illustrates the expansion/compression of magnetic flux necessary to change the ionospheric current system from one steady state to another.

3.2 Real data example

The SH model based on real ground magnetometer measurements was provided by Madelaire et al. 2022a and is the product of a superposed epoch analysis of SCs. Madelaire et al. 2022a presented 12 models determined by dividing the list of SCs presented by Madelaire et al. 2022b into 12 groups based on the Interplanetary Magnetic Field (IMF) clock angle and dipole tilt angle. In this example, we use the model created for SCs during northward IMF and positive dipole tilt (Summer in the northern hemisphere). The model is based on 175 events, the majority of which experience solar wind dynamic pressure increases around 1–2 nPa. The much smaller pressure increases in this model compared to that used in Section 3.1 results in significantly smaller $\frac{\partial}{\partial t} B_r$ and $\boldsymbol{E}_{ind}$. The SH model includes a separation between internal and external sources. Both sets of SH coefficients are upward continued to the ionosphere and combined before deriving $\boldsymbol{E}_{ind}$. Furthermore, to assess uncertainty, 50 realizations of the model were created by resampling the events used as input.

Figure 2 shows a time series of $\frac{\partial}{\partial t} B_r$ and compression flow associated with the SH model, based on real ground magnetometer measurements, starting 2 minutes prior to the initial increase in SYM-H [Iyemori et al. 2010]. Epochs are synonymous with minutes. Here, $\frac{\partial}{\partial t} B_r$ is the median across all 50 model realizations and the compression flow

is the bias vector (e.g. Haaland et al. 2007) scaled with the median magnitude. The preliminary impulse appears in Figures 2a-b. The main impulse appears in Figure 2c, equatorward and with the opposite polarity of the preliminary impulse. Over the following 3 minutes (i.e. Figures 2d-f) the main impulse expands along the flanks toward the nightside while increasing in strength. The compression flow is around 2.5 m/s with a standard deviation of around 0.3 m/s. Additionally, a large-scale southward flow appears shortly after the appearance of the preliminary impulse.

4 Discussion

We presented a technique for estimating the ionospheric induction electric field ($\boldsymbol{E}_{ind}$) using measurements of magnetic field perturbation below the ionosphere. The technique links a SH representation of the temporal derivative of the radial magnetic field ($\frac{\partial}{\partial t}B_r$) to a scalar field W representing $\boldsymbol{E}_{ind}$. In an example with synthetic data, we found that $\boldsymbol{E}_{ind}$ reaches values of 3 mV/m (Figure 1d) which locally can correspond to tens of percent of the combined ionospheric electric field ($\boldsymbol{E} = \boldsymbol{E}_{pot} + \boldsymbol{E}_{ind}$) in the high latitude ionosphere. From estimates of $\boldsymbol{E}_{ind}$ a compression flow of approximately 50 m/s was calculated (Figure 1b), which represents the necessary expansion/contraction of magnetic flux to reach a new steady state. The total Joule heating above 50 degrees latitude increased by approximately 2.4% while local changes were tens of percent (see Figures 1e-f). Inclusion of $\boldsymbol{E}_{ind}$ in the calculation of Joule heating adds two terms, i.e. $\Sigma_P E_{ind}^2$ and $2\Sigma_P(\boldsymbol{E}_{pot} \cdot \boldsymbol{E}_{ind})$. Assuming $E_{ind} = E_{pot}/10$ results in E_{ind}^2 being 1% of E_{pot}^2. Meanwhile, the cross-term can contribute up to 20% of the Joule heating depending on the alignment of $\boldsymbol{E}_{ind}$ and $\boldsymbol{E}_{pot}$. However, the cross-term can be positive or negative. It is, therefore, unclear how much it contributes to the total heating when integrated over the entire ionosphere. The contribution from the cross-term is illustrated in Figure 1f and leads to a significant difference in ionospheric energy dissipation during dynamic events compared to the steady state case, even when E_{ind} is an order of magnitude smaller than E_{pot}. However, the estimated value of 2.4% is specific for the synthetic case being studied as both the magnitude and spatial extent of the temporally varying magnetic field depend on several exogenous parameters. Furthermore, the background level of Joule heating can also vary.

The MHD simulation carried out by Shi et al. 2022, used to create the synthetic data example in Section 3.1, applied the ionospheric solver REMIX [Merkin and J. G. Lyon 2010] which assumes steady state. Therefore, the ionospheric electric field is a potential electric field since ionospheric self-inductance is neglected (i.e $\boldsymbol{\nabla} \times \boldsymbol{E} = \frac{\partial}{\partial t}\boldsymbol{B} = 0$). We calculate $\frac{\partial}{\partial t}\boldsymbol{B}$ as the difference between two steady states for demonstration purposes. The combined ionospheric electric field (i.e. $\boldsymbol{E} = \boldsymbol{E}_{pot} + \boldsymbol{E}_{ind}$) no longer satisfy the current continuity ($\boldsymbol{\nabla} \cdot \boldsymbol{J} = 0$) ensured in REMIX and is fundamentally inconsistent. Furthermore, the rotational current associated with $\boldsymbol{E}_{ind}$ in Figure 1d contributes to the ground magnetic perturbation. This leads to a secondary and weaker induction effect which subsequently leads to a third and so on and so forth. The infinite chain of opposing and progressively induction effects is naturally accounted for when using real data. However, the synthetic data still provide insight into the usefulness of the presented technique. The magnitude of $\boldsymbol{E}_{ind}$ is similar to previous studies [Vanhamäki et al. 2005]; [Vanhamäki et al. 2007].

The presented technique was also used on a SH model of SCs based on real ground magnetometer measurements [Madelaire et al. 2022a]. The retrieved $\boldsymbol{E}_{ind}$ and compression flow is around 0.15±0.015 mV/m and 2.5±0.3 m/s (Figure 2), respectively. Additionally, the compression flow is dominated by a large-scale southward flow. This is consistent with an intensification of the magnetic perturbation from magnetospheric sources due to compression of the magnetosphere. The same intensification gives rise to a step-like increase in SYM-H during SCs [Russell et al. 1994]; [Madelaire et al. 2022b]. A large-scale flow is likewise present in the example with synthetic data, i.e. Figure 1f. In Fig-

ure 3 the contribution from magnetospheric currents to $\boldsymbol{E}_{ind}$ (i.e. Figure 3b) and the associated Joule heating has been separated from that of ionospheric currents and FACs (i.e. Figure 3c) for the synthetic example. Magnetospheric currents (e.g. magnetopause and ring current) produce, to first order, a uniform magnetic field in $\hat{\boldsymbol{z}}$. At the poles, this corresponds to a weakening of the magnetic field, an azimuthal induction electric field (westward on the dayside), and a large-scale southward flow in the northern hemisphere. The induction electric field in the southern hemisphere points in the same direction but $\hat{\boldsymbol{b}}$ points outward giving rise to a large-scale northward compression flow. Essentially, there is a large-scale equatorward compression flow at high latitude in response to rapid increases in solar wind dynamic pressure. Oppositely, there is a large-scale poleward compression flow in response to rapid decreases in solar wind dynamic pressure.

It is unclear how to interpret local changes in Joule heating due to the inclusion of $\boldsymbol{E}_{ind}$. Hesse et al. 1997 showed that $\boldsymbol{E}$ maps between the ionosphere and magnetosphere for ideal MHD, i.e. including inductive terms. If that holds in reality it would lead to an asymmetric spatiotemporal evolution, e.g. during SCs. However, Hesse et al. 1997 also showed that the mapping is non-trivial in the presence of parallel electric fields. Regardless of how $\boldsymbol{E}_{ind}$ maps between ionosphere and magnetosphere the spatiotemporal evolution of dynamic events, e.g. transient current vortices associated with the preliminary and main impulse of a SC and rapid compression/expansion of the magnetosphere, lead to significant local changes in Joule heating. The duration of these local changes can result in ion upflow but are unlikely to cause neutral upwelling [Strangeway 2012]. Zou et al. 2017 observed lifting of the F region ionosphere, large and transient field-aligned ion upflow, and prompt but short-lived ion temperature increase in the transition between the preliminary and main impulse of a sudden commencement using PFISR measurements.

There are significant differences in the magnitude of $\boldsymbol{E}_{ind}$ and the compression flow (Equation 6) between the two models. The SH model provided by Madelaire et al. 2022a is a product of a superposed epoch analysis based on a list of solar wind dynamic pressure increases [Madelaire et al. 2022b]. The majority of the events in the list are not interplanetary shocks, and experience smaller pressure increases compared to what is often seen in case studies and MHD simulations (e.g. Moretto et al. 2000; Slinker et al. 1999; Fujita et al. 2003. Madelaire et al. 2022b showed that the events, on average, contain increases of a couple of nPa. The interplanetary shock simulated by Shi et al. 2022 increased by approximately 10 nPa. The vast difference in the size of the pressure increase along with the smoothing associated with superposing multiple events leads to a $\frac{\partial}{\partial t}B_r$ in the order of 10 nT/min (Figure 2) compared to the 10 nT/s (Figure 1) seen in the MHD simulation. This is likely the explanation for the smaller compression flow.

The presented technique can be extended to the Spherical Elementary Current System (SECS) technique [Amm and Viljanen 1999]. The Lompe technique [Laundal et al. 2022]; [Hovland et al. 2022] models $\boldsymbol{E}_{pot}$ using SECS by combining various measurements (e.g. conductance, convection, and ground/space magnetic field measurements), similar to AMIE/AMGeO [Richmond and Kamide 1988]; [AMGeO Collaboration 2019]. However, the use of SECS in Lompe makes it ideal for regional analysis. In the future, we hope to remove the necessity of assuming steady state when using Lompe by implementing a scheme to co-estimate $\boldsymbol{E}_{pot}$ and $\boldsymbol{E}_{ind}$ using a technique similar to the one shown here.

Acknowledgments
This work was funded by the Research Council of Norway (RCN) under contract 223252/F50. KL. and JR were also funded by the RCN under contract 300844/F50. KL. and SH were also funded by the Trond Mohn Foundation. VM and DL were funded by NASA DRIVE Science Center under cooperative Agreement 80NSSC22M0163.

Data Availability Statement

The synthetic data used in this study is available at Zenodo via https://doi.org/10.5281/zenodo.8116401 Madelaire 2023. The spherical harmonic model based on real ground magnetometer observations was provided by Madelaire et al. 2022a and is available at Zenedo via https://zenodo.org/record/6243103 Madelaire 2022.

References

AMGeO Collaboration (Dec. 2019). "A Collaborative Data Science Platform for the Geospace Community: Assimilative Mapping of Geospace Observations (AMGeO) v1.0.0". In: *Zenodo.* DOI: 10.5281/zenodo.3564914. URL: https://doi.org/10.5281/zenodo.3564914.

Amm, O. and A. Viljanen (June 1999). "Ionospheric disturbance magnetic field continuation from the ground to the ionosphere using spherical elementary current systems". In: *Earth, Planets and Space* 51.6, pp. 431–440. DOI: 10.1186/BF03352247. URL: https://doi.org/10.1186/BF03352247.

Dreher, J. (1997). "On the self-consistent description of dynamic magnetosphere-ionosphere coupling phenomena with resolved ionosphere". In: *Journal of Geophysical Research: Space Physics* 102.A1, pp. 85–94. DOI: https://doi.org/10.1029/96JA02800. eprint: https://agupubs.onlinelibrary.wiley.com/doi/pdf/10.1029/96JA02800. URL: https://agupubs.onlinelibrary.wiley.com/doi/abs/10.1029/96JA02800.

Faraday, M. (1832). "V. Experimental researches in electricity". In: *Philosophical Transactions of the Royal Society of London* 122, pp. 125–162. DOI: 10.1098/rstl.1832.0006. eprint: https://royalsocietypublishing.org/doi/pdf/10.1098/rstl.1832.0006. URL: https://royalsocietypublishing.org/doi/abs/10.1098/rstl.1832.0006.

Finlay, C. C., N. Gillet, J. Aubert, P. W. Livermore, and D. Jault (June 2023). "Gyres, jets and waves in the Earth's core". In: *Nature Reviews Earth & Environment* 4.6, pp. 377–392. DOI: 10.1038/s43017-023-00425-w. URL: https://doi.org/10.1038/s43017-023-00425-w.

Finlay, C. C., C. Kloss, N. Olsen, M. D. Hammer, L. Tøffner-Clausen, A. Grayver, and A. Kuvshinov (2020). "The CHAOS-7 geomagnetic field model and observed changes in the South Atlantic Anomaly". In: *Earth Planets Space* 72.156. DOI: https://doi.org/10.1186/s40623-020-01252-9.

Fujita, S., T. Tanaka, T. Kikuchi, K. Fujimoto, K. Hosokawa, and M. Itonaga (2003). "A numerical simulation of the geomagnetic sudden commencement: 1. Generation of the field-aligned current associated with the preliminary impulse". In: *Journal of Geophysical Research: Space Physics* 108.A12. DOI: https://doi.org/10.1029/2002JA009407.

Haaland, S. E., G. Paschmann, M. Förster, J. M. Quinn, R. B. Torbert, C. E. McIlwain, H. Vaith, P. A. Puhl-Quinn, and C. A. Kletzing (2007). "High-latitude plasma convection from Cluster EDI measurements: method and IMF-dependence". In: *Annales Geophysicae* 25.1, pp. 239–253. DOI: 10.5194/angeo-25-239-2007. URL: https://angeo.copernicus.org/articles/25/239/2007/.

Hesse, Michael, Joachim Birn, and Robert A. Hoffman (1997). "On the mapping of ionospheric convection into the magnetosphere". In: *Journal of Geophysical Research: Space Physics* 102.A5, pp. 9543–9551. DOI: https://doi.org/10.1029/96JA03999.

eprint: https://agupubs.onlinelibrary.wiley.com/doi/pdf/10.1029/96JA03999. URL: https://agupubs.onlinelibrary.wiley.com/doi/abs/10.1029/96JA03999.

Hovland, A. Ø., K. M. Laundal, J. P. Reistad, S. M. Hatch, S. J. Walker, M. Madelaire, and A. Ohma (2022). "The Lompe code: A Python toolbox for ionospheric data analysis". In: *Frontiers in Astronomy and Space Sciences* 9. DOI: 10.3389/fspas.2022.1025823. URL: https://www.frontiersin.org/articles/10.3389/fspas.2022.1025823.

Iyemori, T., M. Takeda, M. Nose, and H. Toh (2010). "Mid-latitude Geomagnetic Indices ASY and SYM for 2009 (Provisional)". In: *Internal Report of Data Analysis Center for Geomagnetism and Space Magnetism, Kyoto University, Japan*.

Laundal, K. M., J. P. Reistad, S. M. Hatch, M. Madelaire, S. Walker, A. Hovland, A. Ohma, V. Merkin, and K. Sorathia (May 2022). "Local Mapping of Polar Ionospheric Electrodynamics". In: *Journal of Geophysical Research: Space Physics* 127. DOI: 10.1029/2022JA030356.

Lyon, J.G., J.A. Fedder, and C.M. Mobarry (2004). "The Lyon–Fedder–Mobarry (LFM) global MHD magnetospheric simulation code". In: *Journal of Atmospheric and Solar-Terrestrial Physics* 66.15. Towards an Integrated Model of the Space Weather System, pp. 1333–1350. DOI: https://doi.org/10.1016/j.jastp.2004.03.020. URL: https://www.sciencedirect.com/science/article/pii/S1364682604001439.

Madelaire, M. (Feb. 2022). *List of rapid solar wind dynamic pressure increases*. Zenodo [Dataset]. DOI: 10.5281/zenodo.6243103. URL: https://doi.org/10.5281/zenodo.6243103.

— (May 2023). *Synthetic data for estimation of the ionospheric induction electric field*. Zenodo. [Dataset]. DOI: 10.5281/zenodo.8116401. URL: https://doi.org/10.5281/zenodo.8116401.

Madelaire, M., K. M. Laundal, J. P. Reistad, S. M. Hatch, and A. Ohma (2022a). "Transient high latitude geomagnetic response to rapid increases in solar wind dynamic pressure". In: *Frontiers in Astronomy and Space Sciences* 9. DOI: 10.3389/fspas.2022.953954. URL: https://www.frontiersin.org/articles/10.3389/fspas.2022.953954.

Madelaire, M., K. M. Laundal, J. P. Reistad, S. M. Hatch, A. Ohma, and S. Haaland (2022b). "Geomagnetic Response to Rapid Increases in Solar Wind Dynamic Pressure: Event Detection and Large Scale Response". In: *Frontiers in Astronomy and Space Sciences* 9. DOI: 10.3389/fspas.2022.904620. URL: https://www.frontiersin.org/article/10.3389/fspas.2022.904620.

Merkin, V. G. and J. G. Lyon (2010). "Effects of the low-latitude ionospheric boundary condition on the global magnetosphere". In: *Journal of Geophysical Research: Space Physics* 115.A10. DOI: https://doi.org/10.1029/2010JA015461. eprint: https://agupubs.onlinelibrary.wiley.com/doi/pdf/10.1029/2010JA015461. URL: https://agupubs.onlinelibrary.wiley.com/doi/abs/10.1029/2010JA015461.

Moretto, T., A. J. Ridley, M. J. Engebretson, and O. Rasmussen (2000). "High-latitude ionospheric response to a sudden impulse event during northward IMF conditions". In: *Journal of Geophysical Research: Space Physics* 105.A2, pp. 2521–2531. DOI: https://doi.org/10.1029/1999JA900475.

Richmond, A. D. and Y. Kamide (1988). "Mapping electrodynamic features of the high-latitude ionosphere from localized observations: Technique". In: *Journal of Geophysical Research* 93.A6, pp. 5741–5759. DOI: 10.1029/JA093iA06p05741. URL: https://doi.org/10.1029/JA093iA06p05741.

Russell, C. T., M. Ginskey, and S. M. Petrinec (Jan. 1994). "Sudden impulses at low-latitude stations: Steady state response for northward interplanetary magnetic field". In: *Journal of Geophysical Research: Space Physics* 99.A1, pp. 253–261. DOI: https://doi.org/10.1029/93JA02288.

Sabaka, T. J., G. Hulot, and N. Olsen (2010). "Mathematical Properties Relevant to Geomagnetic Field Modeling". English. In: *Handbook of Geomathematics*. Springer. DOI: 10.1007/978-3-642-27793-1_17-2.

Sabaka, T. J., L. Tøffner-Clausen, N. Olsen, and C. C. Finlay (June 2020). "CM6: a comprehensive geomagnetic field model derived from both CHAMP and Swarm satellite observations". In: *Earth, Planets and Space* 72.1, p. 80. DOI: 10.1186/s40623-020-01210-5. URL: https://doi.org/10.1186/s40623-020-01210-5.

Schaeffer, N., E. Silva, and M. A. Pais (June 2016). "Can Core Flows inferred from Geomagnetic Field Models explain the Earth's Dynamo?" In: *Geophysical Journal International* 204. DOI: 10.6084/m9.figshare.1439333.

Shi, Xueling et al. (2022). "Geospace Concussion: Global Reversal of Ionospheric Vertical Plasma Drift in Response to a Sudden Commencement". In: *Geophysical Research Letters* 49.19. e2022GL100014 2022GL100014, e2022GL100014. DOI: https://doi.org/10.1029/2022GL100014. eprint: https://agupubs.onlinelibrary.wiley.com/doi/pdf/10.1029/2022GL100014. URL: https://agupubs.onlinelibrary.wiley.com/doi/abs/10.1029/2022GL100014.

Slinker, S. P., J. A. Fedder, W. J. Hughes, and J. G. Lyon (1999). "Response of the ionosphere to a density pulse in the solar wind: Simulation of traveling convection vortices". In: *Geophysical Research Letters* 26.23, pp. 3549–3552. DOI: https://doi.org/10.1029/1999GL010688.

Southwood, D. J. and M. G. Kivelson (1991). "An approximate description of field-aligned currents in a planetary magnetic field". In: *Journal of Geophysical Research: Space Physics* 96.A1, pp. 67–75. DOI: https://doi.org/10.1029/90JA01806. eprint: https://agupubs.onlinelibrary.wiley.com/doi/pdf/10.1029/90JA01806. URL: https://agupubs.onlinelibrary.wiley.com/doi/abs/10.1029/90JA01806.

Strangeway, R. J. (2012). "The equivalence of Joule dissipation and frictional heating in the collisional ionosphere". In: *Journal of Geophysical Research: Space Physics* 117.A2. DOI: https://doi.org/10.1029/2011JA017302. eprint: https://agupubs.onlinelibrary.wiley.com/doi/pdf/10.1029/2011JA017302. URL: https://agupubs.onlinelibrary.wiley.com/doi/abs/10.1029/2011JA017302.

Takeda, Masahiko (2008). "Effects of the induction electric field on ionospheric current systems driven by field-aligned currents of magnetospheric origin". In: *Journal of Geophysical Research: Space Physics* 113.A1. DOI: https://doi.org/10.1029/2007JA012662. eprint: https://agupubs.onlinelibrary.wiley.com/doi/pdf/10.1029/2007JA012662. URL: https://agupubs.onlinelibrary.wiley.com/doi/abs/10.1029/2007JA012662.

Tanaka, T. (2000). "The state transition model of the substorm onset". In: *Journal of Geophysical Research: Space Physics* 105.A9, pp. 21081–21096. DOI: https://doi.

org/10.1029/2000JA900061. eprint: https://agupubs.onlinelibrary.wiley.com/doi/pdf/10.1029/2000JA900061. URL: https://agupubs.onlinelibrary.wiley.com/doi/abs/10.1029/2000JA900061.

Thébault, E. et al. (May 2015). "International Geomagnetic Reference Field: the 12th generation". In: *Earth, Planets and Space* 67.1, p. 79. DOI: 10.1186/s40623-015-0228-9. URL: https://doi.org/10.1186/s40623-015-0228-9.

Vanhamäki, H., O. Amm, and A. Viljanen (2006). "New method for solving inductive electric fields in the non-uniformly conducting ionosphere". In: *Annales Geophysicae* 24.10, pp. 2573–2582. DOI: 10.5194/angeo-24-2573-2006. URL: https://angeo.copernicus.org/articles/24/2573/2006/.

— (2007). "Role of inductive electric fields and currents in dynamical ionospheric situations". In: *Annales Geophysicae* 25.2, pp. 437–455. DOI: 10.5194/angeo-25-437-2007. URL: https://angeo.copernicus.org/articles/25/437/2007/.

Vanhamäki, H., A. Viljanen, and O. Amm (2005). "Induction effects on ionospheric electric and magnetic fields". In: *Annales Geophysicae* 23.5, pp. 1735–1746. DOI: 10.5194/angeo-23-1735-2005. URL: https://angeo.copernicus.org/articles/23/1735/2005/.

Vanhamäki, H., A. Viljanen, R. Pirjola, and O. Amm (Sept. 2013). "Deriving the geomagnetically induced electric field at the Earth's surface from the time derivative of the vertical magnetic field". In: *Earth, Planets and Space* 65.9, pp. 997–1006. DOI: 10.5047/eps.2013.03.013. URL: https://doi.org/10.5047/eps.2013.03.013.

Vasyliūnas, V M (Feb. 2012). "The physical basis of ionospheric electrodynamics". In: *Ann. Geophys.* 30.2, pp. 357–369. DOI: 10.5194/angeo-30-357-2012. URL: https://www.ann-geophys.net/30/357/2012/%20https://www.ann-geophys.net/30/357/2012/angeo-30-357-2012.pdf.

Yoshikawa, A. and M. Itonaga (2000). "The nature of reflection and mode conversion of MHD waves in the inductive ionosphere: Multistep mode conversion between divergent and rotational electric fields". In: *Journal of Geophysical Research: Space Physics* 105.A5, pp. 10565–10584. DOI: https://doi.org/10.1029/1999JA000159. eprint: https://agupubs.onlinelibrary.wiley.com/doi/pdf/10.1029/1999JA000159. URL: https://agupubs.onlinelibrary.wiley.com/doi/abs/10.1029/1999JA000159.

Zou, S., D. Ozturk, R. Varney, and A. Reimer (2017). "Effects of sudden commencement on the ionosphere: PFISR observations and global MHD simulation". In: *Geophysical Research Letters* 44.7, pp. 3047–3058. DOI: https://doi.org/10.1002/2017GL072678. eprint: https://agupubs.onlinelibrary.wiley.com/doi/pdf/10.1002/2017GL072678. URL: https://agupubs.onlinelibrary.wiley.com/doi/abs/10.1002/2017GL072678.

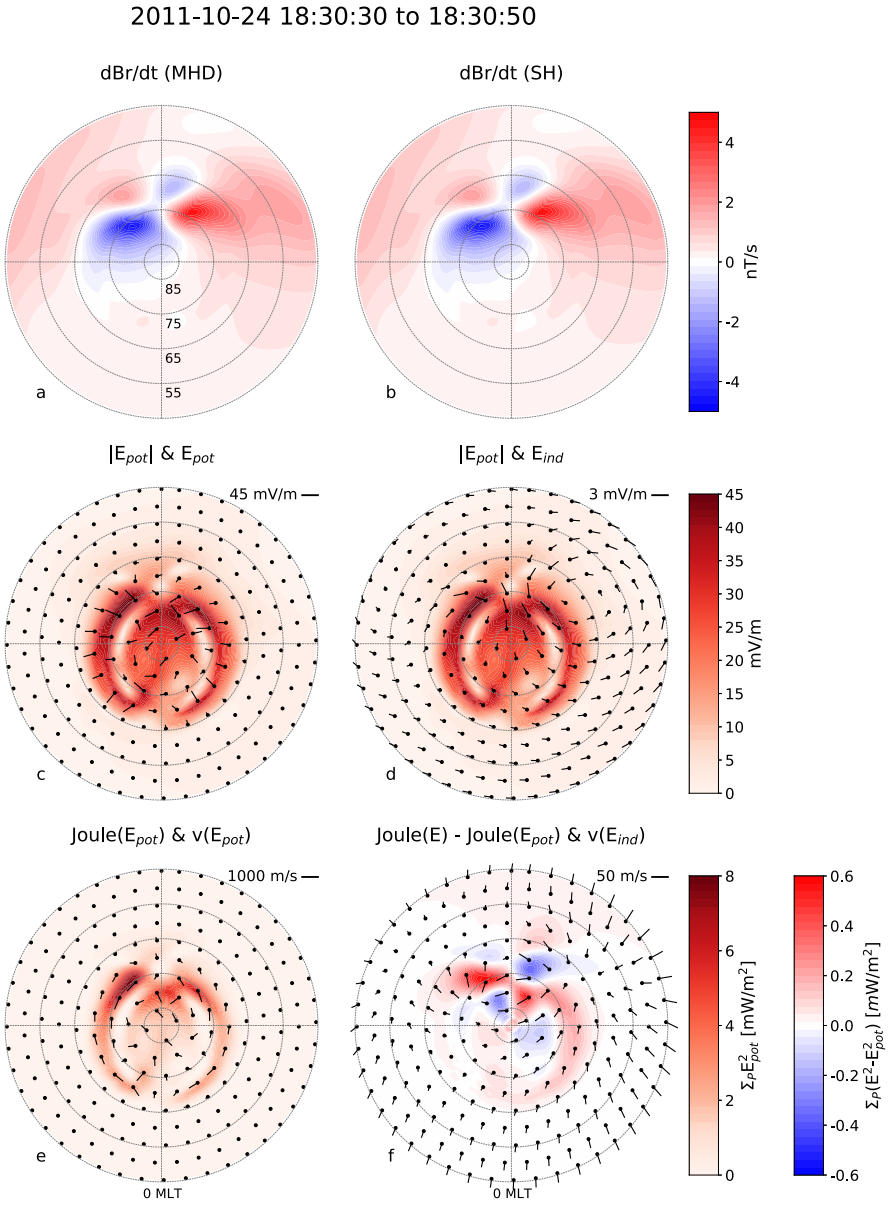

Figure 1. A summary of how $\boldsymbol{E}_{ind}$ is determined based on synthetic ground magnetometer measurements from an MHD simulation [Shi et al. 2022], along with the compression flow and Joule heating. Figures 1a-b show $\frac{\partial}{\partial t}B_r$ from the MHD and SH model, respectively. Figure 1c shows the magnitude of $\boldsymbol{E}_{pot}$ and its orientation as pins. Figure 1d shows the magnitude of $\boldsymbol{E}_{pot}$ with the orientation of $\boldsymbol{E}_{ind}$ overlain. Figure 1e shows the Joule heating and plasma convection associated with $\boldsymbol{E}_{pot}$ as a contour and pins, respectively. Figure 1f shows the difference between Joule heating associated with $\boldsymbol{E}_{pot}$ and $\boldsymbol{E} = \boldsymbol{E}_{pot} + \boldsymbol{E}_{ind}$ as well as the compression flow associated with $\boldsymbol{E}_{ind}$. The purpose of this figure is to validate the SH models' recreation of $\frac{\partial}{\partial t}B_r$ as well as demonstrate the technique for estimating $\boldsymbol{E}_{ind}$.

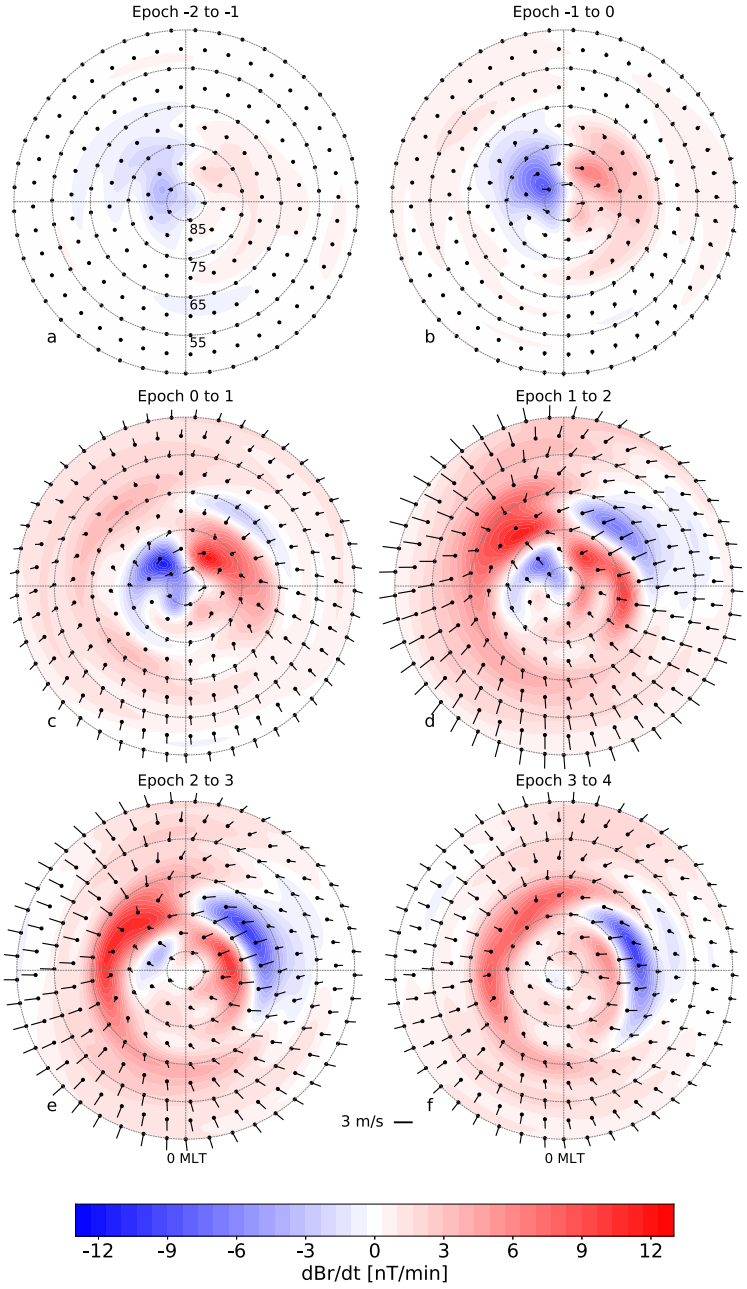

Figure 2. Illustration of $\frac{\partial}{\partial t}B$ and $\boldsymbol{E}_{ind}\times\boldsymbol{B}_0$ drift based on the SH model provided by Madelaire et al. 2022b. Epoch is synonymous with minute. The purpose of this figure is to showcase the estimation of $\boldsymbol{E}_{ind}$ using a SH model that is based on real ground magnetometer measurements. Furthermore, the data includes contributions from magnetospheric sources that give rise to a large-scale southward compression flow.

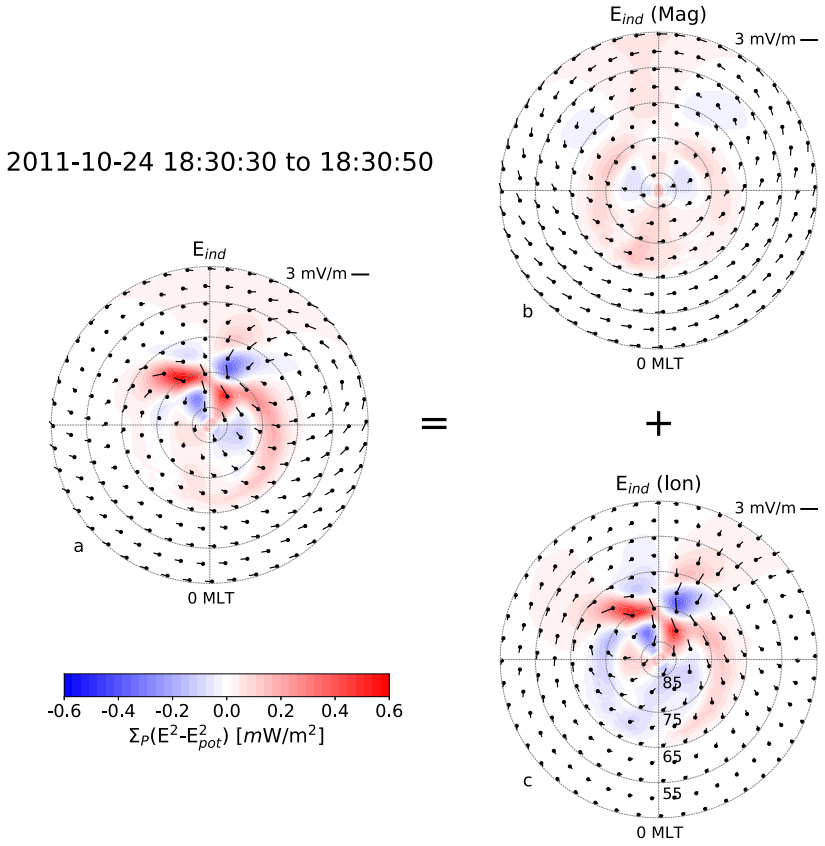

Figure 3. A decomposition of the contribution to $\boldsymbol{E}_{ind}$ and associated Joule heating. Figure 3a shows the modification to the Joule heating when including $\boldsymbol{E}_{ind}$ as a contour similar to Figure 1f with $\boldsymbol{E}_{ind}$ superposed as pins. Figure 3b shows the contribution from magnetospheric currents while Figure 3c shows the contribution from ionospheric currents and FACs.

Graphic design: Communication Division, UiB / Print: Skipnes Kommunikasjon AS

uib.no

ISBN: 978-82-308-5597-3 (PRINT)
978-82-308-4802-9 (PDF)